12-16-92
E7274

NASA Technical Memorandum 105834
ICOMP-92-12; CMOTT-92-08

Center for Modeling of Turbulence and Transition (CMOTT)

Research Briefs–1992

September 1992

NASA

INSTITUTE FOR COMPUTATIONAL MECHANICS IN PROPULSION
NASA
Lewis Research Center
ICOMP
Case Western Reserve University
Ohio Aerospace Institute

NASA Technical Memorandum 105834
ICOMP-92-12; CMOTT-92-08

Center for Modeling of Turbulence and Transition (CMOTT)

Research Briefs–1992

Compiled and Edited by
William W. Liou

Approved by
T.-H Shih
CMOTT Technical Leader

and

Louis A. Povinelli
ICOMP Director

September 1992

NASA

INSTITUTE FOR COMPUTATIONAL MECHANICS IN PROPULSION
NASA Lewis Research Center
ICOMP
Case Western Reserve University
Ohio Aerospace Institute

NASA Technical Memorandum 105834
ICOMP-92-12; CMOTT-92-08

Center for Modeling of Turbulence and Transition (CMOTT)

Research Briefs–1992

Compiled and Edited by
William W. Liou

Approved by
T.-H Shih
CMOTT Technical Leader

and

Louis A. Povinelli
ICOMP Director

September 1992

NASA

Institute for Computational Mechanics in Propulsion
NASA Lewis Research Center
ICOMP
Case Western Reserve University
Ohio Aerospace Institute

Preceding Page Blank

Preceding Page Blank

Table of Contents

Preface

This research brief contains the progress reports of the Research Staff of the Center for Modeling of Turbulence and Transition (CMOTT) from May 1991 to May 1992. It is intended as an annual report to the Institute for Computational Mechanics in Propulsion and NASA Lewis Research Center. A separate report entitled, "Workshop on Engineering Turbulence Modeling," covering some of the 1991 CMOTT Summer research activities was released earlier this year.

The main objective of the CMOTT is to develop, validate and implement the turbulence and transition models for practical engineering flows. The flows of interest are three-dimensional, incompressible and compressible flows with chemical reaction. During this period, the research covers two-equation (e.g., κ-ε) and algebraic Reynolds-stress models, second moment closure models, probability density function (pdf) models, Renormalization Group Theory (RNG), Large Eddy Simulation (LES) and Direct Numerical Simulation (DNS). Last year was CMOTT's second year in operation. CMOTT now has eleven members from ICOMP, NASA LeRC, and Sverdrup Technology Inc., working on various aspects of turbulence and transition modeling in collaboration with NASA-Lewis scientists and Case Western Reserve University faculty members. The CMOTT members have been continuously and actively involved in the international and national turbulence research activities. A biweekly CMOTT seminar series has been conducted with speakers invited from within and without of the NASA Lewis Research Center, including foreign speakers. The current CMOTT roster and its organization are listed in Appendix A. Listed in Appendix B are the abstracts and the scientific and technical issues discussed in biweekly CMOTT seminars. Appendix C gives a list of references which are the papers contributed by CMOTT members in the last two years.

Tsan-Hsing-Shih

Lumley's Energy Cascade Dissipation Rate Model for Boundary-Free Turbulent Shear Flows

B. S. Duncan

1. Motivation and Objective

True dissipation occurs mainly at the highest wavenumbers where the eddy sizes are comparatively small. These high wave numbers receive their energy through the spectral cascade of energy starting with the largest eddies spilling energy into the smaller eddies, passing through each wavenumber until it is dissipated at the microscopic scale. However, a small percentage of the energy does not spill continuously through the cascade but is instantly passed to the higher wave numbers[1]. Consequently, the smallest eddies receive a certain amount of energy almost immediately. As the spectral energy cascade continues, the highest wave number needs a certain time to receive all the energy which has been transferred from the largest eddies. As such, there is a time delay, of the order τ, between the generation of energy by the largest eddies and the eventual dissipation of this energy.

For equilibrium turbulence at high Reynolds numbers, there is a wide range where energy is neither produced by the large eddies nor dissipated by viscosity, but is conserved and passed from wavenumber to higher wavenumber. The rate at which energy cascades from one wavenumber to another is proportional to the energy contained within that wave number. This rate is constant and has been used in the past as a dissipation rate of turbulent kinetic energy. However, this is true only in steady, equilibrium turbulence. Most dissipation models contend that the production of dissipation is proportional the production of energy and that the destruction of dissipation is proportional to the destruction of energy. In essence, these models state that the change in the dissipation rate is proportional to the change in the kinetic energy. This assumption is obviously incorrect for the case where there is no production of turbulent energy, yet energy continues to cascade from large to small eddies. If the time lag between the onset on the energy cascade to the destruction of energy at the microscale can be modeled, then there will be a better representation of the dissipation process. Development of an energy cascade time scale equation will be discussed in Section 2.2.

2. Work Accomplished

2.1 Mean Flow Equations

For incompressible flow, the equations for continuity of mass and axial momentum are written as

$$\frac{\partial U_i}{\partial x_i} = 0$$

and

$$\frac{DU_i}{Dt} = \frac{\partial}{\partial x_j}\left(\nu \frac{\partial U_i}{\partial x_j} + \overline{u_i u_j}\right) - \frac{1}{\rho}\frac{\partial P}{\partial x_i}$$

where, $\overline{u_i u_j}$ is the turbulent Reynolds stress tensor. Using the eddy viscosity concept[2], the Reynolds stress may be related to the mean strain rate and a turbulent eddy viscosity,

$$-\overline{u_i u_j} = \nu_t \left(\frac{\partial U_i}{\partial x_j} + \frac{\partial U_i}{\partial x_j} \right) - \frac{2}{3} k \delta_{ij}. \tag{1}$$

The turbulent viscosity given in the above equation can be interpreted as a measure of the turbulent kinetic energy existing in the flow times a local length scale,

$$\nu_t = c k^{\frac{1}{2}} l$$

where c is an arbitrary constant. The definition used for this length scale is the primary discriminating factor between turbulence models and determines the number of equations which need to be solved. The length scale can be written in terms of the turbulent kinetic energy,k, and its dissipation rate,ϵ,

$$l = \frac{k^{\frac{3}{2}}}{\epsilon}.$$

Now, the momentum equation can be written as

$$\frac{DU_i}{Dt} = \frac{\partial}{\partial x_j} \left((\nu + \nu_t) \frac{\partial U_i}{\partial x_j} \right) - \frac{1}{\rho} \frac{\partial P}{\partial x_i}$$

where,

$$\nu_t = \frac{c_\mu k^2}{\epsilon} \tag{2}$$

and c_μ is a constant. The k and ϵ are determined by solving transport equations for the turbulent kinetic energy and the dissipation. These equations and the modification to the "standard" dissipation equation will be discussed in Section 2.2.

2.2 Turbulence Equations

Taking the Navier-Stokes equations and multiplying by $\hat{u}_i = U_i + u_i$ and then taking the time average yields an equation that contains both the energy equation for the mean velocity, U_i, and a mean energy equation for the fluctuating component of velocity,u_i. Eliminating the energy equation for the mean velocity yields the turbulent energy budget in the absence of a pressure gradient field[3],

$$\frac{Dk}{Dt} = -\frac{\partial}{\partial x_j} \left(\frac{1}{2} \overline{u_i u_i u_j} - 2\nu \overline{u_i s_{ij}} \right) - \overline{u_i u_j} S_{ij} - 2\nu \overline{s_{ij} s_{ij}}. \tag{3}$$

The last term in equation (3) is the rate at which viscous forces perform deformation work to the fluctuating strain rate, defined as

$$s_{ij} = \frac{1}{2} \left(\frac{\partial u_j}{\partial x_i} + \frac{\partial u_i}{\partial x_j} \right).$$

This term is the true viscous dissipation rate which drains kinetic energy from the system, $\epsilon = 2\nu s_{ij}s_{ij}$. This dissipation rate is important to the overall turbulence structure. The next to the last term in equation (3) serves to transport kinetic energy between the mean flow and the turbulence. It is generally referred to as the kinetic energy production term. Writing the mean strain, S_{ij}, as

$$S_{ij} = \frac{1}{2}\left(\frac{\partial U_j}{\partial x_i} + \frac{\partial U_i}{\partial x_j}\right)$$

the production term for incompressible flow is defined as

$$P_k = -\overline{u_i u_j} S_{ij} = \nu_t \left(\frac{\partial U_j}{\partial xi} + \frac{\partial U_i}{\partial x_j}\right)\frac{\partial U_i}{\partial x_j} \tag{4}$$

The last set of terms to be modeled represents the energy redistribution by viscous forces and are contained within the parenthesis on the right hand side of equation (3). From the definition of the fluctuating strain rate,

$$2\nu\overline{u_i s_{ij}} = \nu\frac{\partial k}{\partial x_j}$$

and using a mean gradient hypothesis, the triple correlation can be rewritten as

$$-\overline{u_i u_i u_j} = \frac{\nu_t}{\sigma_k}\frac{\partial k}{\partial x_j}$$

where σ_k is a constant of the order one. Combining all these modeling assumptions yields the high Reynolds number form of the turbulent kinetic equation,

$$\frac{Dk}{Dt} = \frac{\partial}{\partial x_j}\left(\left(\nu + \frac{\nu_t}{\sigma_k}\right)\frac{\partial k}{\partial x_j}\right) + \nu_t\left(\frac{\partial U_i}{\partial x_j} + \frac{\partial U_j}{\partial x_i}\right)\frac{\partial U_i}{\partial x_j} - \epsilon.$$

An equation of the following form has been widely used for modeling of the dissipation,

$$\frac{D\epsilon}{Dt} = \frac{\partial}{\partial x_j}\left(\left(\nu + \frac{\nu_t}{\sigma_\epsilon}\right)\frac{\partial \epsilon}{\partial x_j}\right) + P_\epsilon - \frac{1}{c}\frac{\epsilon^2}{k}.$$

The production term, P_ϵ has been assumed to be proportional to the turbulent kinetic energy production term, equation (4). This approximation places a direct correlation between the production of turbulent energy and the production of dissipation. Although this may be true at equilibrium, where by definition the dissipation equals the turbulent energy production, there are some deficiencies in this statement for the more general case. According to Lumley[1], the modeled dissipation rate equation should be written as,

$$\frac{D\epsilon}{Dt} = \frac{\partial}{\partial x_j}\left(\left(\nu + \frac{\nu_t}{\sigma_\epsilon}\right)\frac{\partial \epsilon}{\partial x_j}\right) + \frac{c_A}{c_D}\epsilon\mathcal{S} - \frac{1}{c_D}\frac{\epsilon^2}{k}. \tag{5}$$

The production term, P_ϵ, now represents the rate at which energy arrives at the dissipative wavenumbers through the energy cascade starting with low wavenumbers. In equation (5), $1/\mathcal{S}$ represents the characteristic time for energy to be transported to the dissipative wave numbers.

In the following equation, the term on the left hand side and the first term on the right represent the transport of the inverse time scale by advection and diffusion, respectively. The remaining terms are the production from the mean straining forces within the large scale mean flow structures and the dissipative losses at the microscale,

$$\frac{D\mathcal{S}}{Dt} = \frac{\partial}{\partial x_j}\left(\left(\nu + \frac{\nu_t}{\sigma_S}\right)\frac{\partial \mathcal{S}}{\partial x_j}\right) + \left(\sqrt{S_{ij}S_{ij}} - \mathcal{S}\right)\frac{1}{c_b T}$$

The production and loss terms have been scaled by a characteristic time, T, which in this study has been taken to be a weighted function of the time scale for the large eddies, τ,

$$T = \frac{\tau}{2C_B}.$$

Since most energy enters the cascade at scales comparable to the integral scale, l, the characteristic time scale of the large eddies dictates the rate of energy transfer and is defined as $\tau = \frac{l}{u}$ for nearly isotropic turbulence. Using the approximation for the integral length scale as, $l = \frac{u^3}{\epsilon}$, the time scale becomes

$$\tau = 2\frac{k}{\epsilon}$$

which is valid even in nonequilibrium flows. Letting C_B be a function of mean and turbulent quantities, the inverse time scale equation can be written as

$$\frac{D\mathcal{S}}{Dt} = \frac{\partial}{\partial x_j}\left(\left(\nu + \frac{\nu_t}{\sigma_S}\right)\frac{\partial \mathcal{S}}{\partial x_j}\right) + \frac{C_B}{c_B}\left(\sqrt{S_{ij}S_{ij}} - \mathcal{S}\right)\frac{\epsilon}{k}$$

where

$$C_B = 1 + \frac{9k\sqrt{S_{ij}S_{ij}}}{\epsilon}.$$

Determination of the modeling constants is discussed in the next section.

2.3 Model Constants

In this paper, only high Reynolds number turbulence has been considered. The model constants are examined for the grid turbulence case where the mean velocity gradients and strain rates vanish. For this case, turbulent intensity decays with the following proportionality,

$$\left(\frac{k}{k_0}\right) \propto \left(\frac{t}{t_0}\right)^{-n}, \text{ where, } t = \frac{x}{U_0}$$

so that the dissipation rate must decay as

$$\left(\frac{\epsilon}{\epsilon_0}\right) \propto \left(\frac{t}{t_0}\right)^{-(n+1)}.$$

Here, n is the decay rate and is typically in the range $1.1 \leq n \leq 1.3$. Substituting these relationships into the inverse time scale equation yields

$$\frac{1}{\mathcal{S}} d\mathcal{S} = -\frac{nC_B}{tc_B} dt.$$

After integration, this equation is

$$\mathcal{S} = \alpha t^{-\frac{nC_B}{c_B}}$$

where α is a constant of integration. For there to be an inverse scaling relationship between $\mathcal{S}$ and t, the exponent in the above equation must reduce to -1 for the grid turbulence case. Since the coefficient C_B reduces to 1.0 in grid turbulence, then

$$c_B = n.$$

In this study, n has been set to 1.1 and held constant[4], which sets the value of c_B. Now using the fact that, initially,

$$\mathcal{S}_0 t_0 = \frac{3}{2\sqrt{2}}$$

the coefficients c_A and c_D are related as follows

$$\frac{1}{c_D} = \frac{3}{2\sqrt{2}} \frac{c_A}{c_D} + \frac{n+1}{n}.$$

The coefficient c_μ has been evaluated for equilibrium turbulence where, where $P_k = \epsilon$. Rewriting equation (2) as

$$c_\mu = \frac{\nu_t \epsilon}{k^2}$$

and using equations (1) and (4), this coefficients is

$$c_\mu = \frac{\overline{u_i u_j}^2}{k^2} = 0.09.$$

After the above analysis, the only adjustable parameters are $\frac{c_A}{c_D}$ and the σ coefficients, which should be of the order one. The complete set of optimized coefficients is given in Table 1.

$\sigma_k = 0.9$	$n = 1.1$
$\sigma_\epsilon = 1.1$	$c_B = n$
$\sigma_S = 1.0$	$C_B = 1 + \frac{9k\sqrt{\mathcal{S}_{ij}\mathcal{S}_{ij}}}{\epsilon}$
$c_\mu = 0.09$	$\frac{1}{c_D} = \frac{3}{2\sqrt{2}} \frac{c_A}{c_D} + \frac{n+1}{n}$
$\frac{c_A}{c_D} = 1.13$	

Table 1. k–ϵ–$\mathcal{S}$ Model Coefficients

2.4 Free Shear Flows

The three turbulent transport equations are solved implicitly using the finite difference technique of Spalding[5] for parabolic equation systems. An initial profile is imposed upon the first marching plane for the turbulent kinetic energy and the dissipation, and $\mathcal{S}$ is initially set to $\mathcal{S}_{,} = \frac{\epsilon_0}{k_0}$. In the mixing layer and jet cases, the initial plane was equally divided into a uniform velocity field and still air. For the case of the plane wake, this initial profile came from a flat plate calculation computed with the same solution technique. Starting with the initial plane, the flow field is developed by marching the transport equations downstream and applying the following boundary conditions,

Planar Jet

Centerline $(y = 0)$ $\quad \frac{\partial k}{\partial y} = 0 \, , \, \frac{\partial \epsilon}{\partial y} = 0$

$$\mathcal{S}_{y=0} = \frac{\mathcal{S}_{old} c_b k U_{y=0} + \frac{\partial}{\partial y}\left((\nu+\nu_t)\frac{\partial \mathcal{S}}{\partial y}\right)}{c_b k U_{y=0} + \epsilon \Delta x}$$

Far Field $(y = y_{max})$ $\quad k = 0 \, , \, \epsilon = 0 \, , \, \mathcal{S} = 0$

Round Jet

Centerline $(r = 0)$ $\quad \frac{\partial k}{\partial r} = 0 \, , \, \frac{\partial \epsilon}{\partial r} = 0$

$$\mathcal{S}_{r=0} = \frac{\mathcal{S}_{old} c_b k U_{r=0} + \frac{\partial}{\partial r}\left((\nu+\nu_t)\frac{\partial \mathcal{S}}{\partial r}\right)}{c_b k U_{r=0} + \epsilon \Delta x}$$

Far Field $(r = r_{max})$ $\quad k = 0 \, , \, \epsilon = 0 \, , \, \mathcal{S} = 0$

Planar Mixing Layer

Centerline $(y = y_{min})$ $\quad \frac{k}{{U^2}_{y=ymin}} = 0.015, \frac{\epsilon L}{U^3_{y=ymin}} = 3.5 \times 10^{-6}$

$$\mathcal{S}_{y=ymin} = \frac{\epsilon}{k}$$

Far Field $(y = y_{max})$ $\quad k = 0 \, , \, \epsilon = 0 \, , \, \mathcal{S} = 0$

Planar Wake

Centerline $(y = 0)$ $\quad \frac{\partial k}{\partial y} = 0 \, , \, \frac{\partial \epsilon}{\partial y} = 0$

$$\mathcal{S}_{y=0} = \frac{\mathcal{S}_{old} c_b k U_{y=0} + \frac{\partial}{\partial y}\left((\nu+\nu_t)\frac{\partial \mathcal{S}}{\partial y}\right)}{c_b k U_{y=0} + \epsilon \Delta x}$$

Far Field $(y = y_{max})$ $\quad k = 0 \, , \, \epsilon = 0 \, , \, \mathcal{S} = 0$

The solutions have been checked after several hundred steps to insure that the profiles have become self-similar.

2.4.1 Planar Jet

The three equation k–ϵ–S model performed very well for planar jet flow when compared to the experimental data of Gutman and Wygnanski[6], Bradbury[7] and Heskestad[8]. Mean velocities profiles given in Figure 1 are well predicted by both the k–ϵ–S model and the standard k–ϵ model, which is reassuring since the coefficients for both of these models were optimized for the planar jet case. The spreading rates predicted by both models are within the experimental range and are given in Table 2.

There is a slight discrepancy between the k–ϵ–S model and the standard k–ϵ model for centerline kinetic energy as can be seen in Figure 2. However, both predictions are well within the range of experimental measurements, which show a considerable spread near the centerline of the jet. Both predictions are closely aligned with the data of Bradbury[7].

Shear stress is also well predicted (see Figure 3) where the standard k–ϵ model over-predicts the shear stress at the edge of the jet in comparison to the data of Gutman and Wynanski[6] and Bradbury[7]. The k–ϵ–S model predicts a narrower profile, also indicated by the smaller spreading rate, which agrees with Bradbury's measurements. Towards the centerline of the jet, both models accurately predict the increase in shear stress and the extrema near $\frac{y}{x} = 0.08$.

For the next two figures, Figures 4 and 5, there is no experimental data available for comparison. The dissipation reaches a maximum at the location of the peak shear stress, Figure 4. From this extrema, the dissipation decreases toward the centerline and also eventually trails off to zero at the edge of the jet. Figure 5 shows the behavior of the time scale for the planar jet. Notice that the minimum energy transfer time between the large scale structure to the dissipative microscale is in the middle of the jet (where $\mathcal{S}$ is a maximum since the dimension of $\mathcal{S}$ is t^{-1}).

2.4.2 Axisymmetric Jet

A primary problem with the standard k–ϵ model is its predictive capability for a 2–D versus a 3–D jet, the free jet anomaly. In Figures 6 – 10, the standard k–ϵ model is unable to predict any of the turbulence quantities correctly, overpredicting not only the turbulent kinetic energy and the shear stress but also the mean velocity. The standard k–ϵ can be "fixed" using a suggestion by Pope[9]. Writing the standard ϵ equation for reference,

$$\frac{D\epsilon}{Dt} = \frac{\partial}{\partial x_j}\left(\left(\nu + \frac{\nu_t}{\sigma_\epsilon}\right)\frac{\partial \epsilon}{\partial x_j}\right) + c_1 P_k \frac{\epsilon}{k} - \frac{1}{c}\frac{\epsilon^2}{k}$$

the correct spreading rate can be obtained by changing c_1 from its standard value of 1.45 to 1.6 (see Table 2). Clearly, by modifying a coefficient, the standard k–ϵ model is capable of predicting the correct spreading rate; however, this model cannot be considered general. The spreading rate predicted by the k–ϵ–S model is very close to the experimentally measured rate and has been obtained with no modifications to the model.

Comparisons between the k–ϵ–S model and the experimental data[10,11,12], Figures 6 – 10, indicates that the new model accurately predicts the mean velocity profiles and the shearing stress across the jet. Less accurately predicted by the k–ϵ–S model is the centerline turbulent kinetic energy, Figure 7, where there is considerable scatter in the experimental data.

2.4.3 Planar Mixing Layer

For the case of a planar mixing layer, neither model accurately predicts the high speed side of the layer (see Figures 11 – 15). The experimental data[13] contains a much more dispersive edge compared to the computations, Figure 11. One explanation may be wind tunnel noise. Adding a boundary condition specifying a given noise level, 12 percent fluctuating velocity, increases the spreading on the high speed side of the computations and improves the comparisons with the data. This boundary condition is used with both models. Unfortunately, there is no way to determine what the true noise level was in the experiments or whether its effect has been properly accounted for computationally.

An analytical solution for the mean velocity profile has been described by Schlichting[14]. This analytic solution lies between the experimental data and the two computational models for the case when $\sigma = 9.5$ (σ is a "tweeking" constant used to tune the analytic solution to match the experimental data. Typical values of σ are between 9[13] and 11[15].)

Both the k–ϵ–S and the standard k–ϵ model predict the peak value of turbulent kinetic energy quite well (Figure 12). However, this peak is shifted toward the low speed side of the mixing layer compared to the experimental peak. Patel[16] indicated that the data of Wygnanski and Fielder[13] had shifted towards the low speed side, which is opposite from the trend noticed in this study. Since the discrepancy between the data and the computations lies on the high speed side of the mixing layer, the problem could be a result of wind tunnel noise as previously mentioned. In the the plot of Reynolds stresses, Figure 13, both models over predict the shear stress by nearly 30 percent and consequently over-predict the spreading rate given in Table 2.

The k–ϵ–S model and the standard k–ϵ model predict almost identical levels of dissipation (Figure 14). Since a turbulent kinetic energy level is specified at the high speed boundary, the dissipation is also specified on this boundary. A constant value of $\frac{\epsilon L}{U_{max}^3} = 6.5 \times 10^{-6}$ gave the best fit to the data. Figure 15 shows the inverse time scale distribution through the mixing layer. The minimum energy transfer time, where $\mathcal{S}$ is a maximum, corresponds to the location of the maximum shear stress. At the high speed edge of the mixing layer, the time scale is specified to be $\mathcal{S} = \frac{\epsilon}{k}$.

2.4.4 Planar Wake

For the case of the planar wake, the mean velocity profile is correctly predicted towards the centerline of the wake, but drops off too quickly at the wake edges (see Figure 16). Although the mean velocity shows the correct shape in Figure 16, the centerline velocity is high compared to the analytical solution described in Reference [14] (see Figure 17). As a result, the spreading rates, $(\frac{U_\infty}{U_\infty - U_0}\frac{dy_{\frac{1}{2}}}{dx})$, predicted by the turbulence models are 6 percent too low for the k–ϵ–S model and 3 percent too low for the k–ϵ model as compared to the analytical solution. In other words, the turbulence models are predicting a much more compact wake with a smaller velocity defect than is seen in the experimental data or the analytical fit. This trend is also seen in the turbulent kinetic energy profiles in Figure 18 where the k–ϵ–S model can predict the correct maximum intensity but drops off too quickly towards the edges. Also, although the computed peak value for shear stress is correct the width of the curve is too narrow, with the location of the extrema lying too near the centerline (see Figure 19).

The dissipation levels computed by the models apparently reduce the turbulent intensity of the flow too much near the edges of the wake, which prevents the wake from spreading. There is unfortunately no experimental data to compare with the dissipation curves in Figure 20. Interestingly, the location of the minimum energy transfer time in Figure 21 is towards the outer edges of the wake where the mean flow should exert its greatest influence.

	Experiment	k–ϵ–$\mathcal{S}$ Model	k–ϵ Model
Planar Jet	0.11–0.12	0.114	0.114
Round Jet	0.085–0.095	0.095	0.126, $c_1 = 1.45$ 0.0928, $c_1 = 1.6$
Planar Mixing Layer	0.16	0.186	0.186
Planar Wake	.101[14]	0.095	0.098

Table 2. Spreading Rate Comparisons for Free Shear Flow

3. Future Work

Future plans include:

i) Extending this model to wall bounded flow. Specifically, a low Reynolds number version of this model will be developed for near wall turbulence.

ii) Continuing to run this model for more test cases over a variety of flow fields.

4. References

[1] Lumley, J. L., "Some comments on turbulence", Physics of Fluids **4** (1992).

[2] Boussinesq, J., "Essai sur la théorie des eaux courantes", Mém. prés. Acad. Sci. **XXIII** (46) (1877).

[3] Tennekes, H. & Lumley, J. L., *A First Course in Turbulence* The MIT Press (1972).

[4] Launder, B. E., "Turbulence transport models for numerical computation of complex turbulent flows",*Measurements and Predictions of Complex Turbulent Flows* Von Karman Institute for Fluid Dynamics, Rhode Saint Genese, Belgium (1980).

[5] Spalding,D. B., *GENMIX: A General Computer Program for Two-Dimensional Parabolic Phenomena* Pergamon Press (1977).

[6] Gutmark, E. & Wygnanski, I., "The Planar Turbulent Jet", Journal of Fluid Mechanics **73**, 465–495 (1976).

[7] Bradbury, L. J. S., "The Stucture of the Self-Preserving Jet" Journal of Fluid Mechanics **23** 31–64 (1965).

[8] Heskestad, G., "Hot-Wire Measurements in a Plane Turbulent Jet" Journal of Applied Mechanics (1965).

[9] Pope, S. B., "An Explanation of the Turbulent Round-Jet/Plane-Jet Anomaly" AIAA Journal **16** (1978).

[10] Wygnanski, I. & Fiedler, H. E., "Some measurements in the self-preserving jet" Journal of Fluid Mechanics **38** 577–612.

[11] Rodi, W., "A New Method of Analyzing hot-wire Signals in Highly Turbulent Flow and Its Evaluation in Round Jet" Disa Information No. 17 (1975).

[12] Abbiss, J. B. & Bradbury, L. J. S. & Wright, M. P., "Measurements in an Axisymmetric Jet Using a Photon Correlator" *Proceeding of LDA Symposium* Copenhagen (1975).

[13] Wygnanski, I. & Fiedler, H. E., "The two-dimensional mixing region", Journal of Fluid Mechanics **41** 327–361 (1970).

[14] Schlichting, H.,*Bounday-Layer Theory* McGraw-Hill (1951).

[15] Liepmann, H. W. & Laufer, J., "Investigations of Free Turbulent Mixing" NACA Technical Note 1257 (1947).

[16] Patel, R, "An Experimental Study of a Plane Mixing Layer", AIAA Journal **11** (1) (1973).

[17] Chevray, R. & Kovasznay, L. S. G., "Turbulence Measurements in the Wake of a Thin Flat Plate" AIAA Journal **7** (1969).

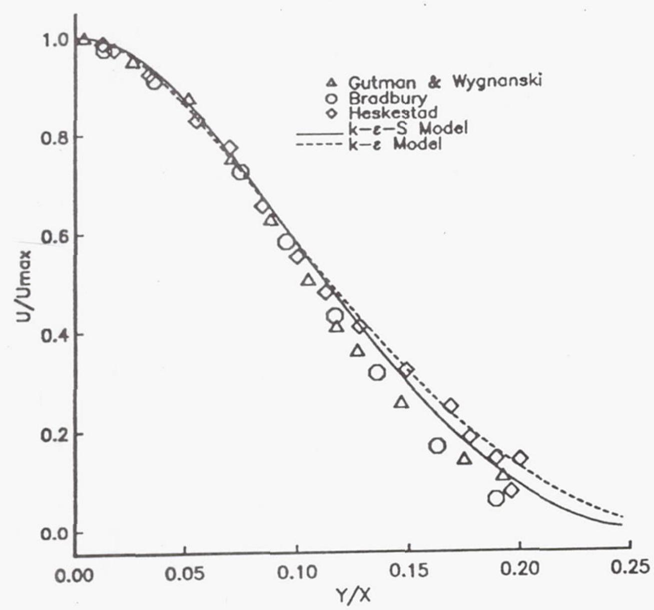

Figure 1: Mean velocity profile for a turbulent, planar jet. U_{max}: centerline velocity.

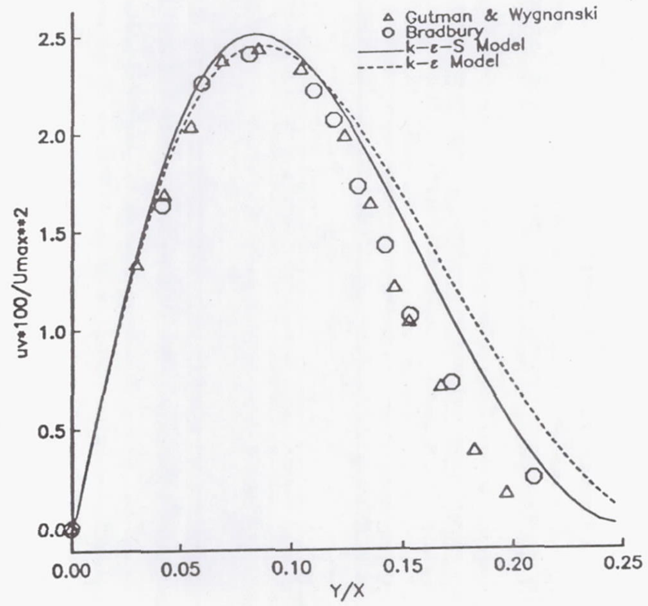

Figure 3: Shear stress profile for a planar jet. U_{max}: centerline velocity.

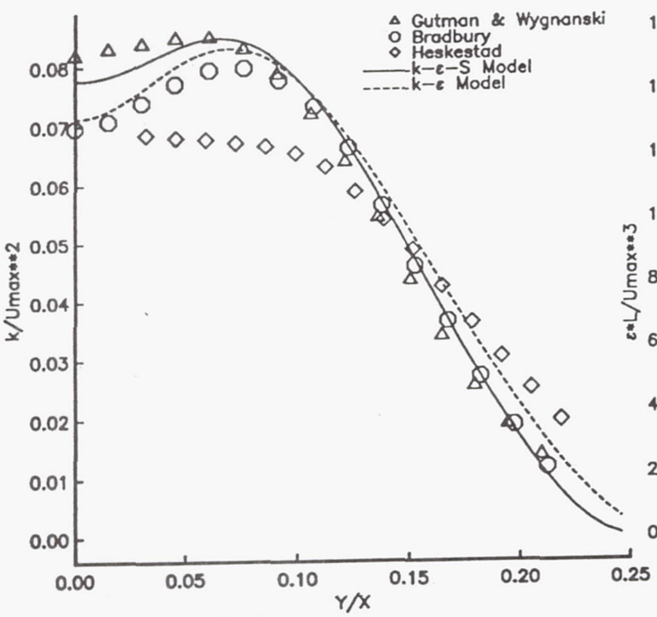

Figure 2: Turbulent kinetic energy profile for a planar jet. U_{max}: centerline velocity.

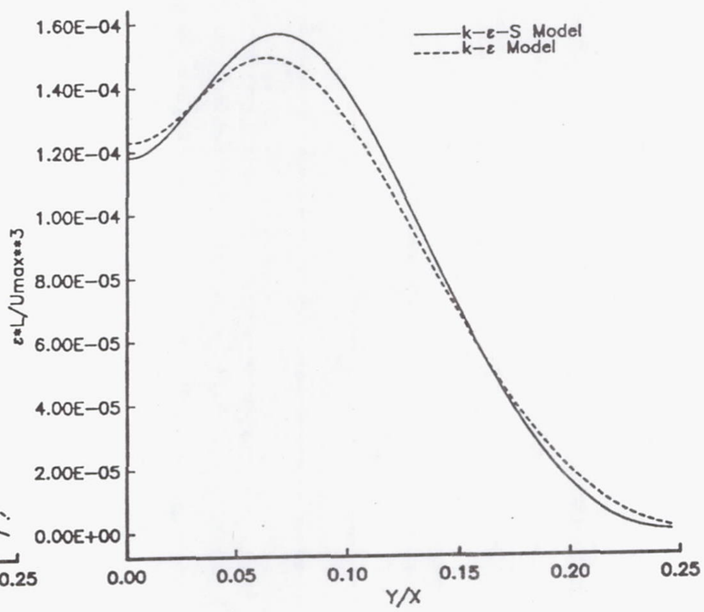

Figure 4: Dissipation rate profile for a planar jet. U_{max}: centerline velocity.

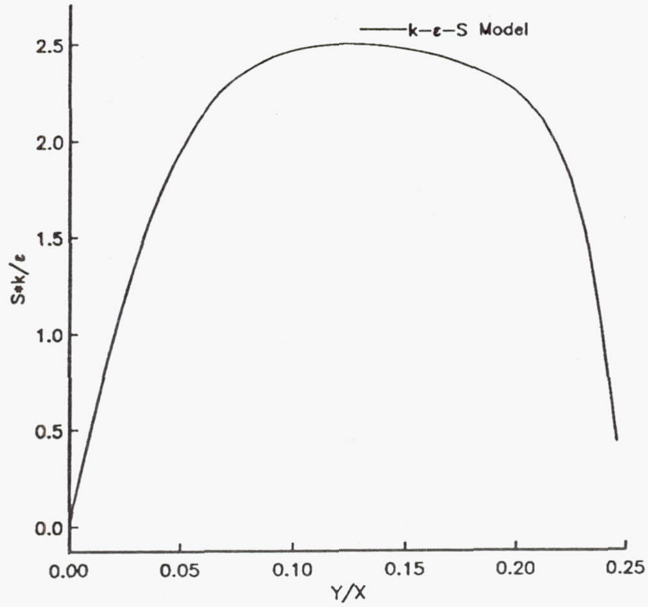

Figure 5: Time scale profile for a planar jet

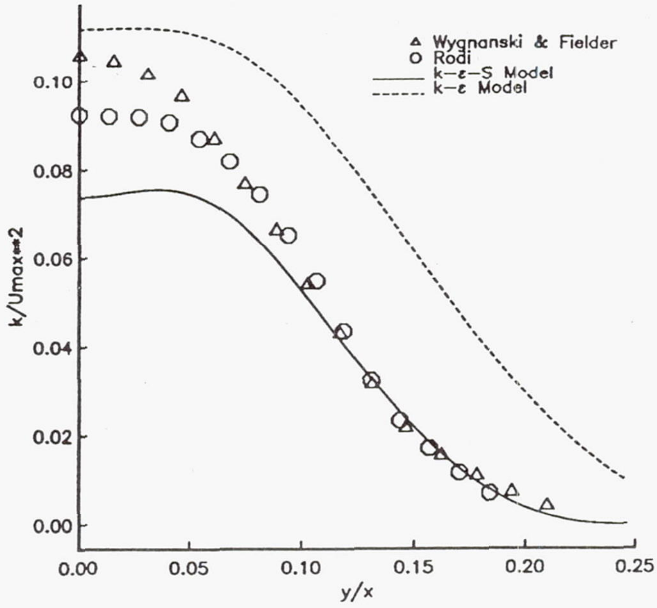

Figure 7: Turbulent kinetic energy profile for an axisymmetric jet. U_{max}: centerline velocity.

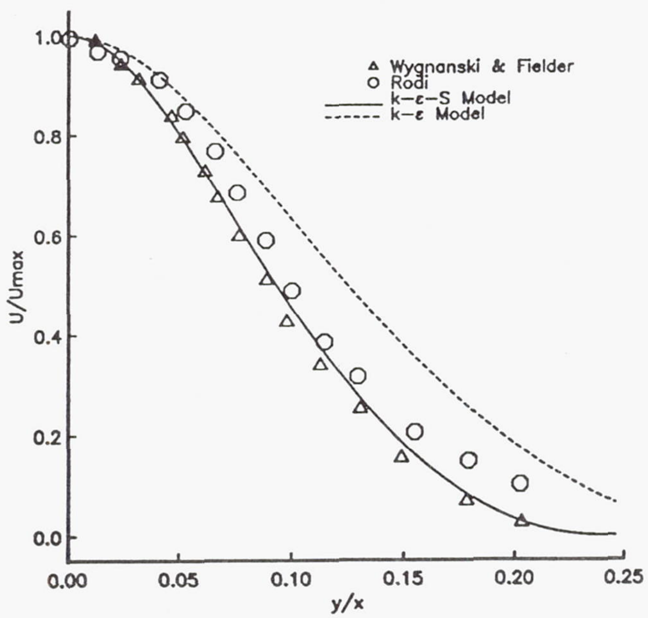

Figure 6: Mean velocity profile for a turbulent, axisymmetric jet. U_{max}: centerline velocity.

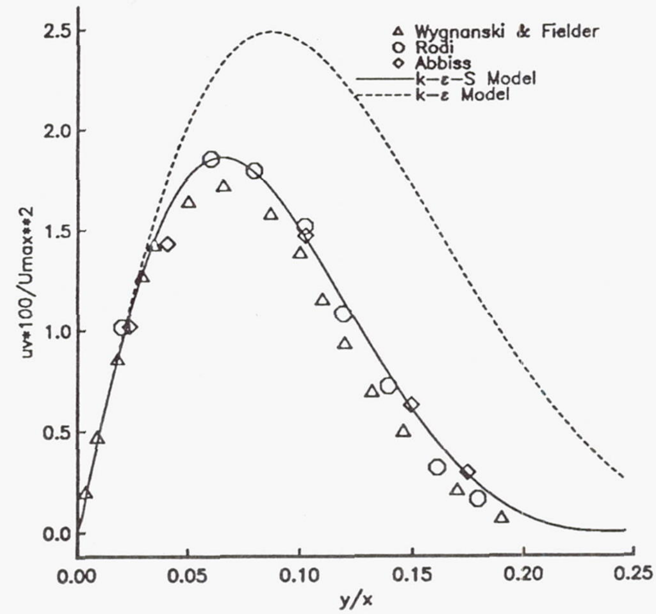

Figure 8: Shear stress profile for an axisymmetric jet. U_{max}: centerline velocity.

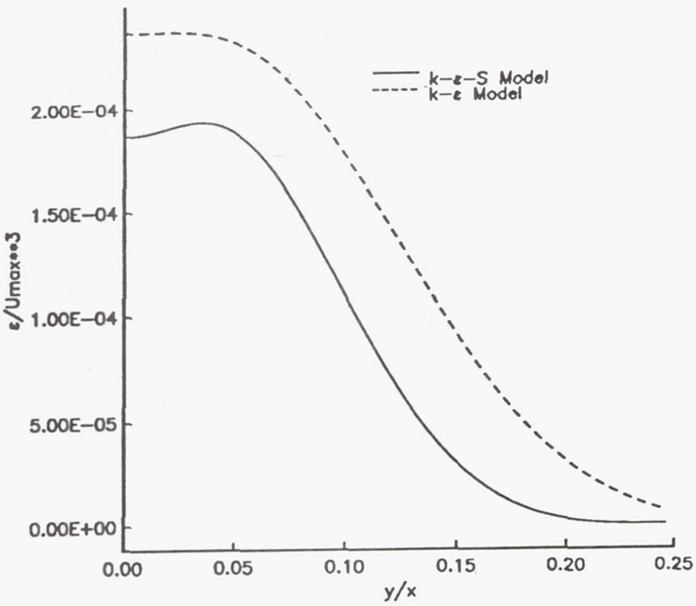

Figure 9: Dissipation rate profile for an axisymmetric jet. U_{max}: centerline velocity.

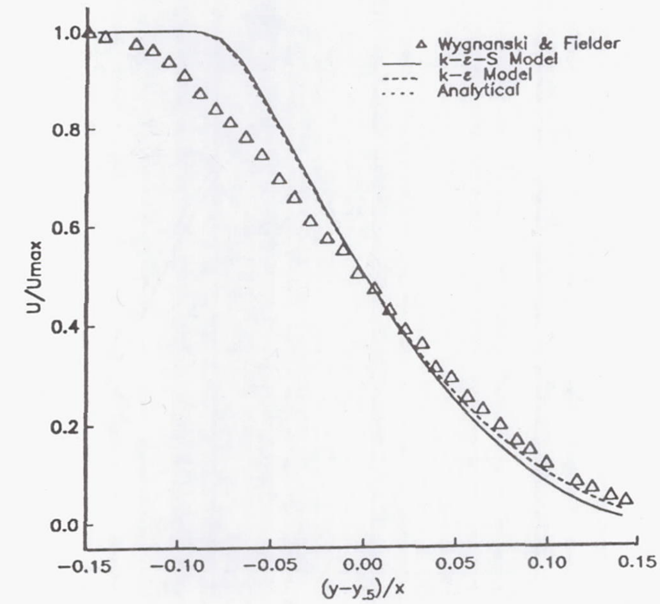

Figure 11: Mean velocity profile for a planar mixing layer. U_{max}: centerline velocity. — analytical solution

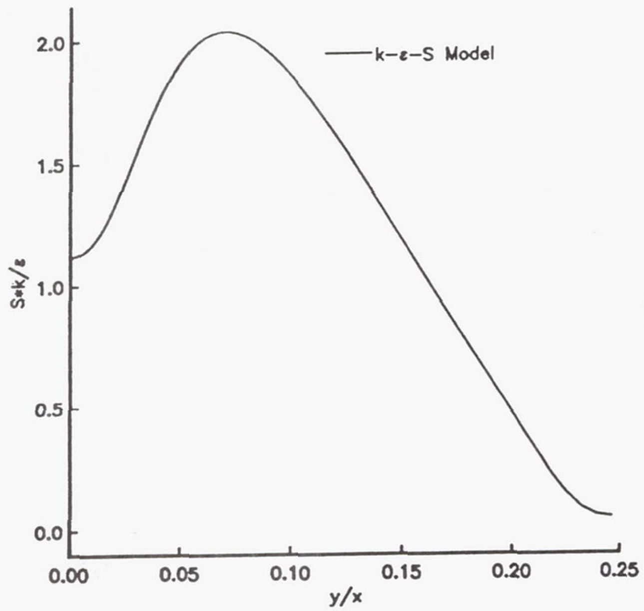

Figure 10: Time scale profile for an axisymmetric jet

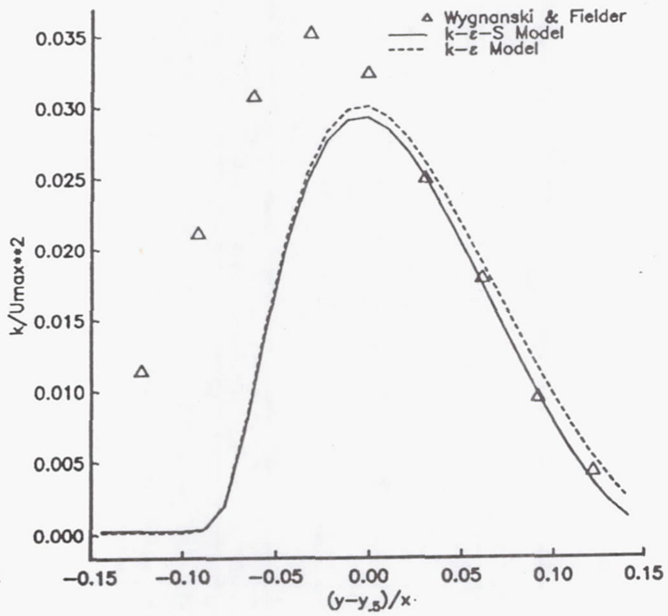

Figure 12: Turbulent kinetic energy profile for a planar mixing layer. U_{max}: centerline velocity.

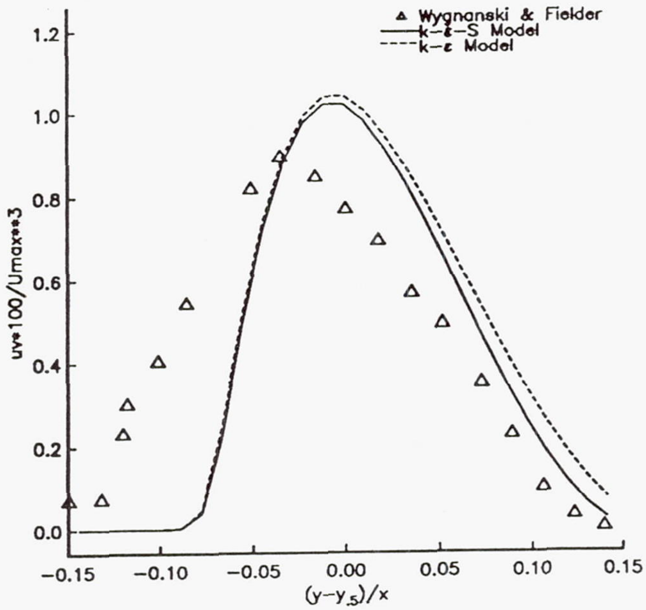

Figure 13: Shear stress profile for a planar mixing layer. U_{max}: centerline velocity.

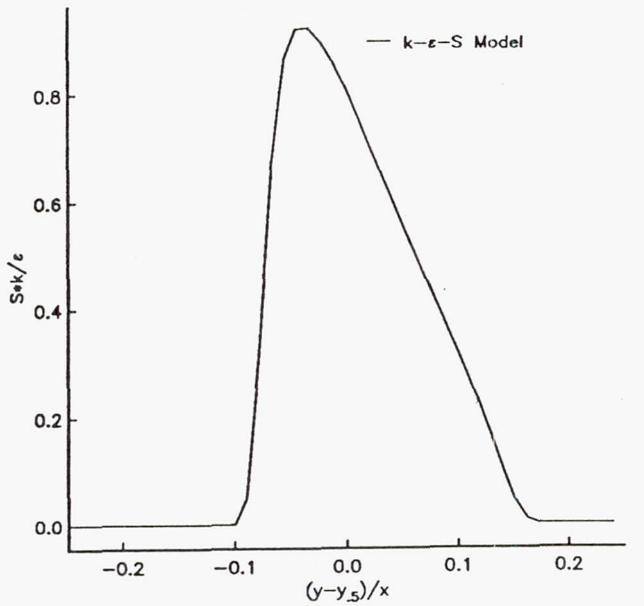

Figure 15: Time scale profile for a planar mixing layer

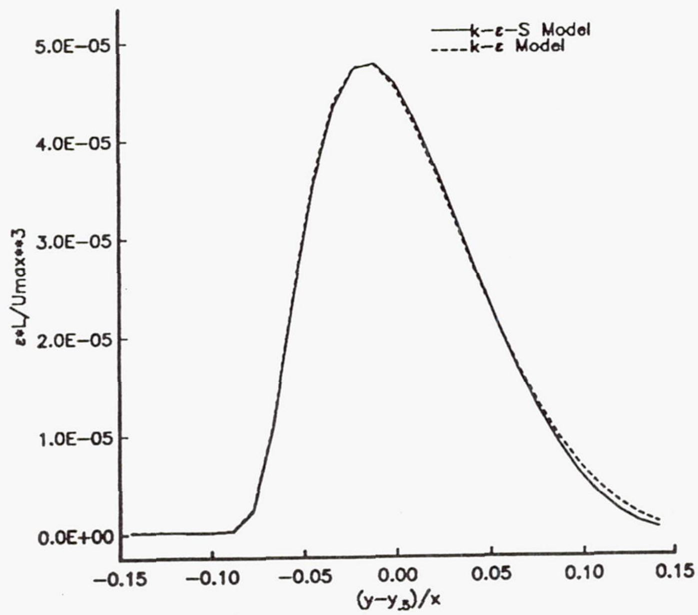

Figure 14: Dissipation rate profile for a planar mixing layer. U_{max}: centerline velocity.

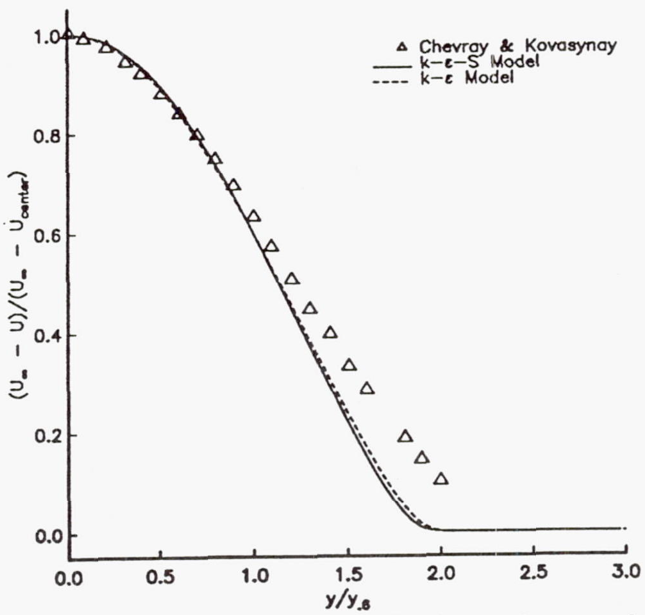

Figure 16: Mean velocity profile for a planar wake behind a flat plate. U_{center}: centerline velocity, U_∞: freestream velocity. — analytical solution

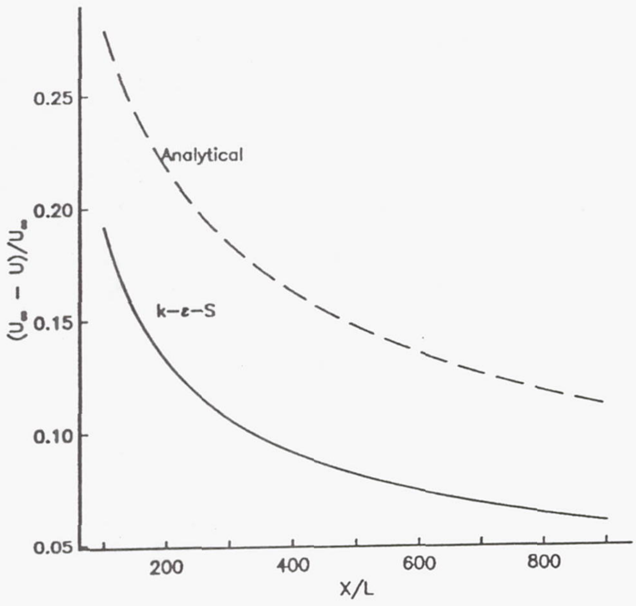

Figure 17: Axial mean centerline velocity for a planar wake behind a flat plate. U_∞: freestream velocity.

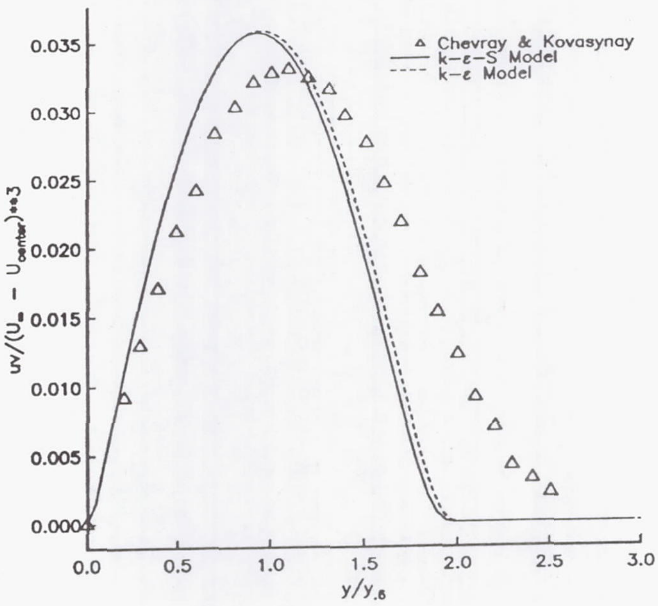

Figure 19: Shear stress profile for a planar wake behind a flat plate. U_{center}: centerline velocity, U_∞: freestream velocity.

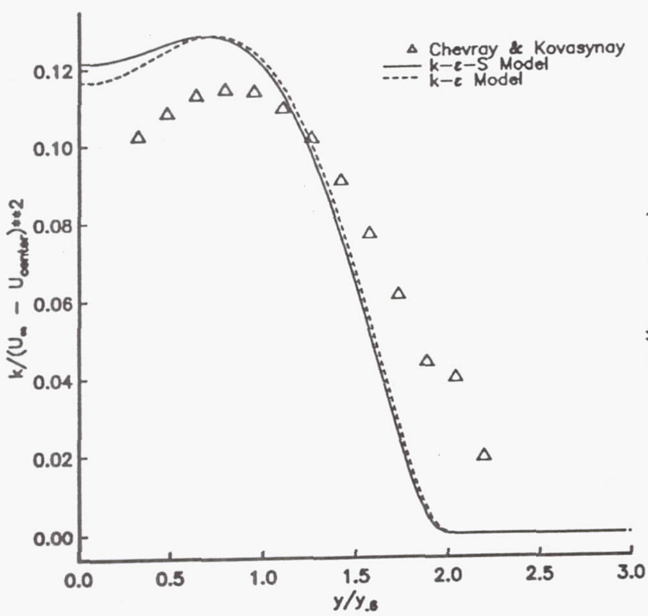

Figure 18: Turbulent kinetic energy profile for a planar wake behind a flat plate. U_{center}: centerline velocity, U_∞: freestream velocity.

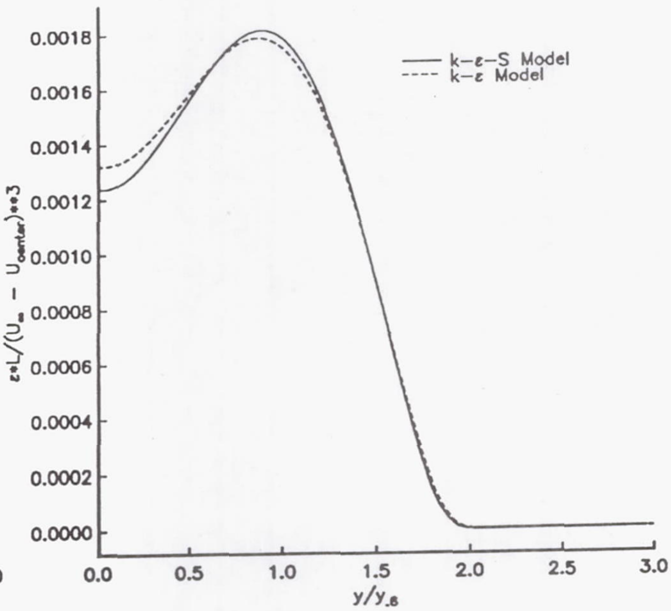

Figure 20: Dissipation rate profile for a planar wake behind a flat plate. U_{center}: centerline velocity, U_∞: freestream velocity.

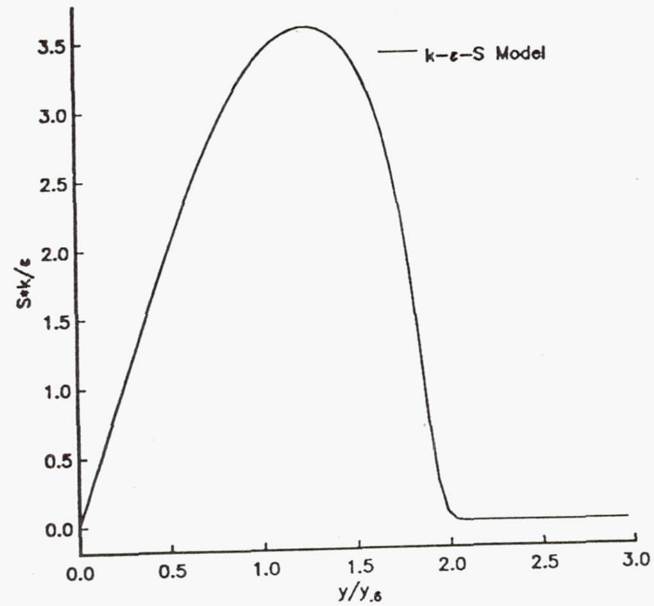

Figure 21: Time scale profile for a planar wake behind a flat plate

PDF Turbulence Modeling and DNS

A. T. Hsu

1. Motivations and Objectives

The problem of time discontinuity (or jump condition) in the coalescence/dispersion (C/D) mixing model is addressed in first part (PDF) of this work. A C/D mixing model continuous in time is introduced. With the continuous mixing model, the process of chemical reaction can be fully coupled with mixing. In the case of homogeneous turbulence decay, the new model predicts a pdf very close to a Gaussian distribution, with finite higher moments also close to that of a Gaussian distribution. Results from the continuous mixing model are compared with both experimental data and numerical results from conventional C/D models.

The effect of Coriolis forces on compressible homogeneous turbulence is studied using direct numerical simulation (DNS). The numerical method used in this study is an eigth order compact difference scheme. Contrary to the conclusions reached by previous DNS studies on *incompressible* isotropic turbulence, the present results show that the Coriolis force increases the dissipation rate of turbulent kinetic energy, and that anisotropy develops as the Coriolis force increases. The Taylor-Proudman theory does apply since the derivatives in the direction of the rotation axis vanishes rapidly. A closer analysis reveals that the dissipation rate of the incompressible component of the turbulent kinetic energy indeed decreases with a higher rotation rate, consistent with incompressible flow simulations (Bardina[17]), while the dissipation rate of the Compressible part increases; the net gain is positive. Inertial waves are observed in the simulation results.

2. Work Accomplished

2.1 PDF Turbulence Model for Combustion

In Collaboration with J.Y. Chen

Accurate prediction of turbulent reacting flows requires the solution of an evolution equation for the probability density function (pdf) of the thermo-chemical variables using Monte Carlo simulation. Since the pdf equation, like most equations describing turbulent motion, is not closed, closure models have to be devised. For the pdf of scalars, the terms in the pdf equation that need modeling are molecular mixing and turbulent convection. The present work deals with the modeling of molecular mixing.

Most of the mixing models are based on the coalescence/dispersion (C/D) model by Curl[6] This model is known to have deficiencies, and efforts had been made to correct these deficiencies, for example, Janicka, et al. 1979 and Pope 1982. The most recent efforts have been devoted to the problem of coupling between mixing and chemical reaction. Chen and Kollmann[4] proposed a reaction conditioned model that allows correct prediction of combustion in the flame-sheet regime. Norris and Pope[10] proposed a new model based on ordered pairing that aimed at the same end.

All the existing models suffer in one respect, namely, they are discontinuous in time: once a pair of particles are chosen to participate in mixing, their properties will jump abruptly regardless of the step size of the time integration. This phenomenon, clearly non-physical, could cause difficulty in coupling the processes of mixing and chemical reaction. In the present work, a new model that is continuous in time is proposed. With this new model, the processes of molecular mixing and chemical reaction can be fully coupled.

In the case of homogeneous turbulence decay of a scalar, one expects a Gaussian distribution for the pdf, and finite values for the higher moments. Pope[11] pointed out the modified Curl model could not produce the correct pdf for this problem, and the higher even moments from that model tend to infinity; he suggested an age biased sampling process to overcome these shortcomings. The present continuous model, as we will show, predicts a pdf distribution very close to Gaussian for homogeneous turbulence decay, and gives finite higher moments with values close to that of a Gaussian distribution.

The continuous mixing model is applied to the study of both non-reacting and reacting flows, and the results are compared with earlier calculations by Hsu[7] as well as with experimental data.

2.1.1 Molecular Mixing Model

The evolution equation of a single point probability density function of scalar random variables $\psi_1, ..., \psi_n$ — representing the species mass fraction and temperature — can be written as

$$\bar{\rho}\partial_t\tilde{P} + \bar{\rho}\tilde{v}_\alpha\partial_\alpha\tilde{P} + \bar{\rho}\sum_{i=1}^{N}\partial_{\psi_i}\{w_i(\psi_1, ..., \psi_N)\tilde{P}\}$$

$$= -\partial_\alpha(\bar{\rho} < v''_\alpha|\phi_k(x) = \psi_k > \tilde{P})$$

$$-\bar{\rho}\sum_{i=1}^{N}\sum_{j=1}^{N}\partial^2_{\psi_i\psi_j}(< \epsilon_{ij}|\phi_k(x) = \psi_k > \tilde{P})$$

where the terms represent the rate of time change, mean convection, chemical reaction, turbulent convection, and molecular mixing, respectively; $\tilde{P}$ is the density-weighted joint pdf:

$$\tilde{P} = \rho P/\bar{\rho},$$

ϵ is the scalar dissipation:

$$\epsilon_{ij} = D\partial_\alpha\phi_i\partial_\alpha\phi_j,$$

(where D is the diffusion coefficient), and $< x|y >$ denotes the mathematical expectation of a random function x conditioned upon y.

The left hand side of the above equation can be evaluated exactly and requires no modeling; the right hand side terms contain the conditional expectation of the velocity fluctuation and the conditional expectation of the scalar dissipation, which are new unknowns and require modeling. In the present work we concentrate on the modeling of the second term, namely, the conditional expectation of the scalar dissipation, referred to as molecular mixing in the following.

The Modified Curl Model

The simplest and most used mixing model is the modified Curl model, which assumes binary interaction between sample fluid particles. As described by Pope[12] in a Monte Carlo simulation, the continuous pdf is replaced by delta functions

$$P^*(\psi;t) = \frac{1}{N}\sum_{n=1}^{N}\delta(\psi - \phi_n(t)),$$

where each delta function represents one sample fluid particle of an ensemble of N particles. The evolution of P^* entails the movement of the particles in the ψ–space, or the evolution of the individual values of ϕ_n's.

With the modified Curl model, the change of ϕ_n due to molecular mixing is achieved by the following binary interaction process: divide the flow domain into small cells, each containing N sample particles. Given a small time interval δt and a turbulent time scale τ, select randomly N_{mx} pairs of particles,

$$N_{mx} = 0.5\frac{\delta t}{C\tau}N,$$

($C = 6.0$) and let a pair, say, m and n, mix as follows

$$\phi_n(t+\delta t) = A\phi_m(t) + (1-A)\phi_n(t) \tag{1}$$

$$\phi_m(t+\delta t) = A\phi_n(t) + (1-A)\phi_m(t) \tag{2}$$

where $A = 0.5\xi$, with ξ a random variable uniformly distributed on the interval [0,1]. The remaining $N - 2N_{mx}$ particles remain unchanged:

$$\phi_n(t+\delta t) = \phi_n(t)$$

This model does not represent the true physical process since the properties of the sample particles change discontinuously regardless the size of the time interval δt. This deficiency can be best illustrated by rearranging eq. (1) and dividing it by δt

$$\frac{(\phi_n(t+\delta t) - \phi_n(t))}{\delta t} = \frac{A}{\delta t}(\phi_m(t) - \phi_n(t)) \tag{3}$$

The derivative $\frac{d\phi_n}{dt}$ does not exist because as δt goes to zero the right hand side of the equation becomes infinite since both A and the difference between $\phi_m(t)$ and $\phi_n(t)$ are finite. This means that there is a sudden jump in the value of the scalar quantities, which is typical of a Poisson process, but is non-physical in the present case since the flow properties of turbulence are continuous.

Continuous Mixing Model

One can see from the previous section that the modified Curl model relies on the parameter N_{mx} to control the extent of mixing. On the individual particle level, it assumes complete mixing once the particle is selected as one of the mixing pair, without considering the size of δt.

In order to achieve continuous mixing, we propose the following model: during a time interval δt, we assume that all the particles within a cell participate in mixing. The extent of the mixing is controlled at the individual particle level. That is to say, the N particles within a given cell are randomly grouped into $N/2$ pairs; the properties of all the particles change according to eqs. (1) and (2) The extent of mixing now has to be controlled at the individual particle level through the parameter A, which is redefined as

$$A = C'\xi\frac{\delta t}{\tau}$$

where $C' = 2.0$. With this new definition, eq. (3) can be written, in the limit $\delta t \to 0$,

$$\frac{d\phi_n}{dt} = C'\frac{\xi}{\tau}(\phi_m(t) - \phi_n(t)).$$

The above equation states that the change of ϕ_n due to mixing is proportional to the difference between ϕ_m and ϕ_n, and inversely proportional to the turbulence time scale τ.

The Coupling of Mixing and Reaction

The processes of mixing and chemical reaction are essentially decoupled when one uses the discontinuous C/D models. In contrast, with the above continuous model, coupling becomes natural since, for a given particle, mixing and chemical reaction can be described with a single equation:

$$\frac{d\phi_n}{dt} = C'\frac{\xi}{\tau}(\phi_m(t) - \phi_n(t)) + w_n,$$

where w_n is the chemical source term.

Since the continuous mixing model allows full coupling of the reaction and mixing processes, the C/D model with reaction zone conditioning by Chen and Kollmann[4] can be easily implemented in the present model to simulate the fast reaction in the flame sheet regime. Here a modified finite difference version of eq. 12 has to be used since w_n is infinity in case of fast reaction.

2.1.2 Results and Discussions

The continuous mixing model described in the previous section has been validated using both non-reacting and reacting flow test cases. The results and their comparisons with earlier calculations (Hsu[7]) using the modified Curl model as well as with experimental data are presented in this section.

Homogeneous Turbulence Decay of a Scalar

The case of decaying fluctuation of a passive scalar in homogeneous turbulence is used to test the continuous mixing model. The initial condition is

$$P^*(\psi;t) = \frac{1}{N}\left[\sum_{n=1}^{N/2}\delta(\psi-1) + \sum_{n=N/2+1}^{N}\delta(\psi+1)\right],$$

that is, in the Monte Carlo simulation, half of the particles are ascribed the value 1, and the other half -1.

The pdf distribution of the normalized variable $(\psi - <\phi>)/\sigma$, where $<\phi>$ is the mean and σ is the standard deviation, in the homogeneous turbulence decay problem converges to a single curve after certain time, and the correct distribution should be Gaussian. Fig. 1 and 2 are the pdf distributions from the modified Curl model and the present model, both compared to a normal distribution. One can see that the pdf from the modified Curl model deviates considerable from Gaussian, while the result from the present model is fairly close to a Gaussian distribution.

The evolution history of the rms and fourth and sixth moments of the scalar fluctuation are calculated using both the modified Curl model and the present continuous model. Fig. 3 shows the results from the modified Curl model. One can see that although the rms from that model behaves well, the fourth and sixth moments grow quickly out of bound, oscillating at a level several order of magnitudes higher than the value of Gaussian distribution. These results are similar to what Pope[11] had observed. Fig. 4 shows the results for the same set of quantities from the present model. The rms behaves similar to that from the modified Curl model. The fourth and sixth moments, on the other hand, are quite different from those of the previous model; they rise smoothly to the value predicted by Gaussian distribution. Although the values do not seem to converge, they remain finite, and are of the same order of magnitude as that of the Gaussian distribution.

The above results clearly demonstrated the advantage of the present model over that of the modified Curl model. Pope[11] had devised an age biased scheme that achieved the same end, which required an additional variable, namely the age of the particles, and two extra adjustable parameters. In contrast, the present model needs no extra work or parameters.

Heated Turbulent Jet

Extensive experimental results for a heated turbulent plane jet have been reported by many authors (Bashir, et al.[2], Browne et al.[3], Uberoi and Singh[13], Jenkins[9], Antonia, et al.[1]). The turbulent jet has a slightly higher temperature than the ambient. Measurements of both the the mean temperature and the rms of temperature fluctuations were given. We compared the solutions for the heated turbulent jet from the new model with experimental data as well as with previous solutions (Hsu[7]) obtained using the modified Curl model.

In the present study, a combined CFD—Monte Carlo algorithm is used. The mean flow field is obtained by solving the Navier-Stokes equation and a two-equation turbulence model using a finite difference scheme. The temperature is treated as a conserved scalar and simulated by the pdf equation.

Fig. 5 shows the comparisons of the the mean temperature distribution from the pdf Monte Carlo simulations and experimental data from various authors. The figure shows that both mixing models predict the mean temperature distribution accurately.

The results for standard variation, or rms, of the temperature distribution are given in Fig. 6. Although the two solutions do not show significant difference, the new model seems to agree slightly better with the experimental data. The skewness and the flatness, i.e., the third and fourth moments of the temperature fluctuation, are given in Figs. 7 and 8; the comparisons show that in the present case of a turbulent jet the statistical behavior of the new model is similar to that of the modified Curl model.

Hydrogen-Fluorine Diffusion Flame

The continuous model has been applied to the H_2—F_2 diffusion flame studied earlier by Hsu[7]. The flow conditions are set according to an experiment performed by Hermanson and Dimotakis[6]. The flame consists two streams. The upper stream contains 96% of N_2 and 4% of F_2, the flow velocity is $U_1 = 22\,m/s$; the lower stream contains 96% of N_2 and 4% of H_2, with velocity $U_2 = 8.8\,m/s$. The estimated Damköhler number ranged from 25 to 130 (Hermanson and Dimotakis[6]), and a fast chemistry model is deemed appropriate in the calculation. Again a modified version of eq. 12 is used to accommodate the fast chemistry.

Fig. 9 shows the temperature rise due to combustion. In the figure, δ_T is the shear layer thickness determined by 1% of the temperature rise, ΔT is the actual temperature rise due to combustion, (the two streams have the same temperatures initially,) and ΔT_{adf} is the adiabatic flame temperature assuming complete reaction. Details on the flow conditions can be found in Hermanson and Dimotakis[6]. The agreement between numerical predictions and experimental data is fairly good, and a comparison of the results from the continuous model and that from the modified Curl model shows that both performed well for this case.

Combination with Reaction Zone Conditioning

Chen and Kollmann[4] developed a mixing model based on reaction zone conditioning, aimed at the coupling of reaction and mixing. We have shown in Section 2.3 that with the present model, the processes of reaction and mixing can be fully coupled; therefore it is only natural to apply the reaction zone conditioning suggested by Chen and Kollmann here.

The H_2—F_2 diffusion flame problem is reformulated such that the chemical reaction is confined to a very narrow zone near stoichiometry. By applying reaction zone conditioning to the continuous mixing model, we were able to produce a scatter plot of the temperature vs. mixture fraction in which all the points reached the equilibrium temperature. This result is shown in Fig. 10. The mixture fraction here is defined as the molar concentration of fuel divided by the total molar concentration, and stoichiometry is located at $f = 0.5$.

2.1.3 Conclusions

A turbulence mixing model that is continuous in time has been introduced. The deficiency of non-physical jump condition in the mixing process is removed in the new model. It has been shown that the new model is superior to the existing modified Curl model (Janicka, et al.[8]) in that it can predict a Gaussian distribution and finite higher moments in the case of homogeneous turbulence decay; it has accomplished what the age biased sampling scheme (Pope[11]) is designed for, without the extra parameters required by that scheme. The numerical results from the present model compare well with experimental data.

2.2 DNS of Homogeneous Compressible Turbulence in a Rotating frame

Rotation is an important factor in many flow phenomena in nature and in engineering. Problems that are strongly affected by rotation include flows in turbomachinery, large scale motions in the atmosphere and oceans, and galactic motions. Turbulence is important in all the above examples. In order to model turbulence in a rotating frame, we need a better understanding on the effects of rotation on turbulence.

Several experiments had been carried out by various researchers[14–16]. However, the conclusions are inconsistent. Some results show that rotation increases the turbulence dissipation rate, others suggest the opposite.

Numerical studies of turbulence in a rotating frame are few. In fact the only two are incompressible flow studies, by Bardina, et al.[17] and by Speziale et al.[18], using the same computer program. Studies other than the present one dealing with compressible flows in a rotating frame are not known to the authors.

Bardina et al.[17] performed both large eddy and full simulations of incompressible isotropic turbulence. Their results show that, in the case of *incompressible* turbulence, the dissipation rate decreases with increasing rotation rate, and that anisotropy does not develop as a result of the Coriolis force. Speziale et al. confirmed these results using a smaller Rossby number, i.e. a faster rotation.

In general, compressible turbulence in a rotating frame is not homogenous or isotropic because of the existence of centrifugal force and density fluctuations. However, when the rotation rate is low, or when the solution domain is very close to the rotation axis, the centrifugal force can be neglected and the flow is approximately homogeneous. In the present study, our goal is to identify the effects of the Coriolis force, as opposed to the effects of the centrifugal force or the combined effects of the centrifugal and Coriolis forces. Therefore, the centrifugal force is dropped from the governing equations, regardless of whether or not it is negligible. A future study will concentrate on the non-homogenous effects of the centrifugal force and the combined effects of the two forces.

The numerical results presented in the following show that although the Coriolis force does not appear explicitly in the turbulence kinetic energy equation, its effect can be significant. Anisotropy does develop as a result of the Coriolis force. The dissipation rate of the compressible and incompressible modes of the turbulent kinetic energy behave differently under Coriolis forces, and the combined effect is a increased dissipation rate.

2.2.1 Method

The governing equations for compressible flows in a rotating frame are

$$\begin{aligned}
&\rho_{,t} + (\rho u_j)_{,j} = 0 \\
&(\rho u_i)_{,t} + (\rho u_j u_i)_{,j} = -p_{,i} + \tau_{ij,j} - \rho\epsilon_{ijk}\epsilon_{klm}\Omega_j\Omega_l x_m - 2\rho\epsilon_{ijk}\Omega_j u_k \\
&(\rho e)_{,t} + (\rho u_j e)_{,j} = -p u_{j,j} + u_{i,j}\tau_{ij} - (kT_{,j})_{,j} \\
&p = \rho RT
\end{aligned}$$

The last two terms in the second equation represent, respectively, the effects of centrifugal force and the Coriolis force. The centrifugal force is a nonuniform body force which would induce nonuniform pressure and density distributions; its effect on turbulence is to destroy homogeneity. The Coriolis force, on the other hand, is a uniform body force, provided that the velocity field is uniform. In the case of incompressible flows, the centrifugal force can be included into a modified pressure term and thus does not appear explicitly; however, this can not be done in the case of compressible flows.

In order to identify the homogeneous effect of the Coriolis force alone, and to compare results with incompressible flow simulations, we simply take away the centrifugal force in our study. This, of course, greatly simplifies the problem: With a homogeneous initial condition, the flow field remains homogeneous under the Coriolis force. The simplified problem is a hypothetical one and can not normally be found in nature except in very restricted situations such as the ones mentioned in the introduction.

The governing equations are solved using a compact difference scheme. Lele[19] has shown that such schemes have spectral accuracy and are well suited for DNS. The spatial derivatives are approximated by 8th order finite differences, and the time integration is performed using a three-stage Runge-Kutta time marching scheme.

The initial condition for the rotating flow simulation is obtained from a simulation of isotropic decaying turbulence. The initial condition for the decaying turbulence is generated using a given 3D spectrum of the form

$$k^4 exp\left[-2\left(\frac{k}{k_0}\right)^2\right].$$

After the decaying turbulence shows the correct skewness, the Coriolis force is imposed onto the flow field.

2.2.2 Results and Discussion

As a primary study, three cases have been calculated, with rotation in the z-direction: The nondimensional rotation rates are $\Omega = 0, 40, 80$, which correspond to turbulent Rossby numbers of ∞, 0.0075, and 0.00375. These Rossby numbers are much smaller than those considered in References 17 and 18.

Figures 11 and 12 show the development of a 1D two-point correlation and a 1D spectrum in the turbulent flow field, where square symbols are initial conditions and lines represent later times. Figure 13 shows a comparison of the energy spectrum obtained using two different grids, one double the size of the other. The agreement affirms sufficient resolution.

Figures 14-19 show the time history of various statistics of the three cases, where time is nondimensionalized using the initial eddy turn over time.

Figure 14 is the ratio of the turbulent kinetic energy, where q_0^2 is the initial turbulent kinetic energy and q^2 the value at later times. It is immediately clear that the Coriolis force causes a faster decay of the turbulence, a conclusion that is contrary to what was observed in the incompressible flow simulations by previous researchers[17,18]. Nevertheless, as we shall see in the following, the present results are in fact consistent with those of Refs 4 and 5.

To prove that the present results are consistent with the previous incompressible simulations, we look at the ratio of the means of the divergence squared and vorticity squared, which are proportional to, respectively, the compressible and incompressible turbulent kinetic energy. Figures 15 and 16 show that while the dissipation rate of the compressible part of the turbulent kinetic energy increases with larger Coriolis forces, the dissipation rate of the *incompressible* part decreases. The combined effect, as we have seen from Figure 14, is an increase in the total dissipation rate. Since the simulations of References 4 and 5 are for incompressible flows, it is not surprising that only a decrease in dissipation rate was observed.

In both References 17 and 18, no anisotropy was observed. Bardina et al.[17] speculated that a reorganization to two-dimensional flows could occur at higher rotation rates, while Speziale et al. suggested that Taylor-Proudman reorganization would not occur in a rapidly rotating isotropic turbulence. The present results show definite signs of anisotropy as soon as the Coriolis force is turned on. The anisotropy can be clearly observed from the time history of the normal components of the Reynolds stress, given in Figures 17, 18, and 19 for the three rotation rates. With the Coriolis force, the x- and y-components of the normal Reynolds stress decrease much faster than the z-component. In fact, it seems that the increased dissipation is primarily in the x- and y-directions, and the z-component of the turbulent kinetic energy is not affected much.

The Taylor-Proudman theory stipulates that under strong rotation, with the rotation axis parallel to, say, the z axis, then for any flow variable u, we have $(\partial u/\partial z) = 0$. Figures 20 and 21 are the contours of the x-component of velocity plotted on three planes. Without the Coriolis force (Figure 20), the flow structure remains isotropic. With the Coriolis force, columns soon appear in the flow field, suggesting that a Taylor-Proudman reorganization has occurred. Using larger Rossby numbers such as those used in References 17 and 18, the results show no appreciable anisotropy, hence there appears to be no contradiction.

Finally, inertial waves can be observed from the time history of various statistics presented in Figures 14-19. The frequency is approximately Ω/π, the theoretical intrinsic frequency for rotating flows.

3. Future Work

3.1 PDF

The pdf model is being implemented into an existing compressible flow solver: the RPLUS2D code. Work on implementing pdf to RPLUS3D will follow.

3.2 DNS

To understand the effect of compressibility, incompressible homogeneous turbulence in a rotating frame will be studied.

4. References

1 Antonia, R.A., Browne, L.W.B., Chambers, A.J., and Rajagopalan, S., "Budget of the Temperature Variance in a Turbulent Plane Jet." Int. J. Heat Mass Transfer,**26-1**, 41-48, (1983).

2 Ashir, J. and Uberoi, M.S., "Experiments on Turbulent Structure and Heat Transfer in a Two Dimensional Jet." Physics of FLuids, **18-4**, 405-410, (1975).

3 Browne, L.W.B., Antonia, R.A., and Chembers, A.J., "The Interaction Region of a Turbulent Plane Jet." J. Fluid Mech., **149,** 355-373, (1984).

4 Chen, J.-Y. and Kollmann, W., "Mixing Models for Turbulent Flows with Exothermic Reactions." Turbulent Shear Flows, Springer-Verlag, **7**, 277, (1991).

5 Curl, R.L., "Dispersed Phase Mixing, I, Theory and Effects of Simple Reactors." A.I.Ch.E.J. **9**, 175, (1963).

6 Hermanson, J.C. and Dimotakis, P.E., "Effects of Heat Release in a Turbulent, Reacting Shear Layer." J. Fluid Mech. **199**, 333-375, (1989).

7 Hsu, A.T., "The Study of Hydrogen Diffusion Flames Using PDF Turbulence Models." AIAA Paper 91-1780, (1991).

8 Janicka, J., Kolbe, W., and Kollmann, W., "Closure of the Transport Equation for the Probability Density Function Scalar Field." J Non-Equilib. Thermodyn. **4**, 47, (1979).

9 Jenkins, P.E. and Goldschmidt, V.W., "Mean Temperature and Velocity in a Plane Turbulent Jet," ASME J. Fluids Eng., **95**, 581-584, (1973).

10 Norris, A.T. and Pope, S.B., "Turbulent Mixing Model Based on Ordered Pairing." Combust. and Flame, **83,** 27-42, (1991).

11 Pope, S.B., "An Improved Turbulence Mixing Model." Combust. Sci. Tech., **28**, 131, (1982).

12 Pope, S.B., "PDF Methods for Turbulent Reactive Flows." Prg. Energy Combust. Sci., **11**, 119-192, (1985).

13 Uberoi, M.S. and Singh, P.I., "Turbulent Mixing in a Two-Dimensional jet," Physics of Fluids, **18-7,** 764-769, (1975).

14 Traugott, S.C., "Influence of Solid-body Rotation on Screen-produced Turbulence." NACA TN 4135, (1958).

15 Ibbetson, A. and Tritton, D.J., " Experiments on Turbulence in a Rotating Fluid." J. Fluid Mech., **56**, 639-672, (1975).

[16] Wigeland, R.A. and Nagib, H.M. "Grid-generated Turbulence With and Without Rotation About the Streamwise Direction." IIT Fluids and Heat Transfer Rep. R78-1, Illinois Inst. of Tech., Chicago, Illinois, (1978).

[17] Bardina, J., Ferziger, J.H. and Rogallo, R.S. "Effect of Rotation on Isotropic Turbulence: Computation and Modeling," J. Fluid Mech., **154**, 321-336, (1985).

[18] Speziale, C.G., Mansour, N.N. and Rogallo, R.S., "The Decay of Isotropic Turbulence in a Rapidly Rotating Frame," Center for Turbulence Research, Proceedings of the Summer Program, (1987).

[19] Lele, S.K., "Compact Finite Difference Schemes with Spectral Like Resolution." Submitted to J. Comp. Physics.

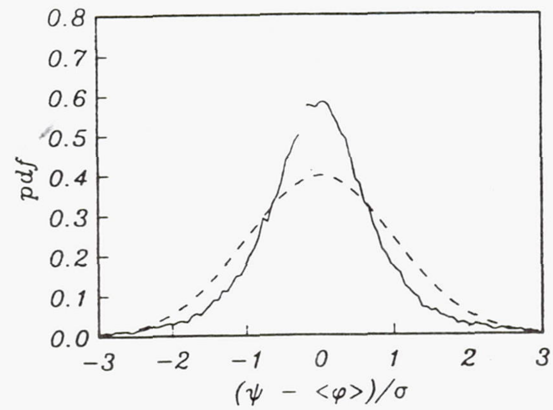

Figure 1. Asymptotic pdf distribution for a scalar in homogeneous turbulence. — modified Curl model; - - - Gaussian.

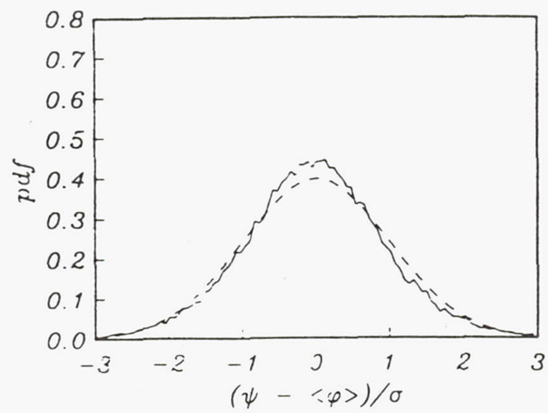

Figure 2. Asymptotic pdf distribution for a scalar in homogeneous turbulence. — present model; - - - Gaussian.

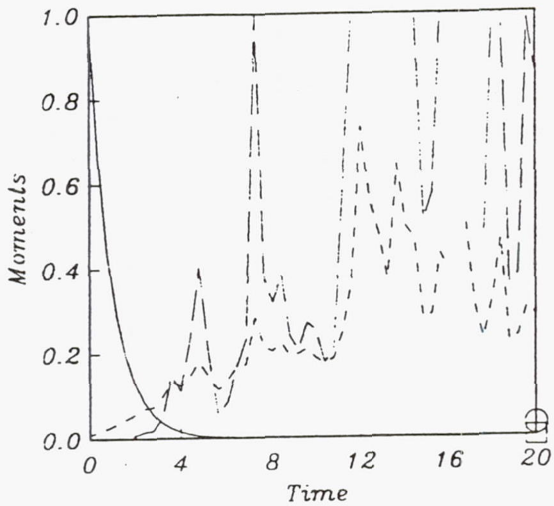

Figure 3. Evolution of moments from the modified Curl model. — standard deviation, - - - 0.01 × fourth central moment, – – 0.0001 × sixth central moment, o 0.01 × fourth moment for Gaussian distribution, □ 0.0001 × sixth moment for Gaussian distribution.

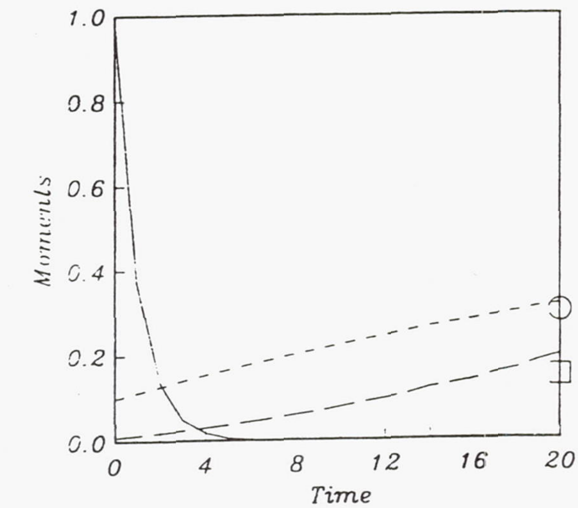

Figure 4. Evolution of moments from the present model. — standard deviation, - - - 0.1 × fourth central moment, – – 0.01 × sixth central moment, o 0.1 × fourth moment for Gaussian distribution, □ 0.01 × sixth moment for Gaussian distribution.

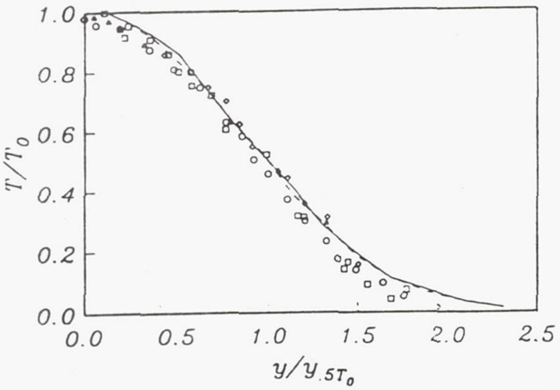

Figure 5. Mean temperature in heated plane jet. — continuous mixing model, - - - modified Curl model, △ Browne et al. (1984), □ Bashir and Uberoi (1975), ◇ Uberoi and Singh (1975), ○ Jenkins and Goldschmidt (1973).

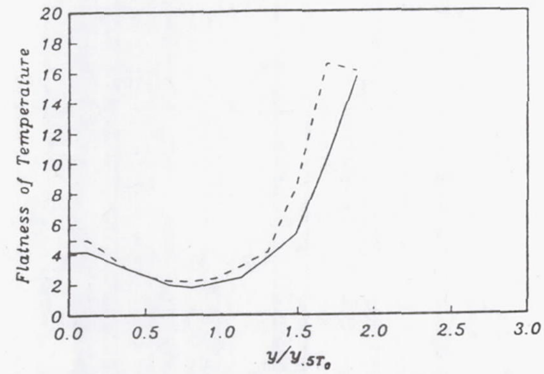

Figure 8. Flatness of temperature variance in heated plane jet. — continuous mixing model, - - - modified Curl model.

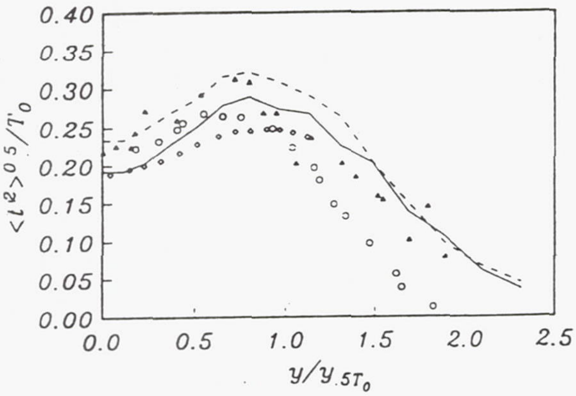

Figure 6. RMS of temperature variance in heated plane jet. — continuous mixing model, - - - modified Curl model, ◇ Antonia et al. (1983), ○ Bashir and Uberoi (1975), △ Uberoi and Singh (1975).

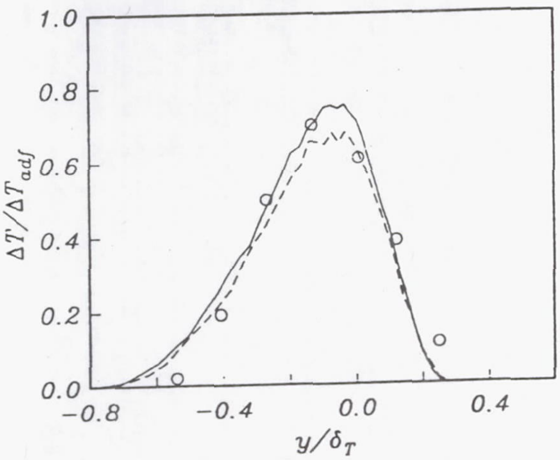

Figure 9. Temperature rise in an H_2–F_2 diffusion flame. — continuous mixing model, - - - modified Curl model, ○ Hermanson and Dimotakis (1989).

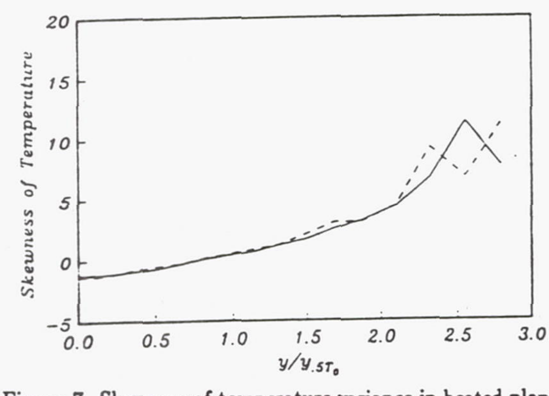

Figure 7. Skewness of temperature variance in heated plane jet. — continuous mixing model, - - - modified Curl model.

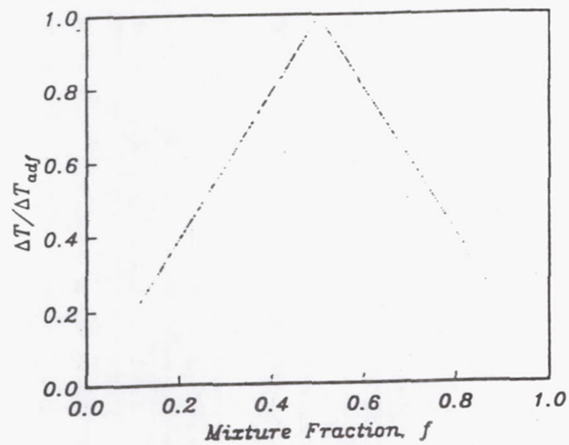

Figure 10. Joint pdf between temperature and mixture fraction on the centerline of the H_2–F_2 diffusion flame; reaction is restricted to a narrow zone at stoichiometry; results are obtained by applying reaction zone conditioning (Chen and Kollmann, 1990) to the continuous mixing model.

Fig. 11 1D Corelation

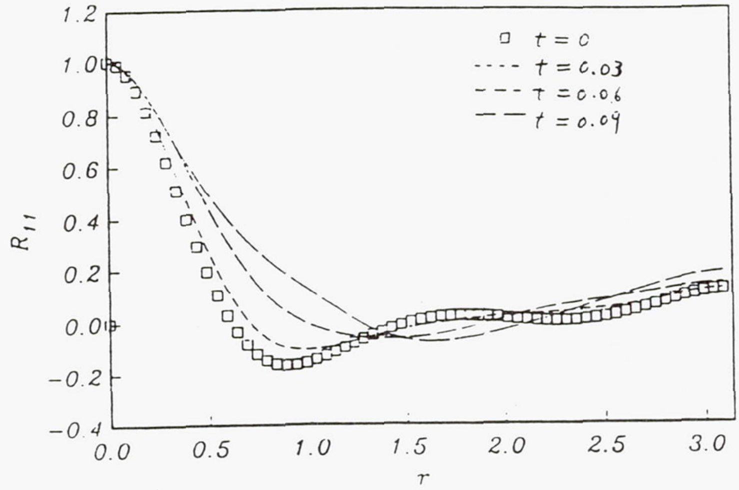

Fig. 12 1D Spectrum

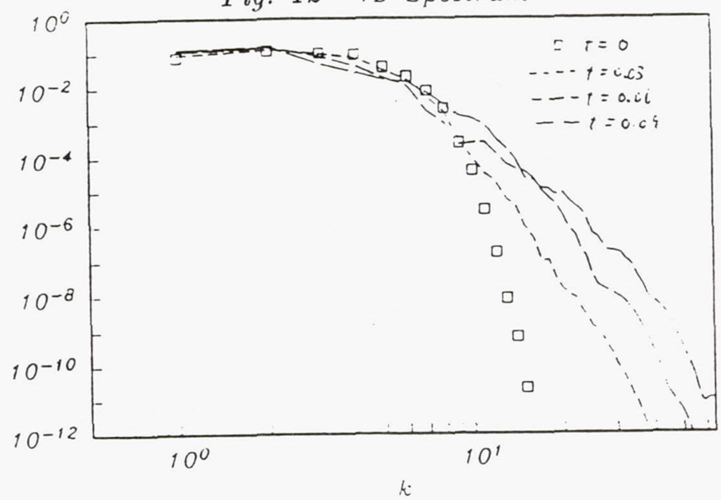

Fig. 13 Energy Spectrum

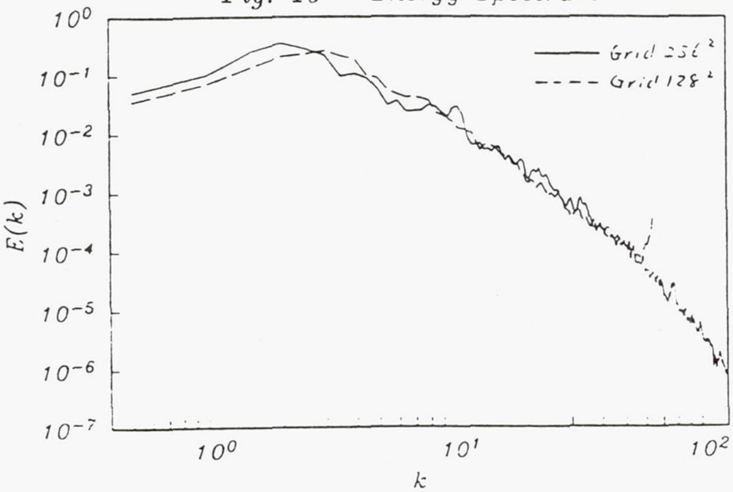

Fig.14 Turbulent kinetic energy

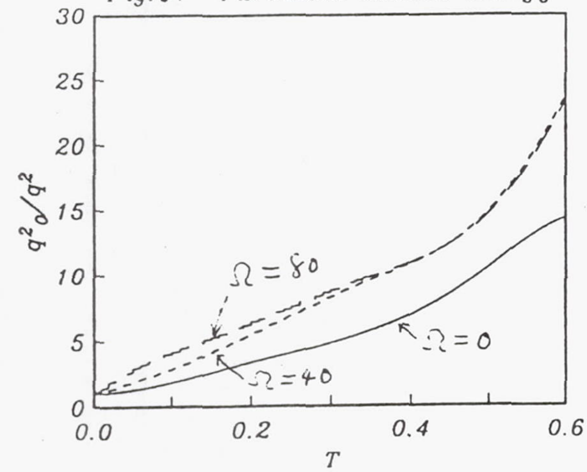

Fig.17 Reynolds stresses, Ω =0., Re=20

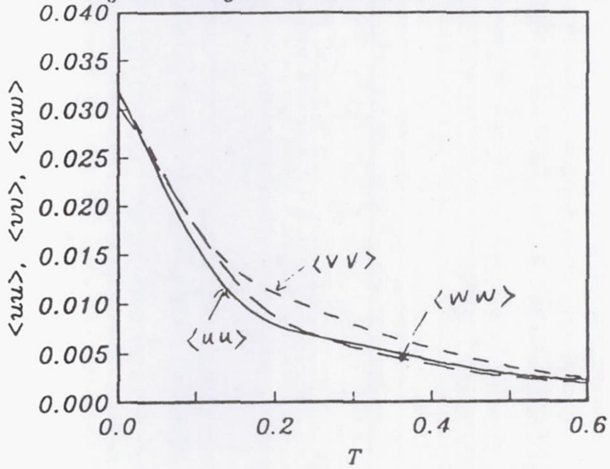

Fig.15 Compresseble energey ratio.

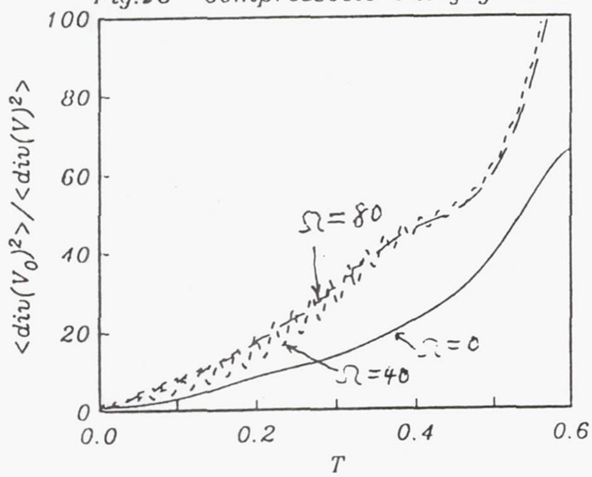

Fig.18 Reynolds stresses, Ω =40., Re=20

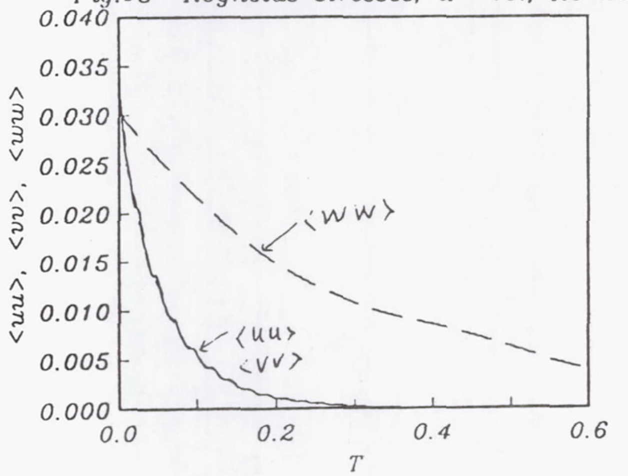

Fig.16 Incompresseble energey ratio.

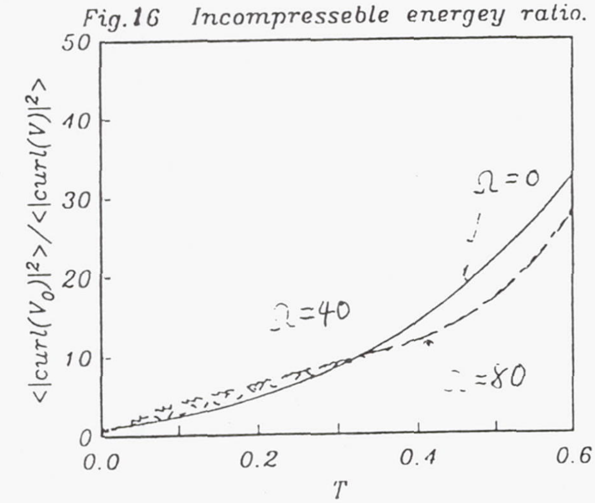

Fig.19 Reynolds stresses, Ω =80., Re=20

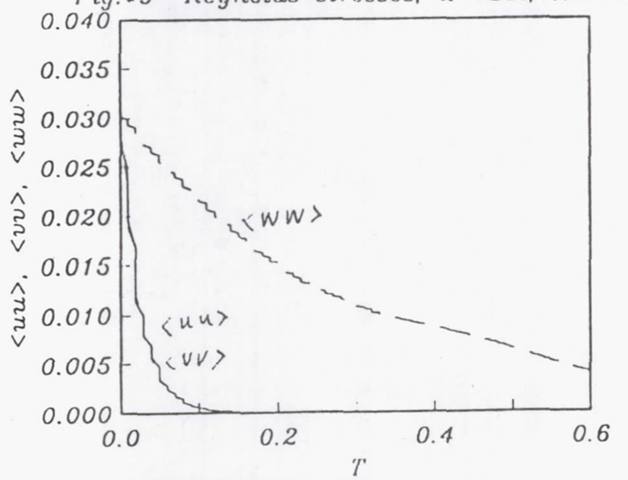

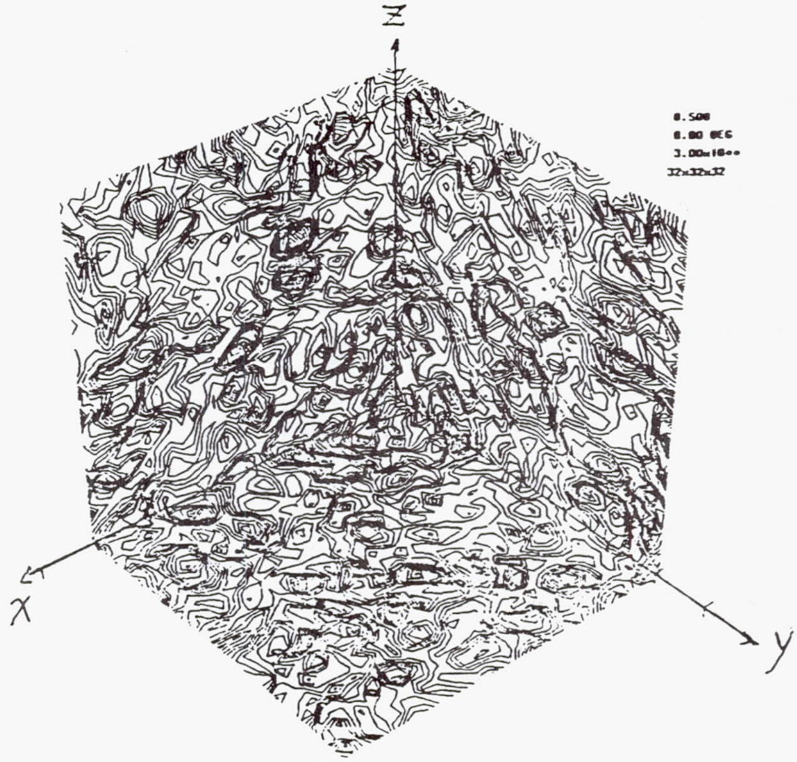

Figure 20 . Flow structure without Coriolis Force, u-velocity.

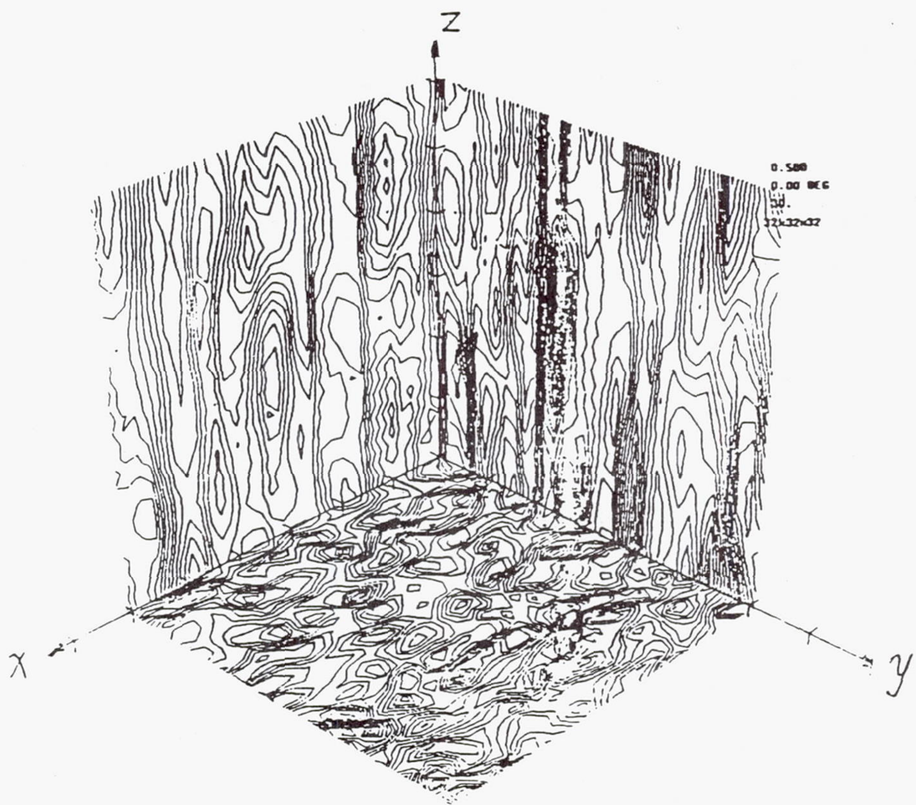

Figure 21 . Flow structure with the Coriolis force, u-velocity.

Modeling of Turbulence and Transition

Tsan-Hsing Shih

1. Motivation and Objective

The first objective is to evaluate current two-equation and second order closure turbulence models using available direct numerical simulations and experiments, and to identify the models which represent the state of the art in turbulence modeling.

The second objective is to study the near-wall behavior of turbulence, and to develop reliable models for an engineering calculation of turbulence and transition.

The third objective is to develop a two-scale model for compressible turbulence.

2. Work Accomplished

2.1 Evaluation of two-equation models (N.J. Lang and T.-H. Shih[1])

Twelve two-equation models including $k-\epsilon$, $k-\tau$, $k-\omega$ and $q-\omega$ models, have been evaluated using a common flow solver code (GENMIX) for wall bounded turbulent flows. For each model, calculations were carried out for two-dimensional, fully developed channel and flat plate boundary layer flows. These flows are appealing for model testing because they are simple and self-similar, yet demonstrate important features of wall bounded turbulent shear flows. In addition, we can compare these calculations with Direct Numerical Simulations (DNS). A list of the models which were tested are shown in the table below:

Ch	Chien[2] 1982	$k-\epsilon$
Sh	Shih[3] 1991	$k-\epsilon$
LB	Lam and Bremhorst[4] 1981	$k-\epsilon$
NH	Nagano and Hishida[5] 1987	$k-\epsilon$
NT	Nagano and Tagawa[6] 1990	$k-\epsilon$
LS	Launder and Sharma[7] 1974	$k-\epsilon$
JL	Jones and Launder[8] 1973	$k-\epsilon$
MK	Myong and Kasagi[9] 1988	$k-\epsilon$
YS	Yang and Shih[10] 1991	$k-\epsilon$
WI1	Wilcox[11] 1984	$k-\omega$
WI2	Wilcox[12] 1991	$k-\omega$
SAA	Speziale, Abid and Anderson[13] 1990	$k-\tau$
Co	Coakley[14] 1983	$q-\omega$

Two dimensional channel flow calculations were made at $Re_\tau = 180$ and $Re_\tau = 395$. These cases were compared with DNS data of Kim et al[15]. Calculations for the two-dimensional flat plate boundary layer flow at $Re_\theta = 1410$ were compared with DNS data of Spalart[16]. Some flat plate boundary layer comparisons were made between the experimental data of Klebanoff[17] at $Re_\theta = 7700$ and solutions of the various models. The detailed results are reported in NASA TM 105237, 1991.

An important criterion for two-equation model comparisons is not only how well the model predicts mean velocity and shear stress, but also the turbulent kinetic energy and dissipation (or specific dissipation) rate. These predictions should provide appropriate turbulent velocity and length scales so that the model can be applied to more complex flows for which a simple mixing length model often fails. Some researchers maintain that it is not critical whether or not the turbulent kinetic energy and the turbulent length scale are predicted with great accuracy. However, one may imagine that a two-equation model making unreasonable turbulent velocity and length scale predictions would be very questionable when applied to more general flows. A model which accurately predicts the shear stress and mean velocity does not imply that it has correctly modeled the turbulent kinetic energy and length scale. In fact, if the turbulent kinetic energy is incorrect, then the length scale must also be incorrect to compensate for the error in the turbulent kinetic energy. For this case, two wrongs are making a right. This warrants some caution when computing flows for other geometries.

Comments on two-equation models:

It is clear that the JL, LS, WI1 and WI2 models underpredict the near wall turbulent kinetic energy compared to the other models.

The standard $k-\epsilon$ model has been proven to provide good results in the high Reynolds number range. It is therefore attractive for a near wall $k-\epsilon$ turbulence model to approach the standard $k-\epsilon$ model away from the wall. The LB, LS and YS models are the only $k-\epsilon$ models in this study which possess this characteristic.

Because boundary layer and channel flows are self-similar, the solutions should be independent of the initial conditions. However, some of the models (SAA, Co, and LB) have difficulty when the initial conditions contain large gradients. The Co Model is particularly dependent on the initial conditions. Even slight perturbations of the initial conditions will yield noticeably different solutions with this model.

JL, LS, WI1 and WI2 are the only models which do not contain y^+. Damping functions which contain y^+ are not desirable because y^+ is erroneous near flow separations and not well defined near complicated geometries. Unfortunately, these are the same models which poorly predict the near wall turbulent quantities.

The Wilcox models (WI1 and WI2) suffer from a numerically awkward boundary condition for ω at the wall:

$$\omega \rightarrow \frac{6\nu}{C_2 y^2} \text{ as } y^+ \rightarrow 0$$

We cannot define ω at $y^+ = 0$. We have tried two ways to approximate ω as y^+ approaches 0. First, we chose a large number for ω_{wall} and, second, we used an asymptotic $\omega_{wall} = \frac{6\nu}{C_2 y^2}$. Test cases showed that the solution does not converge as $\omega_{wall} \rightarrow \infty$ when $y^+ \rightarrow 0$ for either model. In addition, both Wilcox models underpredict the turbulent kinetic energy peak value for both boundary layer and channel flows.

model the new unknowns T_{ij}, Π_{ij} and ε_{ij}. At the level of the second order closure, these new unknowns are usually modeled with algebraic equations in terms of the second moments and the mean quantities (with the exception of the trace $\varepsilon_{kk} = 2\varepsilon$, which is modeled with a transport equation).

In a general turbulent shear flow with moderate inhomogeneity, the turbulent diffusion terms in the second moment equations are usually smaller than the other terms. However, the pressure-strain rate and dissipation rate tensors are always among the leading terms. Therefore, the performance of modeled equations largely depends on the models of pressure-strain rate tensor and dissipation rate tensor.

In this study, we only concentrate on the models of the pressure-strain rate tensor and the dissipation rate tensor for the velocity field: $\Pi_{ij} - \varepsilon_{ij}$, which are modeled as

$$\Pi_{ij} - \varepsilon_{ij} = \Pi_{ij}^{(1)} + \Pi_{ij}^{(2)} - \frac{2}{3}\varepsilon\delta_{ij}$$

where $\Pi_{ij}^{(1)}$, $\Pi_{ij}^{(2)}$ are respectively referred to as the rapid term and the return-to-isotropy term.

Models for the rapid term $\Pi_{ij}^{(1)}$

<u>Launder, Reece and Rodi (LRR):</u>[18]

$$\begin{aligned}\frac{\Pi_{ij}^{(1)}}{2q^2} &= 0.2S_{ij} + \frac{9C_2+6}{22}\left(b_{ik}S_{jk} + b_{jk}S_{ik} - \frac{2}{3}\delta_{ij}b_{kl}S_{kl}\right) \\ &+ \frac{10-7C_2}{22}\left(b_{ik}\Omega_{jk} + b_{jk}\Omega_{ik}\right)\end{aligned} \tag{2.2.1}$$

where $C_2 = 0.4$, and

$$\begin{aligned} b_{ij} &= \frac{\overline{u_i u_j}}{q^2} - \frac{1}{3}\delta_{ij}, \\ S_{ij} &= \frac{1}{2}(U_{i,j} + U_{j,i}), \\ \Omega_{ij} &= \frac{1}{2}(U_{i,j} - U_{j,i}) \end{aligned}$$

This model is linear in the Reynolds-stress. It contains only one model constant C_2. This model satisfies the conventional model constraints[34]. It is the most general form at the level of linear dependence on the Reynolds-stress. However, as Lumley[24] pointed out, this model may violate realizability as the turbulence approaches a two-component state.

<u>Speziale, Sarkar and Gatski (SSG):</u>[19]

$$\begin{aligned}\frac{\Pi_{ij}^{(1)}}{2q^2} &= \frac{0.8 - C_3^{**}}{4}S_{ij} - \frac{C_1^* P}{2q^2}b_{ij} \\ &+ \frac{C_4}{4}\left(b_{ik}S_{jk} + b_{jk}S_{ik} - \frac{2}{3}\delta_{ij}b_{kl}S_{kl}\right) \\ &+ \frac{C_5}{4}\left(b_{ik}\Omega_{jk} + b_{jk}\Omega_{ik}\right)\end{aligned} \tag{2.2.2}$$

where,

$$C_3^{**} = C_3^*(b_{ij}b_{ij})^{1/2}, \quad P = -\overline{u_i u_j}U_{i,j}$$
$$C_1^* = 1.8 \quad C_3^* = 1.3, \quad C_4 = 1.25, \quad C_5 = 0.4$$

This model is quasi-linear in the Reynolds-stress, because the coefficients in the first two terms are not constant, but depend on the invariant of the Reynolds-stress tensor and the production P. This model contains four model constants (C_1^*, C_3^*, C_4, C_5), therefore one may imagine that it will be difficult to correctly calibrate them. In addition, this model does not satisfy the normalization constraint which is one of the basic model constraints[34]. If we impose this constraint, then the four coefficients will reduce to only one, and this model will reduce to the LRR model. Finally, like the LRR model, the SSG model may also violate realizability.

Fu, Launder and Tselepidakis (FLT):[20]

$$\begin{aligned}
\frac{\Pi_{ij}^{(1)}}{2q^2} &= 0.2S_{ij} + 0.3(b_{ik}S_{jk} + b_{jk}S_{ik} - \frac{2}{3}\delta_{ij}b_{kl}S_{kl}) \\
&+ \frac{1.3}{3}(b_{ik}\Omega_{jk} + b_{jk}\Omega_{ik}) \\
&+ 0.2(b_{il}^2 S_{jl} + b_{jl}^2 S_{il} - 2b_{kj}b_{li}S_{kl} - 3b_{ij}b_{kl}S_{kl}) \\
&+ 0.2(b_{il}^2\Omega_{jl} + b_{jl}^2\Omega_{il}) \\
&+ r[4b_{nn}^2(b_{ik}\Omega_{jk} + b_{jk}\Omega_{ik}) \\
&+ 12b_{mi}b_{nj}(b_{mk}\Omega_{nk} + b_{nk}\Omega_{mk})]
\end{aligned} \tag{2.2.3}$$

where $r = 0.7$, $b_{ij}^2 = b_{ik}b_{kj}$.

This model is cubic in the Reynolds-stress. The final form selected contains one model constant. This model only satisfies a part of the realizability condition, corresponding to a two-component state of turbulence. However, when a scalar field is involved, this model cannot satisfy Schwarz' inequality between velocity and temperature. This part of realizability is sometimes called joint realizability.

Shih and Lumley (SL):[21]

$$\begin{aligned}
\frac{\Pi_{ij}^{(1)}}{2q^2} &= 0.2S_{ij} + 3\alpha_5(b_{ik}S_{jk} + b_{jk}S_{ik} - \frac{2}{3}\delta_{ij}b_{kl}S_{kl}) \\
&+ \frac{1}{3}(2 - 7\alpha_5)(b_{ik}\Omega_{jk} + b_{jk}\Omega_{ik}) \\
&+ 0.2(b_{il}^2 S_{jl} + b_{jl}^2 S_{il} - 2b_{kj}b_{li}S_{kl} - 3b_{ij}b_{kl}S_{kl}) \\
&+ 0.2(b_{il}^2\Omega_{jl} + b_{jl}^2\Omega_{il})
\end{aligned} \tag{2.2.4}$$

where,

$$\alpha_5 = \frac{1}{10}(1 + 0.8F^{1/2}), \quad F = 1 + 9b_{ij}b_{jk}b_{ki} - \frac{9}{2}b_{ij}b_{ij}$$

This model is quasi-quadratic in the Reynolds-stress, because the model coefficient α_5 is a function of the invariants of the Reynolds-stress tensor. We emphasize that this model is obtained from a more general form of the expression than the FLT, and satisfies both the two component condition and Schwarz' inequality between the velocity and scalar fields. In addition, the final form is simpler than the model of FLT.

Shih and Mansour (SM):[22]

$$\begin{aligned}\frac{\Pi_{ij}^{(1)}}{2\overline{q^2}} &= 0.2S_{ij} + 3\alpha_5(b_{ik}S_{jk} + b_{jk}S_{ik} - \frac{2}{3}\delta_{ij}b_{kl}S_{kl}) \\ &+ \frac{1}{3}(2 - 7\alpha_5)(b_{ik}\Omega_{jk} + b_{jk}\Omega_{ik}) \\ &+ 0.2(b_{il}^2 S_{jl} + b_{jl}^2 S_{il} - 2b_{kj}b_{li}S_{kl} - 3b_{ij}b_{kl}S_{kl}) \\ &+ 0.2(b_{il}^2\Omega_{jl} + b_{jl}^2\Omega_{il})\end{aligned} \tag{2.2.5}$$

where, $\alpha_5 = \frac{1}{10}\{1 + 3.5[1 - (1-F)^{1/4}]\}$.

This model has the same form as the SL model. It was derived in a different way and contains a different model coefficient α_5 which was calibrated from one of the DNS data (Rogers[30]). This model, like the SL model, fully satisfies realizability conditions.

Models for the return-to-isotropy term $\Pi_{ij}^{(2)}$

Rotta:[23]

$$\Pi_{ij}^{(2)} = -\varepsilon C b_{ij} \tag{2.2.6}$$

where, $C = 3.0$.

This model is linear in the Reynolds stress, and contains one model constant. It was widely used and adopted in the LRR model. We notice that this model will not allow the turbulence to reach a two-component state, because when any turbulent component reduces to $\overline{q^2}/9$, the model Eq.(2.2.6) will force it to grow.

Lumley:[24]

$$\Pi_{ij}^{(2)} = -\varepsilon[\beta b_{ij} + \gamma(b_{ij}^2 + 2II\delta_{ij}/3)] \tag{2.2.7}$$

where, $\gamma = 0$ and

$$\beta = 2 + \frac{F}{9}\exp(-7.77/\sqrt{Re})\{72/\sqrt{Re} + 80.1\ln[1 + 62.4(-II + 2.3III)]\}$$

$$Re = \frac{\overline{q^2}^2}{9\varepsilon\nu}$$

This model is quasi-linear in the Reynolds stress, because γ is set to zero, and β is a function of the invariants of Reynolds stress tensor. This model is simple, and satisfies realizability.

Sarkar and Speziale (SS):[25]

$$\Pi_{ij}^{(2)} = -\varepsilon[C_1 b_{ij} - 3(C_1 - 2)(b_{ij}^2 - \frac{1}{3}b_{kk}^2\delta_{ij})] \tag{2.2.8}$$

where $C_1 = 3.4$.

This is a quadratic model in the Reynolds-stress tensor. It satisfies what is called the weak realizability condition. Like the Rotta model Eq.(2.2.8), this model will not produce unphysical results. However, it will not allow the turbulence to approach a two-component state, which could occur in some situations, for example, in near-wall turbulence.

Haworth and Pope (HP):[26]

$$\Pi_{ij}^{(2)} = -\varepsilon\{C_1 b_{ij} - C_2[\frac{1}{3}b_{ij} + b_{ij}^2 - b_{kk}^2(b_{ij} + \delta_{ij}/3)]\} \tag{2.2.9}$$

where $C_1 = 8.3, \quad C_2 = 14.8$.

Eq.(2.2.9) is a slow part of the Haworth and Pope's model for the situations with no mean velocity gradient. This model, like the SS model, will not produce unphysical results; however, it will also not allow the turbulence to approach a two-component state.

Choi and Lumley (CL):[27]

If $III \geq 0$,

$$\Pi_{ij}^{(2)} = -\varepsilon[\beta b_{ij} + \gamma(b_{ij}^2 + 2II\delta_{ij}/3)] \tag{2.2.10.1}$$

where,

$$\beta = 2 + \frac{\rho^* F^{1/2}}{1 + G\,\chi^2}$$

$$\gamma = \frac{\rho^* F^{1/2}}{1 + G\,\chi^2}\frac{G}{\xi}$$

$$\xi = (III/2)^{1/3}, \quad \eta = (-II/3)^{1/2}$$

$$\chi = \frac{\xi}{\eta}, \quad G = -\chi^4 + 0.8\chi^6$$

$$\rho^* = \exp[-9.29/Re^{1/2}]\{(\frac{7.69}{Re^{1/2}} + \frac{73.7}{Re}) - [296 - 16.2(\chi + 1)^4]II\}$$

$$Re = \frac{\overline{q^2}^2}{9\varepsilon\nu}, \quad II = -b_{ij}b_{ij}/2, \quad III = b_{ij}b_{jk}b_{ki}/3$$

If $III < 0$,

$$\Pi_{ij}^{(2)} = Eq.(28) \tag{2.2.10.2}$$

The model coefficients in Eq.(2.2.10.1) were obtained using their comprehensive measurements of turbulence relaxing from axisymmetric expansion. Both Eq.(2.2.10.1) and Eq.(2.2.10.2) satisfy realizability; however, Eq.(2.2.10.1) is valid only for $III \geq 0$, because ξ is not defined when $III < 0$.

Craft and Launder (C&L):[28]

$$\Pi_{ij}^{(2)} = -C_1\varepsilon[2b_{ij} + 4C_1'(b_{ij}^2 - b_{kk}^2\delta_{ij}/3)] - 2\varepsilon b_{ij} \tag{2.2.11}$$

where,

$$C_1 = 3.1(A_2 A)^{1/2}, \quad C_1' = 1.2$$

$$A_2 = 4\ b_{ij}b_{ji}, \quad A_3 = 8\ b_{ij}b_{jk}b_{ki}, \quad A = 1 - \frac{9}{8}(A_2 - A_3)$$

This model is tensorially quadratic in the Reynolds stress, and satisfies realizability.

Yamamoto and Arakawa (YA):[29]

$$\Pi_{ij}^{(2)} = -\varepsilon[\alpha_1 b_{ij} + \alpha_2(b_{ij}^2 - b_{kk}^2\delta_{ij}/3)] \tag{2.2.12}$$

where,

$$\alpha_1 = 2 + p\ F\ [q\ (b_{kk}^2)^r + |b_{kk}^3|^s sign(b_{kk}^3)]$$
$$\alpha_2 = 3\ (\alpha_1 - 2)$$
$$p = -12, \quad q = -0.65, \quad r = 0.4, \quad s = 0.45$$
$$F = 1 - \frac{9}{2}b_{kk}^2 + 9\ b_{kk}^3$$

The YA model tried to fit situations with both positive and negative b_{kk}^3. It also meets the requirement of realizability.

Shih and Mansour (S&M):[22]

$$\Pi_{ij}^{(2)} = -\varepsilon\{(2.0 + C_f F^{\xi})b_{ij} + \gamma[b_{ij}^2 + (1/3 + 2II)b_{ij} + \frac{2}{3}II\delta_{ij}]\} \tag{2.2.13}$$

where,

$$C_f = (1/9)\exp(-7.77/\sqrt{Re})\{72/\sqrt{Re} + 80.1\ln[1 + 62.4(-II + 2.3III)]\}$$
$$\gamma = \gamma_0(1 - F^{\eta}), \quad Re = \frac{\overline{q^2}^2}{9\varepsilon\nu}$$
$$F = 1 + 9II + 3III$$
$$II = -\frac{1}{2}b_{ij}b_{ij}, \quad III = \frac{1}{3}b_{ij}b_{jk}b_{ki}$$
$$\xi = 17/20, \quad \eta = 1/20, \quad \gamma_0 = -2$$

This model matches the data of Comte-Bellot and Corrsin[21] and meets the requirement that there will be no return to isotropy in the zero Reynolds number limit. This model also satisfies realizability.

Concluding remarks

We notice that the Reynolds number in all these simulations is low and therefore may not represent real turbulence in nature. However, the model terms concerned here are mainly pressure related correlations. The fluctuating pressure is not directly related to the viscosity, hence the pressure related correlation terms may not be directly affected by the Reynolds number, especially the rapid term. The return-to-isotropy term which includes the deviatoric part of the dissipation rate tensor may have some dependence on the Reynolds number. According to the above consideration, we think that direct comparisons with low-Reynolds DNS data are legitimate, although we should keep in mind the possible low-Reynolds number effect of the DNS data.

We have directly compared five rapid models with fifteen DNS flows: four of Rogers et al.'s[30] shear flows, eleven of Lee et al.'s[31] irrotational strain flows (axisymmetric contraction, axisymmetric expansion and plane strain). Comparing the performance of the LRR and SSG models, which are tensorially linear in the Reynolds stress, we conclude that the SSG model gives very little improvement over the LRR model. In fact in many cases, it is worse than the LRR model. The reason is not very clear. However, we notice that the SSG model does not satisfy the normalization condition which may be a cause for its poor behavior. If we impose this constraint on the SSG model, then it will exactly reduce to the LRR model. In fact it can be shown that the most general form of the rapid model, which is tensorially linear in the Reynolds stress, is the LRR model. Therefore, in general, the treatment used in the SSG model would hardly give any improvement over the LRR model. A natural way to improve the model is to use a more general nonlinear form and more general model constraints. A typical example is the SL[21] model. It starts with the most general form, using full realizability constraints together with the other conventional constraints[34]. The result is a well behaved model. Indeed, from the direct comparisons with the DNS data, the SL[21] model and its variation form of SM[22] model give the best performance in most of the cases. As to the FLT[20] model, it is also a nonlinear model. It starts with a tensorially cubic dependance on the Reynolds stress with *constant* coefficients (in general, these coefficients should not be restricted to constants). In addition, the two-component conditions of turbulence have been imposed. However, the FLT model ignores Schwarz' inequality. Its final form contains two undetermined model constants, but one of them is set to zero. The performance of the FLT model, from the direct comparisons with the DNS data, is better overall than the linear models, but does not compare with the performance of the SL and SM models. So from these direct comparisons of the rapid models, we conclude that the SL[21] model and its variation form SM[22] are clearly the best. Having said this we notice that, as Reynolds[33] pointed out, any of these rapid models will not show any effect of rotation on the invariants (II, III) of the anisotropy tensor b_{ij}. This is clearly a theoretical deficiency of the current rapid models. A further investigation is needed to find out how serious this deficiency will be in practice.

We have directly compared eight return-to-isotropy models with thirty four DNS flows: four shear flows and thirty relaxation flows from axisymmetric contraction, axisymmetric expansion and plane strain. As was discussed earlier, all the return-to-isotropy models are variations of Eq.(2.2.7) derived by Lumley[24]. Therefore the differences in the models are due to the different choices of the model coefficients. Two linear models are due to Rotta[23] and Lumley[24] (which is quasi-linear in b_{ij}). Lumley's model satisfies realizability, matches the data of Comte-Bellot and Corrsin[32] and the limit of the final period of decaying turbulence. It performs perfectly when $III < 0$. It also compares well with the DNS data in which $III \geq 0$. Rotta's model does not compare with the performance of Lumley's model. In fact, the nonlinear models of SS, YA, HP and C&L also do not compare with the performance of Lumley's model. Apparently the model coefficients chosen in these models are not appropriate. The CL[27] model is designed for flows with $III \geq 0$ and is based on their experiments on relaxing turbulence. It does work better than Lumley's model when $III \geq 0$. Finally, the S&M[22] model is a nonlinear model; it works just like Lumley's model when $III < 0$. When $III \geq 0$, it shows an improvement over Lumley's model according to the DNS data. So from these direct comparisons of the return-to-isotropy models, we conclude that the combination of Lumley's model and Choi's model, that is the CL[27] model, will give the best performance. The S&M[22] model seems as good as the CL model according to these comparisons. Having said this, we notice that the existing return-to-isotropy models do not follow the relaxation flows from expansion and plane strain very well. Therefore there is still a need to further investigate and improve the return-to-isotropy models.

For detailed comparison in each flow see the reference[34].

2.3 Near-wall behavior of turbulence

The near-wall behavior of turbulence is re-examined in a way different from that proposed by Hanjalic and Launder[35] and followers[36,37,38,3]. It is shown that at a certain distance from the wall, all energetic large eddies will reduce to *Kolmogorov* eddies (the smallest eddies in turbulence). All the important wall parameters, such as friction velocity, viscous length scale, and mean strain rate at the wall, are characterized by *Kolmogorov* microscales. According to this *Kolmogorov* behavior of near-wall turbulence, the turbulence quantities, such as turbulent kinetic energy, dissipation rate, etc. at the location where the large eddies become "*Kolmogorov*" eddies, can be estimated by using both direct numerical simulation (DNS) data and asymptotic analysis of near-wall turbulence. This information will provide useful boundary conditions for the turbulent transport equations. As an example, the concept is incorporated in the standard k-ε model which is then applied to channel and boundary layer flows. Using appropriate boundary conditions (based on *Kolmogorov* behavior of near-wall turbulence), there is no need for any wall-modification to the k-ε equations (including model constants). Results compare very well with the DNS and experimental data.

Here we only list the results from this study, for the detail see NASA TM 105663.

Model equation and boundary condition

The K-ε equations for incompressible flows can be in general modeled as:

$$\frac{DK}{Dt} = [(\nu + \frac{\nu_T}{\sigma_k})K_{,i}]_{,i} + \nu_T U_{i,j}(U_{i,j} + U_{j,i}) - \varepsilon \tag{2.3.1}$$

$$\begin{aligned}\frac{D\varepsilon}{Dt} &= [(\nu + \frac{\nu_T}{\sigma_\epsilon})\varepsilon_{,i}]_{,i} + C_1 f_1 \nu_T U_{i,j}(U_{i,j} + U_{j,i})\frac{\varepsilon}{K} \\ &\quad - C_2 f_2 \frac{\varepsilon^2}{K} + \nu\nu_T U_{i,jk}U_{i,jk}\end{aligned} \tag{2.3.2}$$

$$C_1 = 1.44, \quad C_2 = 1.92$$
$$f_1 = 1, \quad f_2 = 1 - 0.22\exp(-\frac{R_t^2}{36}), \quad R_t = \frac{K^2}{\nu\varepsilon} \tag{2.3.3}$$
$$\sigma_k = 1, \quad \sigma_\varepsilon = 1.3$$

These equations are used only for the flow field outside of the turbulence limit point y_η, where K_η is non-zero. Therefore, Eq.(2.3.2) will not have singularity problems and will not need any near-wall modifications like other K-ε models do.[2,8]
Eddy viscosity:

$$\nu_T = C_\mu f_\mu \frac{K^2}{\varepsilon} \tag{2.3.4}$$

where,

$$\begin{aligned} C_\mu &= 0.09 \\ f_\mu &= [1 - \exp(a_1 R_k + a_3 R_k^3 + a_5 R_k^5)]^{\frac{1}{2}} \\ a_1 &= -1.5 * 10^{-4} \quad a_3 = -1.0 * 10^{-9} \quad a_5 = -5.0 * 10^{-10} \\ R_k &= \frac{K^{1/2} y}{\nu} \end{aligned} \tag{2.3.5}$$

Boundary conditions: at $y_\eta = 6\nu/u_\tau$,

$$\varepsilon_\eta = 0.251 \frac{u_\tau^4}{\nu} \tag{2.3.6}$$
$$K_\eta = 0.250 u_\tau^2 \tag{2.3.7}$$

In practical applications, $R_{e\tau}$ and $R_{e\infty}$ are large numbers, hence y_η/L (L is the length scale of a flow field) is usually very small. Therefore, as an approximation we may let $y_\eta/L = 0$, but ε_η and K_η must be given by Eqs.(2.3.6) and (2.3.7) respectively. These equations have been applied to the calculations of channel and boundary layer flows.

Comparison of models

To compare the present model with the DNS data and other models (e.g. Jones and Launder[8], and Chien[2]), we have made calculations on two channel flows[15,40] and two boundary layer flows[16,17]. In the present model, all the model constants are the same as used in the standard K-ε model[39]. Therefore the present model will also be suitable for flows away from the wall. The other two models used here for comparison do not have this property. Results are shown in figures 1 – 4. In figure 1 and figure 2, three models are compared with two DNS data for channel flows: one with $R_{e\tau} = 180$, the other with $R_{e\tau} = 395$. The profiles of mean velocity, Reynolds stress, turbulent kinetic energy and its dissipation rate are plotted in these figures. The present model is significantly better than the other two models. Figure 3 shows the similar comparison for a turbulent boundary with $R_{e\theta} = 1410$. The agreement between the present model and DNS data is excellent. Figure 4 shows the results compared with Klebanoff[17] and other boundary layer experiments. The skin friction from DNS data[16] is also shown in this figure. The results of present model are more consistent with the DNS data than the experiments.

It is also worthwhile to emphasize that the present model equations with the standard model coefficients have the simplest form among all two-equation models. Hence, we expect that they will have less numerical stiffness in complex turbulent flows.

2.4 Modeling of transition (Z. Yang and T.-H. Shih)

A model of intermittancy based on the shape factor is added to a two-equation k-ε model for prediction of boundary layer transition with a free stream turbulence. The detailed model and calculations are give by Yang in this year's Research Briefs.

2.5 Modeling of compressible turbulence (W.W. Liou and T.H. Shih)

A two-scale model is proposed based on Hanjalic-Launder's multiple-scale concept for compressible turbulence, in which a distinct scale created by the compressibility is modeled separately by considering the effects of pressure-dilatation and dissipation dilatation on large-scale energy transfer rate. The detailed model is given by Liou in this year's Research Briefs.

2.6 Direct numerical simulation of compressible flows (A. Hsu and T.-H. Shih)

In order to have a better understanding of the effect of compressibility on turbulence, especially the effect of the formation of eddy-shocklets on turbulence, a direct numerical simulation of compressible homogeneous shear turbulent flows is been performing. The data of all turbulence statistics are very useful for turbulence modeling. The detailed simulation is given by Hsu in this year's Research Briefs.

3. Future Plans

Development of second order closure models: pay special attention to the effects of inhomogeneity, non-local property, frame-rotation, compressibility, near-wall behavior in the buffer and log-layers.

4. References

1 Lang, H.J. and Shih, T.-H., "A critical comparison of two-equation turbulence models," NASA TM 105237 (1991).

2 Chien, K.-Y., "Predictions of Channel and Boundary-Layer Flows with a Low-Reynolds-Number Turbulence Model," AIAA Journal, **20**, 33-38, (1982).

3 Shih, T. -H., An Improved $k-\epsilon$ Model for Near-Wall Turbulence and Comparison with Direct Numerical Simulation," NASA TM-103221, August (1990).

4 Lam, C. K. G., and Bremhorst, K., "A Modified Form of the k-ϵ Model for Predicting Wall Turbulence," ASME Transaction, Journal of Fluids Engineering, **103**, September (1981).

5 Nagano, Y. and Hishida, M., "Improved Form of the k-ϵ Model for Wall Turbulent Shear Flows," ASME Transaction, Journal of Fluids Engineering, **109**, June (1987).

[6] Nagano, Y., and Tagawa, M., "An Improved k-ϵ Model for Boundary Layer Flows," ASME Transaction, Journal of Fluids Engineering, **112**, March (1990).

[7] Launder, B. E. and Sharma, B. I., "Application of the Energy-Dissipation Model of Turbulence to the Calculation of a Flow near a Spinning Disk," Letters in Heat and Mass Transfer, **1**, 131-138 (1974).

[8] Jones, W. P. and Launder, B. E., "The Calculation of Low-Reynolds Number Phenomena with a Two-Equation Model of Turbulence," International Journal of Heat and Mass Transfer, **16**, 1119-1130 (1973).

[9] Myong, H. K. and Kasagi, N., "A new Proposal for a k-ϵ Turbulence Model and its Evaluation." JSME Transaction, **54**, 3003-3009 and 3512-3520 (1988).

[10] Yang, Z. and Shih, T. -H., "A $k-\epsilon$ Modeling of Near Wall Turbulence," Proceedings of 4th International Symposium on Computational Fluid Dynamics, UC Davis (1991).

[11] Wilcox, D. C., "A Complete Model fo Turbulence Revisited, " AIAA Paper no. 84- 0176, Reno, Nevada (1984).

[12] Wilcox, D. C., "Progress in Hypersonic Turbulence Modeling," AIAA Paper no.91-1785, Honolulu, HI (1991).

[13] Speziale, C. G., Abid, R. and Anderson, E. C., "A Critical Evaluation of Two-Equation Models for Near Wall Turbulence," AIAA Paper no. 90-1481, Seattle, WA (1990).

[14] Coakley, T. J., "Turbulence Modeling Methods for the Compressible Navier-Stokes Equations," AIAA Paper no. 83-1693, Danvers, Massachusetts (1983).

[15] Kim, J., Moin, P. and Moser, R., "Turbulent Statistics in fully Developed Channel Flow at Low Reynolds Number," Journal of Fluid Mechanics, **177**, 133-166 (1987).

[16] Spalart, P. R., "Direct Simulation of a Turbulent Boundary Layer up to $Re_\theta =$ 1410," Journal of Fluid Mechanics, **187**, 61-98 (1988).

[17] Klebanoff, P. S., "Characteristics of Turbulence in a Boundary Layer with Zero Pressure Gradient," NACA-TN-3178 (1954).

[18] Launder, B.E., Reece, G.J., & Rodi, W. , " Progress in the development of a Reynolds-stress turbulence closure," J. Fluid Mech. (1975), **68**, 537-566 (1975).

[19] Speziale, C.G., Sarkar, S. and Gatski, T.B., "Modeling the pressure-strain correlation of turbulence: an invariant dynamical systems approach," *J. Fluid Mech.*, **227**, 245-272 (1991).

[20] Fu, S., Launder, B.E. and Tselepidakis, D.P., "Accommodating the effects of high strain rates in modeling the pressure-strain correlation. *UMIST Mech. Engng Dept Rep.* TFD/87/5, 1987.

[21] Shih, T.-H. & Lumley, J.L., " Modeling of pressure correlation terms in Reynolds stress and scalar flux equations." Rep. FDA-85-3, *Sibley School of Mech. & Aero. Engrg.*, Cornell University (1985).

[22] Shih, T.-H. and Mansour, N.N., "Reynolds Stress Modeling of Homogeneous Turbulence and Comparison with Numerical Simulations," *Center for Turbulence Research* Proceedings of the Summer Program (1987).

[23] Rotta, J.C., Z. Phys. **129**, 547 (1951).

[24] Lumley, J.L., "Computational modeling of turbulent flows," *Adv. Appl. Mech.* **18**, 123 (1978).

[25] Sarkar, S. and Speziale, C.G., "A simple nonlinear model for the return to isotropy in turbulence," Phys. Fluids, A2 (1), January, (1990).

[26] Haworth, D.C. and Pope, S.B., "A generalized Langevin model for turbulent flows," Phys. fluid **29** (2), February (1986).

[27] Choi, K.S. and Lumley, J.L., *Proceedings of the IUTAM symposium, Kyoto, 1983, Turbulence and Chaotic phenomena in Fluids,* edited by T.Tatsumi (North-Holland, Amsterdam), p.267 (1984).

[28] Craft, T.J. and Launder, B.E., "Computation of Impinging Flows Using Second-Moment Closure," Eighth Symposium on Turbulent Shear Flows, Technical University of Munich, September 9-11 (1991).

[29] Yamamoto, M. and Arakawa, c., "Study on the pressure-strain term in Reynolds stress model," *Eighth Symposium on Turbulent Shear Flows*, Technical University of Munich, September, 9-11 (1991).

[30] Rogers, M.M., Moin, P. & Reynolds, W.C., "The structure and modeling of the hydrodynamic and passive scalar fields in homogeneous turbulent shear flow," Dept. Mech. Engng. Rep. TF-24, Stanford University: Stanford California (1986).

[31] Lee, M.J. & Reynolds, W.C., " Numerical experiments on structure of homogeneous turbulence," Dept. Mech. Engng. Rep. TF-24, Stanford University: Stanford California (1985).

[32] Comte-Bellot, G. and Corrsin, S., " The use of a contraction to improve the isotropy of grid-generated turbulence," J. Fluid Mech. **25**, 657-682 (1966).

[33] Reynolds, W.C.," Effect of Rotation on Homogeneous Turbulence," Tenth Australian Fluid Mechanics Conference, December 11-15 (1989).

[34] Shih, T.-H. and Lumley, J.L., "A Critical Comparison of Second Order Closures with Direct Numerical Simulation of Homogeneous Turbulence," NSAS TM 105351 (1991).

[35] Hanjalic, K. and Launder, B.E., "Contribution Towards a Reynolds-stress Closure for Low–Reynolds–Number Turbulence," J. Fluid Mech, **74**, 593–619 (1976).

[36] Patel, V.C., Rodi, W. and Scheuerer, G., "Turbulence models for near–wall and low–Reynolds–number flows: A review," AIAA Journal, **23**, 1308–1319 (1985).

[37] Mansour, N.N., Kim,J. and Moin. P., "Reynolds-Stress and Dissipation Rate Budgets in a Turbulent Channel Flow," J. Fluid Mech., **194**, 15–44 (1988).

[38] Lai, Y.G. and So, R.M.C., "On near-wall turbulent flow modeling," J. Fluid Mech. **221**, 641-673 (1990).

[39] Launder, B.E. and Spalding, D.B., "Computer Methods in Applied Mechanics and Engineering, **3**, 269 (1974).

[40] Kim, J., Personal communication, 1992.

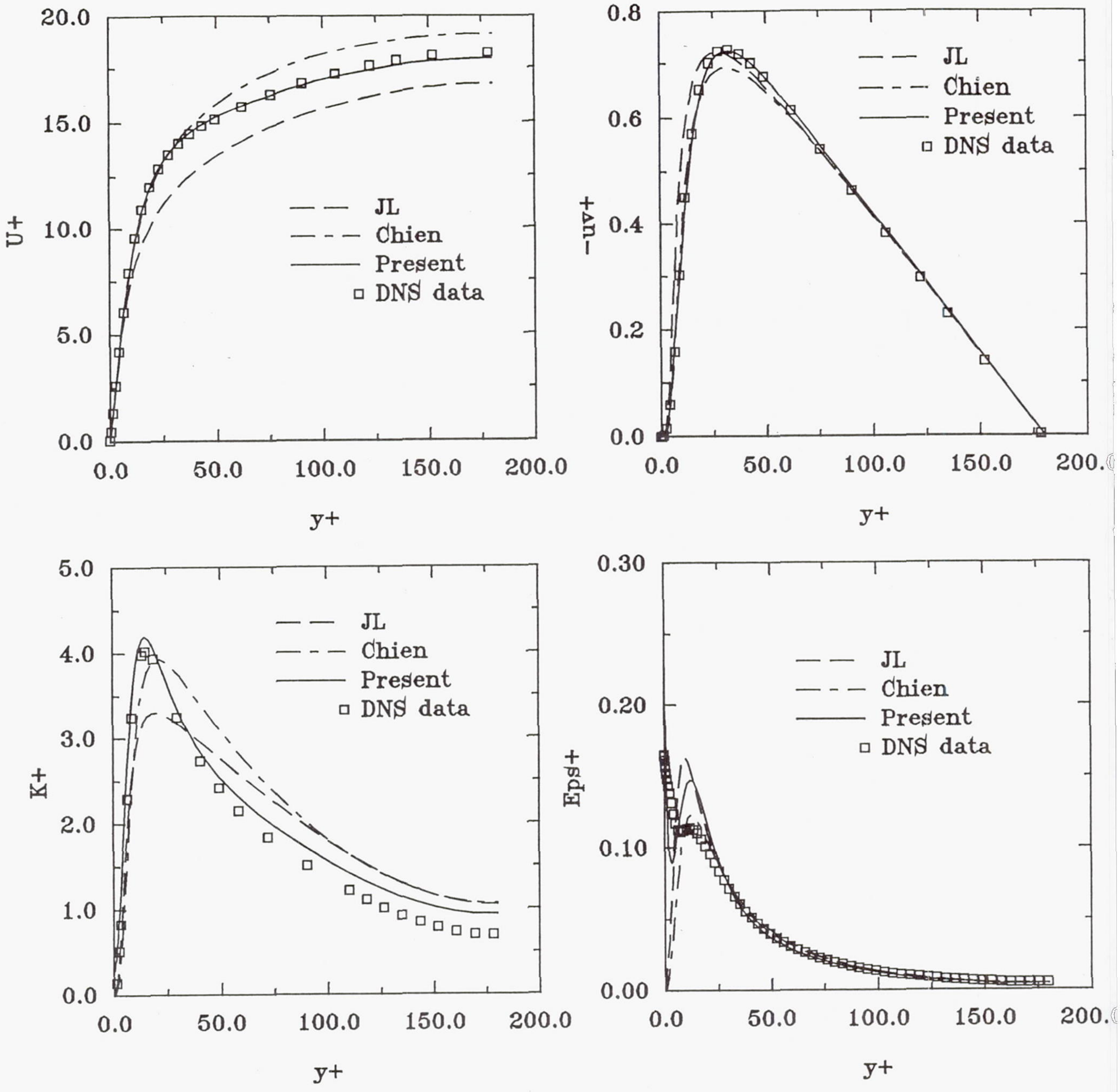

Figure 1. Comparison of models with DNS of 2-D channel with $R_{e\tau}$ = 180.

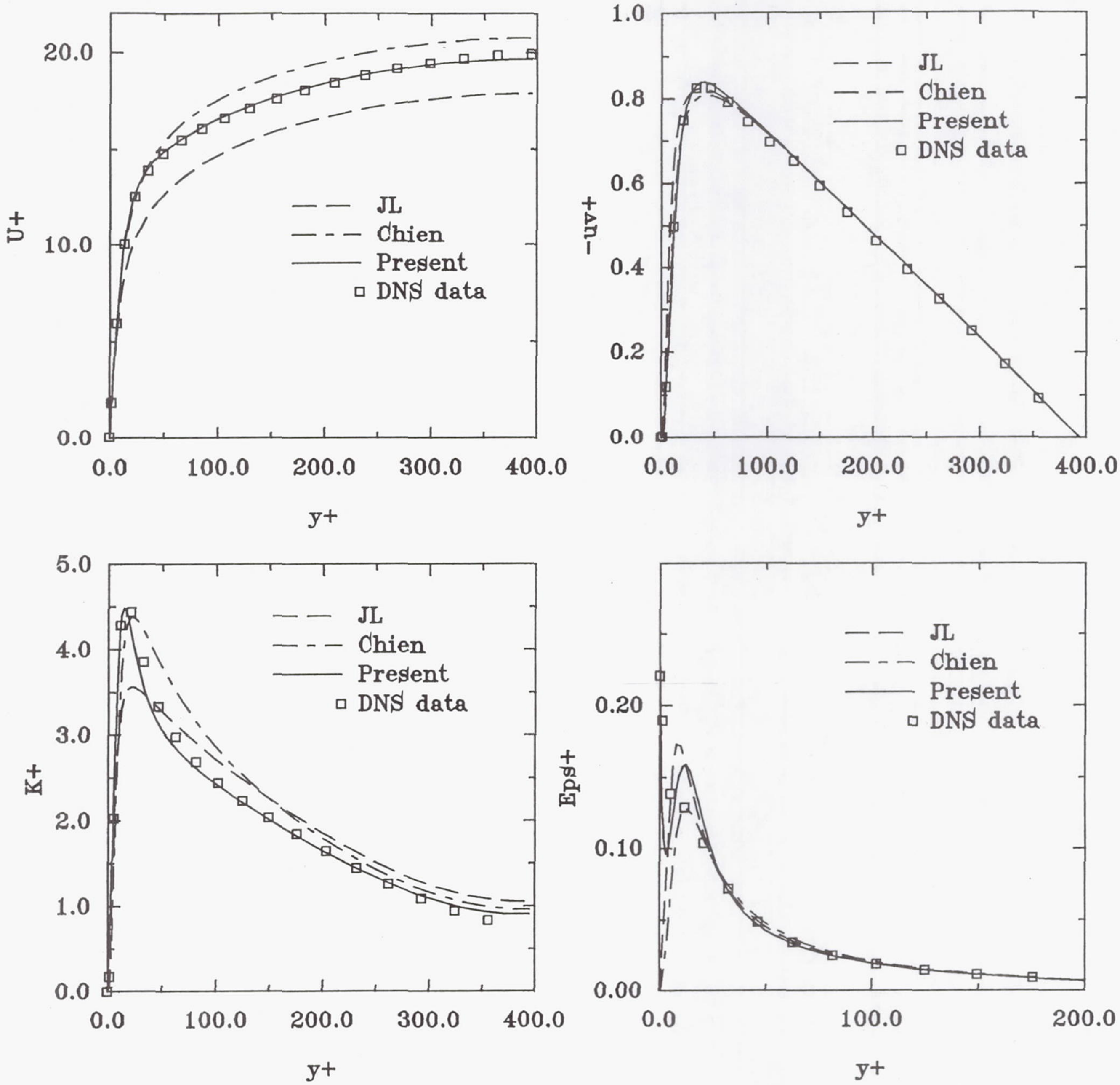

Figure 2. Comparison of models with DNS of 2-D channel with $R_{e\tau} = 395$.

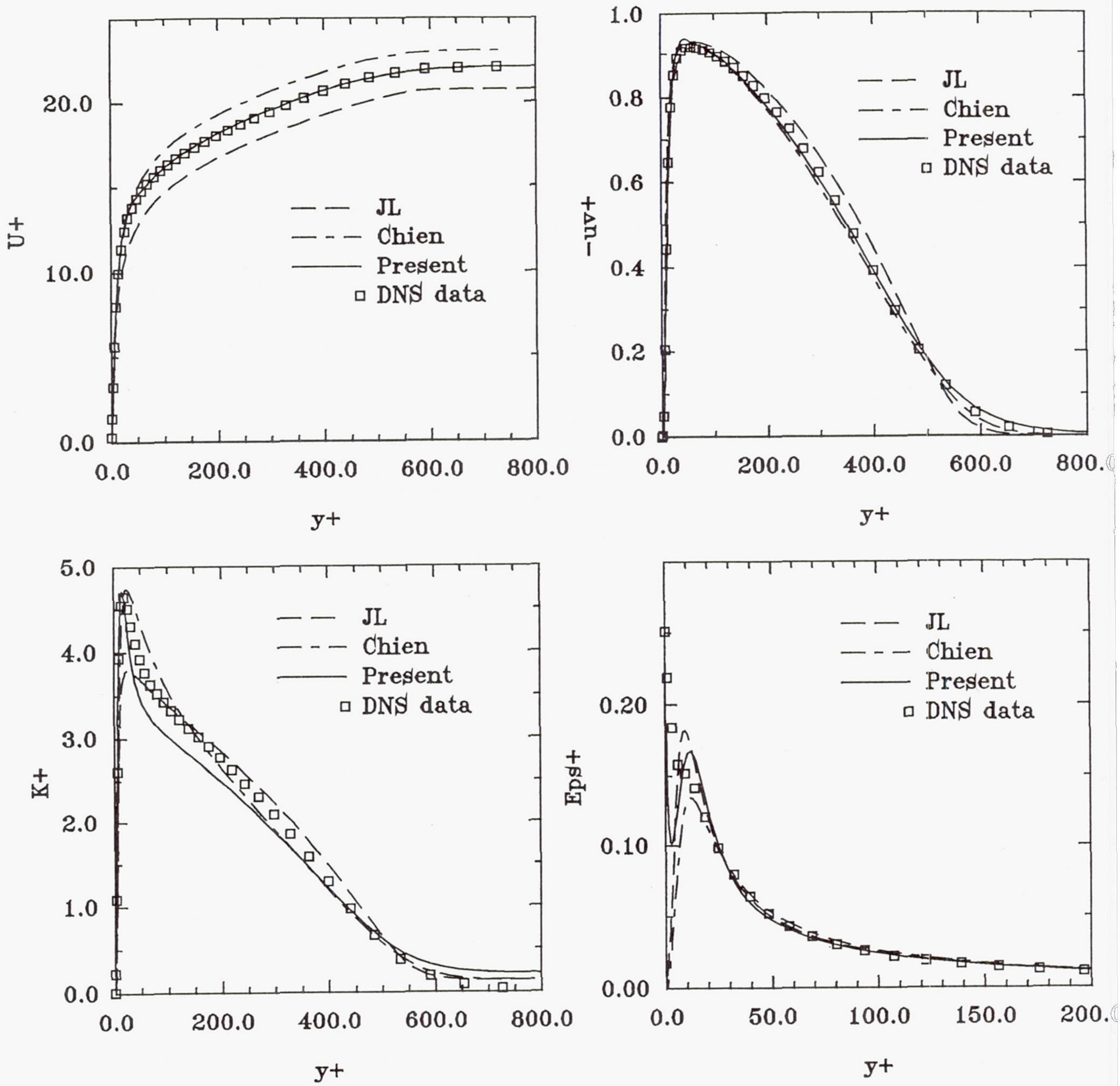

Figure 3. Comparison of models with DNS of 2-D boundary layer flow with $R_{e\theta} = 1410$.

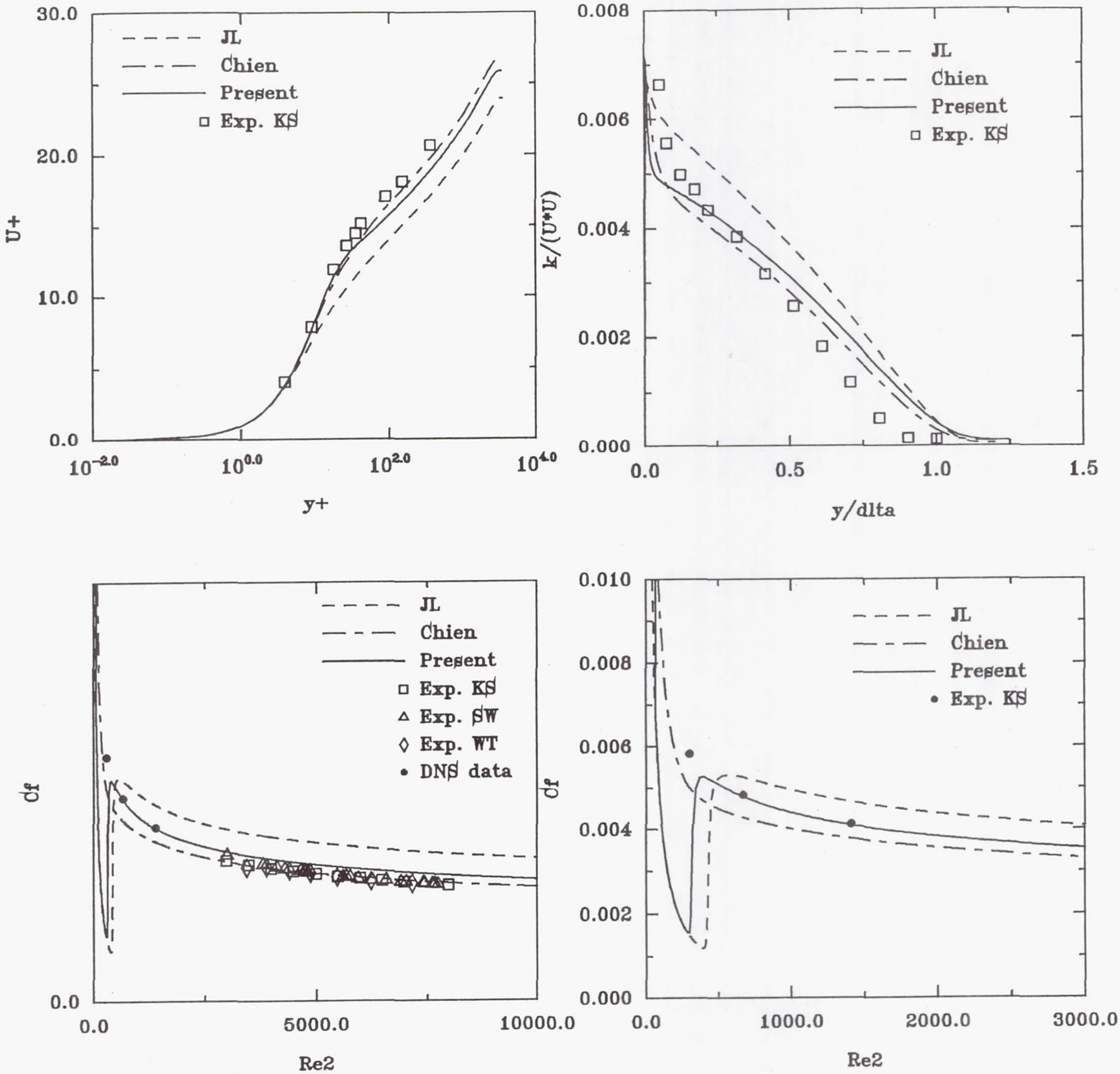

Figure 4. Comparison of models with the experiments of 2-D boundary layer flows (Klebanoff[13] and others).

Turbulence Modeling and Experiments

Aamir Shabbir

1. Motivation and Objective

The best way of verifying turbulence models is to do a direct comparison between the various terms and their models[1,2,3]. The success of this approach depends upon the availability of the data for the exact correlations (both experimental and DNS). The other approach involves numerically solving the differential equations and then comparing the results with the data. The results of such a computation will depend upon the accuracy of all the modeled terms and constants. Because of this it is sometimes difficult to find the cause of a poor performance by a model. However, such a calculation is still meaningful in other ways as it shows how a complete Reynolds stress model performs.

In this study thirteen homogeneous flows are numerically computed using the second order closure models. We concentrate only on those models which use a linear (or quasi-linear) model for the rapid term. This, therefore, includes the Launder ,Reece and Rodi[4] (LRR) model; the isotropization of production [4] (IP) model; and the Speziale, Sarkar and Gatski [5] (SSG) model. The purpose of this study is to find out which of the three models performs better and what are their weaknesses, if any.

The other work reported here deals with the experimental balnces of the second moment equations for a buoyant plume. Despite the tremendous amount of activity toward the second order closure modeling of turbulence, very little experimental information is available about the budgets of the second moment equations. Part of the problem stems from our inability to measure the pressure correlations. However, if everything else appearing in these equations is known from the experiment, pressure correlations can be obtained as the closing terms. This is the closest we can come to in obtaining these terms from experiment, and despite the measurement errors which might be present in such balances, the resulting information will be extremely useful for the turbulence modelers. The purpose of this part of the work reported here was to provide such balances of the Reynolds stress and heat flux equations for the buoyant plume.

2.0.0 Work Accomplished

2.1.0 Comparison of Second Order Models in Homogeneous Flows

Before presenting the results a note about the LRR model constants used in the present study is in order. These constants have evolved to slightly different values than those orginally recommended by LRR[4]. The value of the Rotta constant C_1 (in the return to isotropy term) used in the present study is 3.6 (note that due to a different definition of b_{ij} used here the value of C_1 differs by a factor of two). The

Preceding Page Blank

rapid term constant C_2' was assigned a value of 0.4 in the original LRR model. In the present study the value used for this constant is 0.55 which is slightly higher than the value of 0.5 recommended by Morris[6]. It was found out that the value of 0.55 led to improvement in the performance of LRR model in all the flows tested here. (The improvements were slight for the irrotationally strained flows but

Figure 1 compares the development of Reynolds stresses computed using these three models in a flow through axisymmetric contraction with the DNS data[7].

Here we show a typical case of $S = 100.00$ ($Sk_o/\epsilon_o = 55.73$, case AXM). All the models deviate from the DNS data. However, LRR model gives slightly better results than the SSG model with IP model performing the worst.

Figures 2 and 3 show a similar comparison for flow through axisymmetric expansion for two different strain rates. For the smaller strain rate flow ($S = 0.717, Sk_o/\epsilon_o = .408$, case EXO) SSG model reproduces the $\overline{u^2}$development quite well while both IP and LRR models underpredict it. For the $\overline{v^2}$ component all the models give similar results. Therefore, for this low strain rate flow SSG model is better than the other two models. For the flow with higher strain rate ($S = 7.17, Sk_o/\epsilon_o = 4.08$, case EXP) the LRR model is in excellent agreement with the DNS data for both the components while both IP and SSG models show overprediction So for this flow LRR model works the best.

Now we show comparisons for the distortion of turbulence by plane strain for four cases of differing strain rates. We start from the lower strain rate case. Figure 4 compares the evolution of the three non-zero Reynolds stress components for the flow with strain rate $S = 2.6$ ($Sk_o/\epsilon_o = 2.309$, case PXC), For $\overline{u^2}$component all the models underpredict the DNS data. LRR model is slightly better than the SSG model. IP model is the worst of the three. For $\overline{v^2}$ component IP model works the best. LRR model slightly underpredicts $\overline{v^2}$ while SSG overpredicts it. The third component $\overline{w^2}$ is overpredicted by all the models with LRR model being better than the other two. Figure 5 shows the similar comparisons for the highest strain rate case ($S = 25.0, S_ok/\epsilon_o = 22.227$, case PXE). All the three models underpredict the $\overline{u^2}$component. IP model is the worst of the three models. LRR model gives slightly better result than the SSG model for this stress component. For $\overline{v^2}$ component LRR model is the best and SSG model is the worst of the three. For the $\overline{w^2}$ component all the three models overpredict the DNS data with LRR mdoel being closest to the data. From the above four plane strain flow comparisons, we note that the performance of all the three models deteriorates as the strain rate increases. However, on the overall LRR model works better than the other two models.

Figure 6 shows the same comparison with the homogeneous shear flow experiment[8] ($S = 46.8, Sk_o/\epsilon_o = 6.46$). For the $\overline{u^2}$component LRR model gives the best result whereas SSG and IP models overpredict it. For the $\overline{v^2}$ component also the LRR works the best. SSG model slightly overpredicts the data where as IP model if off by a larger margin. For the $\overline{w^2}$ component both SSG and IP models reproduce the data very well whereas LRR model overpredicts the data. For the shear stress component LRR performs reasonably whereas SSG model slightly overpredicts the data and IP model is off the data by a higher margin. So, for this experiment, LRR model has better overall performance than the other two models.

Last, we discuss the evolution of $\overline{q^2}$ for the case of rotating homogeneous shear flow. Since no experimental or DNS data is available for this flow the comparisons will be made (for two cases) with the LES[9]. Bardina[10] pointed out that in this case we should be careful in interpreting the comparisons for anything more than the trends shown by the LES. In all the cases shown here the initial conditions corresponded to isotropic turbulence with $\epsilon_0/Sk_o = 0.296$. Figure 7 shows the comparisons for the three cases of different Rosby numbers ($= \Omega/S$). For $\Omega/S = .25$ we note that all three models significantly underpredict the LES results for $\overline{q^2}$; SSG being closest to the LES data and the LRR being the furthest. Qualitatively all the three models reproduce the LES trends. For the case of $\Omega/S = 0.50$ SSG is in excellent agreement with the LES results. Both IP and LRR give identical results and give a smaller value of $\overline{q^2}$ than the LES. It should be pointed out that SSG model constants were partially calibrated against this flow. For the third case of $\Omega/S = 1.0$, all the three models give identical results. Since no LES results are available for this case the only purpose of showing the results is to see how the three models compare with each other.

2.1.2 Conclusions

Results were shown from numerical computation of various homogeneous turbulent flows using three different turbulence models. All of these models use a linear (or quasi-linear) model for the rapid part of the pressure strain model. Based on their overall performance it is found that LRR model works better than both SSG and IP models. For the irrotationally flows the differences between the models and DNS data increased with the strain rate with LRR model performing better than the other two models. For the simple homogeneous shear flow LRR model better than the SSG model (for the DNS both performed equally good but for the experiment LRR worked better). For the homogeneous shear flows both SSG and LRR model showed trends similar to those shown by LES with SSG performing better than the LRR model. It is worth noting that SSG model has seven empirical constants as compared to two in LRR model and on the overall it still does not perform better than LRR model. Part of the reason for this may be due to the fact that the SSG model does not satisfy the normalization constraint where as LRR model does. (Normalization is an exact property of the pressure strain correlation; see references 4 and 11 for details.) As has been pointed out by Shih and Lumley[3], for a model of the rapid pressure strain part which is linear in the anisotropic tensor and satisfies all of its *exact* properties, LRR is the most general model.

2.2.0 Experimental Balances for the Second Moments for a Buoyant Plume

2.2.1 Heat Flux Budgets

The transport equation for the vertical (streamwise) heat flux can be written as

$$U\frac{\partial\overline{wt}}{\partial r} + W\frac{\partial\overline{wt}}{\partial z} = -\frac{1}{r}\frac{\partial}{\partial r}(r\overline{uwt}) - \frac{\partial}{\partial z}(\overline{wwt}) - \overline{uw}\frac{\partial T}{\partial r} - \overline{w^2}\frac{\partial T}{\partial z}$$

$$- \overline{ut}\frac{\partial W}{\partial r} - \overline{wt}\frac{\partial W}{\partial z} + g\beta\overline{t^2} - \frac{1}{\rho}\overline{t\frac{\partial p}{\partial z}} - (\nu+\Gamma)\overline{t_{,j}w_{,j}} \qquad (1)$$

Note that the molecular term is written in local cartesian coordinates. The balance of this equation is shown in figure 8. Advection term is the smallest in this balance and, therefore, contributes least to the transport of the heat flux $\overline{wt}$. It is clear that in the central core of the flow.($r/z < 0.04$), the production of this heat flux is maintained by the mean buoyancy gradients and the turbulent buoyancy force i.e. the source of energy is the gravitational field. The shear production is relatively small in this region. Then there is an intermediate region where the production from mean velocity and gravitational field are of the same order. However, for $r/z > 0.1$ (which approximately corresponds to the plume half width), most of the production is maintained by the mean velocity and buoyancy gradients and the turbulent buoyancy production is only a small fraction of these two. The closing term in the heat flux balances is labelled as Π_i and represents the sum of the pressure correlation and the molecular destruction terms i.e.

$$\Pi_i = \frac{1}{\rho}\overline{t\frac{\partial p}{\partial x_i}} - (\nu+\Gamma)\overline{\frac{\partial u_i}{\partial x_j}\frac{\partial t}{\partial x_j}} \qquad (2)$$

The molecular term in (2) is thought to get weaker with increasing Reynolds and Peclet numbers, eventually approaching a value of zero in the limit of local (small scale) isotropy. This term was not measured and, therefore, its magnitude relative to others can not be established. However, in turbulence modeling, it is customary to combine this term with the pressure correlation term[8] and, therefore, from that point of view not knowing each term separately does not reduce the usefulness of these budgets. Notice that the shape of this term is very similar to the shape of the heat flux $\overline{wt}$ and its magnitude remains large throughout the flow field.

The equation for the radial heat flux is

$$U\frac{\partial\overline{ut}}{\partial r} + W\frac{\partial\overline{ut}}{\partial z} = -\frac{1}{r}\frac{\partial}{\partial r}(r\overline{uut}) - \frac{\partial}{\partial z}(\overline{wut}) - \overline{u^2}\frac{\partial T}{\partial r} - \overline{uw}\frac{\partial T}{\partial z}$$
$$- \overline{ut}\frac{\partial U}{\partial r} - \overline{wt}\frac{\partial U}{\partial z} - \frac{1}{\rho}\overline{t\frac{\partial p}{\partial r}} - (\nu+\Gamma)\overline{t_{,j}u_{,j}} \qquad (3)$$

The balance of this equation is shown in figure 9. Again, we note that the advection term is quite small as compared to the other dominant terms in the equation. Unlike the $\overline{wt}$ heat flux balance, the shear production is extremely small here. This is because the gradients of mean radial velocity are much smaller than the gradients in the mean vertical (streamwise) velocity. There is no turbulent buoyancy production in this equation and all the production is due to the mean buoyancy gradients. We note that the term representing sum of the pressure correlation and the molecular destruction makes up a substantial part of the budget and its shape is similar to the radial heat flux. We also note that this budget can not be divided into any subregions, where some phenomenon are more dominant than others, because the relative magnitude of each of the terms in equation (3) remains the same across the flow field.

2.2.2 Reynolds Stress Budgets

The transport equation for the Reynolds stress, within Bussinesq approximation, is

$$U_k\ (\overline{u_iu_j})_{,k} = -\ [\overline{u_iu_ju_k}]_{,k} - (\overline{u_iu_k}\ U_{j,k} + \overline{u_ju_k}\ U_{i,k}) + \beta_i\overline{u_jt} + \beta_j\overline{u_it} + \frac{1}{\rho}(\overline{u_ip_{,j} + u_jp_{,i}}) - 2\nu\overline{u_{i,k}u_{j,k}} \tag{4}$$

where the viscous diffusion term has been neglected since it will be small as compared to the turbulent diffusion.

For reasons of convenience, turbulence modelers do not model the pressure correlation term in the form as it appears in the above equation but re-write it in a different form by separating it into a deviatoric and a non-deviatoric part. Two ways of doing this have been suggested in the literature and we will look at both of these before deciding which one to use in the present study. The traditional way of writing this term is[4]

$$-\frac{1}{\rho}(\overline{u_ip_{,j} + u_jp_{,i}}) = \frac{1}{\rho}\overline{p(u_{i,j} + u_{j,i})} - \frac{1}{\rho}(\overline{pu_i}\delta_{jk} + \overline{pu_j}\delta_{ik})_{,k} \tag{5}$$

where the first term on the right hand side is the deviatoric part. The second term is the so called pressure diffusion term. Lumley[12] (1975) has instead suggested the following separation

$$-(\overline{u_ip_{,j} + u_jp_{,i}}) = -\left[\frac{1}{\rho}(\overline{u_ip_{,j} + u_jp_{,i}}) - (\frac{2}{3\rho})(\overline{pu_k})_{,k}\delta_{ij}\right] - (\frac{2}{3\rho})(\overline{pu_k})_{,k}\delta_{ij} \tag{6}$$

where the term in the square brackets is the deviatoric part and the last term on the right hand side is the pressure diffusion term. Regardless of which separation is employed a correction or model has to be used for the correlation $\overline{pu_k}$. The model used here is due to Lumley[8] is given by $\overline{pu_k} = -\overline{q^2u_k}/5$. This study indicates that the use of this model with (5) produces so much pressure diffusion that it negates the velocity diffusion (i.e. due to $\overline{u_iu_ju_k}$). On this basis it was concluded to use the separation given by (6) in the present study. (For further details see Shabbir[1]3).

Therefore, using (6) the equation for the Reynolds stress can be re-written as

$$\begin{aligned} U_k\ (\overline{u_iu_j})_{,k} = &-\left[\overline{u_iu_ju_k} + \frac{2}{3\rho}(\overline{pu_k})\delta_{ij}\right]_{,k} - (\overline{u_iu_k}\ U_{j,k} + \overline{u_ju_k}\ U_{i,k}) - \beta_i\overline{u_jt} - \beta_j\overline{u_it} \\ &\left\{-[\frac{1}{\rho}(\overline{u_ip_{,j} + u_jp_{,i}}) - \frac{2}{3\rho}(\overline{pu_k})_{,k}\delta_{ij}] \right. \\ &\left. - 2\nu\overline{u_{i,k}u_{j,k}} + \frac{2}{3}\epsilon\delta_{ij}\right\} - \frac{2}{3}\epsilon\delta_{ij} \end{aligned} \tag{7}$$

where $\epsilon = \epsilon_{ii}$. Note that anisotropic part of the dissipation part has been combined with the pressure correlation term[11]. The term in the curly parenthesis has a zero trace and will be denoted by Φ_{ij} in the rest of the paper. It is this term whose models have been proposed. Note that the above equation is exact since no approximations have been used so far. Now we introduce the model for the pressure diffusion term, as given above, and with this approximation the above equation becomes

$$U_k\ (\overline{u_i u_j})_{,k} \approx -\left[\overline{u_i u_j u_k} + \frac{2}{15}(\overline{q^2 u_k})\delta_{ij}\right]_{,k} - (\overline{u_i u_k}\ U_{j,k} + \overline{u_j u_k}\ U_{i,k}) + \beta_i \overline{u_j t} + \beta_j \overline{u_i t}$$
$$+ \Phi_{ij} - \frac{2}{3}\epsilon\delta_{ij} \tag{8}$$

Note that due to the model for the pressure diffusion term this is no longer an exact equation and $\approx$ has been used to emphasize this fact. It is this equation which will be balanced out with the experimental data and the term Φ_{ij} will be obtained as the closing term. It should be reminded that in addition to the measurement errors, any uncertainty in the approximation of the pressure diffusion will also be lumped into Φ_{ij}.

The equation for the streamwise Reynolds stress $\overline{w^2}$ is given by

$$U\frac{\partial\overline{w^2}}{\partial r} + W\frac{\partial\overline{w^2}}{\partial z} \approx -\frac{1}{r}\frac{\partial}{\partial r}(r\overline{uw^2}) - \frac{\partial}{\partial z}(\overline{ww^2}) + \frac{2}{15}\left[\frac{1}{r}\frac{\partial}{\partial r}(r\overline{uq^2}) + \frac{\partial}{\partial z}(\overline{wq^2})\right]$$
$$- 2\overline{uw}\frac{\partial W}{\partial r} - 2\overline{w^2}\frac{\partial W}{\partial z} + 2g\beta\overline{wt} - \Phi_{zz} - \frac{2}{3}\epsilon \tag{9}$$

The balance of this equation is shown in figure 10. Advection is the smallest of all the terms. Diffusion term is a gain near the center of the plume and a loss in the rest of the flow. Also, its magnitude near the center is comparable to the other dominant terms in the balance. We note that the buoyancy production is comparable to the production due to mean velocity gradients near the plume center but over the rest of the flow field the shear production is much larger than the buoyancy production. It is also interesting to note that the buoyancy production and dissipation rate approximately balance each other. The closing term in this balance is Φ_{zz} and represents the sum of the pressure correlation term and the anisotropic part of the dissipation. This term is a loss for the $\overline{u^2}$ budget and we note that beyond $r/z = 0.08$ this term and shear production approximately balance each other.

The equation for the radial component $\overline{u^2}$ is given by

$$U\frac{\partial\overline{u^2}}{\partial r} + W\frac{\partial\overline{u^2}}{\partial z} \approx -\frac{1}{r}\frac{\partial}{\partial r}(r\overline{uu^2}) - \frac{\partial}{\partial z}(\overline{wu^2}) + \frac{2}{15}\left[\frac{1}{r}\frac{\partial}{\partial r}(r\overline{uq^2}) + \frac{\partial}{\partial z}(\overline{wq^2})\right]$$
$$- 2\overline{u^2}\frac{\partial U}{\partial r} - 2\overline{uw}\frac{\partial U}{\partial z} - \Phi_{rr} - \frac{2}{3}\epsilon \tag{10}$$

and its balance is shown in figure 11. Obviously the advection of $\overline{u^2}$ has the same form as the advection of $\overline{w^2}$. The production due to velocity gradients is a loss near the plume center and is a gain after about $r/z = 0.04$. This is because the radial gradient of the radial mean velocity is positive near the plume center. The mechanical production term is not large. The diffusion term is a loss over most of the flow field and becomes a gain toward the outer edge of the flow field. The sum of the pressure correlation term and the anisotropic part of the dissipation rate is obtained as the closing term in the budget and represents a gain for $\overline{u^2}$. We further note that beyond $r/z = 0.08$ it approximately balances the dissipation rate.

Finally we look at the budget for the shear stress $\overline{uw}$ as shown in figure 12. Its equation is given by

$$U\frac{\partial\overline{uw}}{\partial r} + W\frac{\partial\overline{uw}}{\partial z} \approx -\frac{1}{r}\frac{\partial}{\partial r}(r\overline{uuw}) - \frac{\partial}{\partial z}(\overline{wuw}) - \overline{uw}\frac{\partial U}{\partial r} - \overline{uw}\frac{\partial U}{\partial z} - \overline{u^2}\frac{\partial W}{\partial r}$$
$$- \overline{uw}\frac{\partial W}{\partial z} + g\beta\overline{ut} - \Phi_{rz} \qquad (11)$$

Both advection and the turbulent buoyancy production are of very small magnitude and over most of the flow field these approximately balance each other. Neglecting these two terms would not cause any significant change in the shear stress balance. We note that the diffusion term is not negligible in this budget. The term Φ_{rz} is essentially balanced by the difference between the shear production and diffusion processes. The shape of Φ_{rz} is obviously similar to that of the shear stress and its peak approximately corresponds to the peak in the shear production.

3. Future Plans

3.1 Turbulence Modeling (with T.-H. Shih)

(a). Compare the performance of the various non-linear second order models in different homogeneous flows in order to find out their strengths and weakneses. This will be an extension of the work presented in section 1 of this brief.

(b). To develop and test models for turbulent diffusion terms in the Reynolds stress equations using Lumley's theory of third moments[11].

3.2 DNS of Bypass Transistion (with T.-H. Shih and G. Karniadakis).

The bypass transition is an important engineering problem due to its relevence to turbomachinery environment and, therefore, there is a considerable interest both at LeRC and at CMOTT to study this phenomenon. We are interested in carrying out the DNS for this problem both in order to provide a data base for the modeling efforts of bypass transition at CMOTT and to study its physics. For the former we are interesting in finding out what kind of global parameters, if any, are linked to the transition process. For the later we are interested in finding out, for instance, what is the effect of anisotropy in the free stream turbulence velocity and length scale on the transition process.

These simulations will be designed after the experiments of Sohn and Reshotko[14] who studied the bypass transition over a flat plate with differing free stream turbulence intensities. The results of DNS will be compared with these experiments.

3.2.1 Numerical Scheme.

Currently we are exploring the possibility of using a spectral element code for its suitability for doing such a DNS. We are inclined to use a spectral element method because of its higher accuracy and its ease of local grid refinement.

The numerical scheme used in the code involves fractional time discretization which results in three sets of semi discrete equations. In the first step advection term is handled explicitly using a third order Adams-Bashforth scheme. In the second step Poisson equation for pressure is solved implicitly and continuity is satisfied. In the third fractional step the diffusion terms are accounted implicitly by a second order Crank-Nicholson method.

In order to carry out the spatial discretization the flow domain is first decomposed into macro elements. Each of these macro elements uses a local cartesian mesh by employing Gauss-Labatto collocation points. Then within each macro element the flow variables are represented as tensor product of Chebychev polynomial. These representations of the flow variables are then substituted into the governing equations and discrete equations are obtained by applying the weighted residual technique.

3.2.2 Test Cases to be run

Several test cases will have to be run in order to validate the code before a full DNS can be carried out. First of these is to solve the laminar boundary layer flow over a flat plate in order to insure that the numerical method gives the Blasius solution. This will also help us explore the various boundary conditions which can be used at the top boundary and at the outflow and latter can be used for the mean flow during the DNS. After this has been successfully accomplished the most unstable mode disturbances based on the linear stability theory will be intorduced. This will allow comparing their growth rates (in the linear region) with the solutions from the linear stability theory. The third case will be that of suction and blowing through the flat plate and the resutls will be compared with those obtained by previous workers.

4. References

[1] Shabbir, A. and D.B. Taulbee. Evaluation of Turbulence Models for Predicting Buoyant Flows. J. Heat Trans., 112, 945-951 (1990).

[2] Shih, T.-H., A. Shabbir and J.L. Lumley. Advances in the Modeling of Pressure Correlations terms in the Second Moment Equations. NASA TM. 104413 (1991).

[3] Shih,T.-H. and J.L. Lumley. A Critical Comparison of Second Order Closures with Direct Numerical Simulation of Homogeneous Turbulence. NASA TM 105351 (1992).

[4] Launder, B.E., Reece and W. Rodi.Progress in the Development of Reynolds-stress Turbulence Closure. JFM, 68, 537-566 (1975).

[5] Speziale, C.G., S. Sarkar and T.B. Gatski. Modeling the Pressure-Strain Correlation of Turbulence; An Invariant Dynamical Systems Approach. JFM, 227, 245-272, (1991).

[6] Morris, J. Modeling the Pressure Redistribution Terms. Phys. Fluids, 27, 7, 1620-1623 (1984).

[7] Lee, M. and W.C. Reynolds. Numerical Experiments on the Structure of Homogeneous Turbulence. Stanford University Report No. TF-24 (1985).

[8] Tavoularis, S and S. Corrsin. Experiments in Nearly Homogeneous Turbulent Shear Flow with a Uniform Mean Temperature Gradient. Part 1. JFM, 104, 311-347 (1981).

[9] Bardina, J., J.H. Ferziger and W.C. Reynolds Improved Turbulence Models Based on Large-Eddy Simulation of Homogeneous, Incompressible Turbulent Flows. Stanford University Technical Report TF-19 (1983).

[10] Bardina, J. Private communication (1992).

[11] Lumley, J. L. Computational Modeling of Turbulent Flows. Advances in Applied Mechanics, 18, 123-176 (1978).

[12] Lumley, J.L. Phys. Fluids, 18, 750 (1975).

[13] Shabbir, A. of the 8th Symposium on Turbulent Shear Flows (1991).

[14] Sohn, K.-H., and E. Reshotko Experimental Study of Boundary Layer Transition With Elevated Freestream Turbulence on a Heated Flat Plate. NASA CR 187068 (1991).

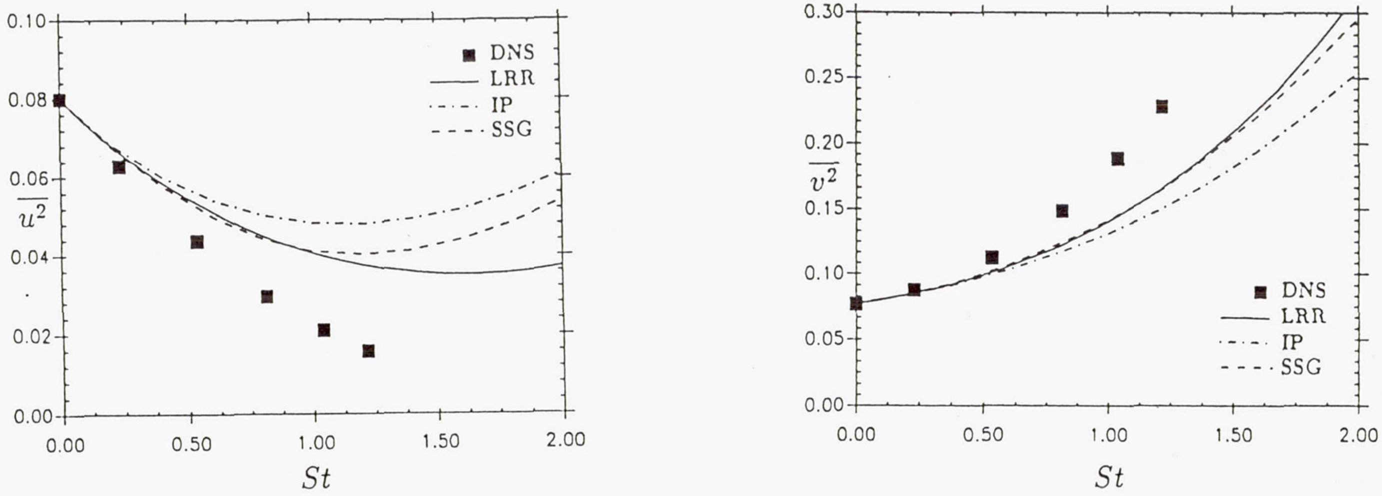

Figure 1. Comparison of the models for flow through axisymmetric contraction with the DNS data of of Lee and Reynolds (1985).

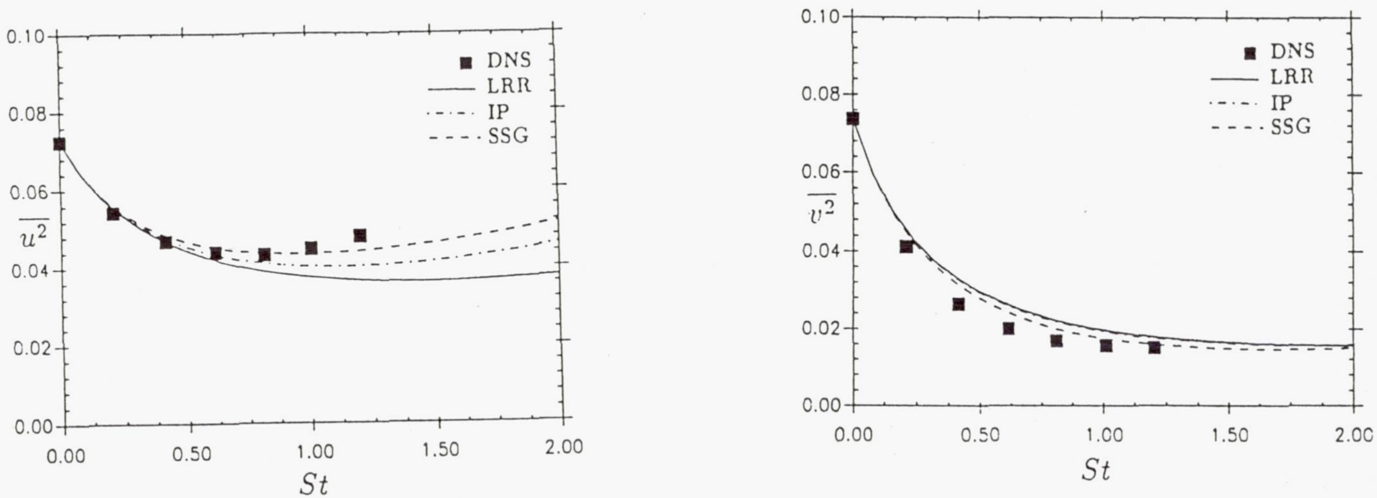

Figure 2. Comparison of the models for flow through axisymmetric expansion with the DNS data of of Lee and Reynolds (1985), case EXO.

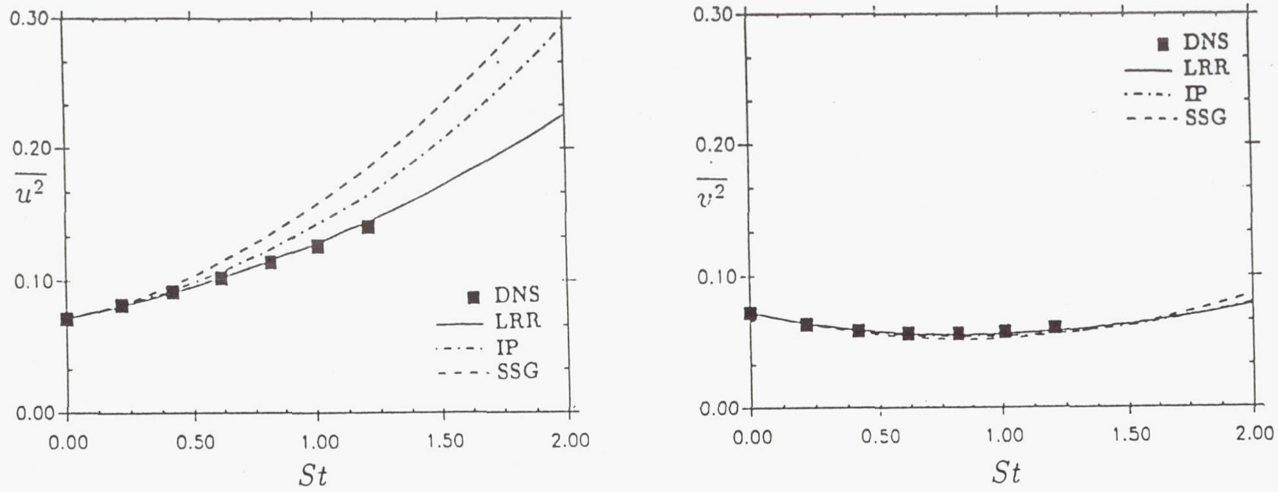

Figure 3 . Comparison of the models for flow through axisymmetric expansion with the DNS data of of Lee and Reynolds (1985), case EXP.

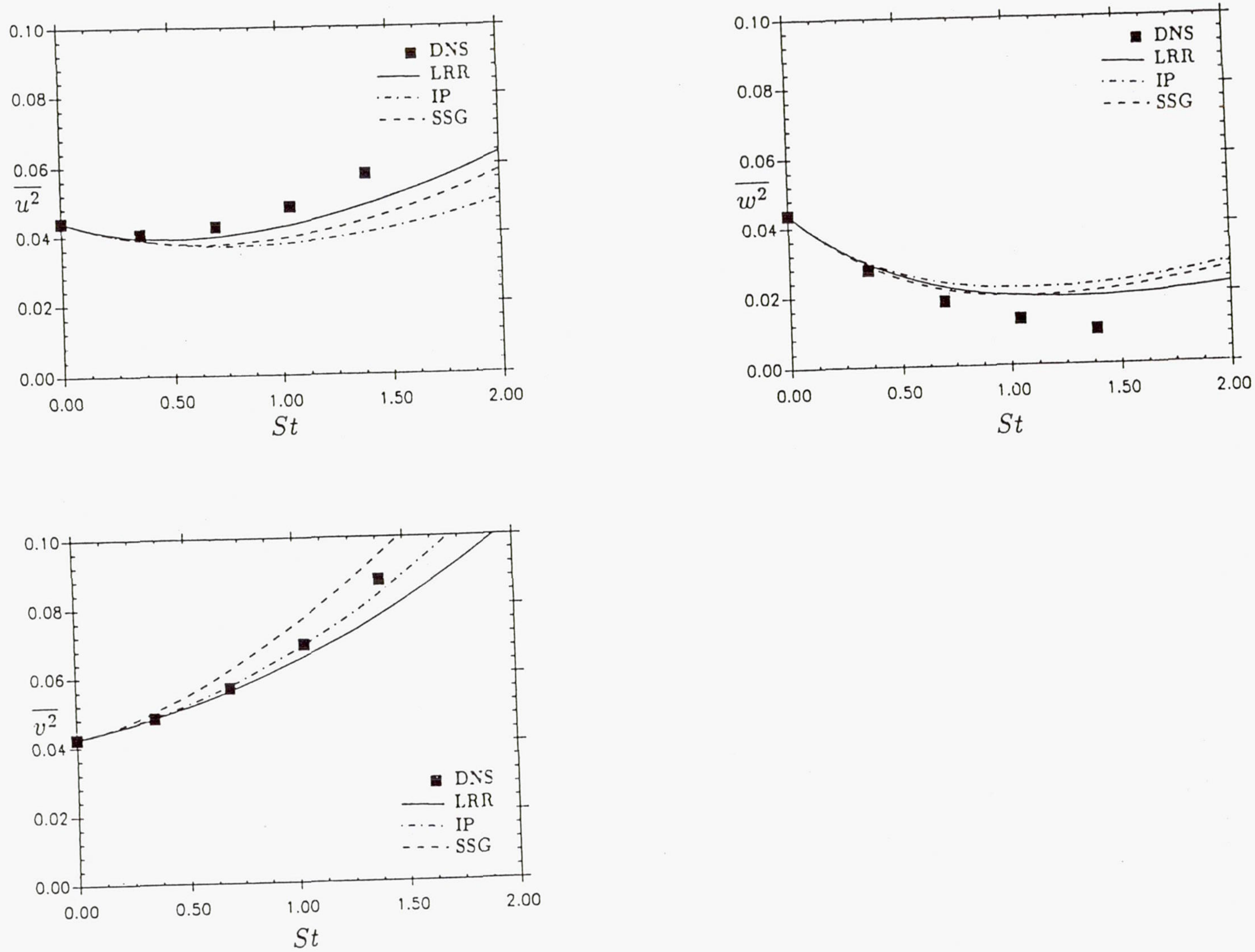

Figure 4 . Comparison of the models for distortion by plane strain with the DNS data of Lee and Reynolds (1985), case PXC, S=2.6.

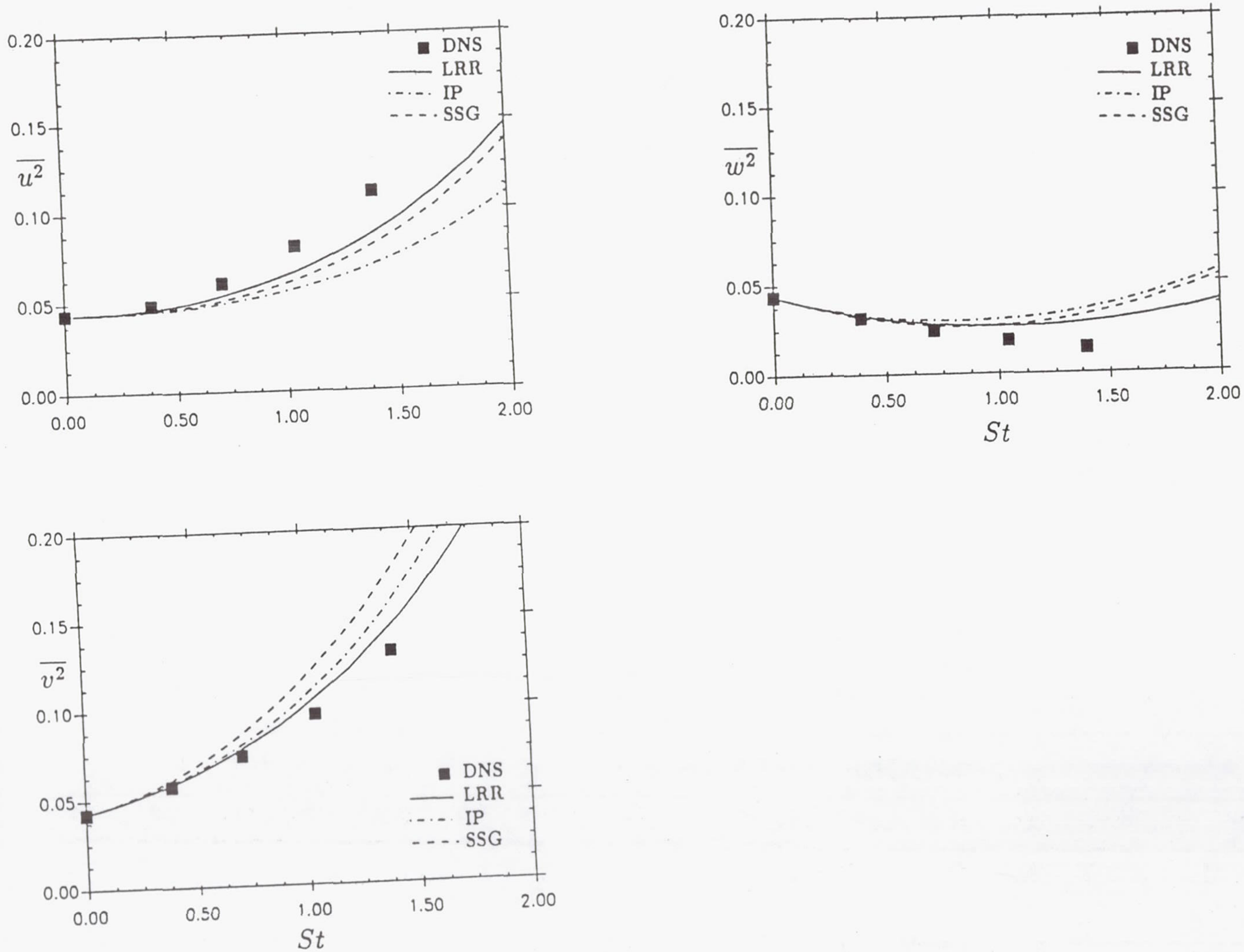

Figure 5 . Comparison of the models for distortion by plane strain with the DNS data of Lee and Reynolds (1985), case PXE, S=25.0

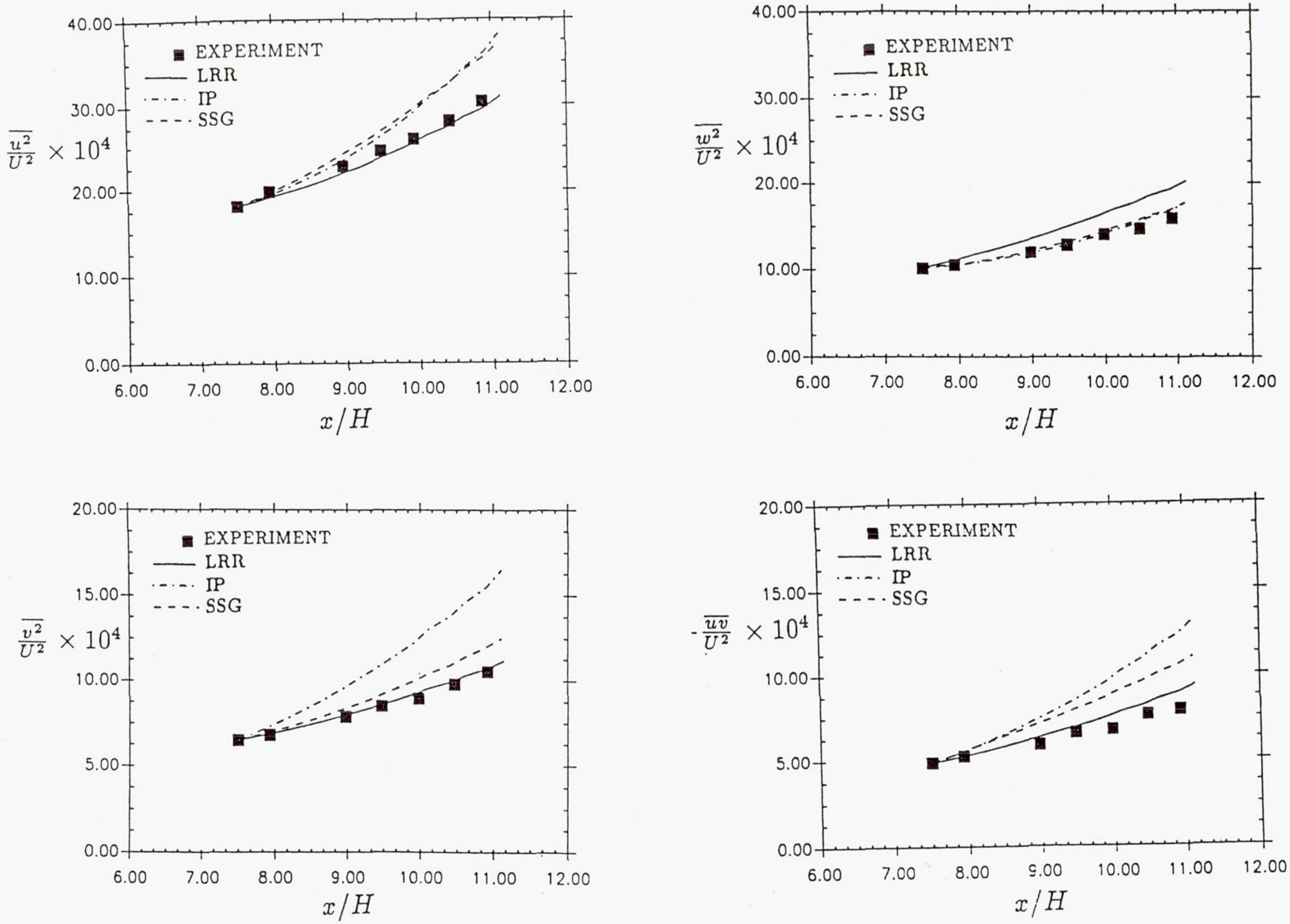

Figure 6 . Comparison of the models for homogeneous shear flow with the data Tavoularis and Corrsin (1981).

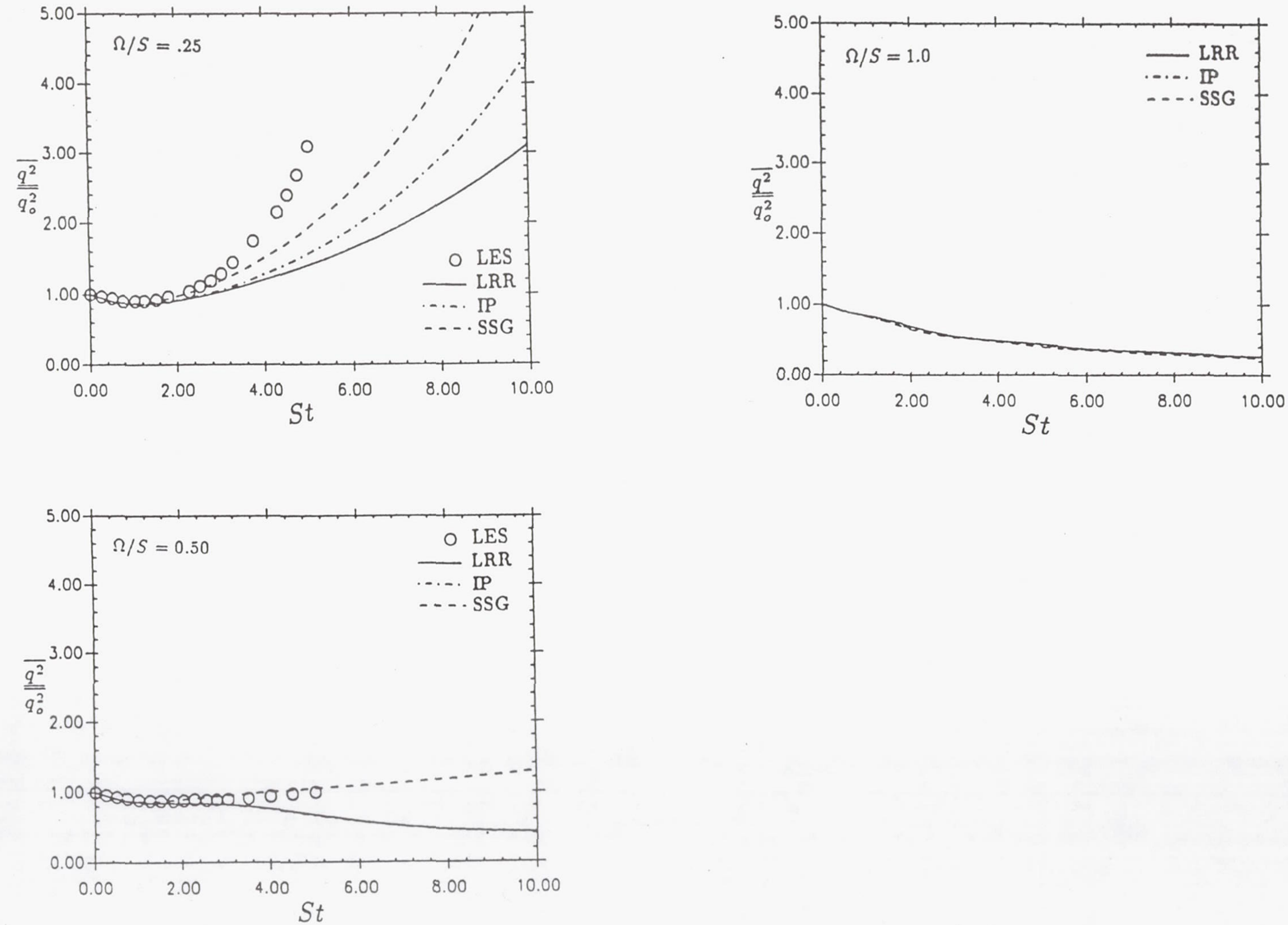

Figure 7.. Comparison of the models for the rotating homogeneous shear flow with the large eddy simulation of Bardina *et al.* (1983).

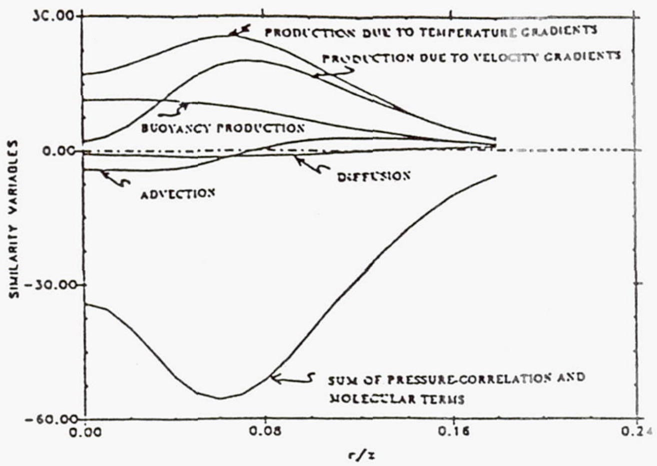

Figure 8 . Budget for $\overline{wt}$ equation.

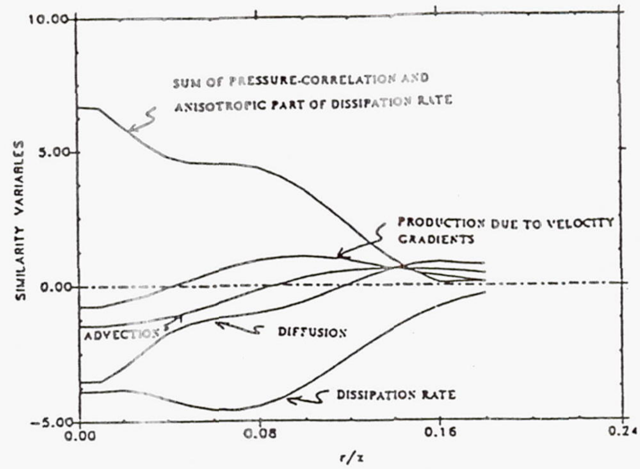

Figure 9 Budget for $\overline{uw}$ equation.

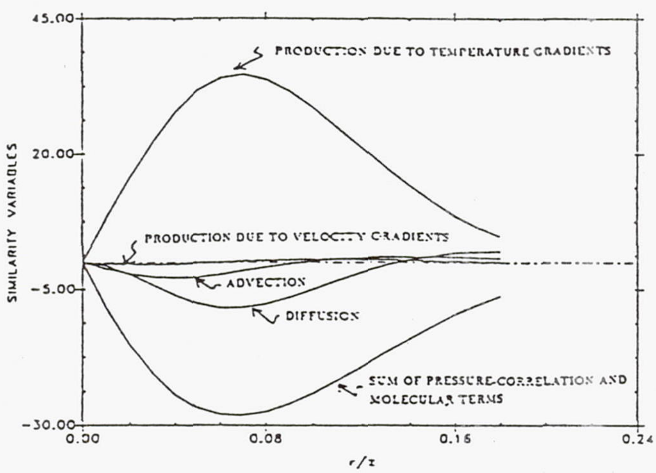

Figure 10 Budget for $\overline{ut}$ equation.

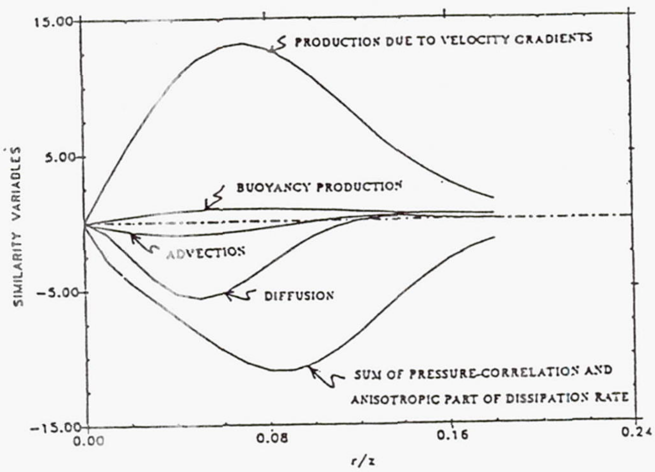

Figure 11. Budget for $\overline{uw}$ equation.

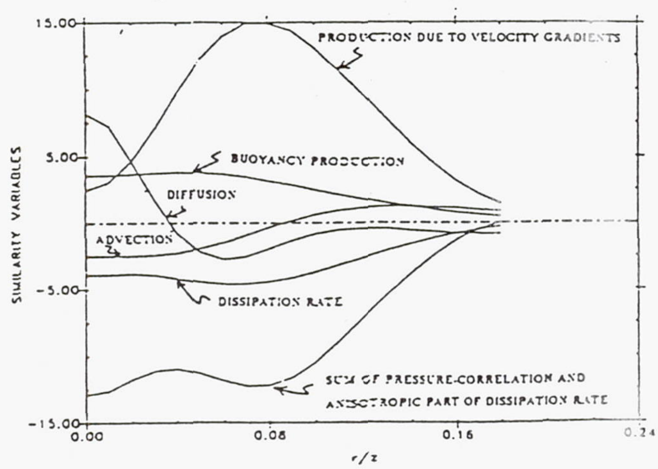

Figure 12. Budget for $\overline{w^2}$ equation.

Modeling of Turbulent Shear Flows

William W. Liou

1. Motivation and Objective

This report documents the current progress in the research and development of modeling techniques for turbulent shear flows. These include a two-scale model for compressible turbulent flows and a new energy transfer model. The former represents the status of our efforts to identify compressibility effects in turbulence. The energy transfer model refines a weakly nonlinear wave model developed earlier, which models directly the turbulent large structures. The objective of these activities is to develop second-order closures for compressible turbulent flows.

2. Work Accomplished

2.1 A Two-Scale Model for Compressible Turbulent Flows

Numerical simulations of 2D and 3D compressible turbulence have shown that the existence of shocklet structures and the energy transfer mechanism between the kinetic energy and the thermal-energy are the two important compressibility effects[1,2,3,4]. These compressibility effects are incorporated into a new two-scale model. The model is based on the proposition that the effect of compressibility in turbulence is mainly on the energetic large eddies in turbulent shear flows. The small eddies are affected only indirectly through the increased spectral energy transfer. The development of the model and some results of its application to compressible free shear layers are briefly described here. A more detailed analysis is included in a NASA TM[5].

Firstly, it is assumed that the shocklet structures that may occur intermittently in compressible turbulent flows are formed mainly by the collision of the energetic turbulent eddies of large scale. The small eddies, which contain much less energy, are less efficient in the formation of shocklet structures when they collide with other eddies. Thus, the eddy shocklets scale with the energy containing eddies and have more direct influence on the evolution of the large eddies than on the smaller ones. The large vortical structures are intensified as they pass through the shocklet. This process, in other words, enhances the vortex stretching mechanism and increases the spectral energy transfer. In addition to the usual route of the vortex stretching mechanism that has already been enhanced, the small eddies may be generated directly from the passage of the large vortical structures through shock waves These processes of enhanced energy transfer may then cause the spectrum to depart from equilibrium. Another mechanism that may also contribute to the non-equilibrium spectrum or the creation of vorticity is strongly related to the pressure fluctuation. It has been shown by Kida and Orszag[3] and Lee *et al.*[2], among others, that substantial vorticity is created by the baroclinic terms. The creation of vorticity, however, occurs mainly at the shock wave.

Based on the picture described above, the effect of compressibility in turbulence is mainly on the energy containing large eddies or the low wavenumber fluctuations. The large eddies respond more readily to changes in the compressible mean flow resulting from either high speed or combustion. The straining of the large eddies due to compressibility effects increases the spectral energy transfer to the small scales through the mechanism of vortex stretching and direct generation. The smaller scales, on the other hand, are only indirectly affected by compressibility. The energy contained in the small scales in the high wavenumber part of the energy spectrum is increased only as more energy is pumped in from the large eddies associated with the low wavenumber part of the spectrum. To model the Favre-averaged mean compressible turbulent quantities associated with these two distinct regimes in the energy spectrum we solve the modeled transport equations for the kinetic energy of the large eddy (k_p) and the small eddy (k_t) and the rate of energy transfer from the large eddy to the small eddy (ϵ_p) and the rate of energy dissipation (ϵ_t). The transport equations are

$$\bar{\rho}\frac{\overline{\mathrm{D}}\widetilde{k_p}}{\overline{\mathrm{D}}t} = \frac{d}{dy}[(\bar{\mu} + \frac{\mu_T}{\sigma_{\widetilde{k_p}}})\frac{d\widetilde{k_p}}{dy}] + \mu_T(\frac{d\tilde{u}}{dy})^2 - \bar{\rho}\widetilde{\epsilon_p} + \text{P.D.} \tag{1}$$

$$\bar{\rho}\frac{\overline{\mathrm{D}}\widetilde{\epsilon_p}}{\overline{\mathrm{D}}t} = \frac{d}{dy}[(\bar{\mu} + \frac{\mu_T}{\sigma_{\widetilde{\epsilon_p}}})\frac{d\widetilde{\epsilon_p}}{dy}] + Cp_1\frac{\widetilde{\epsilon_p}}{\widetilde{k_p}}\mu_T(\frac{d\tilde{u}}{dy})^2 - Cp_2'\bar{\rho}\frac{\widetilde{\epsilon_p}^2}{\widetilde{k_p}} + \text{E.S.} \tag{2}$$

$$\bar{\rho}\frac{\overline{\mathrm{D}}\widetilde{k_t}}{\overline{\mathrm{D}}t} = \frac{d}{dy}[(\bar{\mu} + \frac{\mu_T}{\sigma_{\widetilde{k_t}}})\frac{d\widetilde{k_t}}{dy}] + \bar{\rho}\widetilde{\epsilon_p} - \bar{\rho}\widetilde{\epsilon_t} \tag{3}$$

$$\bar{\rho}\frac{\overline{\mathrm{D}}\widetilde{\epsilon_t}}{\overline{\mathrm{D}}t} = \frac{d}{dy}[(\bar{\mu} + \frac{\mu_T}{\sigma_{\widetilde{\epsilon_t}}})\frac{d\widetilde{\epsilon_t}}{dy}] + Ct_1\bar{\rho}\frac{\widetilde{\epsilon_t}\widetilde{\epsilon_p}}{\widetilde{k_t}} - Ct_2\bar{\rho}\frac{\widetilde{\epsilon_t}^2}{\widetilde{k_t}} \tag{4}$$

P.D. and E.S. denote the effects of pressure-dilatation and eddy shocklets, respectively. The definition of the model constants can be found in the NASA TM. The present two-scale model for compressible turbulence is built upon a parallel model for incompressible flows, Duncan *et al.*[6]. Models for the terms responsible for the compressibility effects are needed to close the equations. In this analysis, we have adopted Sarkar's[7] model for the pressure-dilatation terms. To model the effects of the increased spectral energy transfer due to compressibility, a simple model has been constructed through dimensional reasoning. Its coefficient has a M_t^2 dependence, similar to the dilatation dissipation model proposed by Zeman[8] and Sarkar *et al.*[9]. The compressibility corrections that they proposed have been implemented successfully into $k-\epsilon$ models, Viegas and Rubesin[10], into $k-\omega$ models, Wilcox[11] and into second-order closure models, Speziale and Sarkar[12].

Fig. 1 shows the variation of the vorticity thickness growth rate, $\mathrm{d}\delta_\omega/\mathrm{d}x$, as a function of convective Mach number. The vorticity thickness, δ_ω, is defined by

$$\delta_\omega = \frac{U_f - U_s}{(\mathrm{d}U/\mathrm{d}y)_{max}}. \tag{5}$$

The convective Mach number is defined as the ratio of the average convective velocity of the dominant large scale structures, relative to the free stream, to the free stream speeds of sound, Papamoschou and Roshko[13]. The convective Mach number has been shown to be an appropriate parameter to correlate experimental data and to identify the effects of compressibility. The vorticity thickness growth rates for compressible free shear flows, $(\mathrm{d}\delta_\omega/\mathrm{d}x)(M_c, U_s/U_f, \rho_s/\rho_f)$, have been normalized by the corresponding values for incompressible flows, $(\mathrm{d}\delta_\omega/\mathrm{d}x)_i(0, U_s/U_f, \rho_s/\rho_f)$, and are presented in Fig. 1. The value of $(\mathrm{d}\delta_\omega/\mathrm{d}x)_i$ is obtained by using a relation, Papamoschou and Roshko[13],

$$(\frac{\mathrm{d}\delta_\omega}{\mathrm{d}x})_i \sim \frac{(1-\frac{U_s}{U_f})(1+(\frac{\rho_s}{\rho_f})^{1/2})}{1+\frac{U_s}{U_f}(\frac{\rho_s}{\rho_f})^{1/2}}. \tag{6}$$

The constant of proportionality is obtained by the present model calculations performed in the limit of $M_c \rightarrow 0$. Measured data are denoted by open symbols in Fig. 1. Without the compressibility corrections, the current two-scale model and the two-scale model developed by Kim and Chen[14] (KC) predict a large reduction of the growth rate only at very high convective Mach numbers. With the inclusion of the effects of eddy shocklets and the pressure work, the current compressible two-scale model predicts a smooth reduction of the vorticity thickness growth rate as the convective Mach number increases. The calculated growth rate curve levels off at high convective Mach numbers. It should be noted that in the present analysis the convective Mach number of the shear layer is increased by increasing the Mach number of the high speed stream. According to the definition of the convective Mach number, there exists a maximum convective Mach number for a plane mixing layer of the same fluid with matched total temperature. That is,

$$\lim_{M_f \rightarrow \infty} M_c = \frac{1-r}{(\frac{(\gamma-1)(1-r^2)}{2})^{1/2}} \tag{7}$$

where $r = U_s/U_f$ and γ denotes the ratio of the specific heats of the working fluid. For a value of R=0.1, the limiting convective Mach number for a plane shear layer of air is about 2.0.

Since it is the Reynolds shear stress that appears in the mean momentum equations and influences directly the development of the mean flow, it is interesting to see how its peak value varies as a function of M_c. Note that in the current analysis, the Reynolds shear stress is related to the mean flow by a turbulent eddy viscosity, μ_t. That is,

$$-\bar{\rho}\widetilde{u'v'} = \mu_T \frac{\partial \tilde{u}}{\partial y} \tag{8}$$

and

$$\mu_T = C_\mu \bar{\rho} \frac{(\tilde{k}_p + \tilde{k}_t)^2}{\tilde{\epsilon}_p} \tag{9}$$

In Fig. 2, the peak Reynolds shear stresses predicted by the present compressible two-scale model are compared with measured data, Elliott and Samimy[15]. The predictions of the present model, without compressibility corrections and of the KC model are also shown for comparison. The results show that, without the inclusion of some forms of compressibility corrections, none of the two-scale models tested, including the current model and the KC model, performs satisfactorily in the calculations of compressible free shear layers. The present compressible two-scale model under-predicts the absolute value of the peak Reynolds shear stress. However, the trend observed in the experiment that the level of the peak Reynolds shear stress decreases with increasing convective Mach number is picked up consistently by the current compressible two-scale model. Note that the Reynolds shear stress has been normalized by the square of the velocity difference of the two free streams. The model also shows that the value of the peak Reynolds shear stress appears to be independent of the velocity ratio of the free streams. In fact, the predicted variation of the peak value of the Reynolds shear stress as a function of the convective Mach number is similar to the predicted variation of the normalized vorticity thickness growth rate as a function of the convective Mach number. This characteristic of the present compressible two-scale model is consistent with the observation made by Elliott and Samimy[15]. They argue that, based on an integral analysis, the decreasing trend of the level of the Reynolds shear stress, as the convective Mach number is increased, is due mainly to the decrease of momentum thickness growth rate. However, the two speed ratios considered here, 0.1 and 0.2, are nearly equal to each other. Cases with a wider range of operating conditions, such as the speed ratios and the working fluids, need to be examined before any conclusive statement can be made.

To further validate the present compressible two-scale model, it is applied to the compressible free shear layer corresponding to the Case 1 in Samimy and Elliott[16]. In this case, a fully expanded plane shear layer of air with $M_c = 0.51$ and $r = 0.36$ is examined. The calculated mean profile shown in Fig. 3 agrees reasonably well with the measurement. As described previously, there are many possible causes for the small difference in the outer region of the mixing zone. Fig. 4 shows the comparison of the computed and the measured Reynolds shear stress. The present two-scale model under-predicts the peak Reynolds shear stress by about 12%. The profile of the Reynolds shear shear stress, however, agree very well with the measurement.

2.2 A New Energy Transfer Model for Turbulent Free Shear Flows

The model is built upon the weakly nonlinear wave models developed by Liou and Morris[17]. The development of the energy transfer model and some results of its application to an incompressible free shear layer are briefly described here. A more detailed analysis is included in a NASA TM[18].

The random flow properties are split into three components,

$$\tilde{f}_i = F_i + f_i + f_i' \tag{10}$$

The fluctuation with respect to the long time-average component, F_i, is separated into a component representing the large-scale motion, f_i, and one representing the residual fluctuations, f_i'. The long time-average of the instantaneous value is denoted by an overbar,

$$\bar{\tilde{f}}_i = F_i = \frac{1}{T_1} \int_0^{T_1} \tilde{f}_i \mathrm{d}t \tag{11}$$

For the large-scale fluctuation, a separable form of solution is assumed,

$$\{\mathbf{u},\ \mathbf{v},\ \mathbf{p}\} = A(x)\ [\hat{u}(y), \hat{v}(y), \hat{p}(y)]\ exp\ [i(\alpha x - \omega t)]. \tag{12}$$

The bold face quantities denote a complex solution whose real part describes the physical properties of the large-scale structures. α $(= \alpha_r + i\alpha_i)$ denotes a complex wavenumber and ω the frequency. The governing equations for the local distributions of the large structures can be reduced to the Rayleigh equation in terms of $\hat{v}$,

$$\left\{ (\ \alpha U - \omega\ ) (\ \frac{\mathrm{d}^2}{\mathrm{d}y^2} - \alpha^2\ ) - \alpha \frac{\mathrm{d}^2 U}{\mathrm{d}y^2} \right\} \hat{v} = 0 \tag{13}$$

The amplitude, $A(x)$, appears as a parameter in the local calculation for the $\hat{u}, \hat{v}, \hat{p}$ and is determined separately from the large scale turbulent kinetic energy equation,

$$U_j \frac{\partial k}{\partial x_j} = -\overline{u_i u_j} \frac{\partial U_i}{\partial x_j} - \frac{\partial}{\partial x_j} (\overline{u_j k} + \frac{\overline{p u_j}}{\varrho}) - \overline{(- < u_i' u_j' >) \frac{\partial u_i}{\partial x_j}}$$

$$- \frac{\partial}{\partial x_j} \overline{(u_i < u_i' u_j' >)} + \text{viscous terms} \tag{14}$$

where $k = \frac{1}{2}\overline{u_i u_i}$. k denotes the turbulent kinetic energy of the large-scale structure. Note that in this analysis k denotes the turbulent kinetic energy of large scale structure of a single mode. The $\widetilde{k}_p$ defined in the first part of this report represents the sum of the turbulent kinetic energy of all the modes in the entire large-scale spectrum. $<>$ represents a short time-average with an average interval much smaller than T_1 but much larger than the characteristic time scale of the background small-scale fluctuation, Strange and Crighton[19]. The interaction terms, the third expression on the right hand side of equation (14), describe the transfer of large-scale energy, presumably, to the small scales where energy is eventually dissipated by viscosity. The detailed analysis of the weakly nonlinear wave models and the numerical solution procedure used here can be found in Liou and Morris[17].

The spectral energy transfer results from the interactions between turbulent fluctuations of different scales. For the weakly nonlinear wave turbulence models, the energy transfer is of crucial importance in the determination of the wave amplitude and needs to be considered carefully. Very little information, experimental or theoretical, is available regarding the stresses, $- < u_i' u_j' >$.

The weakly nonlinear analysis seeks normal mode solution of the large-scale turbulent fluctuation. Locally, the fluctuations are described by the linearized Euler equations. On the other hand, the spatial extent of each of the modes of the large-scale structures could be regarded as being determined by the wavenumber, α_r. Therefore, the proposition here is to estimate the characteristic size of the large scales as the wavelength associated with the large structures, which are predicted by the weakly nonlinear analysis. That is,

$$l = l_w = \frac{2\pi}{\alpha_r}. \tag{15}$$

where l_w denotes the wavelength. Through dimensional reasoning, the enregy transfer can be modeled by

$$C_2 \frac{k^{\frac{3}{2}}}{l_w} \tag{16}$$

This is the proposed model for the energy transfer from the large scale to the small scale. This estimate is in accord with the classic assumption of turbulence theory that dissipation ".. proceeds at a rate dictated by the inviscid inertia behavior of the large eddies", Tennekes and Lumley [20]. Computationally, since the wavenumber is already a part of the solution of the equations for the large-scale fluctuation, this model involves no extra efforts in estimating the characteristic size of the energy containing large scales. This rather simple model provides a closure to the equations for the large-scale structure, thereby allowing render the weakly nonlinear wave description of the large-scale structure to be self-contained. This self-contained nature of the weakly nonlinear wave turbulence models may be important in the future applications to other turbulent free shear flows.

The model is tested against an incompressible plane mixing layer. Since the most unstable mode interacts most strongly with the mean flow[17], the most amplifying local instability is used in the modeling of the average, overall interactions between the mean and the large scale motions. Therefore, in the present formulation, the characteristic length scale l_w is determined only by the locally most unstable modes.

Fig. 5 shows the predicted evolution of the streamwise mean velocity profiles with axial distance. η is a similarity coordinate,

$$\eta = \frac{y - y_{1/2}}{x - x_0} \tag{17}$$

where $y_{1/2}$ denotes the location where the local mean velocity is one half of the free stream velocity. The predicted self-similar profiles agree well with that compiled by Patel[21] except at the low speed edge of the layer. Similar differences were also observed by Liou and Morris[17]. They attributed this difference to the single mode representation of the entire large scale spectrum and the uncertainties in the measurements in this region resulting from the local large changes in the instantaneous flow direction.

The streamwise evolution of the amplitude of the large-scale structures is shown in Fig. 6. After a region of establishment, the amplitude reaches a saturated value.

In this region, the rate of the production of the large-scale turbulent kinetic energy from the mean flow is balanced by the rate of energy transfer from the large scales to the small scales. Note that, for the present energy transfer model, the amplitude equation becomes,

$$\frac{\mathrm{d}A^2}{\mathrm{d}x} = G_3(x)\, A^2 - G_4(x)\, A^3 \tag{18}$$

G_3 and G_4 denote the normalized positive definite integrals of the production terms and interaction terms across the layer, respectively. The critical points of the nonlinear equation (18), where $\mathrm{d}A^2/\mathrm{d}x = 0$, are $A_1 = 0$ and $G_4(x_2)A_2 = G_3(x_2)$. Simple analyses by applying the Liapunov function method[22] show that A_1 is an unstable critical point. Any small disturbances to A_1, say A_1' would grow exponentially. In fact,

$$(A_1^2)' \approx e^{G_3(x_1)\, x} \tag{19}$$

A_2, on the other hand, is asymptotically stable. A disturbance about the A_2, say A_2', would decay exponentially,

$$(A_2^2)' \approx e^{-\frac{G_3(x_2)}{2}\, x} \tag{20}$$

The saturated value of the amplitude, A_2, is an asymptotically equilibrium value. It indicates an asymptotically equilibrium state of the large-scale structures. The simple instability analyses also show that any deviation away from this equilibrium state would be damped out exponentially. Consequently, the saturation of the wave amplitude may provide an indication of the the self-similarity of the flow in terms of the development of the large-scale structures.

3. Future Plans

3.1 A Two-Scale Model for Compressible Turbulent Flows

(1) Extend the two-scale model to wall-bounded flows.

(2) Continue the development of second-order closure models that account explicitly for the compressibility effects identified during the development of the two-scale eddy-viscosity model.

3.2 A New Energy Transfer Model for Turbulent Free Shear Flows

(1) Apply the weakly nonlinear wave model to compressible mixing layers to investigate the effects of compressibility on the characteristics of the coherent large-scale structures.

4. References

[1] Passot, T. and Pouquet, A., "Numerical simulation of compressible homogeneous flows in the turbulent regime," J. Fluid Mech., **181**, 441-466 (1987).

[2] Lee, S., Lele, S. K. and Moin, P., "Direct numerical simulation and analysis of shock turbulence interaction," AIAA paper 91-0523.

[3] Kida, S. and Orszag, S. A., "Energy and spectral dynamics in forced compressible turbulence," J. Sci. Comp. **5** (1990).

[4] Kida, S. and Orszag, S. A., "Enstrophy budget in decaying compressible turbulence," J. Sci. Comp. (1991)

[5] Liou, W. W. and Shih, T.-H., "A two-scale model for compressible turbulent flows," NASA TM (to appear) (1992).

[6] Duncan, B. S., Liou, W. W. and Shih, T.-H., "A Multiple-scale turbulence model for incompressible flow," NASA TM (to appear) (1992).

[7] Sarkar, S., Erlebacher, G., Hussaini, M. Y. and Kreiss, H. O., " The analysis and modeling of dilatational terms in compressible turbulence," NASA CR 18195 (1989).

[8] Zeman, O., "Dilatation dissipation: The concept and application in modeling compressible mixing layers," Phys. Fluids A **2** (2), 178-188 (1990).

[9] Sarkar, S., Erlebacher, G. and Hussaini, M. Y., "Compressible homogeneous shear: simulation and modeling," NASA CR 189611 (1992).

[10] Viegas, J. R. and Rubesin, M. W., "A comparative study of several compressibility corrections to turbulence models applied to high-speed shear layers," AIAA paper 91-1783.

[11] Wilcox, D. C., "Progress in hypersonic turbulence modeling," AIAA paper 91-1785.

[12] Speziale, C. G. and Sarkar, S., "Second-order closure models for supersonic turbulent flows," AIAA paper 91-0217.

[13] Papamoschou, D. and Roshko, A., "The compressible turbulent shear layer: an experimental study," J. Fluid Mech. **197**, 453-477 (1988).

[14] Kim, S.-W. and Chen, C.-P., "A multiple-time-scale turbulence model based on variable partitioning of turbulent kinetic energy spectrum," NASA CR-179222 (1987).

[15] Elliott, G. S. and Samimy, M., "Compressibility effects in free shear layers," Phys. Fluids A (1991)

[16] Samimy, M. and Elliott, G. S., "Effects of compressibility on the characteristics of free shear layers," Phys. Fluids A **28**, 439-445 (1990).

[17] Liou, W. W. and Morris, P. J., "Weakly nonlinear models for turbulent mixing in a plane mixing layer," to appear in Phys. Fluids (1992).

[18] Liou, W. W., "A new energy transfer model for turbulent free shear flows," NASA TM (to appear) (1992).

[19] Strange, P. J. R. and Crighton, D. G., "Spinning modes on axisymmetric jets, Part I," J. Fluid Mech. **134**, 231-245 (1983).

[20] Tennekes, H. and Lumley, J. L., *A First Course in Turbulence*, M.I.T. Press, 1972.

[21] Patel, R. P., "An experimental study of a plane mixing layer," AIAA Journal **11**, 67-71 (1973).

[22] Simmons, G. F., *Differential Equations with Applications and Historical Notes*, McGraw Hill, 1972.

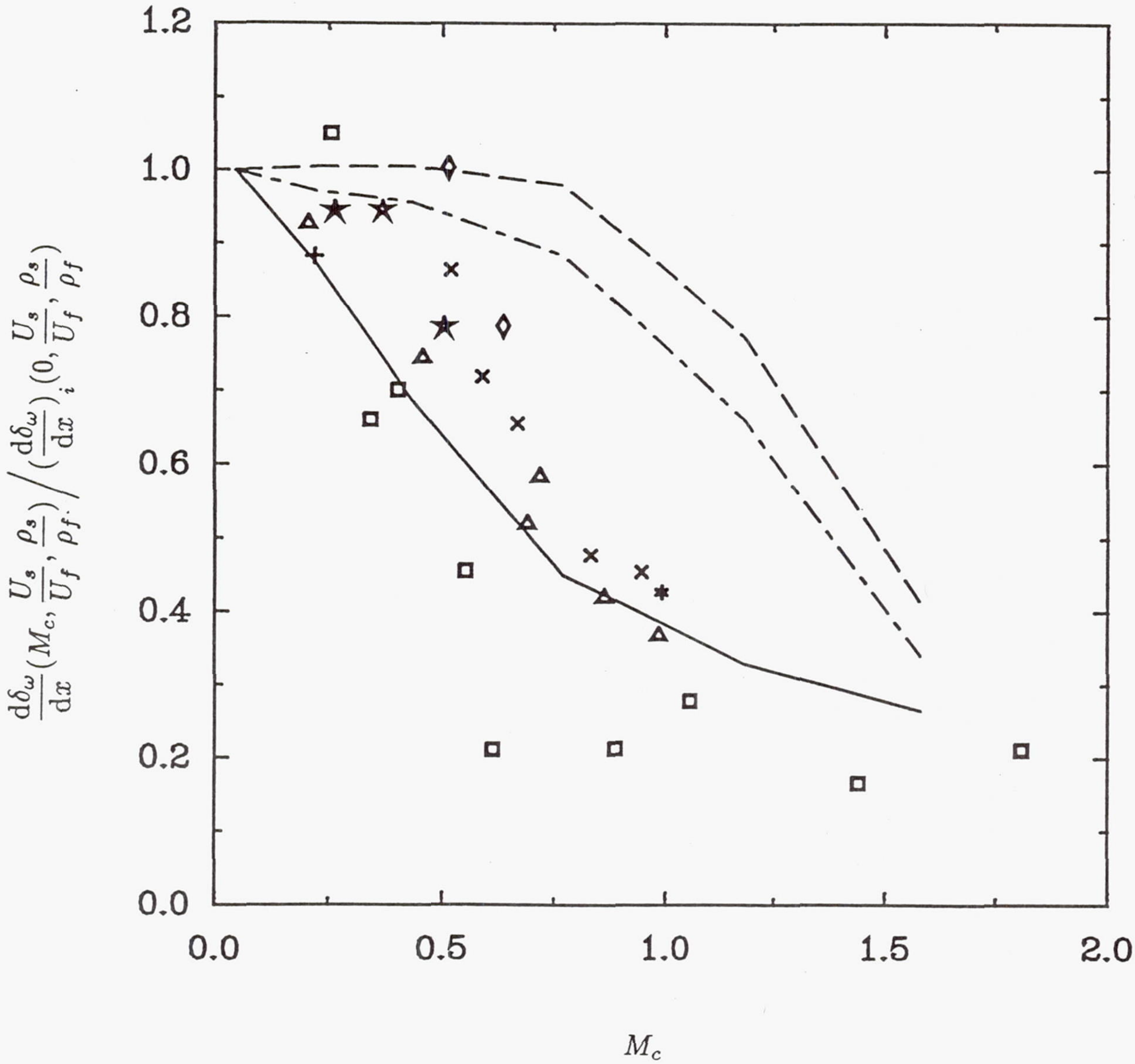

Figure 1. Variation of relative growth rate with convective Mach number, $r = 0.1$. — —, Present: without compressibility corrections; ——— , Present: with compressibility corrections; – ——, KC; □ , Papamoschou and Roshko; △ , Goebel *et al* ; ◇ , Samimy and Elliott; ★ , Sullins *et al*; + , Messersmith *et al*; × , Chinzei *et al*; ✱ , Ikawa and Kubota *et al.*

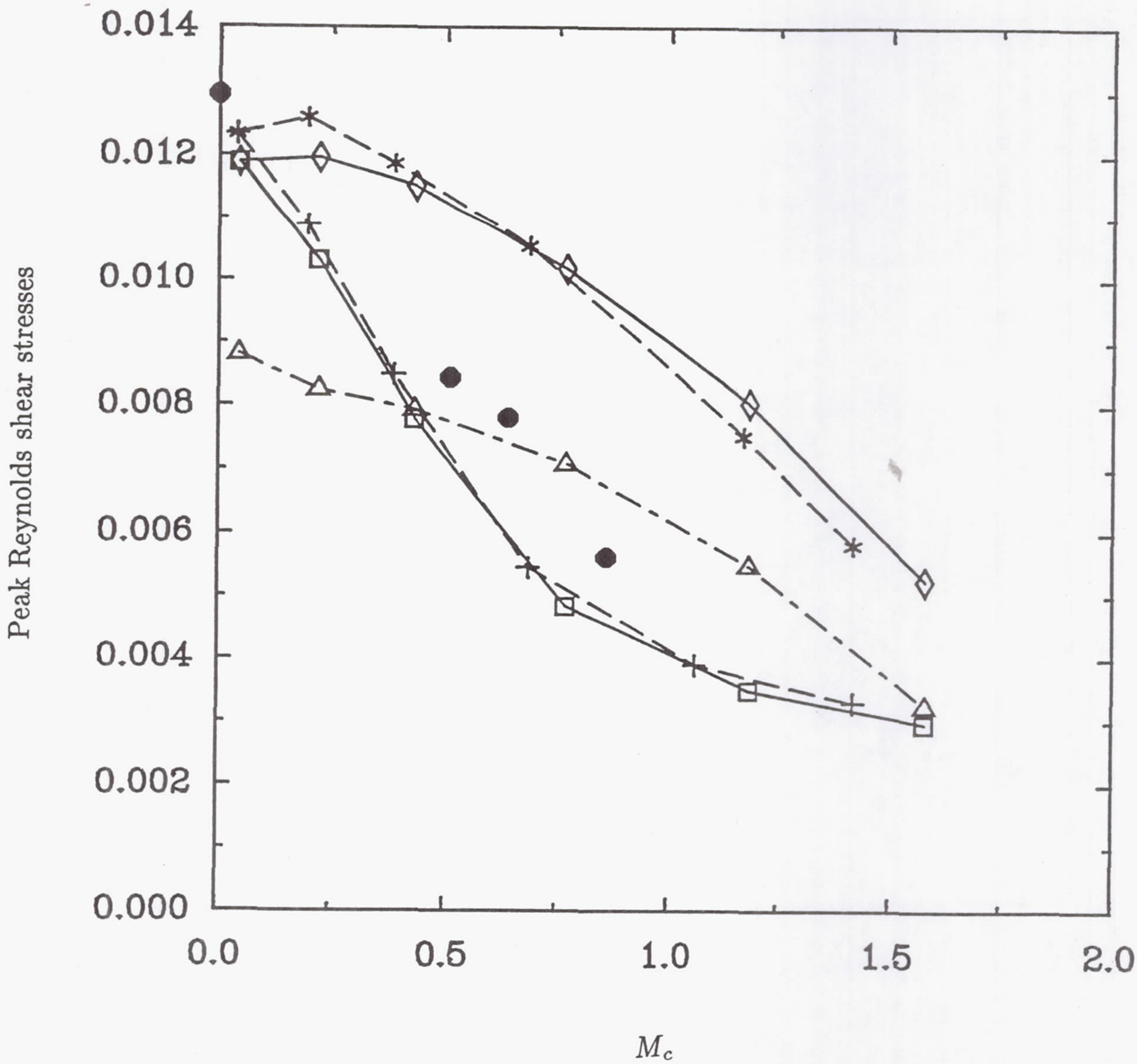

Figure 2. Variation of the peak Reynolds shear stress with convective Mach number. —◇— Present: $r = 0.1$, without compressibility corrections; —□— , Present: $r = 0.$ with compressibility corrections; — ✱ —, Present: $r = 0.2$, without compressibilit corrections; — + —, Present: $r = 0.2$, with compressibility corrections; - ——, K($r = 0.1$; ● , Elliott and Samimy.

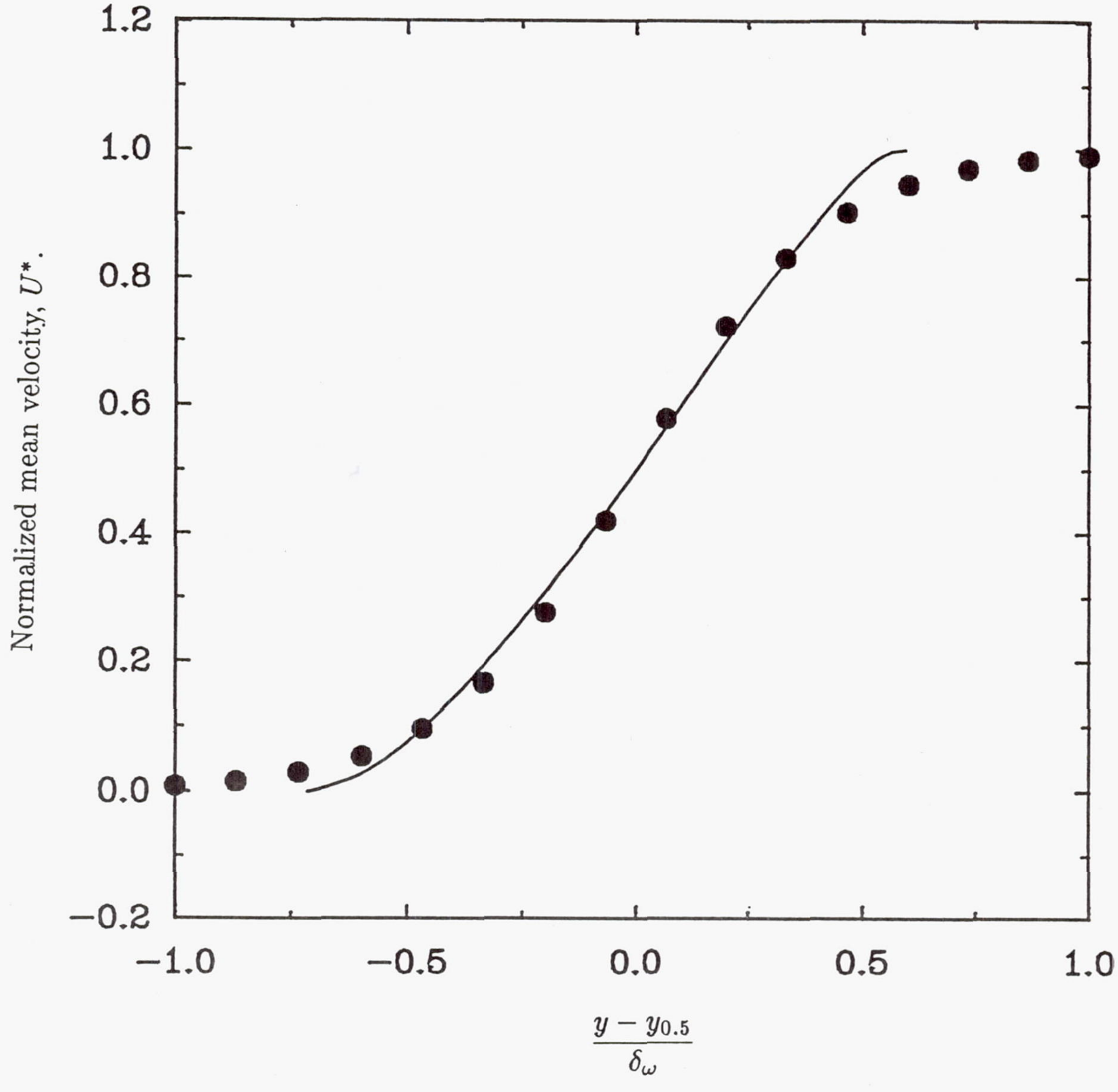

Figure 3. Comparison of mean velocity profiles for the shear layer in Case 1 of Elliott and Samimy (1991). ——, Present; ●, experiment.

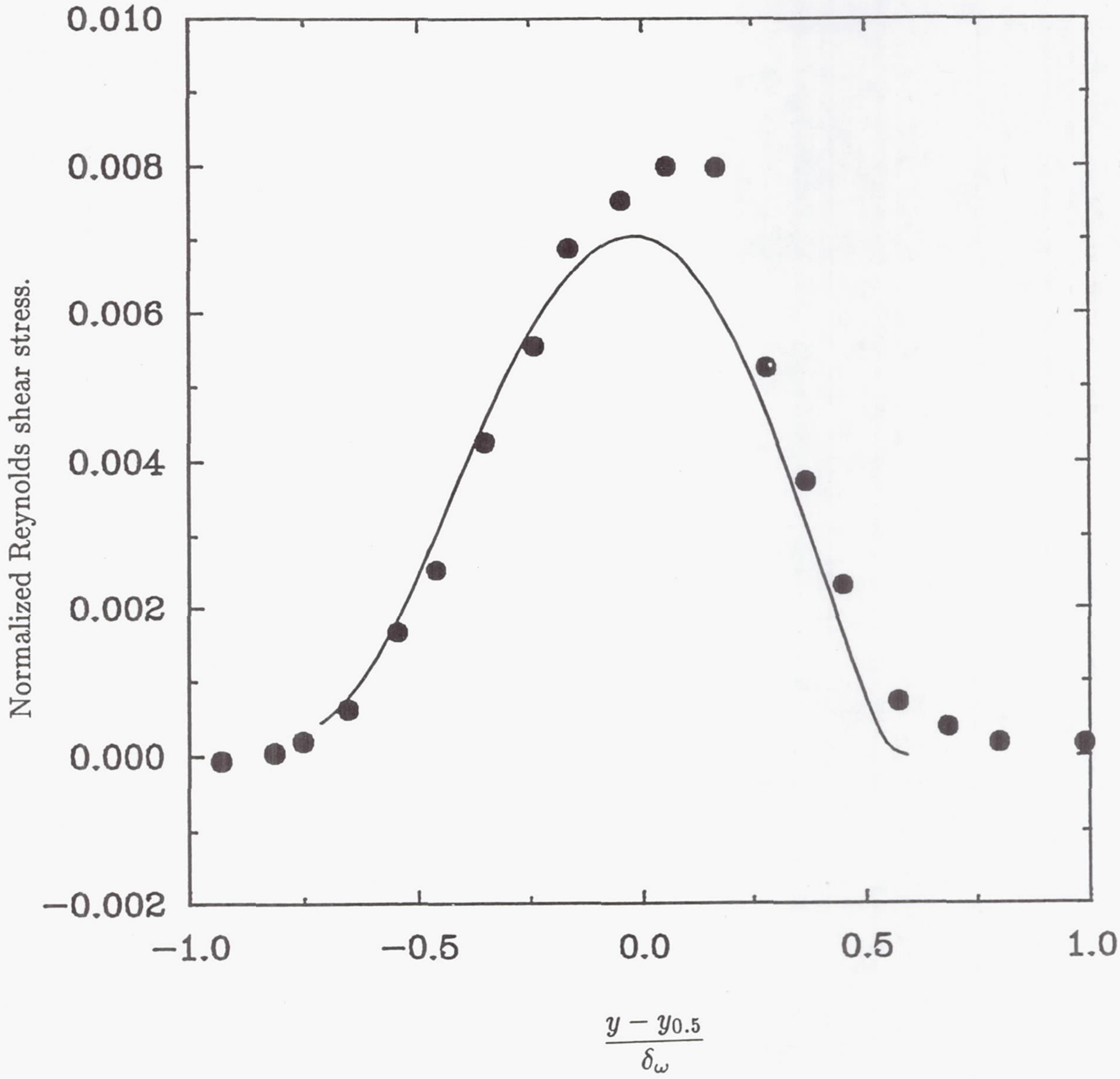

Figure 4. Comparison of Reynolds shear stress for the shear layer in Case 1 of Elliott and Samimy (1991). ——, Present; ●, experiment.

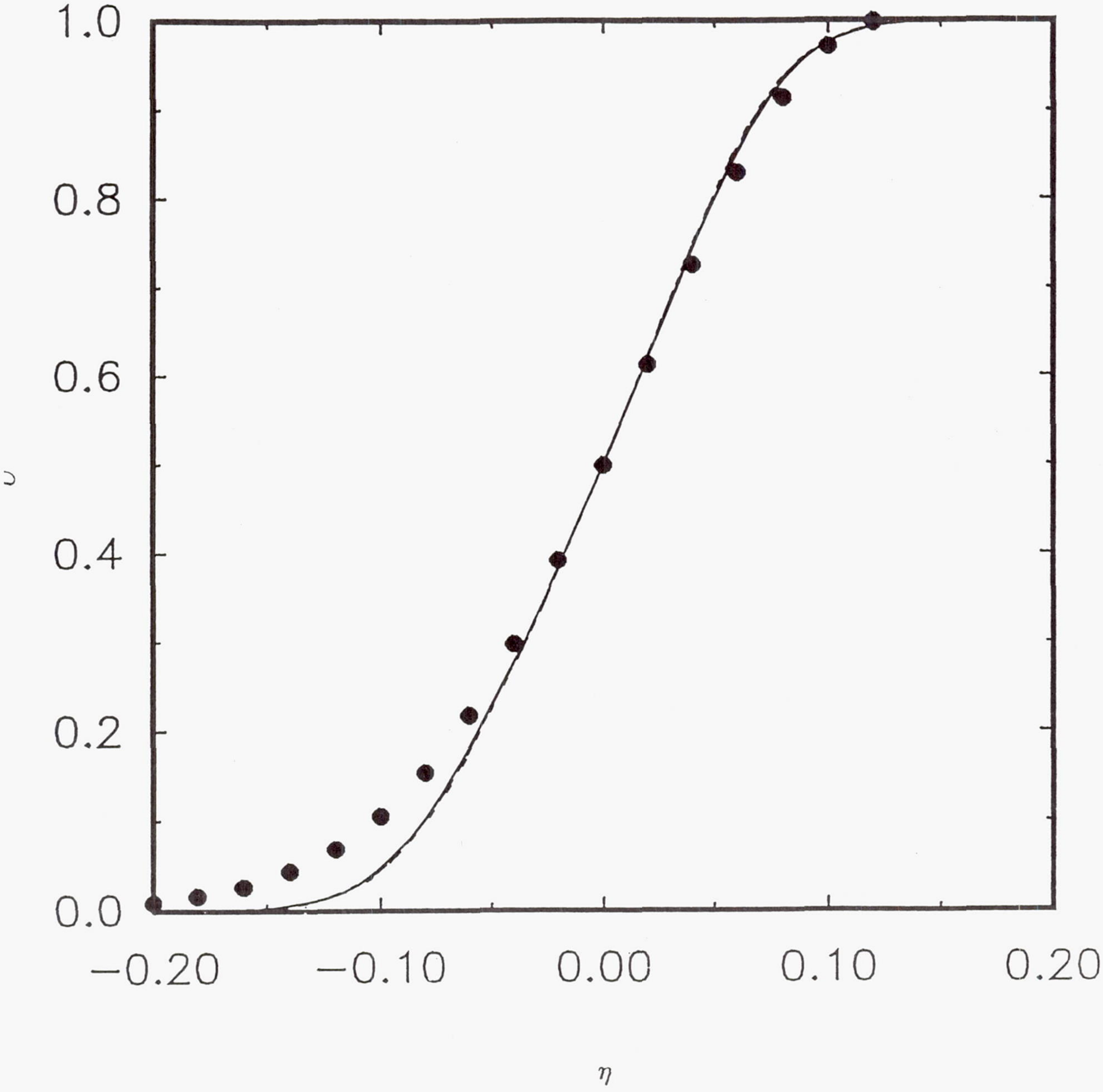

Figure 5. Mean velocity profiles. - - -, $x = 3.82$; - —, 4.43; ——, 5.99; ●, Patel[9].

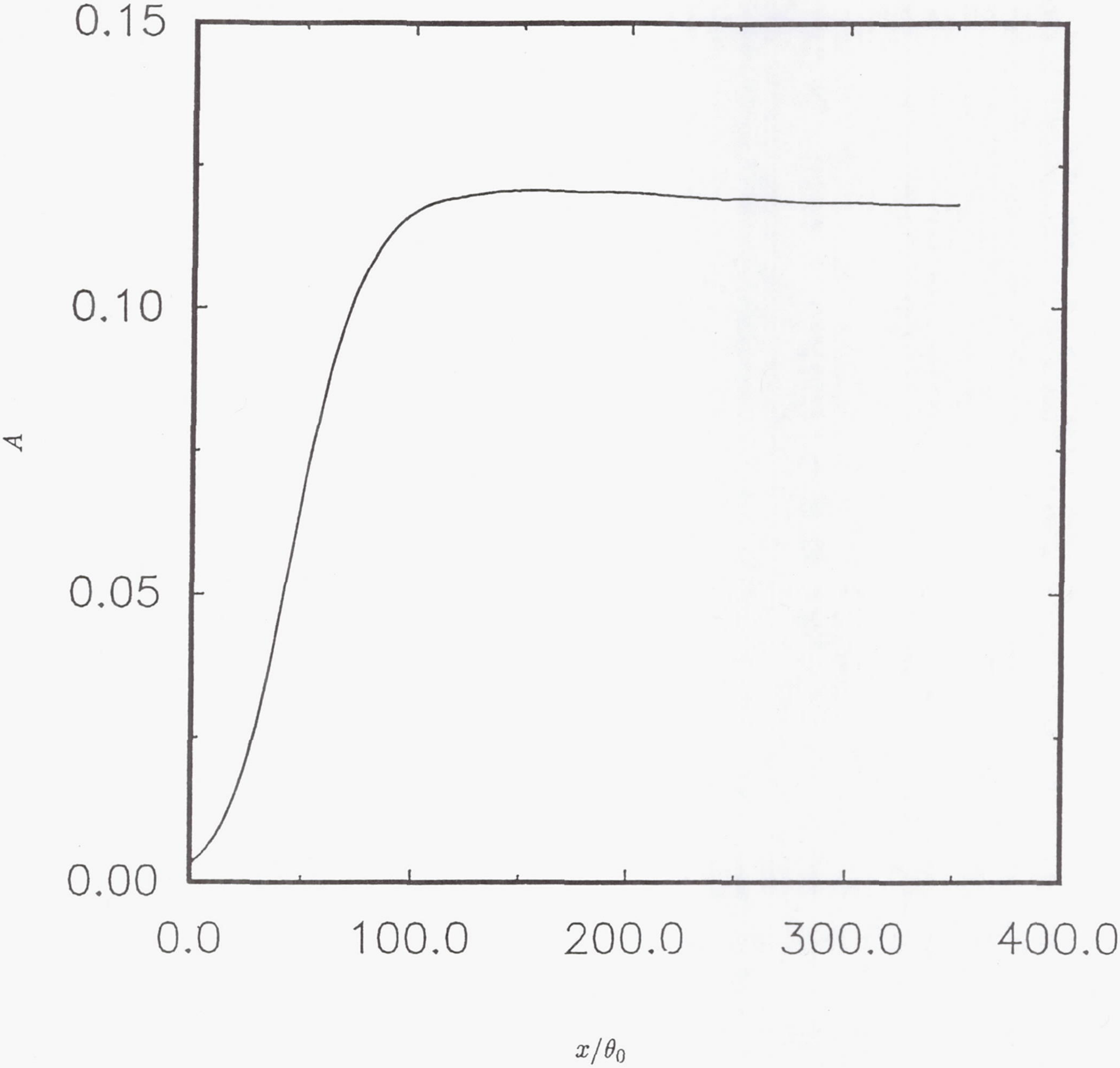

Figure 6. Variation of the wave amplitude with streamwise distance.

Center for Modeling of Turbulence and Transition
Research Briefs - 1991

Modeling of Near Wall Turbulence and Modeling of Bypass Transition

Z. Yang

1. Motivation and Objective

1) Modeling of the near wall turbulence. We aim to develop a second order closure for near wall turbulence. As a first step of this project, we try to develop a $k-\epsilon$ model for near wall turbulence. We require the resulting model to be able to handle both near wall turbulence and turbulent flows away from the wall, computationally robust, and applicable for complex flow situations, flow with separation, for example.

2) Modeling of the bypass transition. We aim to develop a bypass transition model which contains the effect of intermittency. Thus, the model can be used for both the transitional boundary layers and the turbulent boundary layers. We require the resulting model to give a good prediction of momentum and heat transfer within the transitional boundary and a good prediction of the effect of freestream turbulence on transitional boundary layers.

2. Work Accomplished

In the past year, progress has been made in both topics mentioned above (i.e., modeling of the near wall turbulence and modeling of the bypass transition). In the paragraphs below, these two topics will be reported separately.

2.1 Modeling of Near Wall Turbulence

Because of the wide range of scales involved in a turbulent flow, DNS (direct numerical simulation) is limited to flows of moderate Reynolds number and simple geometry. Turbulence modeling is the only viable approach for the calculation of turbulent flows of engineering interest. In turbulence modeling, the k-ϵ model is the most widely used model in engineering calculations. The Standard $k-\epsilon$ Model[1,2] was devised for high Reynolds number turbulent flows and is traditionally used in conjunction with a wall function when it is applied to wall bounded turbulent flows. However universal wall functions do not exist in complex flows and it is thus necessary to develop a form of $k-\epsilon$ model equations which can be integrated down to the wall.

Jones and Launder[3] were the first to propose a low Reynolds number $k-\epsilon$ model for near wall turbulence, which was then followed by a number of similar $k-\epsilon$ models. A critical evaluation of the pre-1985 models was made by Patel et al.[4]. More recently proposed models can be found in Shih[5] and Lang and Shih[6]. Three major deficiencies can be pointed out about existing $k-\epsilon$ models. (Some of the models may have only one or two of the three deficiencies.) First, a near wall pseudo-dissipation rate was introduced to remove the singularity in the dissipation equation at the

 Preceding Page Blank

wall. The definition of the near wall pseudo-dissipation rate was quite arbitrary. Second, the model constants were different from those of the Standard $k-\epsilon$ Model, making the near wall models less capable of handling flows containing both high Reynolds number turbulence and near wall turbulence, which often occurs for real flow situations. Patel et al.[4] put as the first criterion the ability of the near wall models to predict turbulent free shear flows. Third, the variable y^+ is used in the damping function f_μ of the eddy viscosity formulae. Since the definition of y^+ involves u_τ, the friction velocity, any model containing y^+ cannot be used in flows with separation.

Effort is made to propose a new $k-\epsilon$ model for near turbulence which is free of the three deficiencies mentioned above. In this model, $k^{1/2}$ is chosen as the turbulent velocity scale. The time scale is bounded from below by the Kolmogorov time scale. The dissipation equation is reformulated using this time scale and no singularity exists at the wall. Thus, it is no longer necessary to introduce the near wall pseudo-dissipation rate. The model constants used are the same as in the Standard k-ϵ Model. Thus, the proposed model will be also suitable for flows away from the wall. An earlier version of the model, which contains y^+ in the damping function, was proposed and reported in Yang and Shih[7]. The model is now improved by using $R_y = k^{1/2}y/\nu$ instead of y^+ in the damping function. Hence, the present model can be used for flows with separation.

In the present model, the eddy viscosity is given by

$$\nu_T = c_\mu f_\mu k T \tag{1}$$

where the time scale T is written as

$$T = \frac{k}{\epsilon} + (\frac{\nu}{\epsilon})^{1/2}. \tag{2}$$

The first part is the time scale conventionally used for high Reynolds number turbulent flows and the second part is the Kolmogorov time scale. Away from the wall, the first part is much large than the second part while near the wall the second part dominates, giving the Kolmogorov time scale as the turbulent time scale at the wall. The time scale given is bounded from below by the Kolmogorov time scale and is always positive.

The damping function f_μ is given by

$$f_\mu = [1 - exp(-a_1 R_y - a_3 R_y^3 - a_5 R_y^5)]^{1/2} \tag{3}$$

where $a_1 = 1.5 \times 10^{-4}$, $a_3 = 5.0 \times 10^{-7}$, $a_5 = 1.0 \times 10^{-10}$. The damping function is chosen such that the shear stress has the correct near wall asymptotic behavior. Away from the wall, f_μ approaches one as required.

The modeled transport equations for k and ϵ are

$$\dot{k} + U_j k_{,j} = [(\nu + \frac{\nu_T}{\sigma_k})k_{,j}]_{,j} - < u_i u_j > U_{i,j} - \epsilon, \tag{4}$$

$$\dot{\epsilon} + U_j\epsilon_{,j} = [(\nu + \frac{\nu_T}{\sigma_\epsilon})\epsilon_{,j}]_{,j} + (-C_{1\epsilon} < u_i u_j > U_{i,j} - C_{2\epsilon}\epsilon)/T + \nu\nu_T U_{i,jk}U_{i,jk}. \quad (5)$$

Because T is always positive, the dissipation rate equation does not have a singularity at the wall.

Turbulent channel flows and flat plate boundary layer flows at different Reynolds numbers were calculated using the proposed model. The mean velocity, turbulent kinetic energy, turbulent shear stress and turbulent dissipation rate for turbulent channel flow at $Re_\tau = 395$ and turbulent flat plate boundary layer flow at $Re_\theta = 1410$ are shown in Fig 1 and Fig 2, respectively. DNS data for these cases are shown for comparison. Also shown are the predictions using the Jones-Launder model and the $k - \epsilon$ model proposed by Chien[8]. These two models are chosen because the Jones-Launder model is the first $k - \epsilon$ model for near wall turbulence while Chien's model is known to perform quite well for turbulent boundary layer flows. Overall, the proposed model is found to give a better prediction. Calculations were also made for turbulent flat plate boundary layers at larger Reynolds numbers, turbulent boundary layers with pressure gradient (favorable pressure gradient, adverse pressure gradient, and increasingly adverse pressure.) The results of these computation and the comparisons with the available experimental data can be found in Yang and Shih[9].

2.2 Modeling of Bypass Transition

In a quiescent environment, transition is preceeded by the amplification of Tollmien-Schlichting waves. These waves eventually break down, giving rise to turbulent spots, which can be viewed as the onset of transition. In an environment with high freestream turbulence, say the flow passing over a turbine blade, turbulent spots are formed due to the transport of turbulence from the freestream to the boundary layer rather than the T-S wave amplification. This type of transition is called bypass transition. Accurate prediction of bypass transitional boundary layers is very important for internal fluid mechanics because a significant proportion of the turbine blade is in the a transitional boundary layer region. Furthermore, the performance and the life of a turbine are directly related to the peak vales of the momentum and heat transfer both of which occur in the transitional boundary layer.

Priddin[10] was the first to notice that the low Reynolds number two equation models have the potential to predict transitional flows under the influence of the freestream turbulence. This is probably due to the fact that the generation of turbulent spots in a boundary layer is a random process and the flow is almost fully developed turbulent within a turbulent spot. A detailed calculation procedure was given by Rodi and Scheuerer[11], in which the Lam & Bremhorst low Reynolds number $k - \epsilon$ model was used. More recently, a comparative study of the performance of existing low Reynolds number $k - \epsilon$ models in predicting laminar-turbulent transition was made by Fujisawa[12].

While the low Reynolds number $k - \epsilon$ models could mimic transition, the quantitative predictions do not compare very well with the experimental data. This is due to the fact that all these low Reynolds number $k - \epsilon$ models were originally proposed for fully developed turbulent flows and did not take into consideration the distinct feature of a transitional boundary layer – intermittency. The intermittency of a transitional boundary layer is measured by the intermittency factor which can be viewed as the percentage time a transitional boundary layer is in the turbulent state due to the passing of a turbulent spot.

We propose a model for the calculation of transitional boundary layers, which takes the effect of intermittency into consideration. The model is based on the $k-\epsilon$ model for near wall turbulence we have stated above. The effect of intermittency is introduced through the following argument: since the percentage of time that a transitional boundary layer is turbulent is measured by the intermittency factor, a model for transitional boundary layers could be constructed from a model for turbulent boundary layers by multiplying all the terms due to turbulence mechanism by a weighting factor γ, which is linearly related to the intermittency factor. Thus, the governing equations for the flat plate transitional boundary layers are, after using the boundary layer approximation and the eddy viscosity assumption,

$$\frac{\partial U}{\partial x}+\frac{\partial V}{\partial y}=0, \tag{6}$$

$$U\frac{\partial U}{\partial x}+V\frac{\partial U}{\partial y}=\frac{\partial}{\partial y}\left[(\nu+\gamma\nu_T)\frac{\partial U}{\partial y}\right], \tag{7}$$

$$U\frac{\partial k}{\partial x}+V\frac{\partial k}{\partial y}=\frac{\partial}{\partial y}\left[(\nu+\gamma\frac{\nu_T}{\sigma_k})\frac{\partial k}{\partial y}\right]+\gamma\nu_T(\frac{\partial U}{\partial y})^2-\gamma\epsilon, \tag{8}$$

$$U\frac{\partial \epsilon}{\partial x}+V\frac{\partial \epsilon}{\partial y}=\frac{\partial}{\partial y}\left[(\nu+\gamma\frac{\nu_T}{\sigma_\epsilon})\frac{\partial \epsilon}{\partial y}\right]+\gamma\left[C_{1\epsilon}\nu_T(\frac{\partial U}{\partial y})^2-C_{2\epsilon}\epsilon\right]\frac{1}{T}+\gamma\nu\nu_T(\frac{\partial U}{\partial y})^2, \tag{9}$$

where x, y are the coordinates along and normal to the plate and U, V are the mean velocities in the x, y directions, respectively.

In order to close the above equations, an expression for the weighting factor γ is needed. The weighting factor is assumed to be related to both the freestream turbulent level and the intermittency factor of the boundary layer. The intermittency factor is assumed to be determined by the local state of the boundary layer. We use H, the shape factor, to characterize the local state of the boundary layer since both the intermittency factor and the shape factor change monotonically from the laminar boundary layer to the turbulent boundary layer. Experimental results by Abu-Ghannam and Shaw[13] are used as a guide to construct this function. The weighting factor is also assumed to change in the y direction in such a way that outside the boundary layer, the weighting factor is one since the freestream is governed by decaying turbulence. The final expression for the weighting factor is given in Yang and Shih[14].

The above system of parabolic equations need to be supplymented by boundary conditions at the wall and at the freestream and by initial conditions at the starting point of the calculation. At the wall

$$U=V=k=0,$$

$$\epsilon_w = \frac{2}{\gamma}\nu(\frac{\partial k^{1/2}}{\partial y})^2. \quad (10)$$

The boundary condition for ϵ was obtained by applying the equation for turbulent kinetic energy down to the wall.

At the edge of the boundary layer, the flow variables are given by the freestream values, i.e.

$$U = U_e, k = k_e, \epsilon = \epsilon_e. \quad (11)$$

The k_e, ϵ_e in the above are found from the transport equations for k and ϵ, with the condition that the gradient of the flow variables in the y direction vanishes as the free stream is approached. Thus,

$$U_e \frac{dk_e}{dx} = -\epsilon_e, \quad (12)$$

$$U_e \frac{d\epsilon_e}{dx} = -\frac{C_{2\epsilon}\epsilon_e}{T}. \quad (13)$$

k_{e0} and ϵ_{e0} (the values of k_e and ϵ_e at the leading edge, for example) are needed. k_{e0} is obtained from the experiment, and ϵ_{e0} is determined in such a way that the resulting $k_e(x)$ profile agrees with the experiment.

One of the issues in the calculation of transitional boundary layers through the low Reynolds number $k - \epsilon$ models is the prescription of the initial profiles for the turbulence kinetic energy and its dissipation rate, the later of which could not be found from the experiment directly. An expression for the initial profiles were given in Rodi and Scheuerer[11]. However, computations by Yang and Shih[15] which tested the effect of the initial conditions on the transition prediction found, in agreement with the findings of Patankar and Schmit[16], that the predicted onset of the transition is sensitive to the initial profiles. This sensitivity of the results to the initial conditions suggests that the only place where the initial conditions could be specified unambiguously is at the leading edge. At the leading edge, the turbulent kinetic energy and its dissipation rate take constant profiles, the values of which are determined by the law for the decaying turbulence.

With the initial conditions given at the leading edge and the boundary conditions given above, the solutions are marched downstream. Flat plate boundary layers with free stream turbulence levels of 3% (Case T3A) and 6% (Case T3B) respectively were calculated using the present model. These are the benchmark cases in an ongoing project coordinated by Savill[17], testing the capability of turbulence models in predicting transitional flows. Fig. 3 shows the variation of skin friction coefficient c_f against Re_x. Results from the experiment is shown for comparison. In addition, the prediction of the Launder-Sharma model is also shown in the figure because it was reported that among the lower Reynolds number $k - \epsilon$ models, the Launder-Sharma model performs best for transitional boundary layers. It is clear that the present model gives a better prediction. Other features in the transitional boundary layers and the calculations of the transitional boundary layers with other levels of freestream turbulence can be found in Ref. 14.

3. Future Plans

1) Modeling of the near wall turbulence.

The proposed $k-\epsilon$ model is only tested for simple parabolic flows so far. Because of the form of the model equations, the proposed model can be used in complex flow situations, flow with separation for example. The performance of the proposed model in those situations will be tested.

We will work on the second order closure for near wall turbulence. In particular, we will be looking at the effect of the mean flow inhomogeneity on the pressure strain correlation. We are hoping to represent this effect rationally, so that the ad hoc damping functions currently being used in all the near wall second order closures can be avoided.

2) Modeling of bypass transition.

We will apply the proposed model to transitional boundary layers with pressure gradient and curvature. We will also extend the model to thermal boundary layers.

4. References

[1] Launder, B.E. & Spalding, D.B., "The Numerical Computation of Turbulent Flow," Computer Methods in Applied Mechanics and Engineering **3**, 269-289 (1974).

[2] Rodi, W., *Turbulence Models and Their Application in Hydraulics*, Book Pub. of International Association for Hydraulic Research, Delft, the Netherlands, 1980.

[3] Jones, W.P., and Launder, B.E., "The Calculation of Low-Reynolds Number Phenomena with a Two-Equation Model of Turbulence," International Journal of Heat and Mass Transfer **16**, 1119-1130 (1973).

[4] Patel, V.C., Rodi, W., and Scheuerer, G., "Turbulence Models for Near-Wall and Low-Reynolds Number Flows: a Review," AIAA Journal **23**, 1308-1319 (1985).

[5] Shih, T.H., "An Improved $k-\epsilon$ Model for Near-Wall Turbulence and Comparison with Direct Numerical Simulation," NASA TM 103211 (1990).

[6] Lang, N.J. and Shih, T.H., "A Critical Comparison of Two Equation Turbulence Models," NASA TM 105237 (1991).

[7] Yang, Z. and Shih, T.H., "A $k-\epsilon$ modeling of near wall turbulence," Proc. 4th International Symposium on CFD, 1305-1310 (1991).

[8] Chien, K.Y., "Predictions of Channel and Boundary Layer Flow with a Low-Reynolds-Number Turbulence Model," AIAA Journal **20**, 33-38 (1982).

[9] Yang, Z. & Shih, T.H., "A new time scale based $k-\epsilon$ model for near wall turbulence," submitted for publication (1992).

[10] Priddin, C.H., *The behaviour of the turbulent boundary layer on a curved porous wall*, PhD Thesis, Imperial College, London, 1975.

[11] Rodi, W. and Scheuerer, S., "Calculation of laminar-turbulence boundary layer transition on turbine blades," Proc. 65th AGARD-REP Symposium on Heat Transfer and Cooling in Gas Turbine, Bergen, Norway, 18-1 to 18-12 (1985).

12 Fujisawa, N., "Calculation of transitional boundary layers with a refined low Reynolds number version of a $k - \epsilon$ model of turbulence," Proc. Engineering Turbulence Modeling and Experiment, 23-32 (1990).

13 Abu-Ghannam, B.J. & Shaw, R., "Natural transition of boundary layers – the effects of turbulence, pressure gradient, and flow history," Journal of Mechanical Engineering Science **22**, 213-228 (1980).

14 Yang, Z. & Shih, T.H., "A modeling of transitional boundary layers," In preparation (1992).

15 Yang, Z. and Shih, T.H., "A $k - \epsilon$ calculation of transitional boundary layers," *Transition and Turbulence*, Springer-Verlag, 1992.

16 Schmidt, R.C. and Patankar, S.V., "Two-equation low-Reynolds number turbulence modeling of transitional boundary layer flows characteristic of gas turbine blades," NASA CR-4145 (1988).

17 Savill, A.M., "Turbulence model predictions for transition under free-stream turbulence," RAeS Transition and Boundary Layer Conference, Cambridge, England (1991).

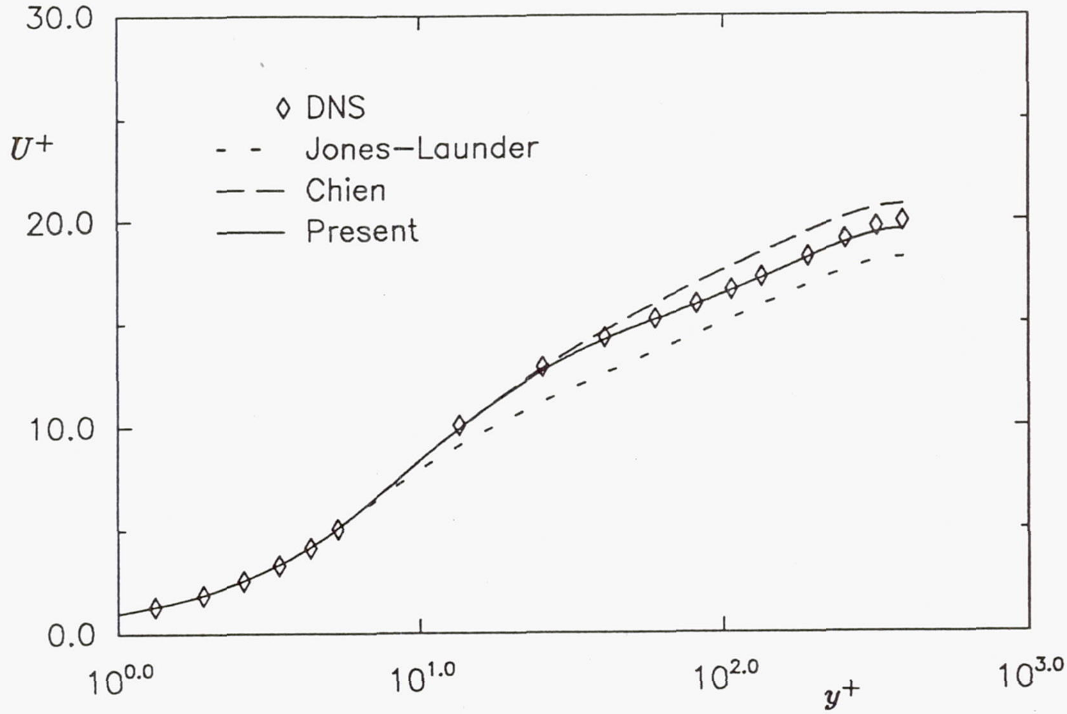

Fig 1a: Mean velocity profile for channel flow at $Re_\tau = 395$.

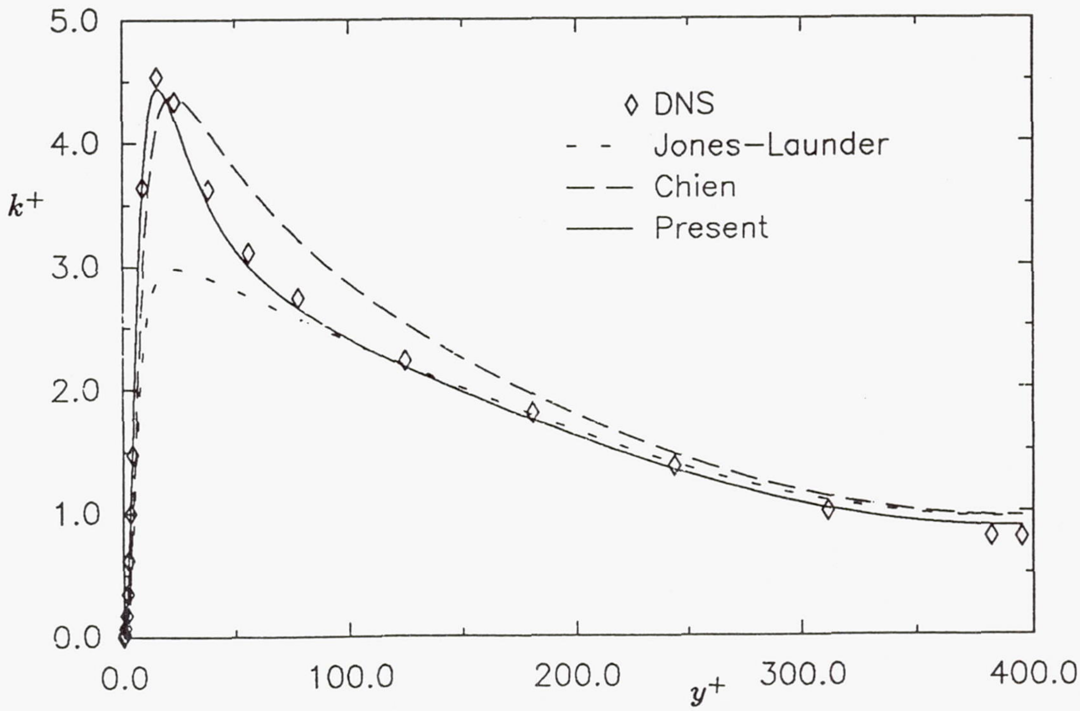

Fig 1b: Turbulent energy profile for channel flow at $Re_\tau = 395$.

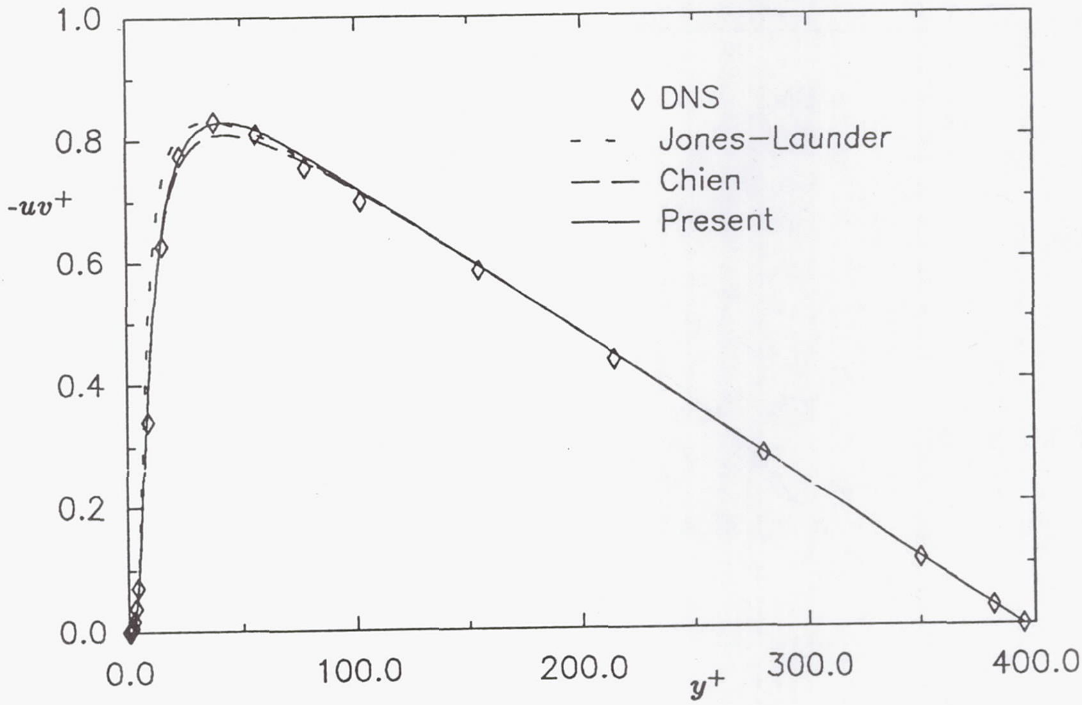

Fig 1c: Shear stress profile for channel flow at $Re_\tau = 395$.

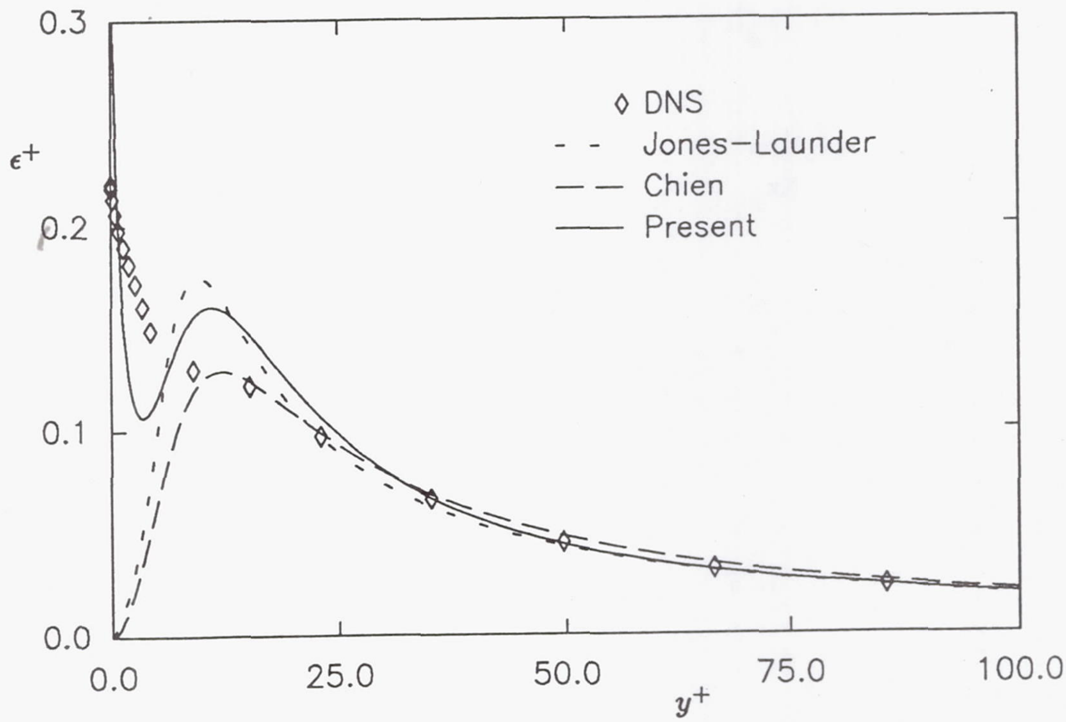

Fig 1d: Dissipation rate profile for channel flow at $Re_\tau = 395$.

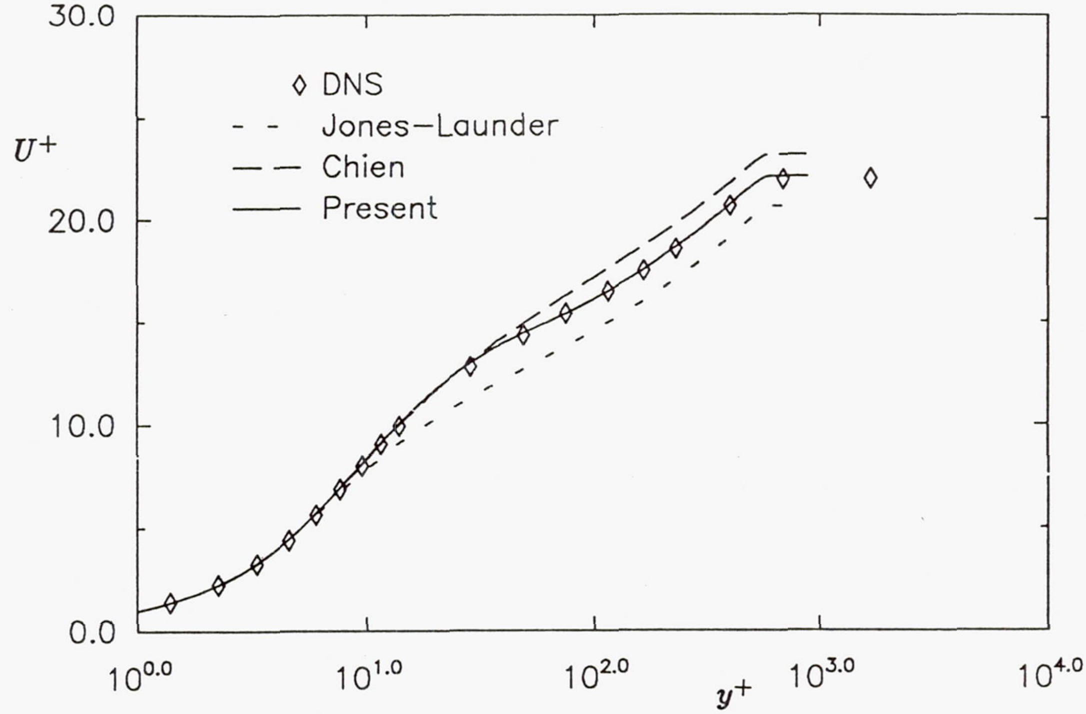

Fig 2a: Mean velocity profile for channel flow at $Re_\theta = 1410$.

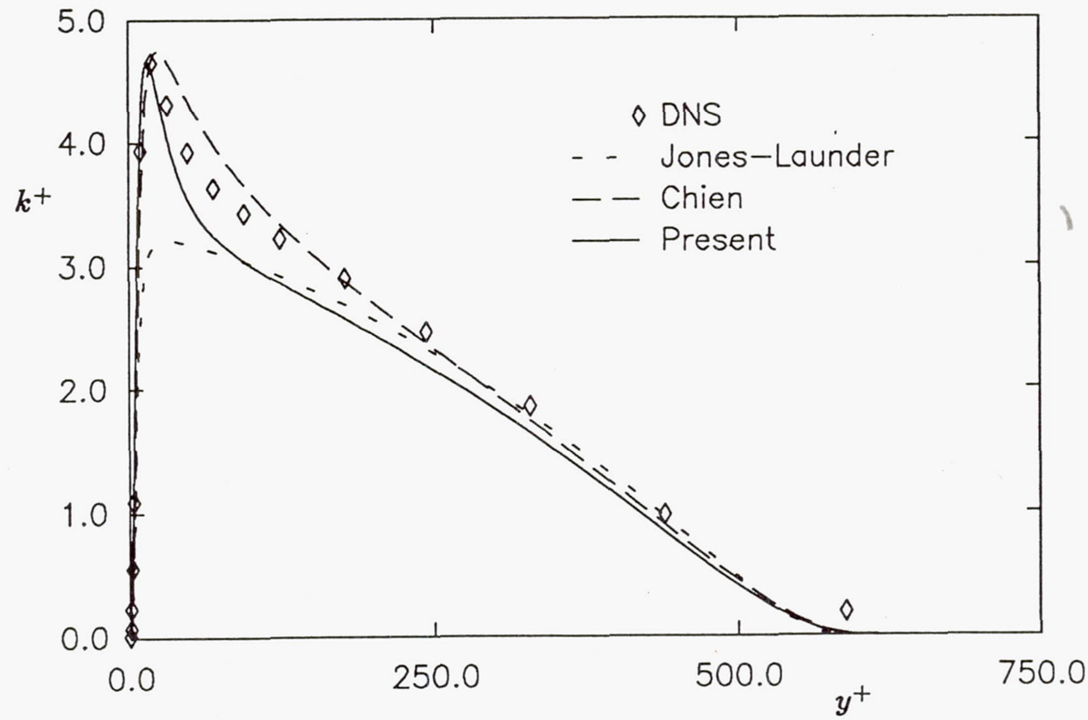

Fig 2b: Turbulent energy profile for channel flow at $Re_\theta = 1410$.

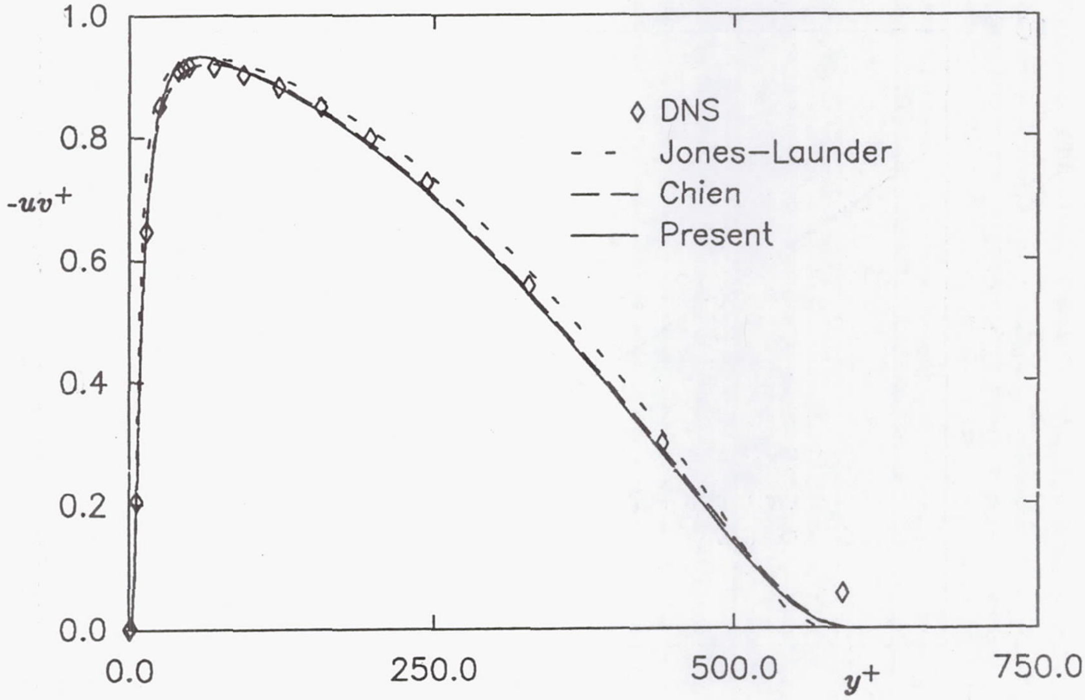

Fig 2c: Shear stress profile for channel flow at $Re_\theta = 1410$.

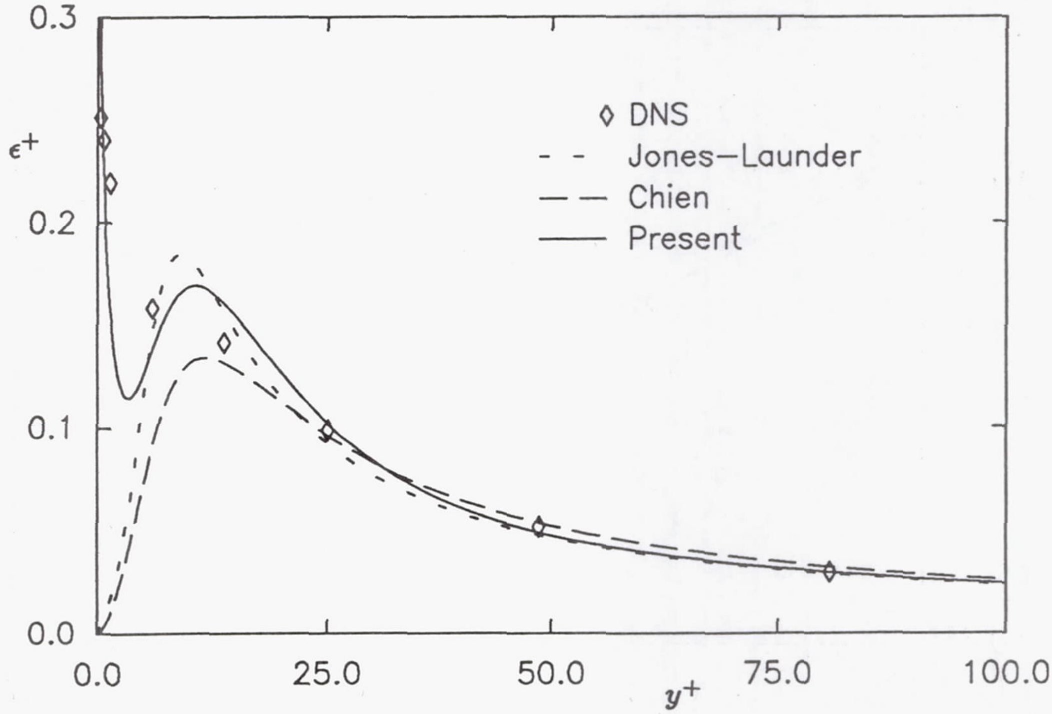

Fig 2d: Dissipation rate profile for channel flow at $Re_\theta = 1410$.

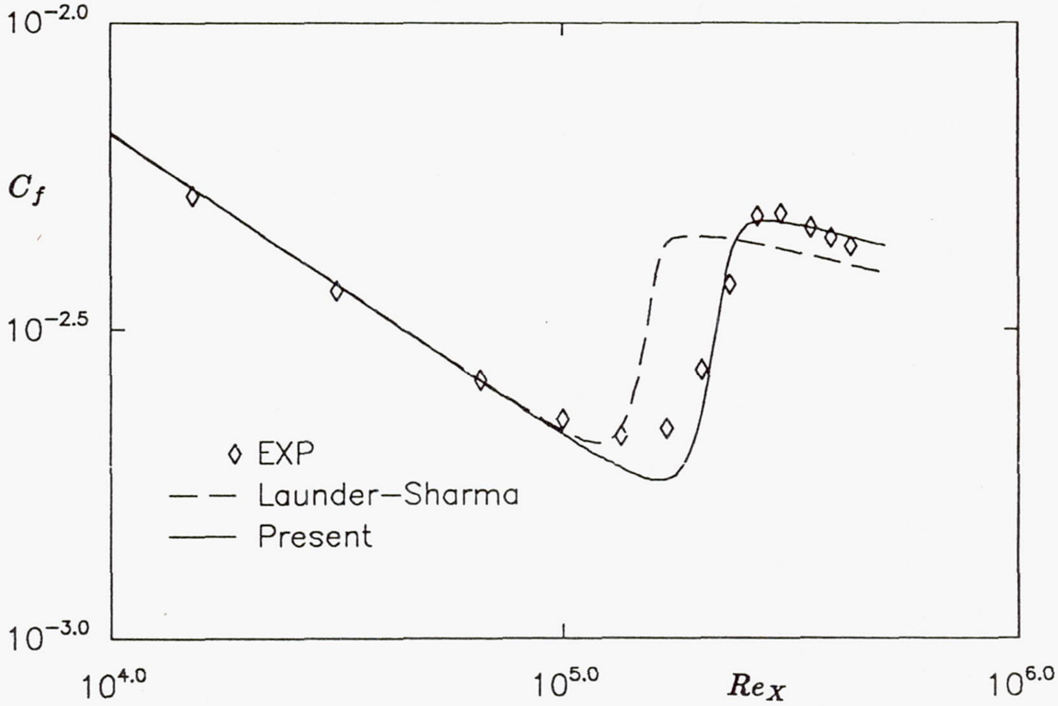

Fig 3a: Skin friction variation for T3A.

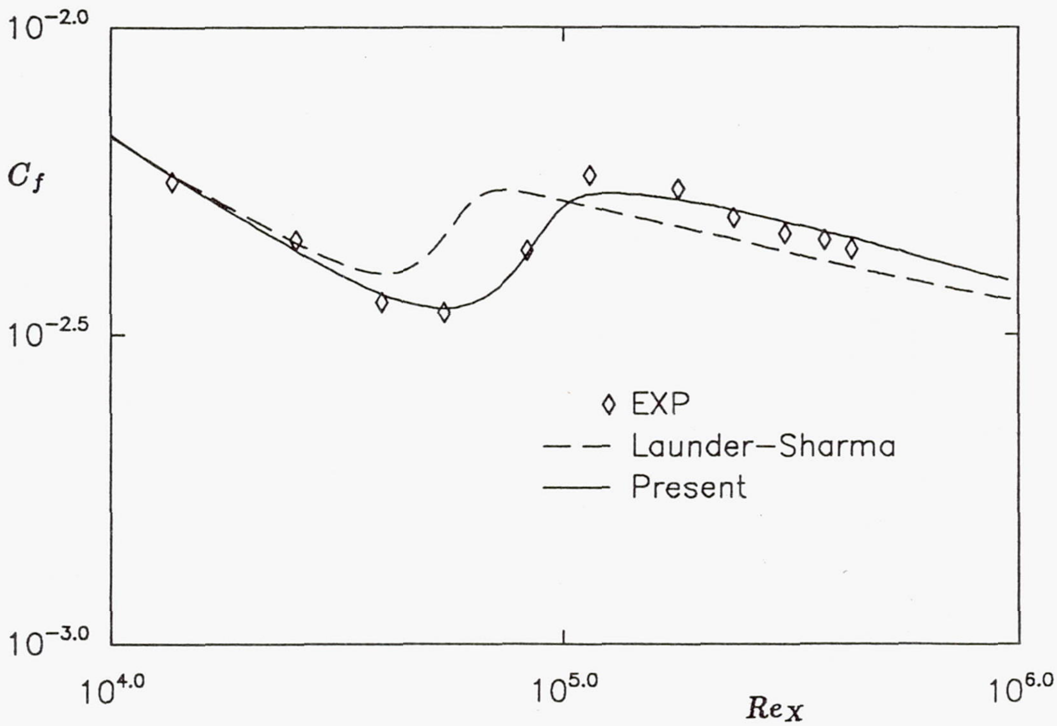

Fig 3b: Skin friction variation for T3B.

Two Equation Modelling and the Pseudo Compressibility Technique

C. J. Steffen, Jr.

1. Motivation and Objective

The primary objective of the Center for Modelling of Turbulence and Transition (CMOTT) is to further the understanding of turbulence theory for engineering applications. One important foundation for this research is the establishment of a data base encompassing the multitude of existing models as well as newly proposed ideas. The research effort described in the next few pages is a precursor to an extended survey of two equation turbulence models in the presence of a separated shear layer.

Recently, several authors have examined the performance of two equation models in the context of the backward facing step flow. Conflicting results, however, demand that further attention is necessary to properly understand the behavior and limitations of this popular technique, especially the low Reynolds number formulations. The objective of this research is to validate an incompressible Navier Stokes code for use as a numerical test-bed. In turn, this code will be used for analyzing the performance of several two equation models.

2. Work Accomplished

To date, the validation of the incompressible code DTNS is complete. The details of this validation study are documented in reference[1]. The code is based upon the pseudo-compressibility technique and incorporates the approximate factorization scheme for time integration. Two laminar benchmark flows are used to measure the performance and implementation of the numerical methods. The classic solution of the Blasius boundary layer is used for validating the flat plate flow, while experimental data is incorporated in the validation of backward facing step flow.

An initial result for the standard high Reynolds number k-ϵ equations has also been calculated to demonstrate an initial performance level of the solution technique for the turbulence equations.

2.1 Numerical Method

The absence of a variable density in the continuity equation governing incompressible flow complicates the numerical integration procedure. One solution technique that has been well received is that of pseudo-compressibility. This idea was first put forward by Chorin[2] and enables the equations to be solved using the primitive variables. Recently, Chang and Kwak[3], Rizzi and Eriksson[4], Kwak and Chakravarthy[5], Michelassi and Shih[6], and Turkel[7] have found this method suitable for resolving incompressible flow. This particular implementation has been validated by Gorski[8–10] for several different benchmark flows.

Examine the system of equations involved in the pseudo compressibility method and notice that they differ from the incompressible Navier Stokes equations by the addition of a time dependant pressure term in the continuity equation.

$$
\begin{aligned}
\frac{1}{\beta}\frac{\partial \mathrm{p}}{\partial t} + \frac{\partial \mathrm{u}}{\partial x} + \frac{\partial \mathrm{v}}{\partial y} &= 0 \\
\frac{\partial \mathrm{u}}{\partial t} + \frac{\partial}{\partial x}\left(\mathrm{u}^2 + \mathrm{p} - \frac{1}{\mathrm{Re}}\frac{\partial \mathrm{u}}{\partial x}\right) + \frac{\partial}{\partial y}\left(\mathrm{uv} - \frac{1}{\mathrm{Re}}\frac{\partial \mathrm{u}}{\partial y}\right) &= 0 \\
\frac{\partial \mathrm{v}}{\partial t} + \frac{\partial}{\partial x}\left(\mathrm{uv} - \frac{1}{\mathrm{Re}}\frac{\partial \mathrm{v}}{\partial x}\right) + \frac{\partial}{\partial y}\left(\mathrm{v}^2 + \mathrm{p} - \frac{1}{\mathrm{Re}}\frac{\partial \mathrm{v}}{\partial y}\right) &= 0
\end{aligned}
\tag{1}
$$

Here, x and y are the independent variables and Re refers to the Reynolds number. The constant β is known as the pseudo compressibility parameter. This system is hyperbolic in nature while the incompressible flow equations are elliptic. The pseudo sound speed, $\mathrm{c} = \sqrt{\mathrm{u}^2 + \beta}$, is governed by the value of the parameter β, whereas the physical sound speed is infinite. Chang and Kwak [3] have shown that for $\beta > 0$ the finite speed pseudo waves vanish as time progresses and yield the proper incompressible solution at the steady state limit. It is through this parameter β that the convective and acoustic waves are decoupled, and thus convergence is governed. In choosing an optimum value for this parameter, the goal is to avoid giving the viscous effects time to react to the passing of the nonphysical transient pressure waves. Thus a lower bound on the acoustic speeds translates into a lower bound on β. However, an upper bound on β is strictly scheme dependent.

The approximate factorization is rather straight forward. Equations (2) can be rewritten as

$$
\begin{gathered}
\frac{\partial}{\partial t}(\mathbf{q}) + \frac{\partial}{\partial x}(\mathrm{f}_1+\mathrm{g}_1) + \frac{\partial}{\partial y}(\mathrm{f}_2+\mathrm{g}_2) = 0 \\
\mathbf{q} = \begin{bmatrix} \frac{\mathrm{p}}{\beta} \\ \mathrm{u} \\ \mathrm{v} \end{bmatrix}, \quad \mathrm{f}_1 = \begin{bmatrix} \mathrm{u} \\ \mathrm{u}^2 + \mathrm{p} \\ \mathrm{uv} \end{bmatrix}, \quad \mathrm{f}_2 = \begin{bmatrix} \mathrm{v} \\ \mathrm{uv} \\ \mathrm{v}^2 + \mathrm{p} \end{bmatrix} \\
\mathrm{g}_1 = \frac{-1}{Re}\begin{bmatrix} 0 \\ \frac{\partial \mathrm{u}}{\partial x} \\ \frac{\partial \mathrm{v}}{\partial x} \end{bmatrix}, \quad \mathrm{g}_2 = \frac{-1}{Re}\begin{bmatrix} 0 \\ \frac{\partial \mathrm{u}}{\partial x} \\ \frac{\partial \mathrm{v}}{\partial y} \end{bmatrix}
\end{gathered}
\tag{2}
$$

or in generalized coordinates $(\xi(x,y), \eta(x,y))$ as seen here in equation (3).

$$
\begin{gathered}
\frac{\partial}{\partial t}(\overline{\mathrm{q}}) + \frac{\partial}{\partial \xi}(\overline{\mathrm{f}_1}+\overline{\mathrm{g}_1}) + \frac{\partial}{\partial \eta}(\overline{\mathrm{f}_2}+\overline{\mathrm{g}_2}) = 0 \\
\overline{q} = \frac{\mathrm{q}}{\mathrm{J}} \\
\overline{\mathrm{f}_1} = \frac{\xi_x \mathrm{f}_1 + \xi_y \mathrm{f}_2}{\mathrm{J}}, \quad \overline{\mathrm{f}_2} = \frac{\eta_x \mathrm{f}_1 + \eta_y \mathrm{f}_2}{\mathrm{J}} \\
\overline{\mathrm{g}_1} = \frac{\xi_x \mathrm{g}_1 + \xi_y \mathrm{g}_2}{\mathrm{J}}, \quad \overline{\mathrm{g}_2} = \frac{\eta_x \mathrm{g}_1 + \eta_y \mathrm{g}_2}{\mathrm{J}} \\
\mathrm{J} = \frac{\partial(\xi,\eta)}{\partial(x,y)}
\end{gathered}
\tag{3}
$$

The third order accurate Chakravarthy and Osher TVD scheme is used to discretize the convective terms while central differencing is used for the viscous fluxes. Thus the approximate factorization of this method is expressed in terms of flux Jacobians A and B as

$$\begin{aligned}
&\left\{\frac{\mathbf{V}}{\boldsymbol{\Delta} t}+\frac{\partial^-}{\partial\xi}\mathbf{A}^+ +\frac{\partial^+}{\partial\xi}\mathbf{A}^- +\frac{\partial^-}{\partial\xi}\mathbf{A}_v\right\}\Delta\overline{\mathbf{q}}^* = \frac{\partial\left(\overline{\mathbf{f}_1}+\overline{\mathbf{g}_1}\right)}{\partial\xi}+\frac{\partial\left(\overline{\mathbf{f}_2}+\overline{\mathbf{g}_2}\right)}{\partial\eta}\\
&\left\{\frac{\mathbf{V}}{\boldsymbol{\Delta} t}+\frac{\partial^-}{\partial\eta}\mathbf{B}^+ +\frac{\partial^+}{\partial\eta}\mathbf{B}^- +\frac{\partial^-}{\partial\eta}\mathbf{B}_v\right\}\Delta\overline{\mathbf{q}} = \frac{\mathbf{V}}{\Delta t}\Delta\overline{\mathbf{q}}^*
\end{aligned} \tag{4}$$

where $\mathbf{V}$ is the cell volume, and $\Delta t = \frac{CFL}{1+\sqrt{\mathrm{J}}}$ is the timestep. The matrices $\mathbf{A}_v$ and $\mathbf{B}_v$ are the viscous flux Jacobians. The interested reader is encouraged to see reference[9] for more details.

The k-ϵ equations are solved in a similar manner as that seen in equation 2. Consider the standard high Reynolds number form of the transport equations of the turbulent kinetic energy and dissipation of turbulent genetic energy as in equation (5):

$$\begin{aligned}
&\frac{\partial}{\partial t}(\mathbf{q}^{\mathrm{t}})+\frac{\partial}{\partial x}(\mathbf{f}_1^{\mathrm{t}}+\mathbf{g}_1^{\mathrm{t}})+\frac{\partial}{\partial y}(\mathbf{f}_2^{\mathrm{t}}+\mathbf{g}_2^{\mathrm{t}}) = \mathbf{S}^{\mathrm{t}}\\
&\mathbf{q}^{\mathrm{t}} = \begin{bmatrix}\mathrm{k}\\ \epsilon\end{bmatrix},\ \mathbf{f}_1^{\mathrm{t}} = \begin{bmatrix}\mathrm{uk}\\ \mathrm{u}\epsilon\end{bmatrix},\ \mathbf{f}_2^{\mathrm{t}} = \begin{bmatrix}\mathrm{vk}\\ \mathrm{v}\epsilon\end{bmatrix}\\
&\mathbf{g}_1^{\mathrm{t}} = -\frac{1}{Re}\begin{bmatrix}\nu_k\frac{\partial \mathrm{k}}{\partial x}\\ \nu_\epsilon\frac{\partial\epsilon}{\partial x}\end{bmatrix},\ \mathbf{g}_2^{\mathrm{t}} = -\frac{1}{Re}\begin{bmatrix}\nu_k\frac{\partial \mathrm{k}}{\partial y}\\ \nu_\epsilon\frac{\partial\epsilon}{\partial y}\end{bmatrix},\ \mathbf{S}^{\mathrm{t}} = \frac{\mathbf{1}}{Re}\begin{bmatrix}\mathrm{P}-\epsilon Re\\ \mathrm{C}_1\frac{\epsilon}{\mathrm{k}}\mathrm{P}-\mathrm{C}_2\frac{\epsilon^2}{\mathrm{k}}Re\end{bmatrix}
\end{aligned} \tag{5}$$

with

$$\begin{aligned}
\nu_k &= \nu+\frac{\nu_t}{\sigma_k}\\
\nu_\epsilon &= \nu+\frac{\nu_t}{\sigma_\epsilon}
\end{aligned} \tag{6}$$

and the production of turbulent genetic energy defined as shown below.

$$P = \nu_t\left[2\left(\mathrm{u_x^2}+\mathrm{v_y^2}\right)+\left(\mathrm{u_y}+\mathrm{v_x}\right)^2\right] \tag{7}$$

Again, we can translate these equations in a manner similar to that of equation (3) and create the following system for generalized coordinates:

$$\frac{\partial}{\partial t}\left(\overline{\mathbf{q}^{\mathrm{t}}}\right)+\frac{\partial}{\partial\xi}\left(\overline{\mathbf{f}_1^{\mathrm{t}}}+\overline{\mathbf{g}_1^{\mathrm{t}}}\right)+\frac{\partial}{\partial\eta}\left(\overline{\mathbf{f}_2^{\mathrm{t}}}+\overline{\mathbf{g}_2^{\mathrm{t}}}\right) = \overline{\mathbf{S}^{\mathrm{t}}} \tag{8}$$

This can be solved via approximate factorization as shown here in equation 9.

$$\begin{aligned}
&\left\{\frac{\mathbf{V}}{\boldsymbol{\Delta} t}+\frac{\partial^-}{\partial\xi}\mathbf{A}^{\mathrm{t}+}+\frac{\partial^+}{\partial\xi}\mathbf{A}^{\mathrm{t}-}+\frac{\partial^-}{\partial\xi}\mathbf{A}_v^{\mathrm{t}}-\alpha_\xi\mathbf{H}^{\mathrm{t}}\right\}\Delta\overline{\mathbf{q}^{\mathrm{t}}}^* = \frac{\partial\left(\overline{\mathbf{f}_1^{\mathrm{t}}}+\overline{\mathbf{g}_1^{\mathrm{t}}}\right)}{\partial\xi}+\frac{\partial\left(\overline{\mathbf{f}_2^{\mathrm{t}}}+\overline{\mathbf{g}_2^{\mathrm{t}}}\right)}{\partial\eta}+\overline{\mathbf{S}^{\mathrm{t}}}\\
&\left\{\frac{\mathbf{V}}{\boldsymbol{\Delta} t}+\frac{\partial^-}{\partial\eta}\mathbf{B}^+ +\frac{\partial^+}{\partial\eta}\mathbf{B}^- +\frac{\partial^-}{\partial\eta}\mathbf{B}_v-\alpha_\eta\mathbf{H}^{\mathrm{t}}\right\}\Delta\overline{\mathbf{q}^{\mathrm{t}}} = \frac{\mathbf{V}}{\Delta t}\Delta\overline{\mathbf{q}^{\mathrm{t}}}^*
\end{aligned} \tag{9}$$

Again, the scheme is written in terms of the turbulence flux Jacobians and the approximate source Jacobian, $\mathbf{H^t}$. The coefficients α_ξ and α_η are provided to enhance the diagonal dominance of the implicit method. While the convective flux terms are linear, the linearization of the source terms is not straight forward. Furthermore, the low Reynolds number formulation of equation 5 includes other nonlinear correction terms in the source vector $\mathbf{S^t}$. The interested reader is encouraged to see the recent paper by Michelassi and Shih[6].

2.2 Discussion

Overall the performance for laminar flow documented in reference[1] is very encouraging. The flat plate results shown agree with the theoretical Blasius solution for several different grid configurations. The laminar back facing step flow was also well resolved both in terms of the primary recirculation zone reattachment length, and corresponding velocity profiles as seen in figures 1 and 2. However, performance of the two dimensional flow code drops off dramatically when the Reynolds number corresponding to the onset of 3D flow is exceeded. Armaly et al [11] observed this phenomenon occur at a Reynolds number of 400, based upon the hydraulic diameter of the inlet channel. Again, the numerical results bear this finding out.

Figure 1 Reattachment length predictions—comparison with experiment [11]. x_1, x_2, and x_3 are the primary reattachment, secondary detachment, and secondary reattachment lengths, respectively.

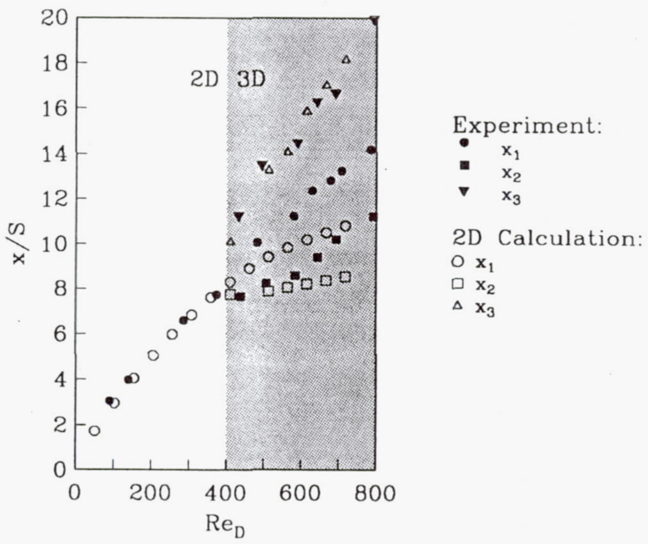

Figure 2 Re_D=389 velocity profiles—comparison with experiment [11].

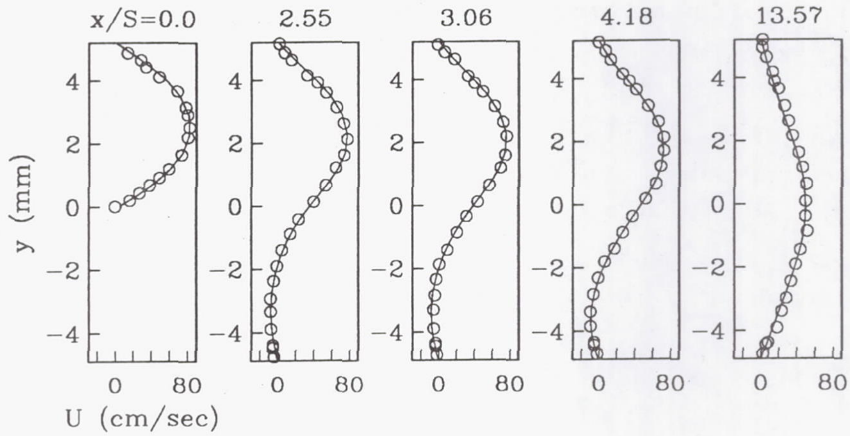

The current thrust of effort is in establishing a comparison between the standard high Reynolds number form k-ϵ model and a version which incorporates the low Reynolds number corrections, such as that of Jones and Launder[12]. This model is particularly convenient in that the damping functions are independent of the parameter, y^+. Thus, multiple walls bounding the computational domain do not need special attention. An initial calculation using the high Reynolds number approach agrees with the published results of Speziale and Thangam[13]. However, the Jones and Launder model is proving to be quite challenging.

3. Future Plans

Eventually, several two equation models will be examined for their behavior in the back facing step flow. The following is a partial list of the two equation models of primary interest:

1. Jones and Launder
2. Chien
3. Yang and Shih
4. Shih and Lumley

The current research effort will result in an increased understanding of the need for proper modelling of the near wall region. However, the increase in accuracy maybe offset by an unwarranted increase in effort. Further numerical experiments are necessary before any conclusions can be drawn.

4. References

1 Steffen, Jr., C. J., "An Investigation of DTNS2D for Use as an Incompressible Turbulence Modelling Test-bed," NASA Technical Memorandum 105593 (1992).

[2] Chorin, A. J., "A Numerical Method for Solving Incompressible Viscous Flow Problems," J. Comput. Phys., **2**, 12–26 (1967).

[3] Chang, J. L. C. and Kwak, D., "On the Method of Pseudo Compressibility for Numerically Solving Incompressible Flows," AIAA paper 84–0252 (1984).

[4] Rizzi, A. and Eriksson, L. E., "Computation of Inviscid Incompressible Flow with Rotation," J. Fluid Mech., **153**, 275–312 (1985).

[5] Kwak, D., Chang, J. L. C., Shanks, S. P., and Chakravarthy, S. R., "A Three Dimensional Incompressible Navier-Stokes Flow Solver Using Primitive Variables," AIAA J., **24**, 390–396 (1986).

[6] Michelassi, V. and T.-H. Shih, , "Elliptic Flow Computation by Low Reynolds Number Two Equation Turbulence Models," NASA Technical Memorandum 105376 (1991).

[7] Turkel, E., "Preconditioned Methods for Solving the Incompressible and Low Speed Compressible Equations," J. Comput. Phys., **72**, 277–298 (1987).

[8] Gorski, J. J., "Incompressible Cascade Calculations Using an Upwind Differenced TVD Scheme," *Advances and Applications in Computational Fluid Dynamics*, **66** of ASME-FED, edited by O. Baysal, 61–69 (1988).

[9] Gorski, J. J., "TVD Solutions of the Incompressible Navier-Stokes Equations With an Implicit Multigrid Scheme," *Proceedings of the AIAA/ASME/SIAM/APS 1st National Fluid Dynamics Congress*, **1**, 394–401 (1988).

[10] Gorski, J. J., "Solutions of the Incompressible Navier-Stokes Equations Using an Upwind Differenced TVD Scheme," *Proceedings of the 11th International Conference on Numerical Methods in Fluid Dynamics*, 278–282 (1988).

[11] Armaly, B. F., Durst, F., Pereira, J. C. F., and Schönung, B., "Experimental and Theoretical Investigation of Backward-Facing Step Flow," J. Fluid Mech., **127**, 473–496 (1983).

[12] Jones, W. P. and Launder, B. E., "The Prediction of Laminarization with a Two-Equation Model of Turbulence," Int. J. Heat Mass Transf., **15**, 301–314 (1972).

[13] Thangam, S. and Speziale, C. G., "Turbulent Separated Flow Past a Backward Facing Step: a Critical Evaluation of Two-Equation Turbulence Models," NASA Contractor Report 187532 ICASE Report No. 91–23 (1991).

Renormalization Group Methods for the Reynolds Stress Transport Equations

R. Rubinstein

1. Motivation and Objective

The Yakhot-Orszag renormalization group is used to analyze the pressure gradient-velocity correlation and return to isotropy terms in the Reynolds stress transport equations. The perturbation series for the relevant correlations, evaluated to lowest order in the ϵ-expansion of the Yakhot-Orszag theory, are infinite series in tensor product powers of the mean velocity gradient and its transpose. Formal lowest order Padé approximations to the sums of these series produce a rapid pressure strain model of the form proposed by Launder, Reece, and Rodi, and a return to isotropy model of the form proposed by Rotta. In both cases, the model constants are computed theoretically. The predicted Reynolds stress ratios in simple shear flows are evaluated and compared with experimental data. The possibility is discussed of deriving higher order nonlinear models by approximating the sums more accurately.

The Yakhot-Orszag renormalization group provides a systematic procedure for deriving turbulence models. Typical applications have included theoretical derivation of the universal constants of isotropic turbulence theory, such as the Kolmogorov constant, and derivation of two equation models, again with theoretically computed constants and low Reynolds number forms of the equations. Recent work has applied this formalism to Reynolds stress modeling, previously in the form of a nonlinear eddy viscosity representation of the Reynolds stresses, which can be used to model the simplest normal stress effects. The present work attempts to apply the Yakhot-Orszag formalism to Reynolds stress transport modeling.

2. Work Accomplished

The modelling of the pressure gradient-velocity correlation and return to isotropy term in the Reynolds stress transport equation remains an area of active research.[1,2,3] Models will be derived here using the Yakhot-Orszag renormalization group[4] partially along the lines of our previous work[5]. The result is a model for the rapid pressure-strain term of the form proposed by Launder, Reece and Rodi[6] (LRR) and a model for return to isotropy of the form proposed by Rotta[7] with theoretically computed constants in good agreement with accepted values. As is usual in investigations of this sort, the priority of Yoshizawa in deriving a pressure strain model analytically[8] must be noted.

The analysis requires some new ideas in renormalization group theory recently introduced by Yakhot et al[9]. As Yakhot et al[9] emphasize, the application of the renormalization group mode elimination formalism to shear flow creates a double perturbation series in powers of ϵ, the parameter of the isotropic theory, and in powers of a dimensionless strain rate, $\eta = SK/\varepsilon$, where K denotes the turbulence kinetic energy, ε denotes the dissipation rate, and S is a measure of the mean strain: in Ref. 9, $S^2 = \left(\frac{\partial U_m}{\partial x_n} + \frac{\partial U_n}{\partial x_m}\right)\frac{\partial U_m}{\partial x_n}$. The present analysis also leads to double expansions of this type, with the powers S^n replaced by tensors $\mathbf{S}^{(n)}$ homogeneous of degree n in the mean velocity gradient ∇U and its transpose. It will be convenient to retain the terminology of Ref. 9 and call this expansion the η-expansion; when the distinction is pertinent, the expansion of Ref. 9 will be called a scalar η-expansion.

The heuristic program of evaluating all scalar amplitudes to lowest order in ϵ has proven successful in the past: apparently, the ϵ-expansion is an asymptotic series with a sum given very nearly by its first term[10]. Unfortunately, there is no analogous basis for truncating the η-expansion. There are fundamental reasons for this distinction between these expansions. The present η-expansion is tensorial: successively higher order terms do not introduce merely numerical corrections, but increasingly complex asymmetries into the theory. Truncation therefore imposes a possibly inappropriate symmetry or other constraint on the model. Thus, in Ref. 5 the η-expansion for the Reynolds stress τ was truncated at second order as suggested by previous work of Yoshizawa[11] and Speziale[12]. Although this type of modelling permits unequal normal stresses in a simple shear flow, it is not maximally asymmetric: for example, in a flow with mean velocity components $U_i(x_1, x_2)$, a cubic model including a term $\tau \sim \nabla U^2 \nabla U^T + \nabla U \nabla U^{T2}$ would permit nonzero τ_{23} in the presence of vanishing $\partial U_2/\partial x_3$ and $\partial U_3/\partial x_2$, an effect which cannot be ruled out in advance.

Although generalizations[13] of the Cayley-Hamilton Theorem limit the number of independent tensors $\mathbf{S}^{(n)}$, anisotropy and asymmetry cannot exist at all without some terms of higher order in η; indeed, truncation at lowest order in η just produces a theory of isotropic turbulence. But the series truncated at any higher order can be unsatisfactory in flow regions in which some components $\left(\frac{\partial U_i}{\partial x_j}\right)K/\varepsilon$ are large. In such regions, the truncated series is dominated by its highest order terms. For the quadratic stress models of Refs. 5, 11, 12, this domination can produce negative normal stresses in the buffer layers of wall bounded flows. Increasing the order of truncation obviously exacerbates this problem.

It follows that finite truncation of the η-expansion is theoretically unsatisfactory. Yakhot et al[9] therefore propose that this expansion must be summed, even if only approximately, and have suggested a prototype summation in a different context. It should be noted that the same issues arise naturally in Yoshizawa's formalism, which also generates infinite series in the mean velocity gradients (and in other quantities as well) for correlations of interest in turbulence modeling. Yoshizawa has concluded independently that summation of this series is essential and has also derived a Reynolds stress transport model by introducing such summations[14].

In this paper, the perturbation series which the Yakhot-Orszag renormalization group generates for the correlation

$$\Pi_{ij} = -\left\langle u_i \frac{\partial p}{\partial x_j} + u_j \frac{\partial p}{\partial x_i} \right\rangle \tag{1}$$

where (0) denotes deviatoric part and (ij) denotes index interchange in the preceding term.

The next order will produce a term T_3 containing cubic products of velocities $u^<$. In view of the form of the LRR model, it is reasonable to ask whether a term with only one gradient, proportional in the high Reynolds number limit to $\tau\nabla U$ might occur at this order. Such terms do occur, but they cancel. Evaluation of T_3 proves to require expansions of the projection operators to second order, leading instead to terms $\mathbf{S}^{(3)}$ homogeneous of degree three in the mean velocity gradient and its transpose. In general, the term T_n of order n has the form $\mathbf{S}^{(n)}(K/\varepsilon)^n$. As noted in the Introduction, it will be imperative to include effects of all orders in $\mathbf{S}K/\varepsilon$ in the model, but because the terms T_n involve ever higher order derivatives of the transverse projection operators, they do not have an obvious law of formation. Therefore, an exact summation does not appear feasible.

A simple approximate summation is obtained by introducing the perturbation series[5] for $\overline{u_i u_j}^{(0)}$ in the form

$$\nu\left(\frac{\partial U_i}{\partial x_j}+\frac{\partial U_j}{\partial x_i}\right)=-\overline{u_i u_j}^{(0)}+\sum_{n\geq 2}\mathbf{S}^{(n)}(K/\varepsilon)^n$$

and dropping the quadratic terms. The resulting model,

$$\begin{aligned}\Pi_{ij}=\frac{2}{5}K\left(\frac{\partial U_i}{\partial x_j}+\frac{\partial U_j}{\partial x_i}\right)&+C_{\dot{\tau}1}\left[\overline{u_i u_p}^{(0)}\frac{\partial U_j}{\partial x_p}+\overline{u_j u_p}^{(0)}\frac{\partial U_i}{\partial x_p}\right]^{(0)}\\ &+C_{\dot{\tau}2}\left[\overline{u_i u_p}^{(0)}\frac{\partial U_p}{\partial x_j}+\overline{u_j u_p}^{(0)}\frac{\partial U_p}{\partial x_i}\right]^{(0)}\end{aligned}\tag{5}$$

with

$$C_{\dot{\tau}1}=\frac{16}{21}=.7619\qquad C_{\dot{\tau}2}=\frac{2}{21}=.0952\tag{6}$$

agrees with the perturbation series (3) and (4) to terms of order $\mathbf{S}^{(3)}$. However, unlike the explicit quadratic model which results from simply dropping the $O(\mathbf{S}^{(3)})$ terms, this model includes effects of all order in $\mathbf{S}K/\varepsilon$. The consequences of this fact will be discussed later. This type of summation has also been applied by Yoshizawa[14]. Eqs. (5) and (6) can be compared with Launder, Reece and Rodi's "model 1", Eq. (5) with the empirically adjusted constants

$$C_{\dot{\tau}1}=.7636\qquad C_{\dot{\tau}2}=.1091\tag{7}$$

In this model, the constants $C_{\dot{\tau}1}$ and $C_{\dot{\tau}2}$ were not chosen independently; instead, to insure some consistency conditions introduced by Rotta[7], Launder, Reece, and Rodi set[6]

$$C_{\dot{\tau}1}=\frac{C_2+8}{11}\quad C_{\dot{\tau}2}=\frac{8C_2-2}{11}$$

where only the constant C_2 is arbitrary. By eliminating C_2 between these equations, there results

$$8C_{\tau 1} - C_{\tau 2} = 6 \tag{8}$$

which is also satisfied by the choice of constants in Eq. (6). The LRR model corresponds to the choice $C_2 = .4$; Eqs. (5) and (6) correspond instead to the choice $C_2 = 8/21 \sim .36$.

The approximate summation used to derive Eq. (5) can be systematically generalized to generate an infinite number of models for Π_{ij}. For example, suppose that the perturbation series for τ is introduced into the cubic terms in the perturbation series instead of in the quadratic terms as above. This substitution will produce a model which can be written symbolically in the form

$$\Pi \sim \mathbf{S}^{(1)} + \mathbf{S}^{(2)} + \tau(\mathbf{S}^{(1)'} + \mathbf{S}^{(2)'})$$

where $\tau\mathbf{S}^{(i)'}$ denotes a sum of matrix products in all possible orders of τ and terms $\mathbf{S}^{(i)}$. The requirement that the original series agree to order $\mathbf{S}^{(4)}$ with the approximation when τ is replaced by its perturbation series determines this approximation uniquely.

2.2 The Return to Isotropy Model

The analytical description of return to isotropy is no less controversial than the modeling of the fast pressure strain term[3]. In the usual approach to turbulence modeling, in which correlations generated by Reynolds averaging are closed phenomenologically, this process is considered to result partly from the pressure correlation through a "slow" term independent of the mean flow, and partly from the deviatoric part of the dissipative correlation $\left\langle \nu_0 \frac{\partial u_i}{\partial x_p} \frac{\partial u_j}{\partial x_p} \right\rangle$. From this viewpoint, the analysis in Sect. I is incomplete because it discloses only a term proportional to the mean velocity gradient, but no slow term. The return to isotropy will be derived here by renormalization group methods following a suggestion of Yakhot[17].

From the renormalization group viewpoint, it is natural to investigate the return to isotropy, even independently of the stress transport equation, by writing the perturbation series for

$$u_i \frac{\partial u_j}{\partial t} + u_j \frac{\partial u_i}{\partial t} = \int u_i(\hat{k} - \hat{q})(-i\omega) u_j(\hat{q}) d\hat{q} + (ij) \tag{9}$$

This perturbation series differs from the perturbation series for the Reynolds stresses previously reported[5] only in the occurence of an additional factor $-i\omega$ in all frequency integrals.

The analysis is straightforward. Only the deviatoric terms require attention because the part of the correlation proporational to δ_{ij} contributes to the transport equation for K which has been analyzed by Yakhot and Smith[15]. The lowest order deviator appears at first order in η; to lowest order in ϵ

$$T_1 = \hat{T}_1\left(\frac{\partial U_i}{\partial x_j} + \frac{\partial U_j}{\partial x_i}\right) \tag{10}$$

where

$$\frac{d\hat{T}_1}{dr} = \frac{1}{15}\frac{\mathcal{D}}{\nu\Lambda^2} \tag{11}$$

In view of the form of the Rotta model, it is reasonable to seek terms at the next order proportional to $u_i u_j$. As in Sect. I, such terms do appear, but cancel exactly. This apparently ubiquitous cancellation was also obtained by Smith and Reynolds[18] in an analysis of the ε transport equation. Accordingly, the second order analysis in η produces quadratic terms in the velocity gradients. Finite truncation of this series violates the requirement that return to isotropy be independent of the mean flow. Therefore, we must seek a reasonable approximate summation. The form of the lowest order term given in Eqs. (10) and (11) suggests

$$\Pi'_{ij} = \frac{\hat{T}_1}{\nu}\nu\left(\frac{\partial U_i}{\partial x_j} + \frac{\partial U_j}{\partial x_i}\right) \sim -\frac{\hat{T}_1}{\nu}\overline{u_i u_j}^{(0)}$$

Despite its triviality, this replacement does produce an approximate sum which agrees exactly with perturbation theory to lowest order. It therefore can be considered a type of Padé approximation.

At the infinite Reynolds number asymptotic limit

$$\Pi'_{ij} = -C_R\frac{\varepsilon}{K}\overline{u_i u_j}^{(0)} \tag{12}$$

where, in the Yakhot-Orszag theory, $C_R = \mathcal{D}/\varepsilon \sim 1.6$. Equation (12) is therefore simply the standard Rotta model with Rotta constant ~ 1.6 in agreement with an earlier proposal of Yakhot[17].

A preliminary discussion of higher order summation may be appropriate. By analyzing the spectral dynamics of the return to isotropy, Weinstock[3] concluded that the shear and normal stresses relax at different rates. Although this behavior is obviously not accommodated by the Rotta model, it is consistent with the present theory: the perturbation series for Π' is obtained from the series for τ by multiplying the term of order n by the factor $C_n\varepsilon/K$ for some constant C_n. The C_n are all unequal; therefore, the Rotta model is not exact. Now comparison with the series for τ shows[5] that relaxation of the shear stress is governed by the linear term $\mathbf{S}^{(1)}$, whereas relaxation of the normal stresses is governed by the quadratic term $\mathbf{S}^{(2)}$. Since $C_2 \neq C_1$, these stresses relax at different rates. The difference is suppressed in the Rotta model, which arose in the present formalism by replacing all of the C_n by C_1.

2.3 Algebraic Reynolds Stress Models

The approximation, due to Rodi[20], of the Reynolds stress transport equation by an algebraic model under the conditions of semi-homogeneous flow (negligible diffusion of τ and τ/K approximately constant) takes the form

$$\frac{P-\varepsilon}{K}\,\overline{u_i u_j}^{(0)} = -\left(\overline{u_i u_p}\,\frac{\partial U_j}{\partial x_p} + \overline{u_j u_p}\,\frac{\partial U_i}{\partial x_p}\right)^{(0)} + \Pi'_{ij} + \Pi_{ij} \tag{13}$$

where Π and Π' depend on τ and ∇U. Explicit solutions for τ can be obtained, at least in principle, for any such approximation[25]. Briefly, one introduces a basis for polynomials in ∇U, and ∇U^T. The basis contains 11 terms of homogeneity order $n \leq 5$. Writing τ as a sum of these terms with unknown coefficients and substituting in Eq. (13) leads to the explicit expression

$$\tau/K = \sum H_i^{(m)}\,\mathbf{S}_i^{(n)}\,\left(\nabla U, \nabla U^T\right) \tag{14}$$

where $H_i^{(m)}$ is a scalar function of ∇U and ∇U^T such that

$$H_i^{(m)} \sim |\nabla U|^m$$

when $|\nabla U| \to \infty$. The assumptions made on the approximate summations require $m+n=0$; thus, τ/K is bounded when $\mathbf{S}K/\varepsilon \to \infty$. For example, the familiar eddy viscosity formula is replaced in Eq. (29) by a term

$$\tau \sim \frac{K^2}{\varepsilon}\,H^{(-1)}\,\left(\nabla U, \nabla U^T\right)\,\left(\nabla U + \nabla U^T\right)$$

Pope observed[25] that the coefficients $H^{(-n)}$ in Eq. (14) would certainly be intractably complex; although they could be explicitly exhibited by symbolic computation, the result would only pertain to the particular implicit equation for the Reynolds stresses assumed initially in Eq. (13). Therefore, it is equally reasonable just to postulate simple forms for the functions $H^{(-n)}$. This type of modeling could be particularly interesting when applied to the coefficients of the quadratically nonlinear models of Refs. 5, 11, and 12.

2.4 Discussion

The present analysis of the Reynolds stress transport equation, based on the Yakhot-Orszag renormalization group and (tensorial) η−expansion summation as suggested by Yakhot et al.[9], has led to a model transport equation incorporating the well-known LRR and Rotta models. The analysis gives theoretical support both to these models and to the constants sometimes used with them. More significantly, it exhibits the LRR and Rotta models as lowest order approximations, and therefore also supports their replacement with higher order nonlinear models which would be deduced by more accurate approximate summations. The consistency of the analysis with higher order effects like the unequal relaxation rates of shear and normal stresses has been discussed.

3. Future Plans

The nonlinear eddy viscosity representation of the Reynolds stresses

$$\tau_{ij} = \overline{u_i u_j} = \frac{2}{3} K \delta_{ij} - C_\nu \frac{K^2}{\varepsilon} \Big(\frac{\partial U_i}{\partial x_j} + \frac{\partial U_j}{\partial x_i} \Big)$$

$$+ \frac{K^3}{\varepsilon^2} \Big[C_{\tau 1} \Big(\frac{\partial U_i}{\partial x_p} \frac{\partial U_j}{\partial x_p} \Big)^{(0)} + C_{\tau 2} \Big(\frac{\partial U_i}{\partial x_p} \frac{\partial U_p}{\partial x_j} + \frac{\partial U_j}{\partial x_p} \frac{\partial U_p}{\partial x_i} \Big)^{(0)} + C_{\tau 3} \Big(\frac{\partial U_p}{\partial x_i} \frac{\partial U_p}{\partial x_j} \Big)^{(0)} \Big] \quad (15)$$

in which K is the turbulence kinetic energy, ε is the dissipation rate, $C_\nu, C_{\tau 1}, C_{\tau 2}, C_{\tau 3}$ are constants, and (0) denotes deviatoric part, was proposed by Yoshizawa[11] in order to model normal stress effects in shear flows by means of an explicit formula for the stresses. The significance of this formula is not limited to this property: Yoshizawa's derivation using a special perturbation expansion, the two-scale direct interaction approximation, showed that the expansion could be continued to any order in the mean velocity gradient and thereby exhibited the Reynolds stress tensor as the result of an infinite number of increasingly complex interactions between the mean velocity field and turbulence. Related expansions are given in Refs. 5, 12.

The infinite expansion which contains Eq. (15) can be written symbolically as

$$\tau = K A_0 S^0 + \frac{K^2}{\varepsilon} A_1 S^1 + \frac{K^3}{\varepsilon^2} \sum_{i \le N_2} A_{i2} S_i^2 + \cdots + \frac{K^{n+1}}{\varepsilon^n} \sum_{i \le N_n} A_{in} S_i^n + \cdots \quad (16)$$

Eq. (16) can be considered a decomposition of the Reynolds stress

$$\tau = \tau^0 + \tau^1 + \cdots \quad (17)$$

where

$$\tau^n = \frac{K^{n+1}}{\varepsilon^n} \sum_{i \le N_n} A_{in} S_i^n = \sum_{i \le N_n} \tau_i^n \quad (184)$$

where S_i^n denotes a symmetric tensor homogeneous of degree n in the mean velocity gradient ∇U and its transpose, N_n denotes the number of linearly independent terms of order n (so in Eq. (15), $N_2 = 3$), and the A_{in} are constants.

In an analysis of the Reynolds stress transport equation by renormalization group techniques[35], we found analogous expansions for the term which governs the return to isotropy,

$$\Pi' = \frac{\varepsilon}{K} \Big[\frac{K^2}{\varepsilon} B_1 S^1 + \frac{K^3}{\varepsilon^2} \sum_{i \le N_2} B_{i2} S_i^2 + \cdots \Big] \quad (19)$$

and for the rapid pressure-strain term

$$\Pi = \frac{2}{5} K \, S^1 + \frac{K^2}{\varepsilon} \Big\{ C_1 \Big[S^1 \nabla U^T + \nabla U S^1 \Big]^{(0)} + D_1 \Big[S^1 \nabla U + \nabla U^T S^1 \Big]^{(0)} \Big\}$$

$$+\frac{K^3}{\varepsilon^2}\sum_{i\leq N_2}\left[C_{i2}\left(S_i^2\nabla U^T+\nabla U S_i^2\right)^{(0)}+D_{i2}\left(S_i^2\nabla U+\nabla U^T S_i^2\right)\right]+\cdots \tag{20}$$

Suppose that these sums are introduced into the Reynolds stress transport equation

$$\dot{\tau}=\Pi'+\Pi-P+D \tag{21}$$

where the dot denotes convective derivative, $P=\tau\nabla U^T+\nabla U\tau$ is production and D denotes the diffusion term. In order to obtain a Reynolds stress transport equation, it is necessary to express the sums (19) and (20) in terms of τ and ∇U. Although the coefficients A, B, C, D can be explicitly exhibited to any order in perturbation theory, they do not have an obvious law of formation. Therefore, the sums (19) and (20) can only be approximated by polynomials in τ and ∇U if some hypotheses relating the coefficients is introduced. There is no unique hypothesis of this sort, but the simplest[35] seems to be

$$\begin{aligned} &B_{in}/B_1=A_{in}/A_1, \qquad n\geq 2\\ &C_{in}/C_1=D_{in}/D_1=A_{in}/A_1, \qquad n\geq 2\end{aligned} \tag{22}$$

which leads to the Rotta return to isotropy model and to an LRR model for the rapid term. The approximation expressed by Eq. (22) can be compared to the summation introduced in an analogous context by Yakhot et al.[9], and to Padé approximation: it agrees with the perturbation theory of Eqs. (19), (20) to lowest order, but includes effects of all order in ∇U.

By evaluating more terms of the perturbation series explicitly and introducing an equation like (8) for coefficients of higher order, a hierarchy of models could be generated. They would initially be nonlinear in ∇U, as advocated by Speziale[33], but one might introduce the perturbation series for $\tau\cdot\tau$ to obtain a model nonlinear in τ[1,2]. However, the close analogy between Eqs. (19) and (20) and Yoshizawa's expansion (16) suggests a different approach: namely, use Eqs. (17) and (18) to replace S_i^n in Eqs. (19) and (20) by τ_i^n/A_{in}. Substitute these modified expressions and Eq. (17) into the transport equation Eq. (21), treat τ_i^n as having order $\mid\nabla U\mid^n$, and separate the terms of like order in $\mid\nabla U\mid$ in the standard perturbation theoretic fashion. The result is that the terms τ_i^n in the decomposition (17), (18) themselves satisfy coupled transport equations.

For simplicity, let us write an approximate system for the τ^n instead of for the τ_i^n and assume the most elementary scalar diffusion model. Then the the single transport equation for τ would be replaced by a system

$$\begin{aligned}\dot{\tau}^n &= -C_R^n\tau^n+C_1^n\left(\tau^{n-1}\nabla U^T+\nabla U\tau^{n-1}\right)^{(0)}\\ &+C_2^n\left(\tau^{n-1}\nabla U+\nabla U^T\tau^{n-1}\right)^{(0)}+C_D^n\frac{K^2}{\varepsilon}\nabla^2\tau^n, n\geq 1\end{aligned} \tag{23}$$

Since $\tau=\sum\tau^n$, the system (6) should be constrained to satisfy Crow's condition and to contain the exact production term following summation over n. Making the coefficients $C_R^n, C_1^n, C_2^n, C_D^n$, independent of n reduces the system to a model of the LRR form for $\tau = \sum \tau^n$.

This conclusion also follows from Leslie's analysis[34] of the direct interaction (DIA) equations for shear flow. Leslie suggested a perturbative solution for the (tensor) correlation function and Green's function

$$\begin{aligned} U &= U^0 + U^1 + \cdots \\ G &= G^0 + G^1 + \cdots \end{aligned} \tag{24}$$

where U^n and G^n are of the order $\mid \nabla U \mid^n$, and observed that this expansion is simultaneously an expansion in powers of the mean strain, and a decomposition into symmetry types of increasing complexity. This is also a feature of the expansion (16). Substitution of Eq. (20) into the equations of the direct interaction approximation gives a coupled system for the U^n and G^n in standard fashion. Then in principle, by integrating each equation of this system over all wavenumbers and introducing the definitions

$$\tau^n = \int U^n d\,\mathbf{k}$$

we could attempt to obtain coupled transport equations for the τ^n. Unfortunately, the derivation of equations for single-point quantities from DIA is not entirely straightforward, and more heuristic methods like two-scale DIA[8,14] and renormalization group are required.

The simplest model of this type is a two component model,

$$\tau - \frac{2}{3}KI = \tau^1 + \tau^2$$

with

$$\begin{aligned} \dot{\tau}^1 =& -C_R^1\tau^1 - \frac{4}{15}K\left(\nabla U + \nabla U^T\right) + \left(C_1^1 - 1\right)\left(\tau^2\nabla U^T + \nabla U\tau^2\right)^{(0)} \\ &+ C_2^1\left(\tau^2\nabla U + \nabla U^T\tau^2\right)^{(0)} + C_D^1\nabla\frac{K^2}{\varepsilon}\nabla\tau^1 \\ \dot{\tau}^2 =& -C_R^2\tau^2 + \left(C_1^2 - 1\right)\left(\tau^1\nabla U^T + \nabla U\tau^1\right)^{(0)} \\ &+ C_2^2\left(\tau^1\nabla U + \nabla U^T\tau^1\right)^{(0)} + C_D^2\nabla\frac{K^2}{\varepsilon}\nabla\tau^2 \end{aligned} \tag{25}$$

The appearance of τ^2 in the equation for τ^1 is required by the production term constraint which is violated by direct truncation of the system (20) at the second order. The properties of this model for simple shear flow, in which $\partial U_i/\partial x_j = S\delta_{i1}\delta_{j2}$ follow by setting

$$\tau^1 = \tau_{12}\begin{bmatrix} & 1 & \\ 1 & & \\ & & 0 \end{bmatrix} \qquad \tau^2 = \begin{bmatrix} \tau_{11} & & \\ & \tau_{22} & \\ & & \tau_{33} \end{bmatrix}^{(0)} \tag{26}$$

Then C_R^1 describes the return to isotropy of the shear stress, and C_R^2 the return to isotropy of the normal stresses. These relaxation rates can be unequal in this theory, an effect predicted by Weinstock's analysis[3] of the spectral dynamics of the return to isotropy. Weinstock suggested further that the individual normal stresses relax at different rates: this effect is not accommodated by the present model, but could occur in a model in which τ^2 is divided into the three tensor components $\tau_1^2, \tau_2^2, \tau_3^2$ of Eq. (18).

The inequality of the Rotta constants in the present model can be used to overcome a defect of models of the LRR type, that in semi- homogeneous flows in which $a_{ij} = \tau_{ij}^{(0)}/K$ is approximately constant, the ratio a_{11} is too small whereas a_{12} is too big[10]. Following Speziale[19], write Eq. (21) as a system of equations for the ratios a_{ij} and set $\dot{a}_{ij} = 0$. There results,

$$2a_{12}\eta = \left(C_R^1 - 1\right) - \left\{\left(C_R^1 - 1\right)^2 - 4\eta^2\left[\left(C_1^1 - 1\right)a_{22} + C_2^1 a_{11} - \frac{4}{15}\right]\right\}^{1/2}$$

$$a_{11} = \frac{\left[-\frac{4}{3}\left(C_1^2 - 1\right) + \frac{2}{3}C_2^2\right]\eta a_{12}}{\left(-C_R^2 + 1\right) + \eta a_{12}} \qquad (27)$$

$$a_{22} = \frac{\left[\frac{2}{3}\left(C_1^2 - 1\right) - \frac{4}{3}C_2^2\right]\eta a_{12}}{\left(-C_R^2 + 1\right) + \eta a_{12}}$$

When $P/\varepsilon = -\eta a_{12} = 1$,

$$a_{12}^2 = \frac{4}{15}\frac{1}{C_R^1} - \frac{C_1^1 - 1}{C_R^1}a_{22} - \frac{C_2^1}{C_R^1}a_{11}$$

$$a_{11} = \left[-\frac{4}{3}\left(C_1^2 - 1\right) + \frac{2}{3}C_2^2\right]/C_R^2 \qquad (28)$$

$$a_{22} = \left[\frac{2}{3}\left(C_1^2 - 1\right) - \frac{4}{3}C_2^2\right]/C_R^2$$

Eq. (28) shows that setting $C_R^2 < C_R^1$ both increases a_{11} and decreases a_{12} and thus improves the agreement between theory and experiment. The trend required here is consistent with Weinstock's findings[3] that the Rotta constant for the normal stresses should be smaller than the shear constant and should take values close to 1.0.

The inequality of the coefficients describing the rapid terms affects the behavior of the model under rapid distortion. The rapid distortion analysis of passively strained turbulence predicts that a one-component limit state is reached in which $\tau_{ij} = 2K\delta_{i1}\delta_{j1}$, $\eta = SK/\varepsilon \to \infty$ and P/ε is finite[21]. Whether or not this limit can in fact occur as an asymptotic state, a stress model should accommodate it because it can exist approximately in steady flows as a "spatial transient" in strongly inhomogeneous regions of very high convective or diffusive transport[17]. Moreover, models of the LRR form do not capture the transient evolution of rapidly distorted flows well. Let us assume that all model coefficients are functions of the "state" of turbulence, following Shih and Lumley[2]; the precise parametrization of the state will be left to future investigations. From Eq. (13), it is evident that $P/\varepsilon = -\eta a_{12}$ will be of order η in the one-component state in which $a_{11} = 4/3, a_{22} = -2/3$ unless

$$-\frac{2}{3}\left(C_1^1 - 1\right) + \frac{4}{3}C_2^1 = \frac{4}{15}$$

in this state. But Eq. (13) also shows that $a_{11} = 4/3, a_{22} = -2/3$ requires

$$C_1^2 \sim 0, \qquad C_2^2 \sim 0$$

in this state. These conditions are inconsistent in a model in which $C_1^1 = C_1^2$ and $C_2^1 = C_2^2$, but are clearly consistent with the present proposal.

The advantages of this model are consistency with a systematic perturbation theory, the possibility of unequal relaxation rates for normal and shear stresses in relaxing strained turbulence, improved agreement with experimental data for universal ratios in simple shear flows, and the possibility of accommodating the one-component limit of rapid distortion theory.

4. References

[1] C. G. Speziale, S. Sarkar, and T. Gatski, "Modeling the pressure-strain correlation of turbulence - an invariant dynamical systems approach," J. Fluid Mech. to appear.

[2] T.H. Shih and J.L. Lumley, "Modeling of pressure correlation terms in Reynolds stress and scalar flux equations," Rept. FDA-85-3, Sibley School of Mech. and Aero. Eng. Cornell U. (1985).

[3] J. Weinstock, "Theory of the pressure-strain rate: Part II, diagonal elements" J. Fluid Mech. **116**, 1 (1982).

[4] V. Yakhot and S. A. Orszag, "Renormalization group analysis of turbulence I. Basic theory," J. Sci. Comp. **1**, 3 (1986).

[5] R. Rubinstein and J.M. Barton, "Nonlinear Reynolds stress models and the renormalization group," Phys. Fluids A **2**, 1472 (1990).

[6] B. E. Launder, G. Reece, and W. Rodi, "Progress in the development of a Reynolds-Stress turbulence closure," J. Fluid Mech. **68** 537 (1975).

[7] J. Rotta, "Statistical theory of non-homogeneous turbulence," Z. Phys. **129**, 547 (1951).

[8] A. Yoshizawa, "Statistical evaluation of the triple velocity correlation and the pressure-velocity correlation in shear turbulence," J. Phys. Soc. Jpn. **51**, 2326 (1982).

[9] V. Yakhot, S. Thangam, T. Gatski, S. A. Orszag, and C. G. Speziale, "Development of turbulence models for shear flows by a double expansion technique," submitted to Phys. Fluids A.

[10] V. Yakhot and S. A. Orszag, "Analysis of the ϵ-expansion in turbulence theory: approximate renormalization group for diffusion of a passive scalar in a random velocity field," Princeton Univ. preprint (1989).

[11] A. Yoshizawa, "Statistical analysis of the deviation of the Reynolds stress from its eddy-viscosity representation," Phys. Fluids **27**, 1377 (1984).

[12] C. G. Speziale, "On nonlinear K-l and K-ϵ models of turbulence," J. Fluid Mech. **178**, 459 (1987).

[13] A. J. M. Spencer and R. S. Rivlin, "Further results in the theory of matrix polynomials," Arch. Rational Mech. Anal. **4**, 214 (1960).

[14] A. Yoshizawa, "Deviation of a model Reynolds stress transport equation using a renormalization of the eddy-viscosity-type representation," preprint.

[15] V. Yakhot and L. M. Smith, "The ϵ-expansion for derivation of turbulence models," submitted to Phys. Fluids A.

[16] S. Crow, "Viscoelastic properties of fine grained incompressible turbulence," J. Fluid Mech. **41**, 81 (1968).

[17] V. Yakhot, private communication.

[18] L. M. Smith and W. C. Reynolds, "A critical assessment of the Yakhot-Orszag renormalization group method for deriving turbulence models and statistics," submitted to Physics of Fluids A (1991).

[19] C. G. Speziale and N. MacGiolla Mhuiris, "On the prediction of equilibrium states in homogeneous turbulence," J. Fluid Mech. **209**, 591 (1989).

[20] W. Rodi, "A new algebraic relation for computing the Reynolds stresses," Z. Ang. Math. Mech. **56**, 219 (1976).

[21] W. C. Reynolds, "Fundamentals of turbulence for turbulence modeling and simulation," AGARD Lecture Series No. 86, 1 (1987).

[22] B. E. Launder, "Second-moment closure: present . . . and future?," Int. J. Heat and Fluid Flow **10**, 282 (1989).

[23] R. Rubinstein and J.M. Barton, "Renormalization group analysis of anisotropic diffusion in turbulent shear flow," Phys. Fluids A **3**, 415 (1991).

[24] A. Yoshizawa, "Statistical modelling of passive scalar diffusion in turbulent shear flows," J. Fluid Mech. **195**, 541 (1988).

[25] S. G. Pope, "A more general effective-viscosity hypothesis," J. Fluid Mech. **72**, 331 (1975).

[26] K. Horiuti, "Higher order terms in the anisotropic representation of Reynolds stresses," Phys. Fluids A **2**, 1708 (1990).

[27] S. Tavoularis and S. C. Corrsin, "Experiments in nearly homogeneous turbulent shear flow with a uniform mean temperature gradient Part 1," J. Fluid Mech. **104**, 311 (1981).

[28] M. M. Rogers, P. Moin and W. Reynolds, "The structure and modeling of the hydrodynamic and passive scalar fields in homogeneous shear flows," Dept. Mech. Eng. Rep. TF-25, Stanford U. (1986).

[29] S. Tavoularis and U. Karnik, "Further experiments on the evolution of turbulent stresses and scales in uniformly sheared turbulence," J. Fluid Mech. **204**, 457 (1989).

[30] P. Spalart, "Direct simulation of a turbulent boundary layer up to $R_\theta = 1410$," NASA TM 89407 (1986).

[31] J. Laufer, "The structure of turbulence in fully developed pipe flow," NACA Tech. Rep. 1174 (1954).

[32] V. G. Harris, J. A. Graham and S. C. Corrsin, "Further experiments in nearly homogeneous turbulent shear flow," J. Fluid Mech. **81**, 657 (1977).

[33] C. G. Speziale, "Comments on the present state of second-order closure models for incompressible flows, " *Workshop on Engineering Turbulence Modeling*, NASA CP-10088, 229 (1991).

[34] D. C. Leslie, *Developments in the Theory of Turbulence*, Clarendon Press, Oxford (1973).

[35] R. Rubinstein and J. M. Barton, "Renormalization group analysis of the Reynolds stress transport equation," to appear in Physics of Fluids A, (1992).

Bypass Transition in Compressible Boundary Layers

J. J. Van der Vegt

1. Motivation and Objectives

Transition to turbulence in aerospace applications usually occurs in a strongly disturbed environment. For instance, the effects of free-stream turbulence, roughness and obstacles in the boundary layer strongly influence transition. Proper understanding of the mechanisms leading to transition is crucial in the design of aircraft wings and gas turbine blades, because lift, drag and heat transfer strongly depend on the state of the boundary layer, laminar or turbulent. Unfortunately, most of the transition research, both theoretical and experimental, has focused on natural transition. Many practical flows, however, defy any theoretical analysis and are extremely difficult to measure. Morkovin[5] introduced in his review paper the concept of bypass transition as those forms of transition which bypass the known mechanisms of linear and non-linear transition theories and are currently not understood by experiments.

In an effort to better understand the mechanisms leading to transition in an disturbed environment, experiments are conducted studying simpler cases, viz. the effects of free-stream turbulence on transition on a flat plate, Sohn and Reshotko[14] and Wang et al.[19]. It turns out that these experiments are very difficult to conduct, because the generation of free-stream turbulence with sufficiently high fluctuation levels and reasonable homogeneity is non trivial. For a discussion see Morkovin[5]. Serious problems also appear due to the fact that at high Reynolds numbers the boundary layers are very thin, especially in the nose region of the plate where the transition occurs, which makes the use of very small probes necessary.

The effects of free-stream turbulence on transition are the subject of this research and are especially important in a gas turbine environment, where turbulence intensities are measured between 5 and 20%, Wang et al.[19]. Due to the fact that the Reynolds number for turbine blades is considerably lower than for aircraft wings, generally a larger portion of the blade will be in a laminar-transitional state. Turner[15] shows that the effect of free-stream turbulence on transition significantly increases when the free-stream turbulence levels become larger than 5% and is accompanied with a significant increase in heat transfer. Recently Rai and Moin[11] presented a direct numerical simulation of transition to turbulence on a flat plate in a free-stream with Mach number .1 and turbulence levels at the leading edge of about 2.75%. Direct numerical simulations offer a unique opportunity to study specific phenomena, while excluding disturbances from other sources. The computations from Rai and Moin show some impressive results, especially regarding intermittency and turbulent spots. Their numerical simulation, however, has the same problem as with most of the experiments, namely a very low Mach number, while many applications operate in the transonic regime. Due the nature of their numerical scheme, a non-conservation formulation of the Navier-Stokes equations, it is a non-trivial extension to compute flow fields in the transonic regime.

This project aims at better understanding the effects of large free-stream turbulence in compressible boundary layers at Mach numbers both in the subsonic and transonic regime using direct numerical simulations. The present project aims at computing the flow over a flat plate and curved surface. This research will provide data which can be used to clarify mechanisms leading to transition in an environment with high free stream turbulence. This information is useful for the development of turbulence models, which are of great importance for CFD applications, and are currently unreliable for more complex flows, such as transitional flows.

2. Accomplishments

Direct simulations of transition in compressible flows with both shocks and boundary layers requires an extremely accurate and efficient scheme. Several conflicting requirements present a serious challenge which cannot be met by existing numerical schemes:

- The small grid spacing in the boundary layer makes an implicit scheme necessary, because an explicit scheme would have a severe time step limitation. Implicit schemes usually are not time accurate and rather dissipative.
- Higher order accurate schemes are necessary but higher order accurate schemes generally do not give non-oscillatory solutions around discontinuities, such as shocks. Many of the popular non-oscillatory shock capturing schemes, such as TVD (Total Variation Diminishing) methods, are only first order accurate in multi-dimensional flows and even in one-dimension they reduce to first order at non-sonic local extrema.

In order to satisfy these conflicting requirements a significant effort has been made to improve and combine several successful numerical schemes. A fully implicit and time accurate code for the solution of the three-dimensional compressible Navier-Stokes equations in general geometries has been written and tested. Higher order accuracy and shock capturing are implemented using an Essentially Non-Oscillatory (ENO) scheme. Time accuracy is obtained using a Newton method.

In the next section a brief description of the numerical scheme will be given followed by the discussion of a series of tests aimed at validating the code.

2.1 Numerical Scheme

The compressible Navier-Stokes equations are solved using a finite volume method. A detailed discussion of finite volume and difference methods can be found in Vinokur[18]. The integral formulation of the Navier-Stokes equations, assuming all variables are continuous in time, is given by:

$$\frac{\partial}{\partial t}\int_{V(t)} \mathbf{U} dV + \oint_{S(t)} \mathbf{n}\cdot\mathcal{F} dS = 0 \tag{2.1.1}$$

Here $V(t)$ and surface $S(t)$ are the volume and outer surface of the domain Ω and $\mathbf{n}$ an outward unit normal vector at S. The vector $\mathbf{U}$ represents the conserved variables: $(\rho, \rho u, \rho v, \rho w, e)^T$, with ρ the density, u, v and w the velocity components, and e the total energy. The tensor $\mathcal{F}$ is defined as $\mathcal{F} = \mathcal{E} + \mathcal{V}$, with $\mathcal{E}$ the inviscid contribution defined as:

$$\mathbf{E}_1 = \begin{pmatrix} \rho u \\ \rho u^2 + p \\ \rho uv \\ \rho uw \\ (e+p)u \end{pmatrix}; \quad \mathbf{E}_2 = \begin{pmatrix} \rho v \\ \rho uv \\ \rho v^2 + p \\ \rho vw \\ (e+p)v \end{pmatrix}; \quad \mathbf{E}_3 = \begin{pmatrix} \rho w \\ \rho uw \\ \rho vw \\ \rho w^2 + p \\ (e+p)w \end{pmatrix} \tag{2.1.2}$$

and $\mathcal{V}$ the viscous contribution:

$$\mathbf{V}_1 = \begin{pmatrix} 0 \\ \tau_1 \\ \mathbf{u}\cdot\tau_1 + q_1 \end{pmatrix}; \quad \mathbf{V}_2 = \begin{pmatrix} 0 \\ \tau_2 \\ \mathbf{u}\cdot\tau_2 + q_2 \end{pmatrix}; \quad \mathbf{V}_3 = \begin{pmatrix} 0 \\ \tau_3 \\ \mathbf{u}\cdot\tau_3 + q_3 \end{pmatrix} \tag{2.1.3}$$

The shear stress tensor $\mathcal{T}$, with components (τ_1, τ_2, τ_3) is defined as:

$$\mathcal{T} = \frac{1}{Re}(\mu(\nabla\mathbf{u} + \nabla\mathbf{u}^T) + \lambda(\nabla\cdot\mathbf{u})\mathcal{I}) \tag{2.1.4}$$

and the heat flux $\mathbf{q}$ as:

$$\mathbf{q} = \frac{\kappa\nabla T}{(\gamma-1)ReM_\infty^2 Pr} \tag{2.1.5}$$

The variables p, T, μ, λ and κ represent the pressure, temperature, first and second viscosity coefficient and thermal conductivity, respectively. The coefficients Re, M_∞, and Pr are the Reynolds, Mach, and Prandtl numbers. All variables are non-dimensionalized using free-stream variables and a characteristic length L.

The Navier-Stokes equations are solved using a finite volume method because we seek a weak solution in order to capture shocks in high Reynolds number flows. The finite volume method is also the most natural way to satisfy the conservation properties of the differential equations. After subdividing the volume V into a set of disjunct cells we obtain the finite volume discretization for a cell with index i, j, k:

$$\frac{\partial}{\partial t}\left(V\overline{\mathbf{U}}_{i,j,k}\right) + \hat{\mathbf{F}}^1_{i+\frac{1}{2},j,k} - \hat{\mathbf{F}}^1_{i-\frac{1}{2},j,k} + \hat{\mathbf{F}}^2_{i,j+\frac{1}{2},k} - \hat{\mathbf{F}}^2_{i,j-\frac{1}{2},k} + \hat{\mathbf{F}}^3_{i,j,k+\frac{1}{2}} - \hat{\mathbf{F}}^3_{i,j,k-\frac{1}{2}} = 0 \tag{2.1.6}$$

where a barred quantity with index i, j, k is an average of the unbarred quantity over the cell with index i, j, k and indices $i \pm \frac{1}{2}$, $j \pm \frac{1}{2}$ and $k \pm \frac{1}{2}$ refer to values at the cell faces. The fluxes $\hat{\mathbf{F}}^i$ at the cell faces are defined as:

$$\hat{\mathbf{F}}^l = \mathbf{S}^l \cdot \mathcal{F} \tag{2.1.7}$$

with $\mathbf{S}^l$ the cell face in the direction i. The computation of the cell face $\mathbf{S}^l$ and volume V has to be done with great care in order satisfy the geometric conservation law, for details see Vinokur[19]:

Flux Approximation

The crucial part in the development of a finite volume method is the approximation of the fluxes at the cell faces. The flux $\hat{\mathbf{F}}^1_{i+\frac{1}{2}}$ is computed using the Osher approximate Riemann solver. The first order accurate conservative flux is given by:

$$\hat{\mathbf{F}}^1_{i+\frac{1}{2},j,k} = \frac{1}{2}(\hat{\mathbf{F}}^1_{i,j,k} + \hat{\mathbf{F}}^1_{i+1,j,k} - \int_{\Gamma^i} |\partial\hat{\mathbf{F}}^1| du) \tag{2.1.8}$$

with equivalent expressions for the other two directions. The integral is computed along a path in phase space, connecting the points with index (i, j, k) and $(i+1, j, k)$. Along each subpath a Riemann problem is solved, which is used to determine the intermediate states. In this way exact expressions can be derived for the path integrals. More details about the implementation of the Osher scheme can be found in Osher and Solomon[6], Osher and Chakravarthy[7], Chakravarthy and Osher[1] and Rai and Chakravarthy[10]. The Osher approximate Riemann solver is the most accurate approximate Riemann solver and satisfies the entropy condition, contrary to the Roe approximate Riemann solver which needs an entropy fix to eliminate steady expansion shocks. The Osher scheme captures steady shocks in at most two points.

The most important reason for the choice of the Osher scheme, however, has been its low numerical dissipation in boundary layers, Koren[4]. Most schemes for the Euler equations are very dissipative in the boundary layer and not well suited for direct numerical simulations. In earlier work, Van der Vegt[17], modifications to flux vector splitting schemes were discussed to alleviate this problem, but although significant improvement was achieved on steady laminar boundary layers, it was not possible to reach accuracy levels necessary for direct simulations.

Higher order spatial accuracy

Direct simulations require a high accuracy which cannot be achieved with standard second order schemes. It is fairly straightforward to derive higher order accurate finite difference schemes, but shock capturing then will not be possible. The development of higher order accurate, multi-dimensional finite volume schemes, capable of shock capturing still is an area of active research, and has been an important subject in this project. A significant effort has been made to combine the Osher approximate Riemann solver, discussed in the previous section, with an ENO scheme. Results of this work are described in Van der Vegt[17], where the different ENO methods are discussed and results of various tests are discussed.

Higher order accuracy of a finite volume method can be defined is various ways. One approach is to define higher order accuracy with respect to the cell averaged values. This resembles most closely the finite volume description, which gives equations for the cell averaged values. Another definition of higher order accuracy uses the point values at the cell center, which is used in conservative higher order finite difference methods. Both approaches are being used. For subsonic flows currently the fifth order scheme, developed by Rai[9], is used, which is based on a Taylor series expansion of the flux vector along the lines presented by Osher and Chakravarthy[8]. This method is a conservative finite difference scheme. It has the benefit that it is simple to implement in more dimensions, but does not allow shock capturing. Osher and Chakravarthy[8] demonstrated how to make these schemes TVD and allow shock capturing, but they are not very useful and only first order accurate globally. The scheme therefore is used in its unlimited form, limiting its application to flows without discontinuities such as shocks. The scheme also is rather expensive and work is in progress to improve its efficiency.

For flows with shocks research has been carried out to develop higher order accurate ENO schemes. ENO schemes use an adaptive stencil where a searching algorithm tries to find that part of the flow field surrounding a cell which is the smoothest. Then a conservative, higher order accurate interpolation method is used to "reconstruct" the point values from the cell averaged values. Due to the fact that the interpolation process only uses data from the smooth part of the flow field numerical oscillations will be minimized. In this way uniform higher order accuracy can be obtained. The first ENO methods were developed by Harten et al.[3], and later modifications were proposed by Shu and Osher[12,13]. In Van der Vegt[17] the different methods were compared and it was found that the ENO scheme, using primitive function reconstruction from cell averaged variables with the Cauchy-Kowalewski procedure for time integration combined with the Osher approximate Riemann solver, was the most accurate and robust. In one dimension it has been successfully used up to fifth order accuracy, but due to the fact that in multi-dimensional flows currently dimension splitting is used, its accuracy is limited to second order in more than one dimension. Work to extend this scheme to higher order accuracy in multi-dimensional flows is in progress.

Time integration

Due to the very small gridspacing necessary at the wall and in critical layers explicit time integration would result in a serious time step limitation. To alleviate this problem implicit time integration has to be used, but most implicit time integration schemes make assumptions in the implicit part which reduce or eliminate time accuracy. The development of implicit and time accurate numerical schemes therefore has been a significant part of this research. Time accuracy is obtained using the Newton method discussed in Rai[9], which solves the non-linear system of equations in the implicit time integration scheme using a Newton method. Rai uses this method also to reduce the error caused by approximate factorization. We do not use approximate factorization but solve the whole matrix system iteratively, see Van der Vegt[16], and need the Newton scheme only to reduce the error due to the time linearization. This iterative scheme also has the benefit that it is not necessary to use an exact linearization of the flux vectors, which can be very difficult and time consuming to obtain. First order Steger-Warming flux vector splitting is used in the implicit scheme, while a higher order accurate spatial discretization is used for the explicit part. At each time step the Newton iteration is performed such that the accuracy of the higher order explicit part is maintained. The use of an approximate linearization, however, limits the maximum time step and work is in progress to evaluate if a more accurate linearization would improve the performance and robustness of the scheme. Especially at high Mach numbers there still are convergence problems for large Courant numbers when the scheme is used to obtain steady state solutions.

2.2 Results and Discussion

Several computations have been carried out to test the code and the various numerical schemes. In order to test the Osher approximate Riemann solver and the ENO schemes a large number of shock tube calculations have been carried out, a detailed description of this work can be found in Van der Vegt[17]. The different ENO schemes tested were the ENO method from Harten et al.[3], using primitive function reconstruction and either Runge-Kutta time integration or the Cauchy-Kowalewski procedure, and the Shu and Osher flux-ENO scheme. In all cases the Osher approximate Riemann solver was used and the effect of the ordering of the eigenvalues, viz. natural and reversed ordering, has been investigated. Four cases with different difficulties were tested, see Table 1. The performance of the different schemes was reasonable in most cases, but it turned out that the ENO scheme with primitive function reconstruction and the Cauchy-Kowalewski procedure for time integration (ENO-CK) was the most accurate and robust. Some of the results obtained with this method, are shown in Figures 1 and 2. Figure 1 shows a left moving shock followed by a contact discontinuity and a right moving expansion wave. A difficult problem for the ENO schemes in case A is the fact that in the initial stages there are not enough grid points available in the region between the shock and contact or shock-shock. The ENO scheme searches for the stencil which gives the smoothest part of the flow field around a grid point or cell. In these cases there exist in both directions a discontinuity and there are not enough points available to build a non-oscillatory higher order reconstruction. This problem exist for all ENO schemes but the ENO Cauchy Kowalewski scheme is the least sensitive for it. The other methods have mild to strong oscillations in these areas. One way to solve this problem is to reduce the accuracy locally till enough grid points are available to create a higher order reconstruction, but this is a problem which still needs further attention. Case B, Figure 3, shows a left moving expansion wave and a right moving contact discontinuity and shock. One of the problems in this case is the appearance of a sonic point, which gives a small jump of $O(\triangle x)$ at first order. The shock tube tests showed that it is possible to use a higher order scheme for flows with discontinuities, but the convergence of these higher order schemes can

Case	P_L	P_R	U_L	U_R	T_L	T_R
A	15000	98400	0	0	1378	4390
B	988000	9930	0	0	2438	2452
C	10000	100000	0	0	2627	272
E	573	22300	2200	0	199	546

Table 1. Initial Conditions Shock Tube Tests.

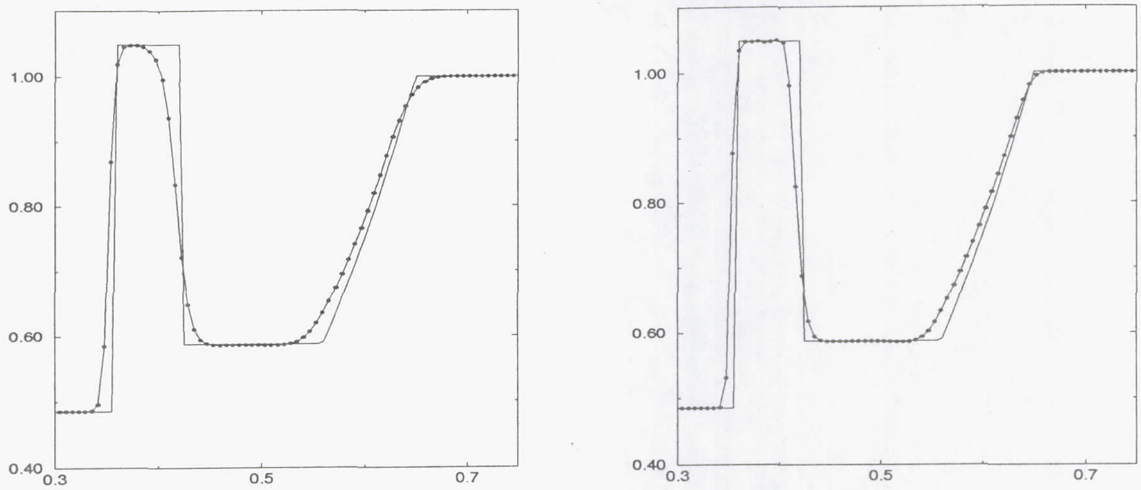

Fig. 1. Case A, density at $t = .2$, 2nd and 5th order ENO-CK.

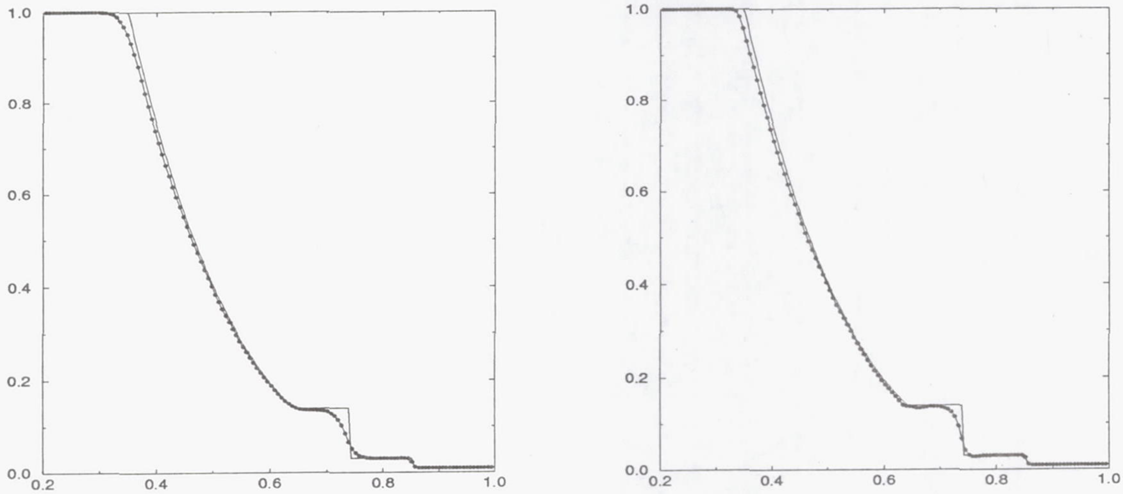

Fig. 2. Case B, density at $t = .2$, 2nd and 5th order ENO-CK.

be at most first order around these discontinuities. Tests of all the ENO schemes on smooth solutions showed that they all reached the proper level of accuracy. Test are currently underway to check if the ENO schemes give higher order accuracy in regions outside discontinuities as they are supposed to. This is an important test to see if these methods are capable of shock-turbulence interaction simulations.

In order to test the shock capturing properties of the code the flow field around a circular cylinder at Mach 8 has been computed. Although the flow field was two-dimensional the three-dimensional code was used to check if the flow field remained exactly two-dimensional and the geometric conservation law was satisfied. Figure 3. presents contours of the pressure at a spanwise station along the cylinder. The solution is the same at all stations. The flow field consists of a strong bow shock where the Mach number changes from 8 to about 2.8 behind the shock at the symmetry line. Apart from the strong shock another aspect of this case is the

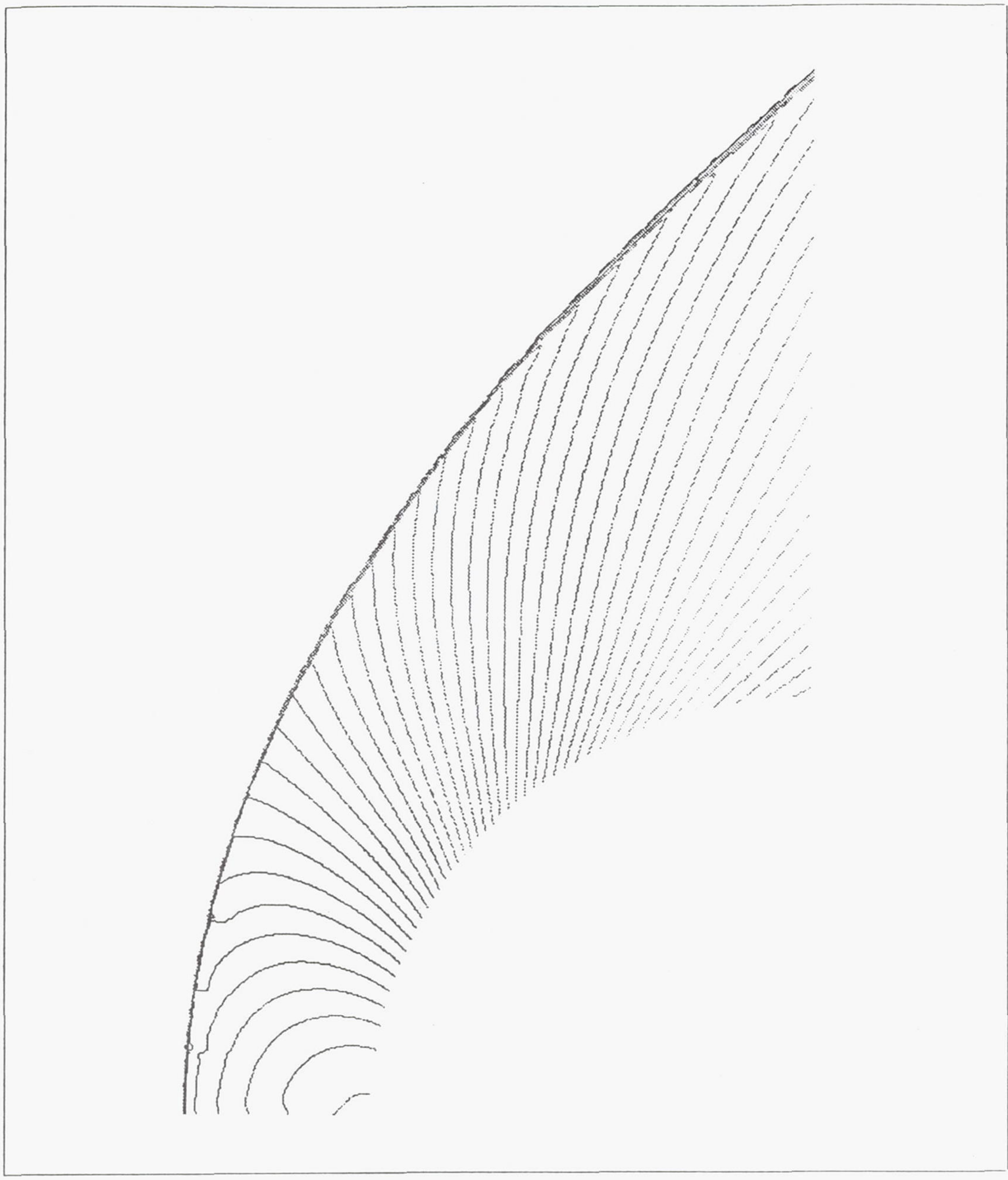

Figure 3. Pressure field of flow around a cylinder at Mach 8

fact that the flow field in the stagnation region ahead of the cylinder is subsonic. The sonic line is at about 45 degrees with the flow angle and a smooth transition is observed from the subsonic to the supersonic region. This case has also been computed by Osher and Chakravarthy[7] and the results compare well. To test the ability of the code to simulate transitional flows which is a crucial test before bypass transition can be simulated currently computations are done on natural transition in a flat plate boundary layer. A comparion is made with the results of Fasel et

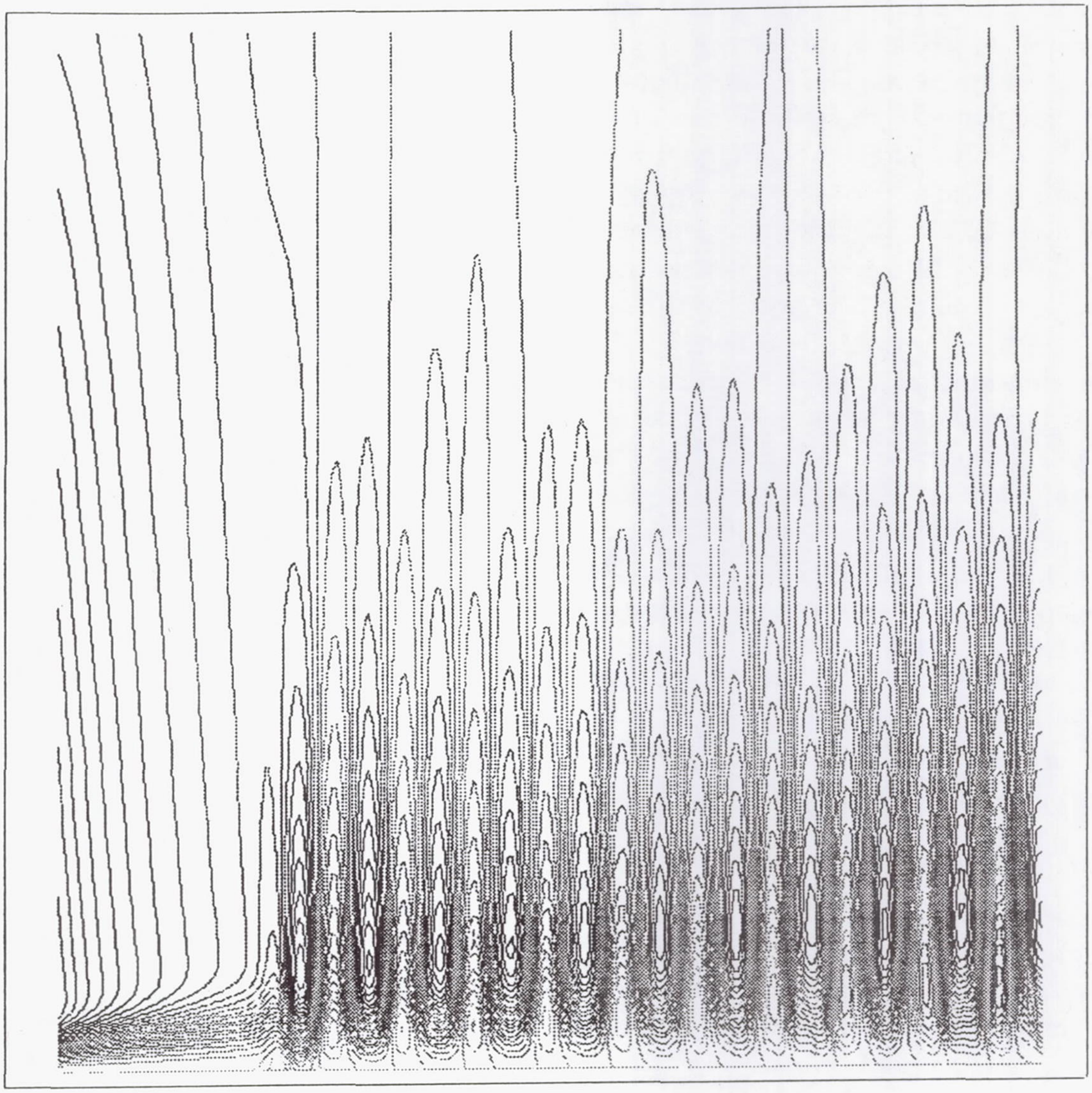

Figure 4. Vertical velocity field in a flat plate boundary layer at Mach 0.08 with periodic suction and blowing (vertical direction enlarged 20 times).

al.[2], which computed transition in an incompressible boundary layer. In order to make the comparison as accurate as possible a very low Mach number, [illegible] = .08 was chosen. This Mach number is approximately the lower limit for the numerical scheme and despite the fact that the computations are fully implicit a severe time step limitation is imposed by the sound waves. To start the simulation first a steady laminar boundary layer is computed, which is a non-trivial task because a very high accuracy is needed in this computation. The disturbances at the beginning of the plate have an amplitude of 10^{-4} and transition simulations require a very low numerical dissipation. The disturbances are generated by periodic suction and blowing in a strip somewhat downstream of the inflow boundary. This is done because there are always numerical disturbances due to the fact that the inflow boundary conditions are not perfect. The disturbances are generated in a region of the boundary layer which is linearly stable. When they move downstream first the transients are damped and after they move in the unstable region the Tolmien Schlichting waves, which are the most unstable two-dimensional waves, are amplified. In order to accommodate for the fact that the subsonic outflow boundary conditions, which are essentially inviscid, are not perfect in a boundary layer a buffer layer is added to the plate to damp as much as possible the reflections coming from this boundary layer. This is the same procedure as used by Rai and Moin[11]. The number of grid points in this computation is 340×82. It turned out that the most efficient way to obtain the steady boundary layer was to first start with the second order scheme running at a Courant number of 120 using the implicit Euler time integration and to switch to the fifth order scheme after most of the transients are damped out. The fifth order scheme has a very low dissipation and would otherwise take a long time to converge. The maximum CFL number for which the fifth order scheme is stable is approximately 160. Ater the steady state was obtained periodic suction and blowing were added and the fifth order scheme was used with the Newton time integration scheme at a CFL of 60. Figure 4. shows a preliminary result of this computation and it clearly shows the gradual build up of the boundary layer instability. The results are currently analysed to make a comparison with the incompressible results of Fasel et al.[2].

3. Future Plans

Further testing of the code will have to be done for more complicated cases. Currently a comparison with the results of stability of a flat plate boundary layer at low Mach number with the results from Fasel et al.[2] is being completed. If this comparison and equivalent tests for high Mach number boundary layers are satisfactory a simulation of bypass transition on a subsonic flat plate boundary layer will be made, followed by simulations of a boundary layer on a curved plate. Also work has to be continued to develop higher order accurate ENO schemes for multi-dimensional flows. This is crucial for direct simulations of transonic flows with both shocks and turbulence.

4. References

1 Chakravarthy, S.R. & Osher, S., "Numerical Experiments with Osher Upwind Scheme for the Euler Equations", AIAA Journal, **21**, 1241-1248, (1983).

2 Fasel, H. F., Rist, U. and Konzelmann, U., "Numerical Investigation of the Three-Dimensional Development in Boundary-Layer Transition", AIAA Journal, **28**, 29-37, (1990).

3 Harten, A., Engquist, B., Osher, S. & Chakravarthy, S.R., "Uniformly High Order Accurate Essentially Non-Oscillatory Schemes III", Journal of Computational Physics, **71**, 231-303, (1987).

4 Koren, H., "Upwind Discretization of the Steady Navier-Stokes Equations", International Journal for Numerical Methods in Fluids, **11**, 99-117, (1990).

[5] Morkovin, M. V., "Bypass Transition to Turbulence and Research Desiderata in *"Transition in Turbines"*, NASA Conf. Publ. 2386, 161-204, (1984).

[6] Osher, S. & Solomon, F., "Upwind Difference Schemes for Hyperbolic Systems of Conservation Laws", Mathematics of Computation, **38**, 339-374, (1982).

[7] Osher, S. & Chakravarthy, S.R., "Upwind Schemes and Boundary Conditions with Applications to Euler Equations in General Geometries", Journal of Computational Physics, **50**, 447-481, (1983).

[8] Osher, S. & Chakravarthy, S.R., "Very High Order TVD Schemes", Mathematics and its Applications, **2**, 229-274, (1986).

[9] Rai, M. M., "Navier-Stokes Simulations of Blade-Vortex Interaction using High-Order Accurate Upwind Schemes", AIAA paper 87-0543, (1987).

[10] Rai, M.M. & Chakravarthy, S.R., "An Implicit Form for the Osher Upwind Scheme", AIAA Journal, **24**, 735-743, (1986).

[11] Rai, M. M. Moin, P., "Direct Numerical Simulation of Transition and Turbulence in a Spatially Evolving Boundary Layer", AIAA paper 91-1607-CP, (1991).

[12] Shu, C.-W. & Osher, S., "Efficient Implementation of Essentially Non-Oscillatory Shock-Capturing Schemes", Journal of Computational Physics, **77**, 439-471, (1988).

[13] Shu, C.-W. & Osher, S., "Efficient Implementation of Essentially Non-Oscillatory Shock Capturing Schemes, II", Journal of Computational Physics, **83**, 32-78, (1989).

[14] Sohn, K. H. and Reshotko, E., "Experimental Study of Boundary Layer Transition with Elevated Freestream Turbulence on a Heated Plate, NASA Contractor Report 187068, (1991).

[15] Turner, A. B., "Local Heat Transfer Measurements on a Gas Turbine Blade", J. of Mech. Eng. Sciences, **13**, 1-12, (1971).

[16] Van der Vegt, J. J. W., "Assessment of Flux Vector Splitting for Viscous Compressible Flows", AIAA paper 91-0243, (1991).

[17] Van der Vegt, J.J.W., "ENO-Osher Scheme for Euler Equations", submitted for publication, (1992).

[18] Vinokur, M., "An Analysis of Finite-Difference and Finite-Volume Formulations of Conservation Laws", Journal of Computational Physics, **81**, 1-52, (1989).

[19] Wang, T., Simon, T. W. and Buddhavarapu, J., "Heat Transfer and Fluid Mechanics Measurements in Transitional Boundary Layer Flows", in *"Transition in Turbines"*, NASA Conf. Publ. 2386, 69-79, (1984).

Center for Modeling of Turbulence and Transition
Research Briefs - 1991

Runge-Kutta Methods Combined with Compact Difference Schemes for the Unsteady Euler Equations

Sheng-Tao Yu

1. Motivation and Objective

Recent development using compact difference schemes to solve the Navier-Stokes equations show spectral-like accuracy[1,2]. In this paper, we report further study of the numerical characteristics of various combinations of the Runge-Kutta (RK) methods and compact difference schemes to calculate the unsteady Euler equations. Conventionally, the accuracy of finite difference schemes is assessed based on the evaluations of dissipative error. The objectives are reducing the numerical damping and, at the same time, preserving numerical stability. While this approach has tremendous success solving steady flows, numerical characteristics of unsteady calculations remain largely unclear. For unsteady flows, in addition to the dissipative errors, phase velocity and harmonic content of the numerical results are of concern. As a result of the discretization procedure, the simulated unsteady flow motions actually propagate in a dispersive numerical medium. Consequently, the dispersion characteristics of the numerical schemes which relate the phase velocity and wave number may greatly impact the numerical accuracy. The objective of the present paper is to assess the numerical accuracy of the simulated results. To this end, the Fourier analysis is performed to provide the dispersive correlations of various numerical schemes.

First, a detailed investigation of the existing RK methods is carried out. A generalized form of an N-step RK method is derived. With this generalized form, the criteria are derived for the three and four-step RK methods to be third and fourth-order time accurate for the non-linear equations, e.g., flow equations. These criteria are then applied to commonly used RK methods such as Jameson's 3-step and 4-step[3,4] schemes and Wray's algorithm[5] to identify the accuracy of the methods. For the spatial discretization, compact difference schemes are presented. The schemes are formulated in the operator-type[6] to render themselves suitable for the Fourier analyses. The results of the analyses provide CFL limits, the numerical dispersion relations, and the artificial damping required for stable and time-accurate solutions.

Finally, the performance of the numerical methods is demonstrated by numerical examples. The first case is a quasi-one-dimensional calculation of the acoustic admittance in a converging nozzle. The CFD results are compared with Tsien's analytical solution[7]; the harmonic content of this flow field is limited to one frequency mode. All numerical schemes of concern provide accurate solutions. The second case is a one-dimensional simulation of a shocked sound wave. The harmonic content is complex and distinct differences between various schemes are observed. The results are also compared with the analytical solution provided by Morse and Ingard[8]. In the one-dimensional cases, details of the numerical methods in setting up the initial conditions and the perturbation on the computational boundary are described.

The third case is a two-dimensional simulation of a Lamb vortex[9] in an uniform flow. This calculation provides a realistic assessment of various finite difference schemes in terms of the conservation of the vortex strength and the harmonic content after travelling a substantial distance. The numerical implementation of Giles' non-reflective equations[17] coupled with the characteristic equations as the boundary condition is discussed in detail. Finally, the single vortex calculation is extended to simulate vortex pairing[10]. For the distance between two vortices less than a threshold value, numerical results show crisp resolution of the vortex merging.

2. Work Accomplished

2.1 Numerical Method

The Euler equations in Cartesian coordinates can be cast into a vector form:

$$\frac{\partial \mathbf{Q}}{\partial t} + \sum_{i=1}^{3} \frac{\partial \mathbf{E}_i}{\partial x_i} = 0, \tag{1}$$

where $\mathbf{Q}$ is the unknown vector and $\mathbf{E}_i$ is the inviscid flux in the x_i direction. The Runge-Kutta algorithm is applied as the temporal discretization and the second, fourth, and sixth-order compact difference schemes are applied to the spatial discretization.

2.2.1 The Runge-Kutta Method

The use of the Runge-Kutta methods for flow equations stems from the application of the methods to solve ordinary differential equations (ODEs). An ODE has one independent variable and its solution is obtained by integrating the equation from its initial condition. When one applies the Runge-Kutta method to the flow equations, time is treated as the independent variable as is in an ODE, and the convective terms are taken as the inhomogeneous part of the equations, such as

$$\frac{\partial Q}{\partial t} = R(Q). \tag{2}$$

Notice that the boldface symbols which represent vectors have been temporarily dropped for typographic convenience. In addition, all results in the following discussion are valid for both scalar and vector equations.

The Runge-Kutta methods have algorithms of the form

$$Q^{n+1} = Q^n + \Delta t \hat{R}(Q^n, \Delta t), \tag{3}$$

where the increment function $\hat{R}(Q^n, \Delta t)$ is a suitable chosen approximation to the inhomogeneous part of the equation, that is, $R(Q)$. In general, the calculation of the increment function $\hat{R}$ is subdivided into N steps on the interval $t^n \leq t \leq t^{n+1}$. And the final increment function $\hat{R}$ is a weighted average of the inhomogeneous terms evaluated at the different steps on the interval $t^n \leq t \leq t^{n+1}$, that is

$$
\begin{aligned}
Q^1 &= Q^n + \Delta t(\alpha_{11} R^n), \\
Q^2 &= Q^n + \Delta t(\alpha_{21} R^n + \alpha_{22} R^1), \\
Q^3 &= Q^n + \Delta t(\alpha_{31} R^n + \alpha_{32} R^1 + \alpha_{33} R^2), \\
&\vdots \\
Q^{n+1} &= Q^n + \Delta t(\alpha_{N1} R^n + \alpha_{N2} R^1 + \cdots + \alpha_{NN} R^{N-1}),
\end{aligned}
\tag{4}
$$

where the superscript $n, 1, 2, \ldots,$ and $n+1$ denote the time steps on the time interval $t^n \leq t_1 \leq t_2 \leq \ldots \leq t_N \leq t^{n+1}$, and α_{ij} is the weighting factor for the step i and term j. There are $\sum_{i=1}^{N} i$ weighting coefficients to be determined and an infinite number of coefficient sets can be chosen. However, certain criteria must be met for the algorithm to retain high-order accuracy.

In what follows, the criteria of the coefficient set of a 3-step Runge-Kutta method to be third-order accurate is given. To proceed, we follow the conventional approach and expand all inhomogeneous terms R^i in Eqn. (4) to a Taylor's series about R^n and drop all terms in which the exponent of Δt is greater than 3. The result is compared with its analytical counterpart by equating terms in like powers of Δt. The result is tabulated in Table 1. For the convenience of the discussion, the following simplification of symbols is activated: R denotes $R(Q^n)$, Q denotes Q^n, R' denotes $(\partial R/\partial Q)^n$, and R'' denotes $(\partial^2 R/\partial Q^2)^n$. In addition to the equality of the coefficients of all the powers of Δt, we also want the equality of the coefficients of the functions of R, R', and R''. As a result, we find the criteria of the coefficients for the 3-step RK methods to be third-order accurate as,

$$\alpha_{31} + \alpha_{32} + \alpha_{33} = 1, \tag{5a}$$

$$\alpha_{11}\alpha_{32} + \alpha_{33}(\alpha_{21} + \alpha_{22}) = \frac{1}{2}, \tag{5b}$$

$$\alpha_{11}^2\alpha_{32} + (\alpha_{21} + \alpha_{22})^2\alpha_{33} = \frac{1}{3}, \tag{5c}$$

$$\alpha_{11}\alpha_{22}\alpha_{33} = \frac{1}{6}. \tag{5d}$$

Equations (5a) and (5b) are the criteria of first and second order accuracy, respectively. The remaining equations are of third order term. Since four equations contain six unknowns, the system is underdetermined, and two of the coefficients may be chosen arbitrarily. The obvious choice is to let the two coefficients be null to reduce intermediate storage and numerical operations. According to Eqn. (5d), none of α_{ii} where $i = 1, 2, 3$, could be zero, and one can set the two of the three remaining coefficients to be zero. Therefore, at least one of the intermediate steps has two non-zero coefficients. Consequently, one needs to store two steps of intermediate solutions for the 3-step, third-order RK methods.

A 3-step Runge-Kutta method proposed by Jameson et al.[3] to solve flow equations is

$$\begin{aligned} Q^1 &= Q^n + \Delta t R^n, \\ Q^2 &= Q^n + \frac{\Delta t}{2}(R^n + R^1), \\ Q^{n+1} &= Q^n + \frac{\Delta t}{2}(R^n + R^2). \end{aligned} \tag{6}$$

It can be shown that the weighting coefficients of the 3-step method satisfy only Eqns. (5a) and (5b). And the method is second-order accurate in time.

Wray[5] proposed another 3-step method,

$$\begin{aligned} Q^1 &= Q^n + \Delta t(\frac{8}{15}R^n), \\ Q^2 &= Q^1 + \Delta t(\frac{5}{12}R^n - \frac{17}{60}R^1), \\ Q^{n+1} &= Q^2 + \Delta t(\frac{3}{4}R^n - \frac{5}{12}R^2). \end{aligned} \tag{7}$$

This formula may be manipulated to fit the generalized form as proposed in Eqn. (4), and we obtain,

$$\begin{aligned} Q^1 &= Q^n + \Delta t(\frac{8}{15}R^n), \\ Q^2 &= Q^n + \Delta t(\frac{1}{4}R^n + \frac{5}{12}R^1), \\ Q^{n+1} &= Q^n + \Delta t(\frac{1}{4}R^n + \frac{3}{4}R^2). \end{aligned} \tag{8}$$

Wray's coefficients match all the equations in Eqn. (5) and therefore the scheme is third-order accurate. In this formula, α_{32} is set to zero and two sets of solutions are needed in the second and the third steps. The calculation can be carried out by either the vectorized algorithm proposed by Wray, or straightforward calculation according to Eqns. (7) and (8).

A similar procedure can be applied to the 4-step Runge-Kutta methods, and the criteria for the scheme to be fourth-order accurate are:

$$\alpha_{41} + \alpha_{42} + \alpha_{43} + \alpha_{44} = 1, \tag{9a}$$

$$\alpha_{11}\alpha_{42} + (\alpha_{21} + \alpha_{22})\alpha_{43} + (\alpha_{31} + \alpha_{32} + \alpha_{33})\alpha_{44} = \frac{1}{2}, \tag{9b}$$

$$\alpha_{11}^2\alpha_{42} + (\alpha_{21}+\alpha_{22})^2\alpha_{43} + (\alpha_{31}+\alpha_{32}+\alpha_{33})^2\alpha_{44} = \frac{1}{3}, \tag{9c}$$

$$\alpha_{11}\alpha_{22}\alpha_{43} + \left[\alpha_{11}\alpha_{32} + (\alpha_{21}+\alpha_{22})\alpha_{33}\right]\alpha_{44} = \frac{1}{6}, \tag{9d}$$

$$\alpha_{11}^3\alpha_{42} + (\alpha_{21}+\alpha_{22})^3\alpha_{43} + (\alpha_{31}+\alpha_{32}+\alpha_{33})^3\alpha_{44} = \frac{1}{4}, \tag{9e}$$

$$\begin{aligned} &\frac{1}{2}\alpha_{11}^2\alpha_{22}\alpha_{43} + (\alpha_{21}+\alpha_{22})\alpha_{11}\alpha_{22}\alpha_{43} \\ &+\frac{1}{2}\left[(\alpha_{21}+\alpha_{22})^2\alpha_{33} + \alpha_{11}^2\alpha_{32}\right]\alpha_{44} \\ &+(\alpha_{31}+\alpha_{32}+\alpha_{33})\left[\alpha_{11}\alpha_{32} + (\alpha_{21}+\alpha_{22})\alpha_{33}\right]\alpha_{44} = \frac{1}{6}, \end{aligned} \tag{9f}$$

$$\alpha_{11}\alpha_{22}\alpha_{33}\alpha_{44} = \frac{1}{24}. \tag{9g}$$

Equations (9a) and (9b) are for first and second-order accuracy, respectively. Equations (9c) and (9d) are for third-order accuracy. The remaining equations are for the fourth-order terms. Here, seven equations contain ten unknowns, and three of the coefficients may be chosen arbitrarily.

A 4-step RK method attributed to Kutta[11] for solving ODEs was adopted by Jameson et al.[3] to solve the flow equations. The algorithm can be expressed as,

$$\begin{aligned} Q^1 &= Q^n + \frac{\Delta t}{2}R^n, \\ Q^2 &= Q^n + \frac{\Delta t}{2}R^1, \\ Q^3 &= Q^n + \Delta t R^2, \\ Q^{n+1} &= Q^n + \frac{\Delta t}{6}(R^n + 2R^1 + 2R^2 + R^3). \end{aligned} \tag{10}$$

The coefficients satisfy Eqn. (9) and the algorithm is fourth-order accurate. However, this method requires all four intermediate solutions in the final step. As a result, the use of this scheme for large-scale calculations is undesirable.

Later on, Jameson and Baker[4] proposed another 4-step algorithm,

$$\begin{aligned} Q^1 &= Q^n + \frac{\Delta t}{4}R^n, \\ Q^2 &= Q^n + \frac{\Delta t}{3}R^1, \\ Q^3 &= Q^n + \frac{\Delta t}{2}R^2, \\ Q^{n+1} &= Q^n + \Delta t R^3. \end{aligned} \tag{11}$$

This scheme was proposed to calculate the steady state solutions and the transient solutions were not of concern. For that purpose, the algorithm is convenient to program and no intermediate solution needs to be stored. For the present investigation, however, the weighting coefficients of this method satisfy only part of Eqn. (9) and the algorithm is second-order accurate. Nevertheless, this formulation is favorable compared to a 2-step, second-order RK method because part of the third and fourth-order terms are satisfied, namely, Eqns. (9d) and (9g). Consequently, a larger marching step, i.e., a larger CFL number, could be used.

2.2.2 Compact Difference Schemes

The remaining task of discretizing the flow equations is the spatial differencing of the inviscid fluxes. An effective manner for generating a high-order, central difference scheme is the compact difference method. The scheme is obtained by using only three and five points to achieve fourth-order and sixth-order accuracy in space, respectively. The gain in the accuracy is not based on the involvement of more points as in the conventional approach, but on implicitly solving the derivatives simultaneously at all locations. According to Hermite's generalization of a Taylor's series,[12] one can get

$$u'_{i-1} + 4u'_i + u'_{i+1} = \frac{3}{\Delta x}(u_{i+1} - u_{i-1}) + O(\Delta x^4), \tag{12}$$

$$u'_{i-1} + 3u'_i + u'_{i+1} = \frac{1}{12\Delta x}(u_{i+2} + 28u_{i+1} - 28u_{i-1} - u_{i-2}) + O(\Delta x^6), \tag{13}$$

where the superscript $'$ represents the spatial derivatives. Equation (12) is the fourth-order method and Eqn. (13) is the sixth-order one. When the fourth-order method is used in the interior nodes, a third-order biased implicit scheme[13] is adopted for grid nodes at the computational boundary, such as

$$\begin{aligned} 2u'_1 + 4u'_2 &= \frac{1}{\Delta x}(-5u_1 + 4u_2 + u_3) + O(\Delta x^3), \\ 2u'_{max} + 4u'_{max-1} &= \frac{1}{\Delta x}(5u_{max} - 4u_{max-1} - u_{max-2}) + O(\Delta x^3). \end{aligned} \tag{14}$$

When the sixth-order method is used in the interior nodes, the fourth-order scheme, Eqn. (12), is used at locations one grid node away from the boundary and the third-order biased scheme is used at the boundary. The application of the implicit compact difference schemes with the appropriate boundary conditions involves the inversion of a scalar tridiagonal matrix. The inversion of the matrix incurs little penalty in terms of CPU time.

2.3 Fourier Analysis

By definition, any function, $u(x,t)$, which is continuous, periodic, and square summable can be expressed in a Fourier series expansion at a constant time,

$$u(x,t) = \sum_{k=-\infty}^{\infty} \hat{u}(k,t)e^{i2\pi kx/L} \tag{15}$$

where L is the period of the function $u(x,t)$, k is the wave number, and i is $\sqrt{-1}$. The Fourier coefficient is defined as,

$$\hat{u}(k,t) = \frac{1}{L}\int_{-L/2}^{L/2} u(x,t)e^{-i2\pi kx/L}dx. \tag{16}$$

In the Fourier analysis of a finite difference scheme, functions are defined at discrete points. The discrete Fourier series and its coefficients are defined analogous to their continuous counterparts,

$$\begin{aligned} u_j^n &= \sum_{k=0}^{K-1} \hat{u}^n(k)e^{i2\pi kj/K}, \quad j = 0, \pm 1, \pm 2, \cdots, \pm\infty, \\ \hat{u}^n(k) &= \frac{1}{K}\sum_{j=1}^{K} u_j^n e^{-i2\pi kj/K}, \quad k = 0, 1, \cdots, K-1. \end{aligned} \tag{17}$$

Here, the length of the computational domain L is decomposed into K grid nodes ($L = K\Delta x$). The superscript n denotes the time step and the subscript j is the spatial location index. Similar to the continuous function, the algebraic system in terms of the function $exp(i2\pi kj/K)$ is periodic over the computational domain L (or K) and orthonormal, such as

$$\begin{aligned} &e^{i2\pi kj/K} = e^{i2\pi k(j+K)/K} \\ &\frac{1}{K}\sum_{j=0}^{K-1} e^{i2\pi k_1 j/K}e^{-i2\pi k_2 j/K} = \delta_{k_1 k_2} \end{aligned} \tag{18}$$

where $\delta_{k_1 k_2}$ is the Kronecker delta. Therefore, the establishment of the discrete Fourier series and coefficients is self-sufficient, and is not an approximation of its continuous counterpart.

As shown in Eqns. (17) and (18), the harmonic content of the discretized equation is limited to the number of grid nodes used in the computational domain. A discrete solution u_j^n at a location (j) and time (n) is a linear combination of K wave modes. The Fourier analysis is performed by substituting each wave mode of the discrete Fourier expansion, Eqn. (17), into the discretized flow equations to calculate the amplification factor, $g(k)$, which is defined as

$$g(k) = \frac{\hat{u}^{n+1}(k)}{\hat{u}^n(k)}. \tag{19}$$

The procedure is repeated for all wave modes ($k = 0, 1, \cdots, K-1$) and the full spectrum of the amplification factor is obtained. In this process, we map the function u in terms of spatial variable x on the interval $[-L/2, L/2]$ to the wave number space on $[-\pi, \pi]$ assuming that the analysis is local for an infinite and periodic domain. Therefore, the solution of the amplification factor on the interval $[-\pi, 0]$ is the complex conjugate of that on $[0,\pi]$. For this reason, the results of our Fourier analyses are presented on the interval $[0,\pi]$.

In the present investigation, one-dimensional equations are considered for the Fourier analysis. In addition, we can perform a similarity transformation to transform the one-dimensional Euler equations to their characteristic form, i.e., three decoupled scalar equations. Consequently, a scalar, advective equation on a periodic domain is adopted as the model equation in our analysis,

$$\frac{\partial u}{\partial t} + \lambda \frac{\partial u}{\partial x} = 0, \tag{20}$$

where the phase velocity (λ) is equivalent to the eigenvalues of the Euler equations, namely $u - c$, $u + c$, and u where u is velocity and c is the speed of sound. The phase speed (λ) is treated as a parameter in the Fourier analysis to avoid the Fourier convolution, therefore the analysis is linear. For the unsteady calculations, the requirement of the time resolution of the flow field restricts the time marching step. In other words, the variations of flow properties between time steps are small. Thus, linear analysis is a viable tool.

In what follows, the procedure to obtain the amplification factor of the model equation discretized by Runge-Kutta methods and compact differences is illustrated. First, the generalized forms of the amplification factor for the 3 and 4-step Runge-Kutta methods are derived. These representations of the amplification factors are independent of the spatial discretization schemes. From the equations of Wray's 3-step scheme, Eqn.(7), we have

$$\begin{aligned} g^1 &= 1 + \frac{8}{15} Z, \\ g^2 &= 1 + \frac{1}{4} Z + \frac{5}{12} Z g^1, \\ g &= 1 + \frac{1}{4} Z + \frac{3}{4} Z g^2, \end{aligned} \tag{21}$$

where

$$\begin{aligned} g^1 Q^n &= Q^1, \\ g^2 Q^n &= Q^2, \\ g Q^n &= Q^{n+1}. \end{aligned} \tag{22}$$

The variable Z represents the spatial discretization applied to the convective term ($-\lambda \partial u / \partial x$). By substituting the amplification factors of the intermediate steps, g^1 and g^2, into the last step of Wray's algorithm, we obtain the amplification factor, g, for the 3-step scheme,

$$g = 1 + Z + \frac{1}{2} Z^2 + \frac{1}{6} Z^3. \tag{23}$$

It is interesting to note that Eqn. (23) can be directly derived from the Taylor's series expansion by adopting the invariance property of the time and spatial derivatives of the model equation, i.e., $Z = -\lambda \partial u/\partial x = \partial u/\partial t$. This is valid because the coefficients satisfy Eqn. (5), which is deduced from the Taylor's series expansion up to the third-order term. On the other hand, the amplification factor of the 3-step scheme proposed by Jameson et al., Eqn. (6), can be derived as

$$g = 1 + Z + \frac{1}{2}Z^2 + \frac{1}{4}Z^3. \tag{24}$$

It is obvious that the scheme is not third-order accurate.

A similar analysis can be applied to the 4-step methods. Identical forms of the amplification factors of both 4-step methods of concern (Eqns. (10) and (11)) are obtained, such as

$$g = 1 + Z + \frac{1}{2}Z^2 + \frac{1}{6}Z^3 + \frac{1}{24}Z^4. \tag{25}$$

Unlike the case of the 3-step schemes, the effect of the order of accuracy of these two 4-step schemes does not appear in the expression of the amplification factor. This is because the amplification factor is derived based on the linearized equation. Only by using Eqns. (5) and (9), which take into account nonlinear terms, can one justify the order of the accuracy of the RK schemes.

The remaining task is to derive the explicit form of the spatial discretization operation, Z, of compact difference schemes. The fourth-order compact difference method, Eqn. (12), can be cast into the operator-type by defining

$$\delta^2 u_i = u_{i+1} - 2u_i + u_{i-1}, \tag{26}$$

where u_i could be any flow property of interest at grid point i. As a result, the fourth-order method can be rewritten as,

$$\left(1 + \frac{\delta^2}{6}\right)\left(\frac{\partial u}{\partial x}\right)_i = \frac{1}{2\Delta x}\left(u_{i+1} - u_{i-1}\right) + O(\Delta x^4). \tag{27}$$

This equation allows us to express $(\partial u/\partial x)_i$ in an explicit form,

$$\left(\frac{\partial u}{\partial x}\right)_x = \left(1 + \frac{\delta^2}{6}\right)^{-1}\left(\frac{u_{i+1} - u_{i-1}}{2\Delta x}\right) + O(\Delta x^4). \tag{28}$$

To proceed, we substitute this explicit, discretized form, Eqn. (32), into the model equation, and we obtain

$$Z^{(4)} = -\frac{6F sin(\hat{k})i}{4 + 2cos(\hat{k})}, \tag{29}$$

where F is the CFL number which is defined as $F = \lambda\Delta t/\Delta x$, and $\hat{k}$ is the normalized wave number ($\hat{k} = 2\pi k/K$) .

It is interesting to note that if the solution reaches a steady state solution, i.e., the time derivative term is zero, the operator $(1+\delta^2/6)^{-1}$ in the discretized equation becomes futile and the spatial discretization is represented by $(u_{i+1}-u_{i-1})/2\Delta x$, which is only second-order accurate. However, the steady state solution of the one-dimensional wave equation is a constant and the spatial accuracy is meaningless. On the other hand, the accuracy of multi-dimensional calculations is more complex. For example, consider a two-dimensional version of the model equation discretized by the fourth-order compact difference method, and we have

$$\frac{\partial u}{\partial t} + \lambda_x \left(1+\frac{\delta_x^2}{6}\right)^{-1}\left(\frac{u_{i+1,j}-u_{i-1,j}}{2\Delta x}\right) + \lambda_y \left(1+\frac{\delta_y^2}{6}\right)^{-1}\left(\frac{u_{i,j+1}-u_{i,j-1}}{2\Delta y}\right) = 0. \tag{30}$$

Again, the operators $(1+\delta_x^2/6)$ and $(1+\delta_y^2/6)$ are scalar tridiagonal matrices with the dimensions $IL \times IL$ and $JL \times JL$, respectively. IL and JL are the numbers of the grid nodes in the x and y directions of the computational domain. When $IL = JL$, two operators are identical. We then multiply Eqn. (30) by the operator $(1+\delta_x^2/6)$ and obtain the steady state equation as

$$\lambda_x \frac{u_{i+1,j}-u_{i-1,j}}{2\Delta x} + \lambda_y \frac{u_{i,j+1}-u_{i,j-1}}{2\Delta y} = 0. \tag{31}$$

Therefore, the steady state solution is only second-order accurate.

Similarly, the spatial discretization of the sixth-order compact difference scheme can be represented in the operator-type such as,

$$\frac{\partial u}{\partial x} = \left(1+\frac{\delta^2}{5}\right)^{-1}\frac{1}{60\Delta x}\left(u_{i+2}+28u_{i+1}-28u_{i-1}-u_{i-2}\right) + O(\Delta x^6). \tag{32}$$

And we obtain,

$$Z^{(6)} = -\frac{F[4\sin(\hat{k})\cos(\hat{k}) + 56\sin(\hat{k})]i}{12[2\cos(\hat{k})+3]}. \tag{33}$$

Again, when solving the steady state solution with same number of grid nodes in each direction of the computational domain, the spatial discretization is represented by $(u_{i+2}+28u_{i+1}-28u_{i-1}-u_{i-2})/60\Delta x$. Unlike the case of the fourth-order scheme, this representation does not match any conventional central difference scheme and it is at most second-order accurate.

According to the above discussion, we can obtain the amplification factor $g(\hat{k})$ for various combinations of the Runge-Kutta methods and compact difference schemes. The amplification factor $g(\hat{k})$ is a complex number and can be expressed as $g(\hat{k}) =$

$exp[i\hat{\omega}(\hat{k})]$, where $\hat{\omega}$ is the normalized frequency and is defined as $\hat{\omega} = 2\pi\omega\Delta t/\tau$, ω is the frequency, τ is the the time period of function u_j^n, and the phase speed (λ) is equal to L/τ. Here, the dissipative and dispersive artifacts of the numerical schemes can be assessed:

1. Dissipation. The normalized frequency $\hat{\omega}$ is a complex number ($\hat{\omega} = \alpha + i\beta$) and its imaginary part represents the magnitude of the amplification factor, i.e.,

$$
\begin{aligned}
g(\hat{k}) &= e^{i\hat{\omega}} = e^{-\beta}e^{i\alpha} \\
|g(\hat{k})| &= e^{-\beta}
\end{aligned}
\tag{34}
$$

   The magnitude of the amplification factor is the artificial dissipation. When $|g| \geq 1$, the scheme is unstable. For the calculations of unsteady flows, we want $|g|$ to be less than unity but very close to it to ensure numerical stability with minimum artificial dissipation. In the following section, we plot $|g|$ against $\hat{k}$ to illustrate the artificial dissipation.

2. Dispersion. According to Eqn. (34), the relation of $\alpha(\hat{k})$ and $\hat{k}$ represents the artificial dispersion. We plot $\hat{\alpha} = \alpha/F$ against $\hat{k}$ to show phase velocities. Notice that the model equation is dispersionless and the phase velocity is a constant, i.e., λ. After being normalized by the CFL number, the exact solution is a straight line with 45^o angle on the plot of $\hat{\alpha}$ against $\hat{k}$.

Figure 1 shows the results of the Fourier analysis of the third-order Runge-Kutta (RK3) method combined with fourth (CD4), and sixth (CD6) order compact difference schemes and the conventional second-order central difference scheme (CD2). The figures show the dissipative as well as dispersive effects at CFL numbers from 0.4 to 1.4 with an increment of 0.2 between neighboring curves. Figure 1a shows the dissipation of the RK3-CD6 scheme. The method is unstable for CFL numbers greater than 0.8. As the order of spatial differencing decreases (compare Figs. 1a, 1c, and 1e), the limit of the CFL number increases for stable calculation.

Figure 1b shows the dispersive effect of the RK3-CD6 scheme. For a CFL number of 0.4, the phase velocity is correct for wave numbers up to 1.8. The phase velocities are slower than they should be at large wave numbers. Increasing the CFL number makes phase velocities deviate from the 45^o straight line at smaller wave numbers. Decreasing the CFL number merges the curves together to reach an asymptotic curve. However, the dispersive effect at high wave numbers does not improve. Comparing Figs. 1b, 1d, and 1f shows that the increase of the order of the spatial differencing reduces the numerical dispersion at high wave numbers. Specifically, a significant improvement is achieved by changing the spatial differencing from CD2 to CD4, whereas only a limited gain is obtained by switching from CD4 to CD6.

Figure 2 shows the results of the Fourier analyses of the fourth-order Runge-Kutta (RK4) method combined with various central difference schemes. The CFL numbers are the same as that in Fig. 1. Similar to the case of RK3, for the same CFL number and wave number, e.g., CFL = 1.4, $\hat{\omega} = 1.5$, higher-order spatial discretization introduces more artificial damping (see Figs. 2a, 2c, and 2e) and therefore reduces the CFL number limit for stable calculation. Again, the dispersive error at high wave numbers decreases as the order of the spatial differencing increases (see Figs. 2b, 2d, and 2f).

Figures. 1c and 2c can be compared to show the difference of the dissipation effects between the RK3 and RK4 methods. For the same CFL and wave numbers, the RK4 method introduces more artificial damping, and a larger CFL number could be used. On the other hand, Figs. 1d and 2d show that an increase of the order of the time marching scheme does not improve the dispersive effect at high wave numbers.

From the above discussion, it is clear that reliable solutions of the finite difference schemes are at low wave numbers. For example, for the RK4-CD6 method at CFL = 0.8 (see Figs. 2a and 2b) the solution with wave numbers less than $1/3\pi$ (6 grid nodes per wave) is fairly accurate. Numerical solutions with higher wave numbers (wave length less than 6 grid nodes) suffer significant dispersive and dissipative errors. On the other hand, for the conventional RK4-CD2 method at the same CFL, 12 to 16 grid nodes per wave are needed for an accurate solution.

It is interesting to note that compact difference schemes have no dissipative effect at the highest wave number resolved by a given numerical grid, i.e., two grid nodes per wave (see Figs. 1a, 1c, 1e, 2a, 2c, and 2e). Nevertheless, a significant dispersive error is introduced to these highest-wave-number waves and cause the even-odd decoupling of the numerical solutions. Furthermore, applying the compact difference scheme twice to calculate the viscous terms of the Navier Stokes equations does not eliminate the erroneous oscillation, owing to the linearity of the operation. These high-wave-number waves continue oscillating with erroneous phase speeds throughout the course of computation and eventually destroy the solution. It is therefore appropriate to impose a small amount of high-order artificial damping to filter out these waves while at the same time keeping the resolution at low wave modes intact. Figure 3 shows the dissipation and dispersion effects of the RK4-CD6 method at CFL=0.8 with various amounts of sixth-order artificial damping, defined as

$$\text{A.D.} = \frac{\eta}{8}[u_{i+3} + u_{i-3} - 6(u_{i+2} + u_{i-2}) + 15(u_{i+3} + u_{i-3}) - 20u_i]. \qquad (35)$$

The range of η is from 0.01 to 0.05 with an increment of 0.01 between the neighboring curves. Comparison between Fig. 3 and Figs. 2a and 2b shows that no additional damping at low wave numbers is introduced into the system by the imposed artificial dissipation for $\eta \leq 0.03$, whereas the undesirable high-wave-number waves are dissipated.

2.4 Numerical Examples

2.4.1 Acoustic Admittance of A Nozzle Flow

The first case is a forced oscillatory quasi-one-dimensional flow in a converging nozzle. The governing equations are

$$\frac{\partial \mathbf{Q}}{\partial t} + \frac{\partial \mathbf{E}}{\partial x} = \mathbf{H} \tag{36}$$

where

$$\mathbf{Q} = \begin{pmatrix} \rho \\ \rho u \\ e \end{pmatrix} a, \quad \mathbf{E} = \begin{pmatrix} \rho u \\ \rho u^2 + p \\ (e+p)u \end{pmatrix} a, \quad \mathbf{H} = \begin{pmatrix} 0 \\ p\frac{da}{dx} \\ 0 \end{pmatrix}, \tag{37}$$

ρ is density, p is pressure, and e is the total energy defined as $e = \rho(C_v T + \frac{1}{2}u^2)$. C_v is the constant volume specific heat. The variable a is the cross sectional area and is prescribed as a function of x. The theoretical solution of the acoustic admittance of a choked nozzle was provided by Tsien[7] under the assumption that the velocity of the base flow is a linear function of axial location as shown in Fig. 4. The nozzle shape can be inversely derived according to Tsien's assumption, and we have

$$a = \frac{1}{M}\left(\frac{2}{\gamma+1} + \frac{\gamma-1}{\gamma+1}M^2\right)^{\frac{\gamma+1}{2(\gamma-1)}}, \tag{38}$$

where γ is the specific heat ratio and M is the Mach number which can be expressed as

$$M = \frac{x}{x^*}\sqrt{\frac{\gamma+1}{2} - \frac{\gamma-1}{2}\left(\frac{x}{x^*}\right)^2}. \tag{39}$$

The superscript $*$ denotes the property at the nozzle throat. According to Tsien's derivation, the linearized quasi-one-dimensional equations can be manipulated to the following form under the isentropic condition,

$$z(1-z)\frac{d^2P}{dz^2} - 2\left(1 + \frac{i\beta}{1+\gamma}\right) z\frac{dP}{dz} - i\beta\frac{(2+i\beta)}{2(\gamma+1)}P = 0 \tag{40}$$

$$(\gamma+1)(1-z)\frac{dP}{dz} - (\gamma - 1 + i\beta)P + (2+i\beta)U = 0 \tag{41}$$

where

$$\begin{aligned} \frac{p'}{\gamma\bar{p}} &= P(z)e^{i\beta\tau}, \\ \frac{u'}{\bar{u}} &= U(z)e^{i\beta\tau}. \end{aligned} \tag{42}$$

$\bar{u}$ and $\bar{p}$ are the velocity and pressure of the base flow, β is the normalized frequency which is defined as $\beta = \omega(1-z)/(\bar{c}^* - \bar{u})$, and τ is the non-dimensionalized time which is defined as $\tau = \bar{c}^* t/x^*$. The independent variable z can be expressed in different forms due to the linearity between the base flow velocity $\bar{u}$ and axial location x, and we have

$$z = \frac{x}{x^*} = \frac{\bar{u}}{c^*} = \frac{(\gamma+1)M^2}{2+(\gamma-1)M^2} \tag{43}$$

With Eqn. (43), it is clear that P and U are functions of the Mach number (M) with prescribed frequency (β). Equation (40) is a hypergeometric equation[14] that can be solved by a power series expansion. The converged solution does not exist in the supersonic region because the Mach number is greater than unity. $U(z)$ can be easily solved with $P(z)$ known as shown in Eqn. (41). Finally, the acoustic admittance function defined as $A(z) = U(z)/P(z)$ can be obtained as a function of the Mach number.

In what follows, the procedure of the CFD calculation to compare with Tsien's solution is illustrated. First, the base flow field is obtained by solving the quasi-one-dimensional equations, Eqns. (36) and (37), using the RK4-CD2 method with the nozzle area ratio prescribed by Eqns. (38) and (39). The results are checked by the area Mach number relation[15] and the solution is accurate up to five decimal digits. The perturbation at the inlet is obtained by specifying sinusoidal pressure fluctuations in terms of magnitude and frequency. With the prescribed pressure and isentropic correlation, the temperature fluctuation is also determined. Numerically, these boundary conditions are enforced by defining a vector $\mathbf{k} = \mathbf{k}(\mathbf{Q})$ at the upstream boundary, such as

$$\mathbf{k} = \begin{pmatrix} p \\ T \\ 0 \end{pmatrix} = \begin{pmatrix} \xi_1 \\ \xi_2 \\ 0 \end{pmatrix}, \tag{44}$$

where ξ_1 and ξ_2 are the specified values of p and T. To proceed, Equation (44) is linearized to become a function of $\Delta\mathbf{Q}$, such as

$$\mathbf{k^{n+1}} = \mathbf{k}^n + \frac{\partial \mathbf{k}}{\partial \mathbf{Q}}\Delta\mathbf{Q}, \tag{45}$$

where $\mathbf{k^{n+1}}$ is equal to the specified pressure and temperature at the time step $n+1$ and $\partial\mathbf{k}/\partial\mathbf{Q}$ is a 3×3 matrix. In order to close the system, the null entry in the vector $\mathbf{k}$ may be filled by the out-running characteristic relation deduced from the flow equations. Numerically, the similarity transformation is applied to the discretized flow equations (see Eqn. (4)), and we get

$$\mathbf{LM}^{-1}(\mathbf{Q}^i - \mathbf{Q}^n) = \mathbf{LM}^{-1}\Delta t \sum_{k=1}^{i} \alpha_{ik}\mathbf{R}^{k-1}, \quad i = 1, \cdots, N \tag{46}$$

where $i = 1, \cdots, N$ represents the N-step RK method. Here, $\mathbf{M}^{-1}$ is the eigenvector matrix of Jacobian matrix $\mathbf{A} = \partial\mathbf{E}/\partial\mathbf{Q}$, and $\mathbf{L}$ is a selection matrix with zeros and ones on the diagonal in such a fashion that the proper outrunning characteristics are selected. By combining the imposed conditions, Eqn. (45), with the outrunning characteristic relations, Eqn.(46), we form the complete equation at the boundary point as,

$$\left(\mathbf{LM}^{-1} + \frac{\partial\mathbf{k}}{\partial\mathbf{Q}}\right)\left(\mathbf{Q}^i - \mathbf{Q}^n\right) = \mathbf{LM}^{-1}\Delta t\sum_{k=1}^{i}\alpha_{ik}\mathbf{R}^{k-1} + \mathbf{k}^{n+1} - \mathbf{k}^n, \qquad (47)$$
$$i = 1, \cdots, N$$

For the supersonic out-flow condition, Eqn. (46) is used with the selection matrix $\mathbf{L}$ equal to an identity matrix. In both cases, the out-running characteristic equations are solved with one-sided difference as shown in Eqn. (14). In other words, the characteristic boundary conditions are always discretized by an upwinding scheme which is physically sound and the numerical stability is enhanced. These boundary conditions are applied at each of the Runge-Kutta stages.

The acoustic admittance is a complex number and can be written as $A = |A|e^{i\theta}$. In the present paper, a small pressure perturbation of 1.1% ($p' = 0.011\bar{p}$) is imposed at the nozzle inlet. The length of the converging part of the nozzle is 0.9 L^* (see Fig. 4) and the inlet Mach number is about 0.09. The frequency of the perturbation is set at $\beta = 6$, which corresponds to about 2000 Hz.

Figure 5 shows the comparisons between the CFD results of the RK4-CD6 method and the theoretical solution of the acoustic admittance in terms of the magnitude $|A|$ and the phase angle θ in the subsonic region of the nozzle. Both the magnitude and the phase angle of the acoustic admittance decrease as the flow speeds up. As shown in the figure, perfect agreement is obtained for the comparison of $|A|$, while the predicted phase angle is slightly off due to the resolution of the numerical grid for the phase angle. In this case, the harmonic content of the solution is limited to one frequency with a wave length comparable to the computational domain which is resolved by 61 grid nodes. Therefore, all numerical schemes of concern provide accurate solutions. The numerical errors of $|A|$ and θ are tabulated in Table 2. There is slight advantage in using the higher-order schemes for the prediction of $|A|$; however, no obvious advantage of using the higher-order scheme for the phase angle calculation is observed.

2.4.2 Shocked Sound Waves

The second case is the propagation of shocked sound waves in a tube with a periodic boundary condition. The governing equations are the same as in the first case, namely, Eqns. (36) and (37), with cross section area (a) equal to a constant. This case is interesting for its complex harmonic content compared to the first case. In addition, the capability of the high-order compact difference schemes for shock capturing can also be studied. At time equal to zero, a sinusoidal pressure distribution is given. Because of the periodic boundary condition, only one cycle resolved by 61 grid nodes is imposed in the computational domain. According to the isentropic condition, the distributions of temperature, density, and speed of sound are also determined. The velocity profile is determined by the simple wave correlation[16], such as

$$\begin{aligned} u(x) &= \int_{\bar{p}}^{p(x)} \frac{dp}{\rho(x)c(x)}, \\ &= \frac{2\gamma}{\gamma-1}\sqrt{\frac{\bar{p}^{\frac{1}{\gamma}}}{\gamma\bar{\rho}}}\left(p(x)^{\frac{\gamma-1}{2\gamma}} - \bar{p}^{\frac{\gamma-1}{2\gamma}}\right), \end{aligned} \tag{48}$$

where the average flow properties are denoted by a bar. With the simple wave correlation, the wave forms of all flow properties are in phase and the initial condition of the present CFD computation matches the theoretical analysis provided by Morse and Ingard[8]. It is interesting to note that the simple wave correlation is an extension of a linear, plane, acoustic wave. For a variation of pressure less than 5%, the plane wave relations could be adopted, such as

$$\begin{aligned} T(x) &= \bar{T}\left(1 + \frac{\gamma-1}{\gamma}\frac{p'(x)}{\bar{p}}\right), \\ \rho(x) &= \bar{\rho}\left(1 + \frac{p'(x)}{\gamma\bar{p}}\right), \\ u(x) &= c(x)\frac{p'(x)}{\gamma\bar{p}}, \end{aligned} \tag{49}$$

where $p'(x)$ is the prescribed pressure fluctuation. As shown in Eqns. (48) and (49), the wave speeds $u+c$, $u-c$ and u vary as a result of the flow property distribution. The distortion of the wave form is a cumulative effect resulting from the wave speed distribution. For simple waves, i.e., all flow properties are in phase, the wave crest will quickly overtake the trough and form a shock.

Figure 6 shows the time history of the pressure fluctuation at one end of the computational domain for various finite difference schemes. According to Morse and Ingard, the first shock appears after about two cycles for the case of a 10% pressure perturbation ($p'/\bar{p} = 0.1$)[8]. All schemes of concern predict the wave steepening rate correctly. After the wave shocked, the flow evolution is no longer isentropic and the kinetic energy is gradually converted to thermal energy due to the existence of the shock wave. As a result, the strength of the shock wave diminishes as time passes.

The shock front is a combination of many wave modes travelling at the same speed. The dispersion error introduced by the finite difference schemes will cause the high-wave-number waves to travel with erroneous speeds. As shown in Fig. 6, the methods of RK4-CD6 and RK4-CD4 with a small amount of the sixth-order artificial damping ($\eta = 0.02$) crisply resolve the shock except for the over-shoots.

These over-shoots are caused by the Gibbs phenomenon and can be fixed only by TVD type shock-capturing schemes. Almost no difference can be observed between the results of the CD4 and CD6 methods. On the other hand, the method of RK4-CD6 without background filtering shows that significant high-wave-number waves lag behind the shock front because the compact difference scheme introduces no dissipative but high dispersive effects on the highest wave number waves. As shown in the figure, these oscillations eventually contaminate the whole solution. For the conventional RK4-CD2 method, results show significant oscillations of moderate wave numbers behind the shock front because of dispersion errors.

Figure 7 shows the normalized power spectrums of the pressure profiles after about 17 cycles calculated by different methods. The analytical solution is plotted as the solid line. The power of each wave mode is roughly inversely proportional to the square of the wave number ($\propto 1/n^2$). Since 61 grid nodes are used, only 30 Fourier modes are resolved for the power spectrum (the other 30 modes are the complex conjugates). Clearly, the method of RK4-CD2 has significant errors in low wave modes. On the other hand, the methods of RK4-CD4 and RK4-CD6 compare well with the analytical solution.

2.4.3 Vortex Propagation in an Uniform Flow

A Lamb vortex propagated in an uniform flow is chosen as a two-dimensional numerical example. The vortex can be characterized by the circulation Γ and the core radius a. The azimuthal velocity u_θ at a distance r from the vortex center is given as,

$$u_\theta = \frac{\Gamma}{2\pi} \frac{r}{r^2 + a^2}, \tag{50}$$

The flow near the vortex center is a rigid-body rotation ($u_\theta \propto r$). The flow far outside the core is irrotational ($u_\theta \propto 1/r$) with u_θ decreasing as r increases. Eqn. (50) is a continuous function to connect the two extremes. With the prescribed velocity field, the pressure and density distributions of the vortex can be determined by the momentum and the energy equations,

$$\frac{\partial p}{\partial r} = \rho \frac{u_\theta^2}{r}, \tag{51}$$

$$\frac{\gamma}{\gamma - 1} \frac{p}{\rho} + \frac{u_\theta^2}{2} = h_o, \tag{52}$$

where h_o is the total enthalpy and is set to be a constant such as $h_o = \gamma \bar{p}/(\gamma - 1)\bar{\rho}$ with the free stream condition denoted by a bar. To proceed, substitute Eqns. (50) and (52) into Eqn. (51) and integrate the equation over r. As a result, the pressure distribution is obtained. Consequently, the density distribution and the whole flow field is determined. The solutions of this stationary vortex can be superimposed to any uniform flow with arbitrary speed. Physically, this process may be interpreted as a stationary vortex being observed from a moving coordinate system with constant velocity. Thus, the vortex in an uniform flow can be constructed as,

$$u = \bar{u} + u',$$
$$v = \bar{v} + v', \tag{53}$$

where the velocities of the background flow are denoted by a bar and the superscript $'$ denotes the vortex velocities specified by Eqn. (50). The pressure and density distribution of the moving vortex is the same as that of the stationary vortex and may be obtained from the solutions of Eqns. (51) and (52).

The boundary condition of the present case is an extension of the characteristic type treatment discussed in Case 1. Essentially, only one-dimensional characteristics (derived from two-dimensional flow equations) normal to the computational boundary are considered. For the purposes of this discussion, the subsonic out-flow condition is considered. The coupled equations of three out-running characteristics and one specified boundary condition, similar to that in Eqn. (47), should be solved. For steady state calculations, a back pressure (p_b) is specified to regulate the flow rate, such as

$$\mathbf{k} = \begin{pmatrix} 0 \\ 0 \\ 0 \\ p_b \end{pmatrix} \tag{54}$$

Similarly, the dimension of vectors $\mathbf{Q}$ and $\mathbf{R}$ is four and the matrix $\mathbf{M}^{-1}$ is a 4×4 eigenvector matrix for the flux vector normal to the computational boundary.

For a non-reflective boundary condition, Giles' formulation[17] instead of the back pressure is used to fill the entry for the specified boundary condition, such as

$$\frac{\partial c_4}{\partial t} + (0, u, 0, v)\frac{\partial}{\partial y}\begin{pmatrix} c_1 \\ c_2 \\ c_3 \\ c_4 \end{pmatrix} = 0 \tag{55}$$

where y is in the direction parallel to the computational boundary. The variables $c_i, i = 1, \cdots, 4$ are the characteristic variables and can be obtained by the similarity transformation from the non-conservative form equations as illustrated by Giles. In our case, the characteristic variables are derived from the conservative-form equations using the same eigenvector matrix $\mathbf{M}^{-1}$ as in the aforementioned discussion. Giles' non-reflective formulation, Eqn. (55), is relatively simple to used with an existing one-dimensional characteristic boundary condition. Nonetheless, according to Giles' analysis, some two-dimensional effect is considered in the equation. Numerically, Eqn. (55) may be discretized according to the finite difference scheme of the interior nodes and combined with the discretized out-running characteristic equations (the two-dimensional version of Eqn. (46)) to form the complete subsonic out-flow boundary condition. It is interesting to note, however, according to Huff's study[18] and our experience, that stretching the numerical grid nodes downstream to dampen the outgoing unsteady waves is just as effective.

For the in-flow conditions, the characteristic-type treatment combined with Giles' equation (different from Eqn. (55)) may be adopted. For the present calculations, however, the upstream condition is relatively insensitive to various forms of non-reflective treatment as long as the proper out-running characteristic equation is selected and solved with the prescribed incoming conditions similar to that in Eqn. (47). In the present case, constant total pressure and total temperature are prescribed as the forcing boundary conditions upstream.

As in the one-dimensional cases, dissipative and dispersive effects of various schemes are assessed. The prescribed vortex flow field contains a broad band of frequencies due to the distribution of the azimuthal velocity. Theoretically, all wave modes travels at the same speed to ensure the integrity of the vortex structure. For numerical methods with dispersive error, the shape of the vortex could deform, even break up in the later stage of the time marching procedure. In addition, the dissipation effect of finite difference schemes can be evaluated by the conservation of the sharp pressure dip at the center of the vortex propagated in the numerical grid.

In the present calculations, the Mach number of the background flow is 0.4. The grid size is 301×91 in the streamwise and transverse directions, respectively. Uniform grids are used in the axial direction and the transverse grids are stretched near the outside boundary. The CFL number calculated based on the background flow is about 0.7 for all calculations. As discussed before, a small amount of background filtering ($\eta = 0.02$) is applied for all calculations. The core radius (a) is about 1 cm and is resolved by about 4 grid nodes.

Figure 8 shows the vorticity and Mach number contours of the initial condition prescribed by Eqns. (50) - (53). Figure 9 shows the contours after the eddy propagates about 60 core radii downstream as simulated by various numerical schemes. The comparison between Fig. 8 and Fig. 9 shows that the structure of the eddy is retained by the compact difference schemes (CD4 and CD6). In contrast, the eddy predicted by the second-order central difference is shattered due to the excessive dispersive error.

Figure 10 shows pressure distributions of the eddy at various instances. In this figure, the x axis represents the streamwise locations non-dimensionalized by the core radius of the vortex and the y axis is the pressure. For both CD4 and CD6 methods, the pressure at the vortex center increases about 1 % through the process. In comparison, the results of the second-order scheme show pressure fluctuations with an overall increase about 3 %. The pressure fluctuation predicted by the second-order scheme is due to the deviation of the vortex path.

2.4.4 Vortex Pairing

Finally, the calculation of the single vortex is extended to the simulation of the vortex pairing. The vortex pairing is the controlling mechanism for the growth of the mixing layer[10]. In theory, vortex pairing occurs when the distance between two vortices is less than a threshold value. Unfortunately, no theoretical analysis is available for compressible flows. In the present paper, the RK4-CD6 method is used to simulate the pairing process to demonstrate the resolution of the high-order compact difference scheme.

The initial condition is specified by two identical vortices placed 5 core radii apart in a quiescent gas. The core radius is 1 cm and circulation is 15 m^2/s. At the center of each vortex, there is a pressure deficit about 15% compared to the ambient gas. The grid size is 201×201. Uniform grids are used at the center of the computational domain to resolve the vortices. The grids are slightly stretched in all four directions to prevent erroneous wave reflection. In addition, one-dimensional characteristic equations combined with Giles' unsteady, subsonic, out-flow equation is solved on the boundary as the non-reflective boundary condition.

Figure 11 shows the contours of the vorticity magnitude at various stages of the vortex interaction. The whole sequence is about one and a half revolutions. Finally, a single larger vortex emerges as the result of the vortex pairing interaction. Figure 12 shows the corresponding Mach number contours for the same flow.

3. Concluding Remarks

In this work, the quasi-one-dimensional and two-dimensional Euler solvers using various combinations of the Runge Kutta methods and the compact difference schemes were developed for numerical simulations of unsteady flows. The accuracy of the finite difference schemes is assessed by Fourier analysis and numerical examples in terms of numerical dissipation and dispersion. The dispersive characteristic is improved by high-order compact difference schemes compared to the second-order central difference. The increase of the order of time stepping scheme, on the other hand, enlarges the CFL limit for stable computations. In particular, significant improvement of the dispersive effect is obtained by adopting the fourth-order compact scheme (6 to 8 grid nodes to resolve a wave) instead of the conventional second-order central difference (12 to 16 grid nodes for one wave). The use of the sixth-order compact scheme (5 to 8 grid nodes for one wave), however, gains little improvement compared with the fourth-order scheme. It was also found that the compact difference schemes have no dissipative but high dispersive effects to the highest-wave-number waves resolved by a given numerical grid. Consequently, a small amount of background filtering is necessary to dissipate the high-wave-number waves and, at the same time, keep the low-wave-number solution intact. Other issues such as the order of accuracy of the Runge-Kutta schemes for nonlinear equations are analyzed. Specifically, the criteria for the 3 and 4-step methods to be third and fourth-order accurate are derived. The accuracy of the compact difference schemes for the steady state solution is also addressed.

In general, simulation of unsteady flow provides an overwhelming amount of information. It is our experience that the initial and boundary conditions must be carefully set up to obtain interpretable and physically meaningful solutions. For practical purposes, Giles' non-reflective equations combined with one-dimensional characteristic equations and their implementation to the present numerical scheme were illustrated in detail. In addition, the initial conditions of the simple wave, plane acoustic wave, and the Lamb vortex were also provided. Finally, as illustrated in the numerical examples, for flows of simple harmonic content, e.g., one frequency in Case 1, the conventional second-order central difference scheme is adequate provided enough grid nodes are used to resolve the very wave mode. On the other hand, for flows of complex harmonic content, the use of the Runge-Kutta method combined high-order compact difference schemes shows crisp resolution of unsteady flows.

4. References

[1] Lele, S. "Direct Numerical Simulations of Compressible Free Shear Flows," AIAA Paper 89-0374 (1989).

[2] Lele, S. "Compact Finite Difference Schemes with Spectral-Like Resolution," CTR Manuscript 107, Center for Turbulence Research, Stanford University, C. A. (1990).

[3] Jameson, A., Schmidt, W. and Turkel, E. "Numerical Solutions of the Euler Equations by Finite Volume Methods Using Runge-Kutta Time-Stepping Schemes," AIAA Paper 81-1259 (1981).

[4] Jameson, A. and Baker, T. J. "Solution of Euler Equations for Complex Configuration," AIAA Paper 83-1929 (1983).

[5] Wray, A. A., "Very Low Storage Time Advancement Schemes," *Internal Report*, NASA Ames Research Center, Moffett Field, C. A. (1986).

[6] Ciment, M., Leventhal, S. H., and Weinberg, B., *J. Comput. Phys.* **28**, 135 (1978).

[7] Tsien, H. S., *J. Am. Rocket Soc.* **22**, 139 (1952).

[8] Morse, P. M. and Ingard, K. U., "Theoretical Acoustics," *McGraw-Hill*, 874 (1968).

[9] Liu, N.-S., Davoudzadeh, F., Briley, W. R., and Shamroth, S. J., *J. Fluids Eng.* **12**, 501 (1990).

[10] Winant, C. D. and Browand, F. K., *J. Fluid Mech.* **63**, 237 (1974).

[11] Carnahan, B., Luther, A. A., and Wilkes, J. O., "Applied Numerical Methods," *John Wiley & Sons, Inc.*, 363 (1969).

[12] Colatz, L., "The Numerical Treatment of Differential Equations," *Springer Verlag*, 538 (1966).

[13] Adam, Y., *J. Comput. Phys.* **24**, 10 (1977).

[14] Williams, F. A., "Combustion Theory" *Benjamin & Cummings,* 306 (1985).

[15] Anderson, J. D., "Modern Compressible Flow," *McGraw-Hill*, 128 (1982).

[16] Lighthill, J., "Waves in Fluids," *Cambridge University Press*, 142 (1978).

[17] Giles, M. B., *AIAA J.* **28**, 12, 2050 (1990).

[18] Huff, D. L., "Pressure Waves Propagation Studies for Oscillating Cascades," NASA-TM-105406 (1992).

Table 1. The Accuracy of the 3-Step Runge-Kutta Methods.

Δt	Expansion	3-step R-K methods
0	R	R
1	R	$(\alpha_{31} + \alpha_{32} + \alpha_{33})R$
2	$\frac{1}{2}RR'$	$[\alpha_{11}\alpha_{32} + \alpha_{33}(\alpha_{21} + \alpha_{22})]RR'$
3	$\frac{1}{6}(R^2R'' + RR'^2)$	$\frac{1}{2}[\alpha_{11}^2\alpha_{32} + (\alpha_{21} + \alpha 22)^2\alpha_{33}]R^2R''$ $+\alpha_{11}\alpha_{22}\alpha_{33}RR'^2$

Table 2. The Relative Error of the Acoustic Admittance Calculation (%).

Numerical Schemes	Error of $\|A\|$	Error of θ
RK4-CD6	0.45	3.6
RK4-CD4	0.52	3.3
RK4-CD2	1.65	4.1

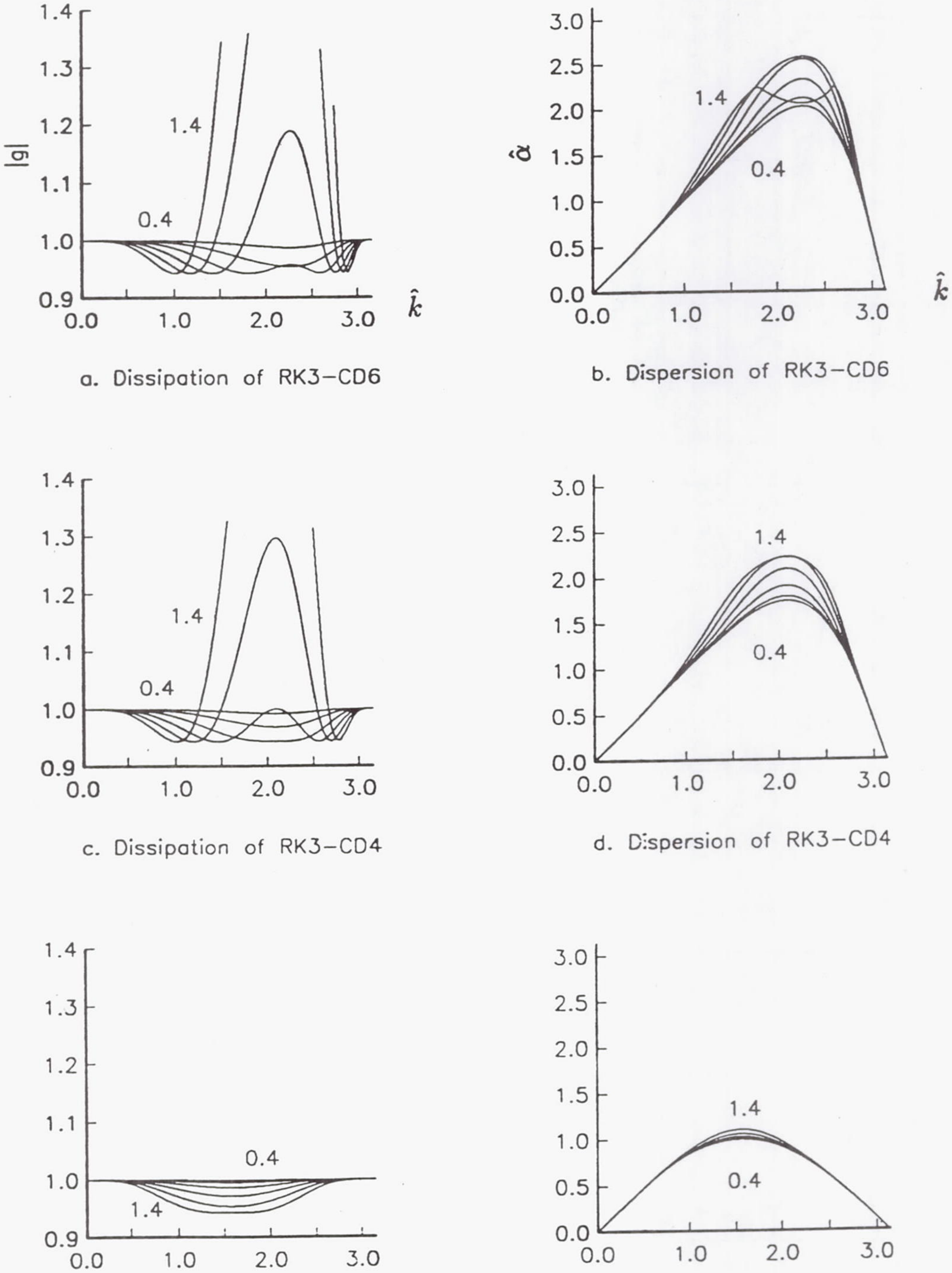

a. Dissipation of RK3–CD6

b. Dispersion of RK3–CD6

c. Dissipation of RK3–CD4

d. Dispersion of RK3–CD4

e. Dissipation of RK3–CD2

f. Dispersion of RK3–CD2

Fig. 1 Dissipation and dispersion characteristics of the RK3 time-stepping combined with various spatial discretization schemes.

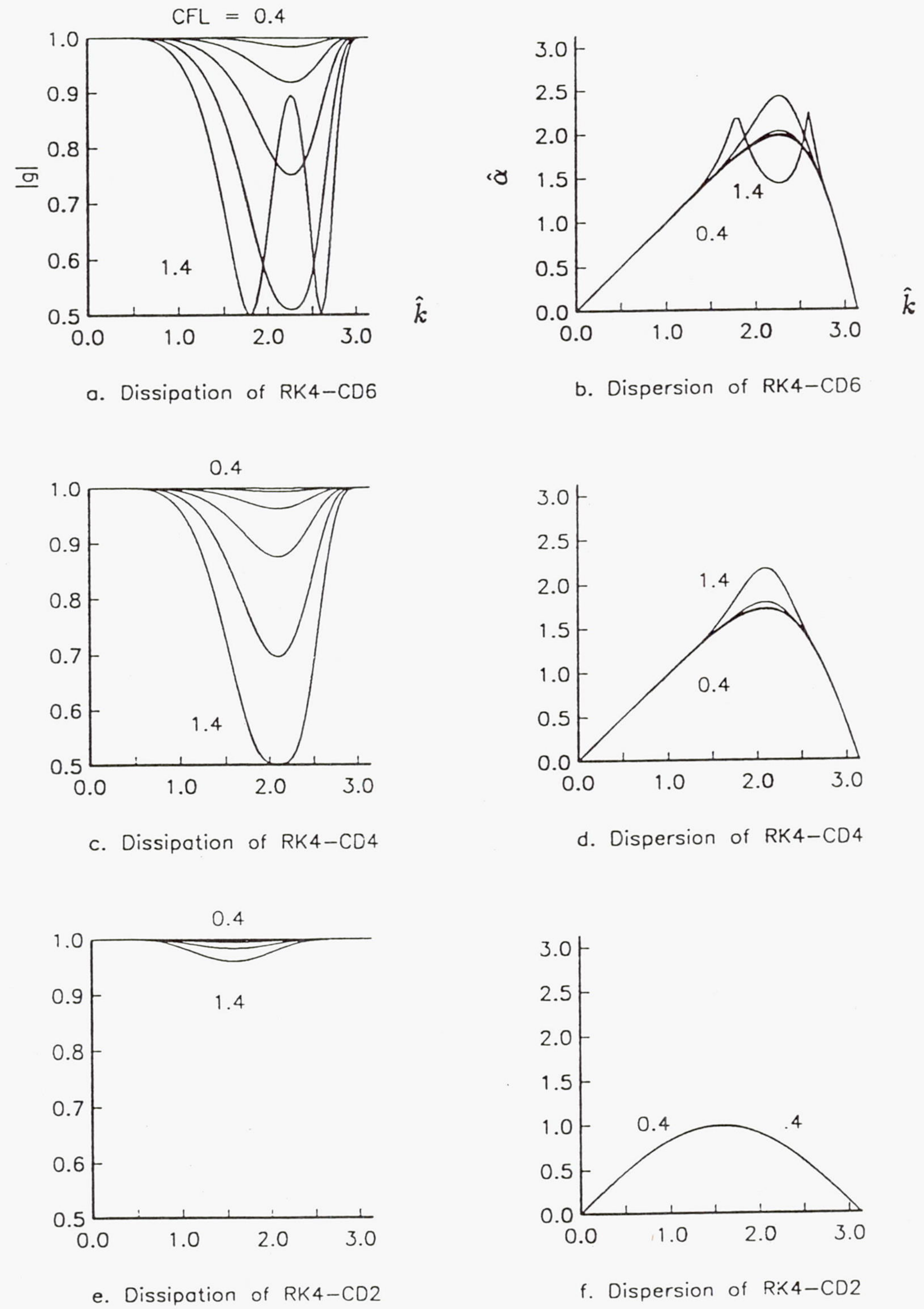

Fig. 2 Dissipation and dispersion characteristics of the RK4 time-stepping combined with various spatial discretization schemes.

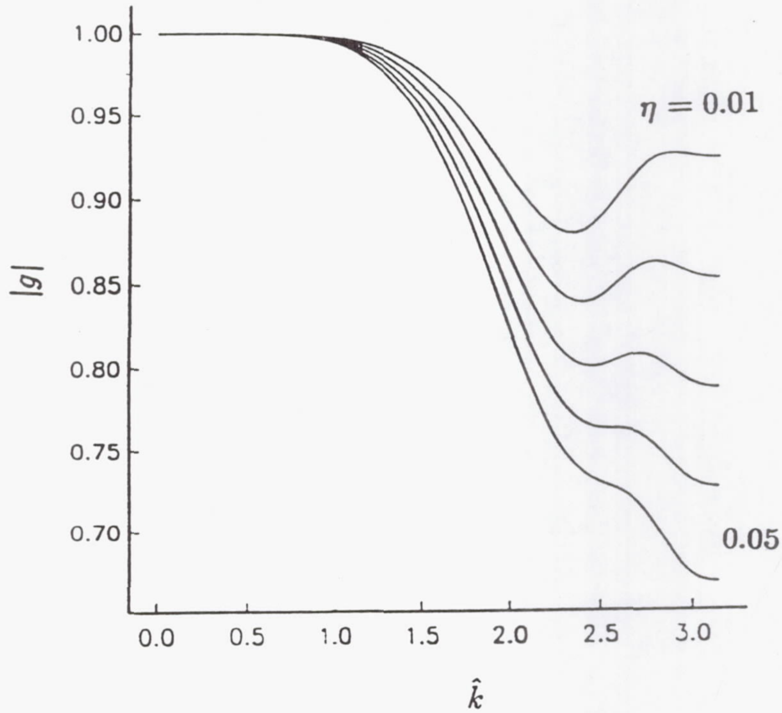

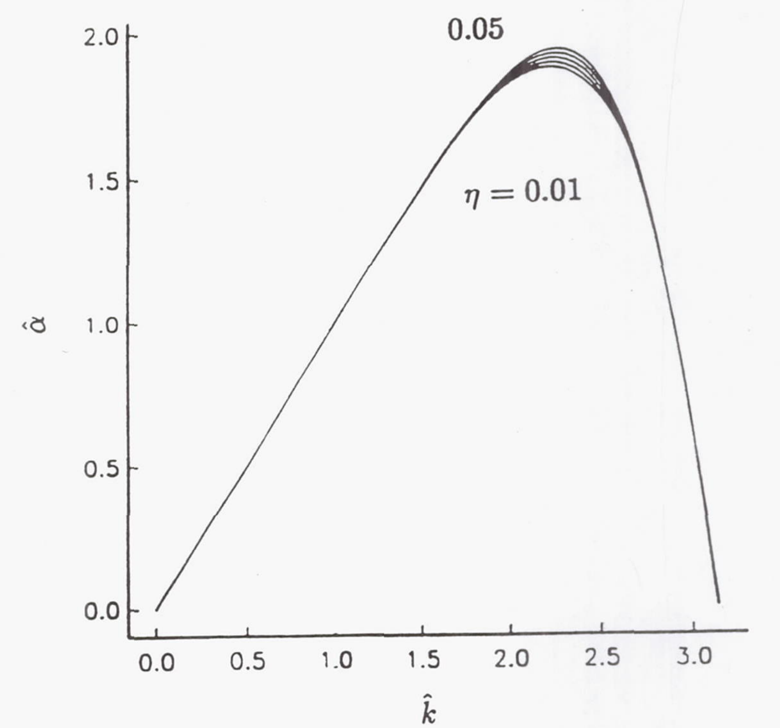

Fig. 3 Dissipation and dispersion characteristics of the RK4-CD6 method with various amount of the sixth-order numerical damping.

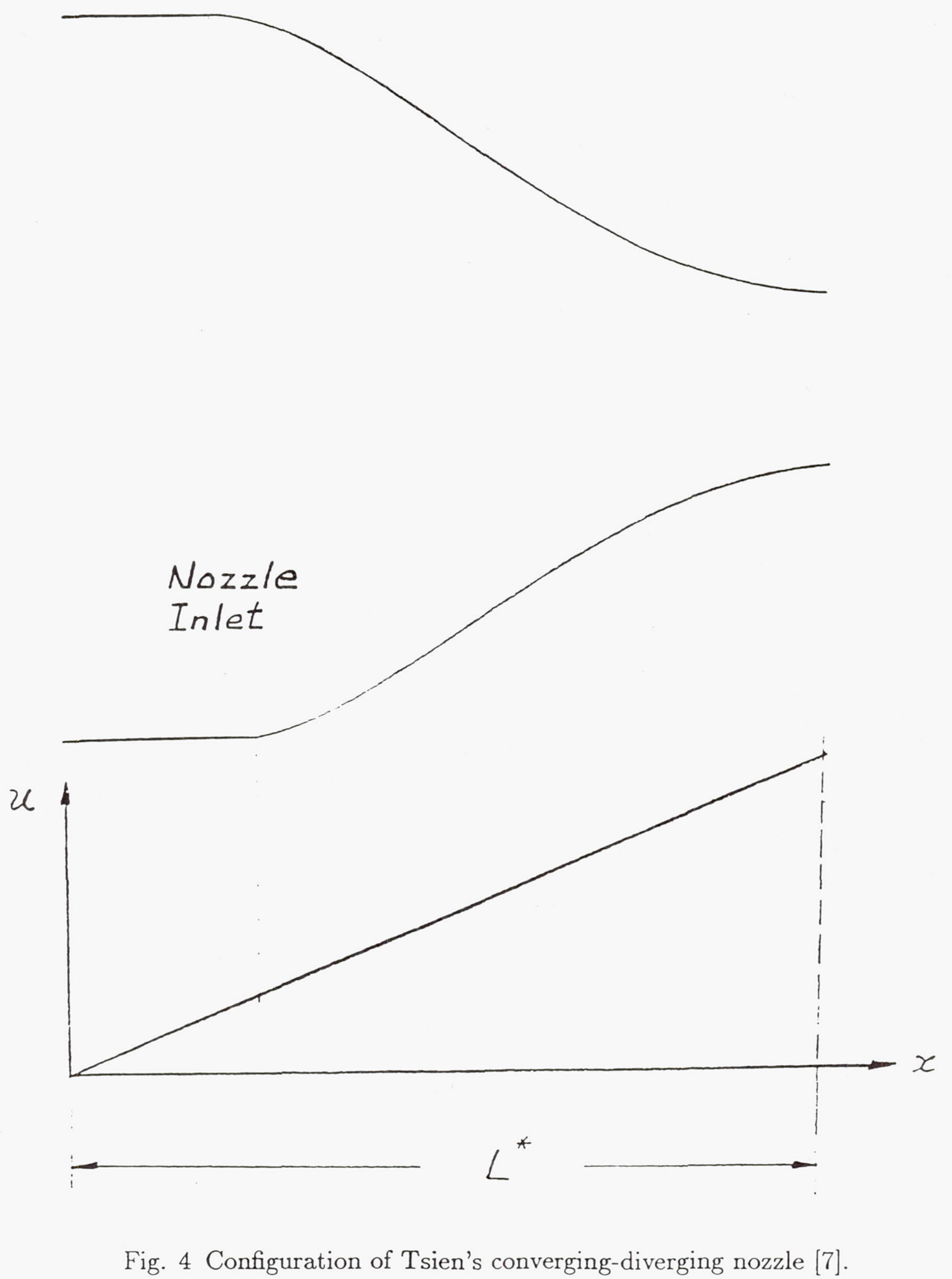

Fig. 4 Configuration of Tsien's converging-diverging nozzle [7].

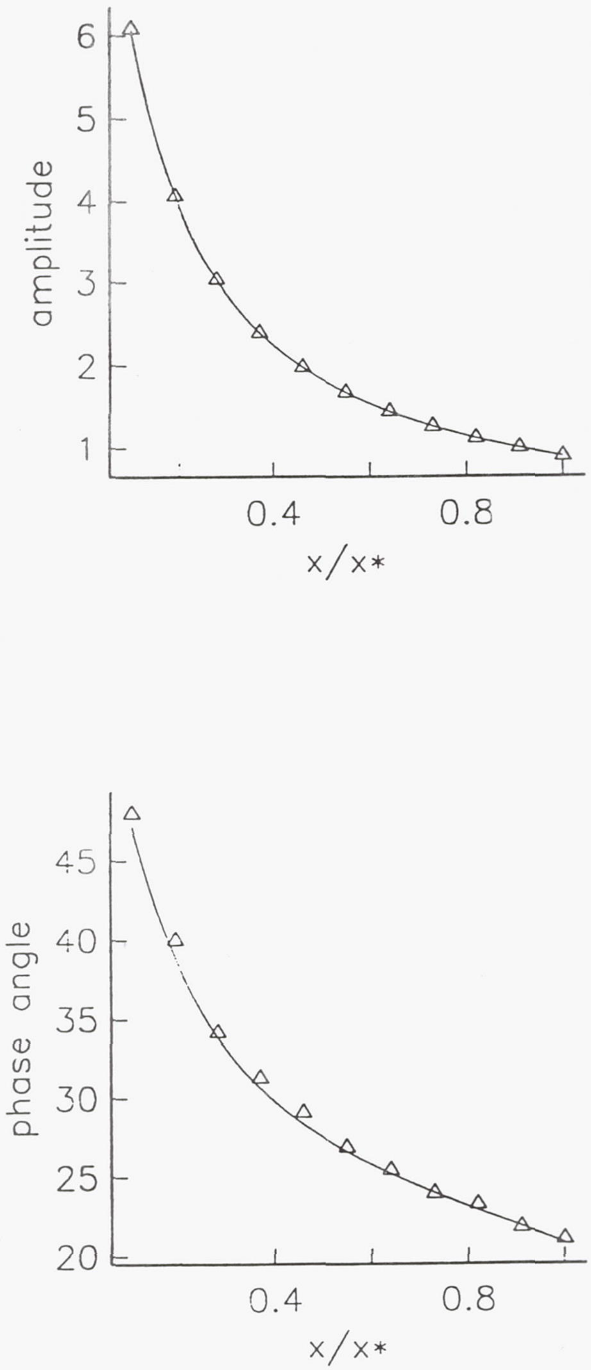

Fig. 5 Acoustic admittance calculation using the RK4-CD6 method for the inlet perturbation as $\beta = 6$, $p'/\bar{p} = 0.011$. The solid line is Tsien's theorem and the triangles are the CFD results. (a) Magnitude. (b)Phase angle.

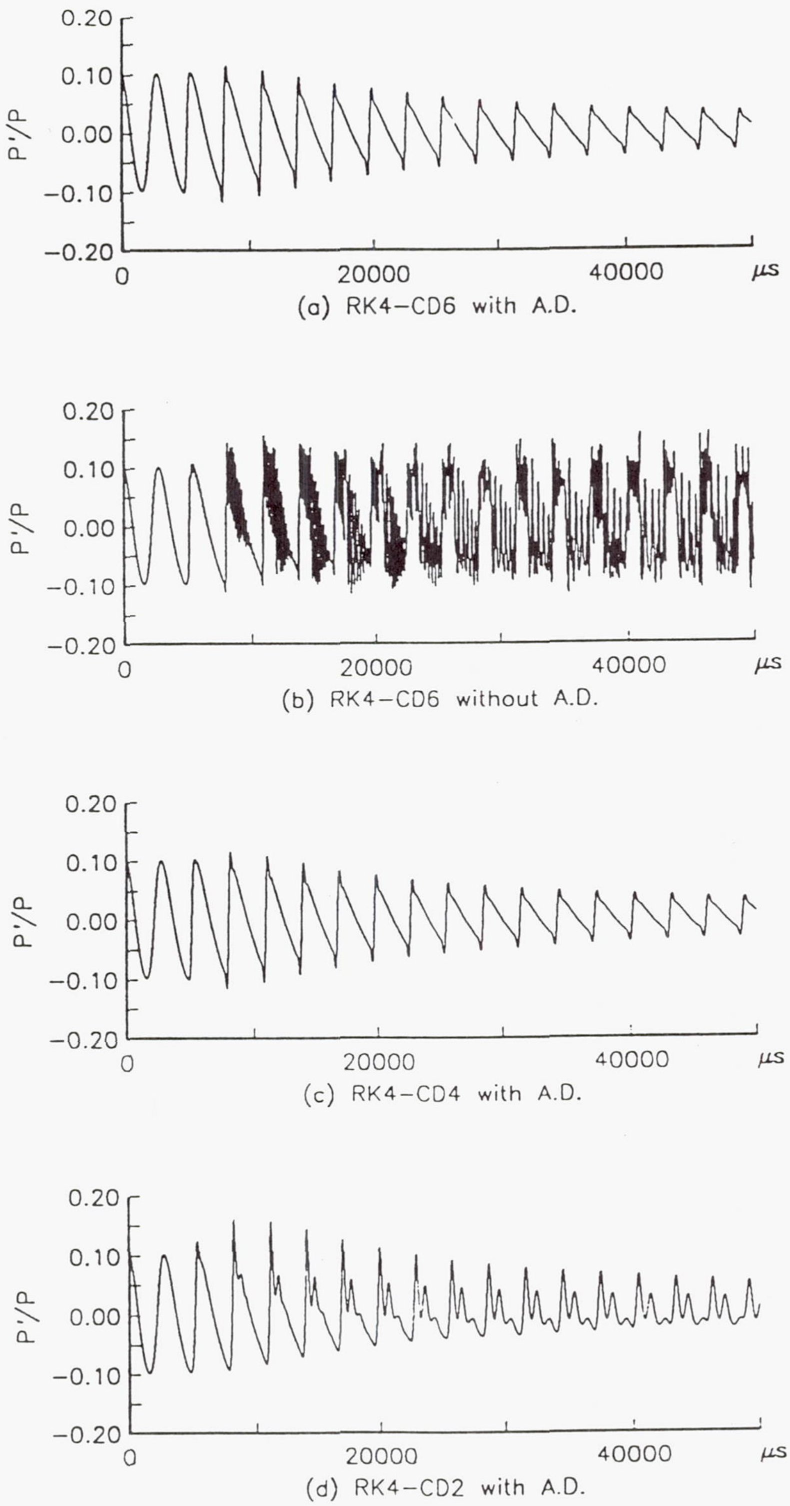

Fig. 6 Time histories of the pressure fluctuations of the N-wave calculation at one end of the periodic domain by various numerical schemes.

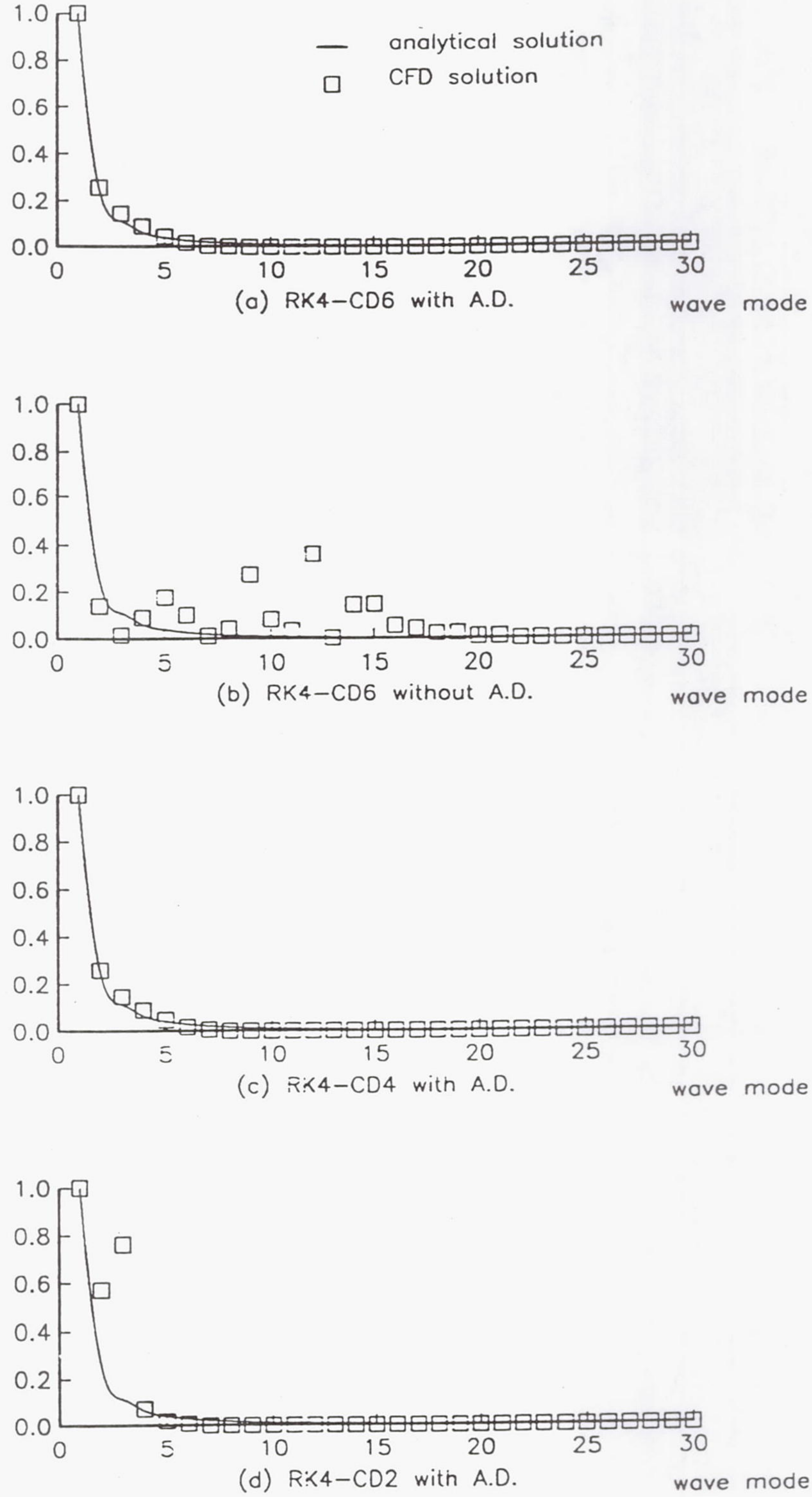

Fig. 7 Power spectrum of the pressure distribution after about 17 cycles of the N-wave propagation by various numerical schemes.

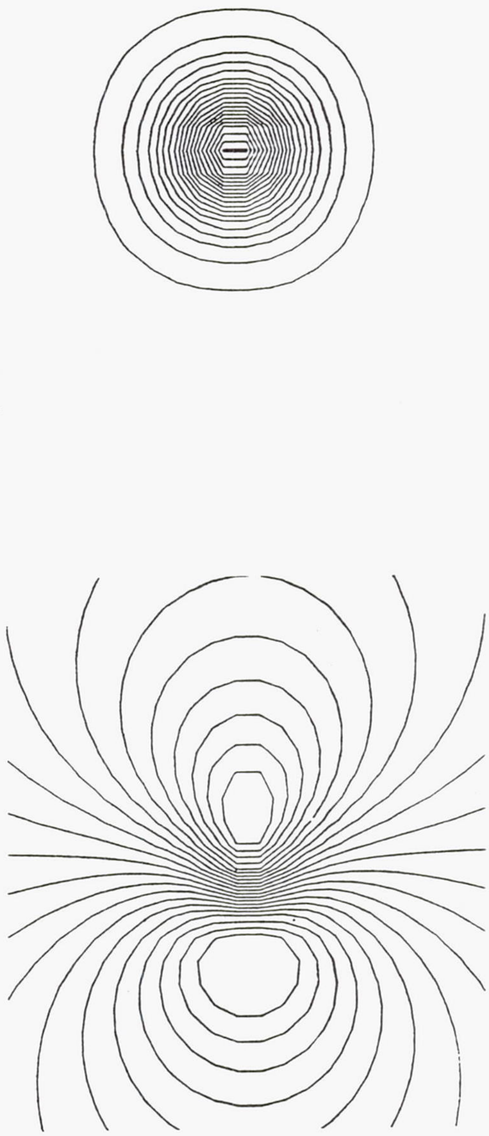

Fig. 8 Vorticity and Mach number contours of an analytical Lamb vortex.

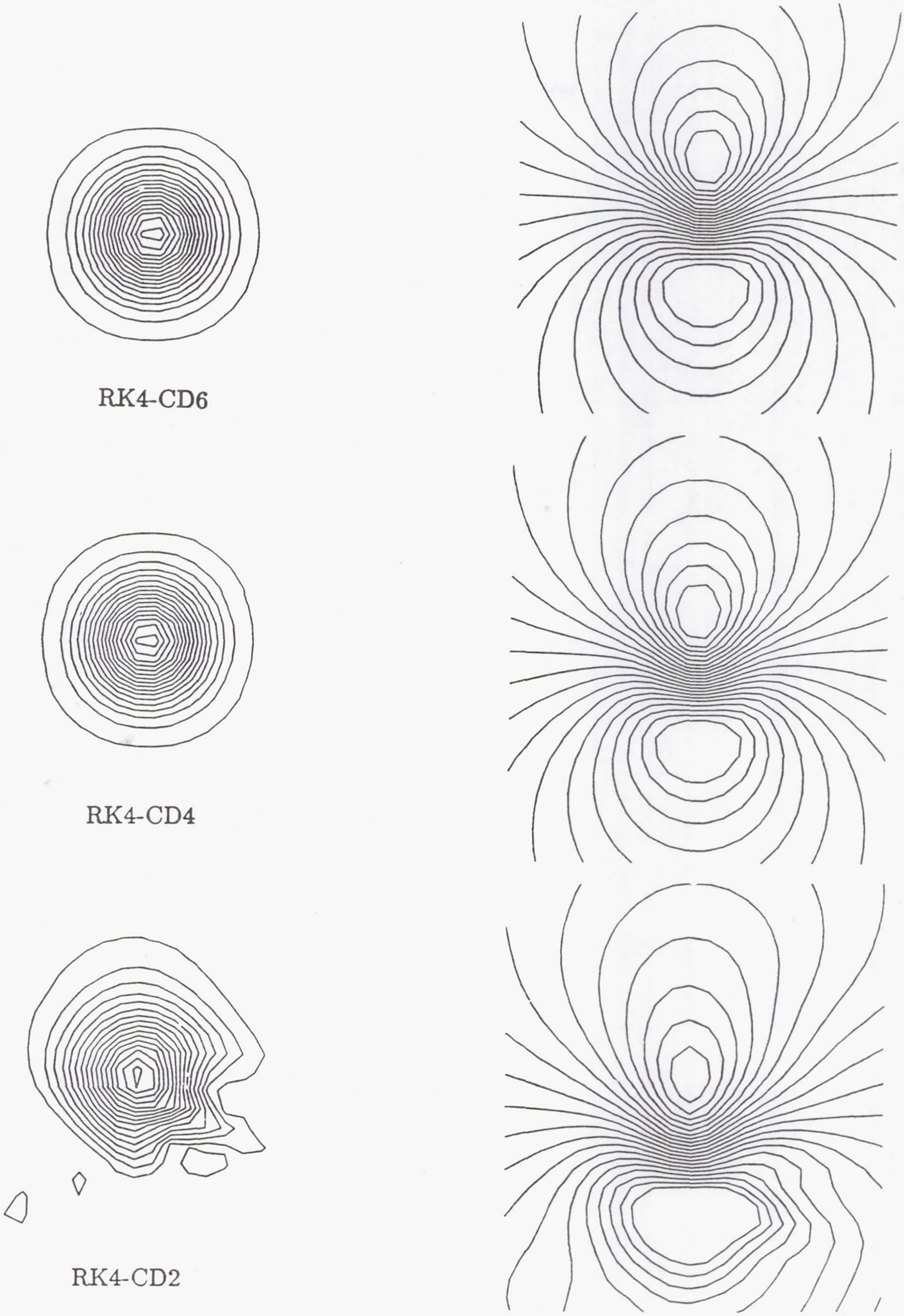

Fig. 9 Vorticity and Mach number contours of the lamb vortex after travelling about 60 core diameters predicted by various numerical schemes.

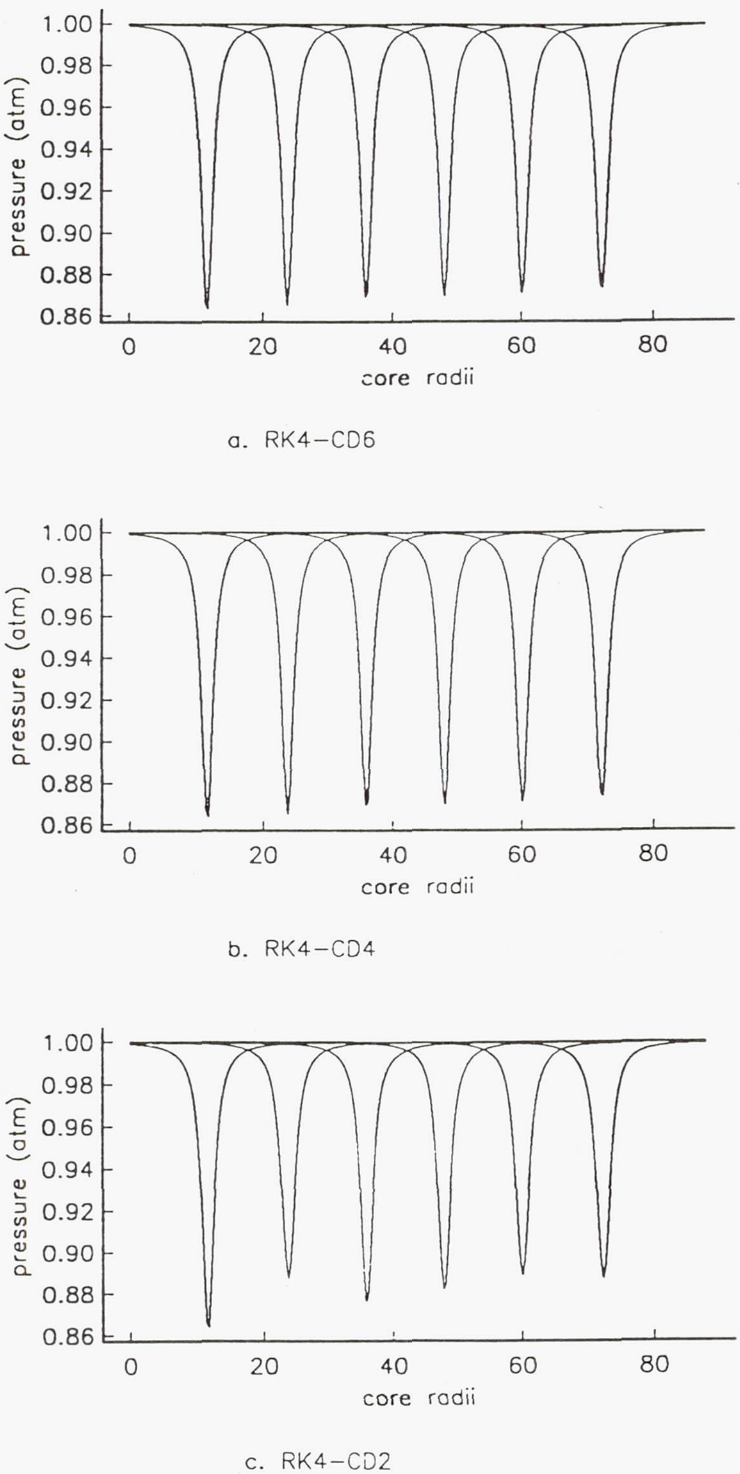

Fig. 10 Vortex pressure profiles at the center line at various instances predicted by different numerical schemes.

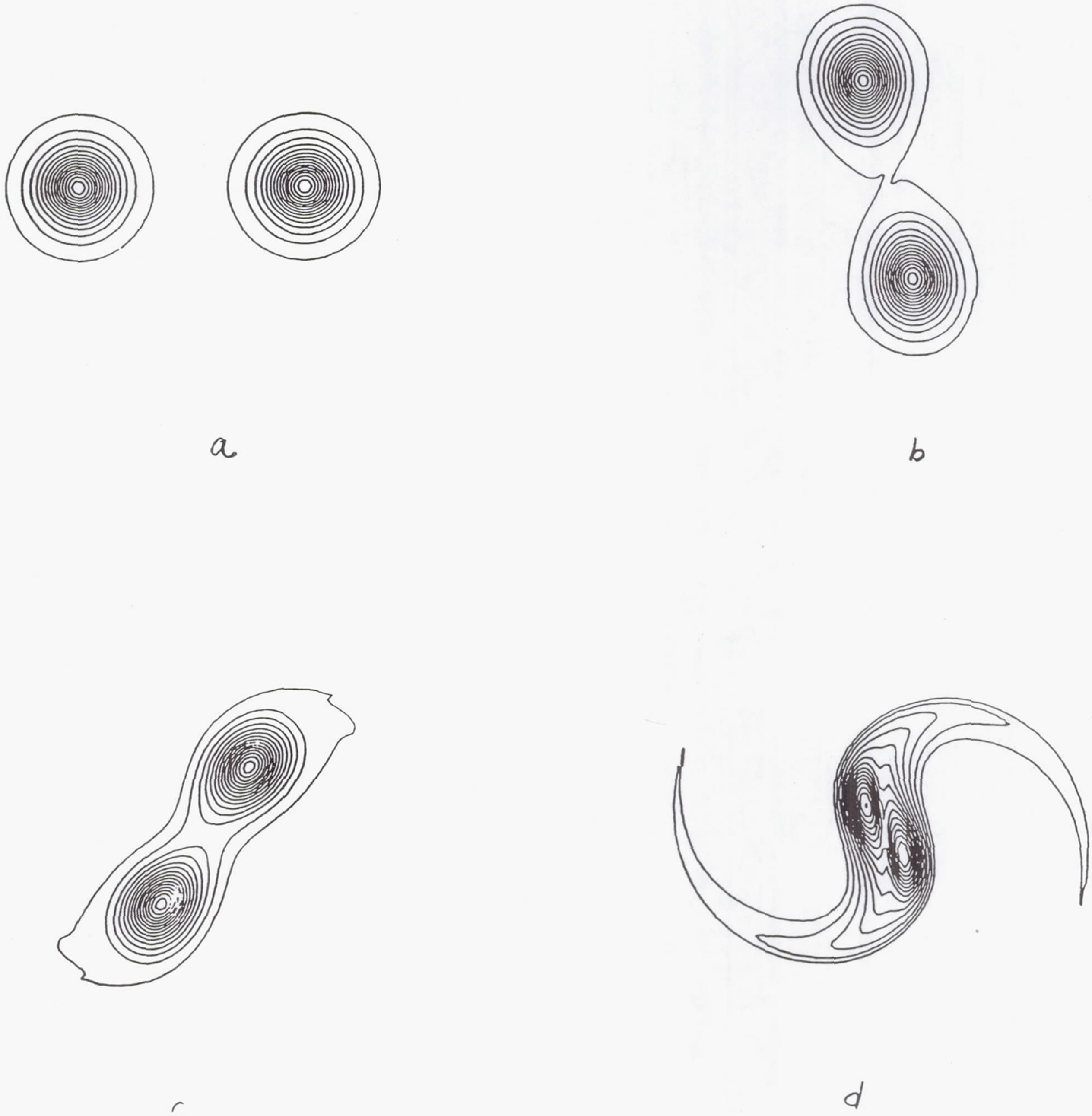

Fig. 11 The vorticity magnitude contours for the vortex pairing.

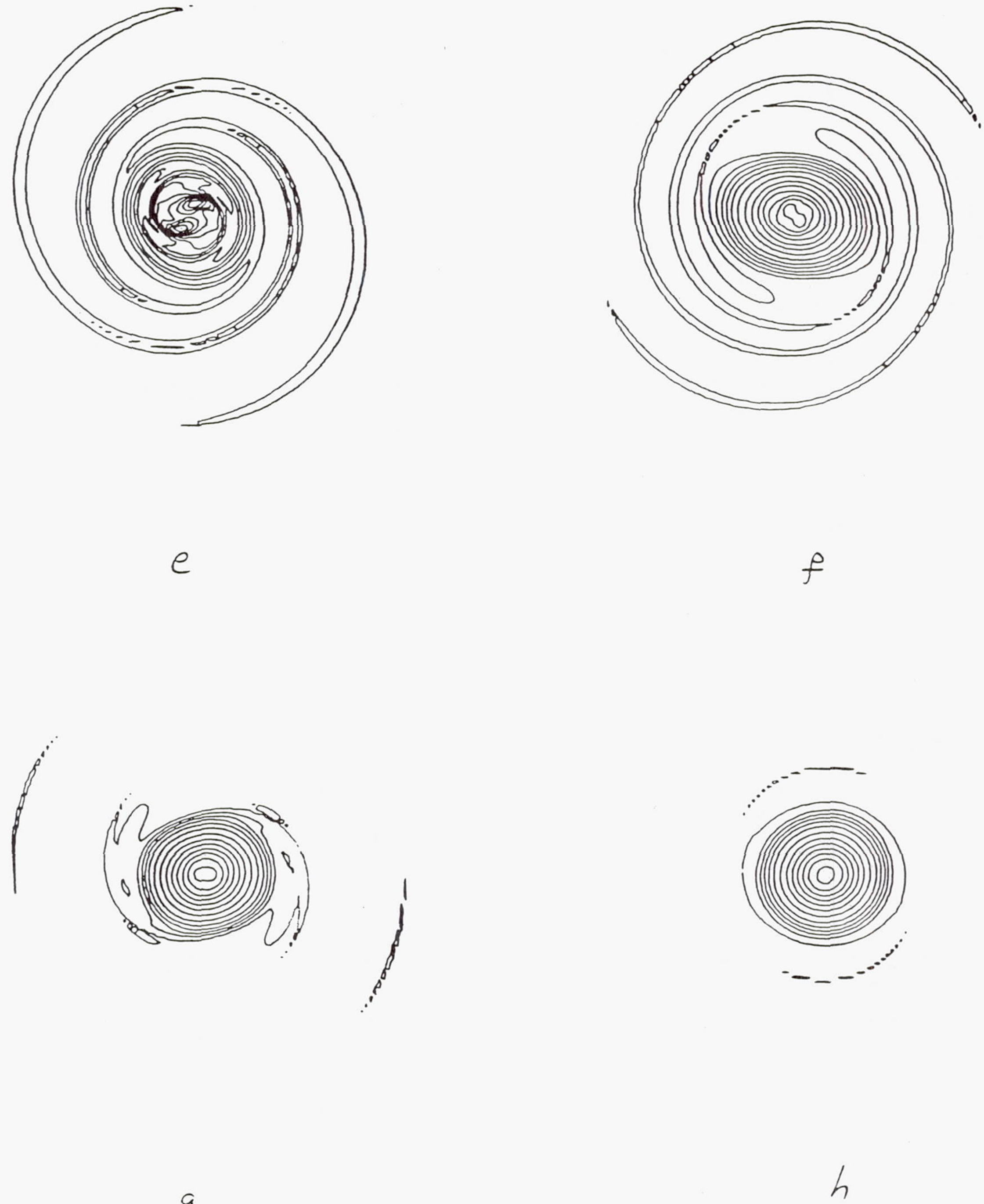

Fig. 11 The vorticity magnitude contours for the vortex pairing.

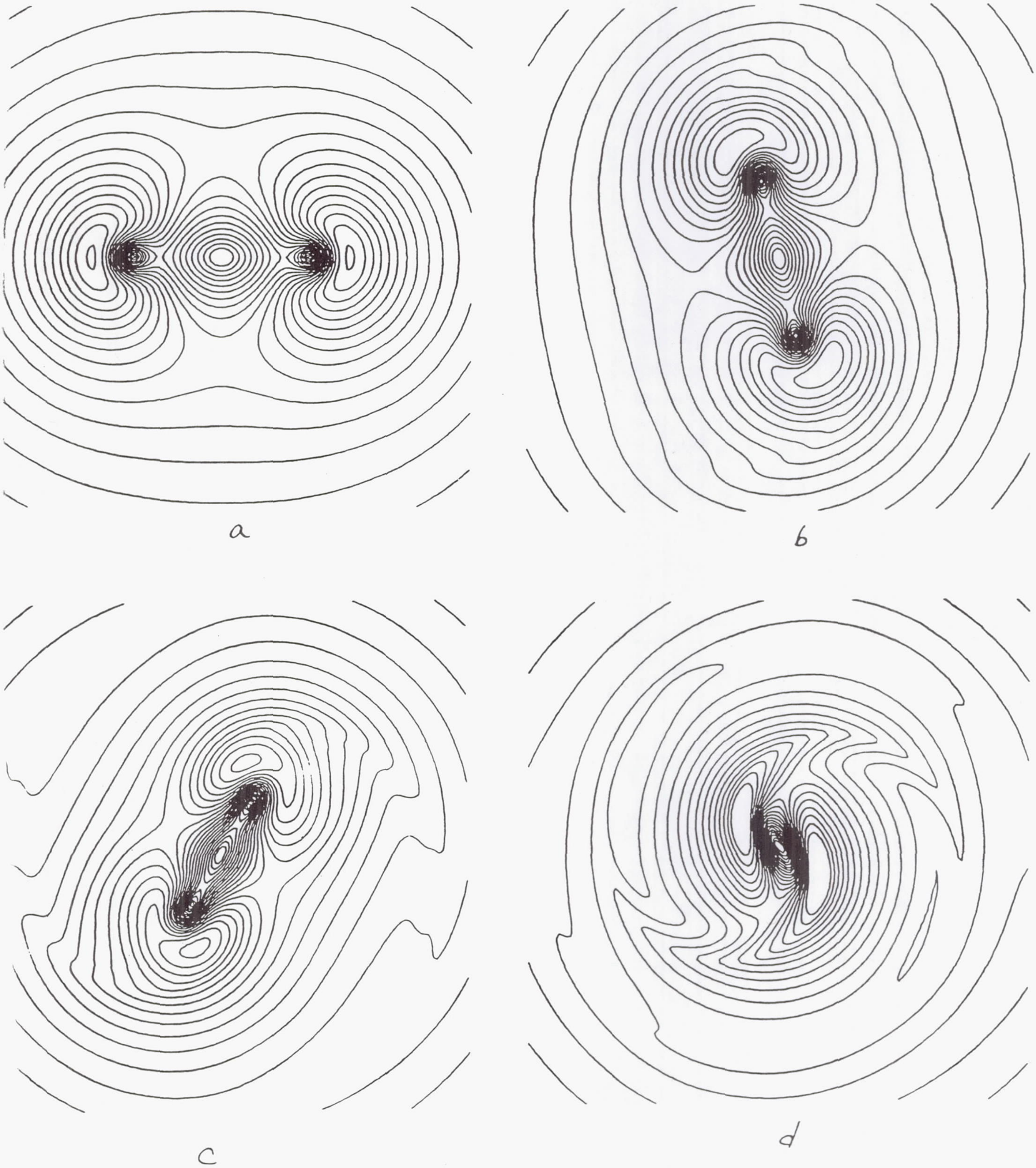

Fig. 12 The Mach number contours for the vortex pairing.

Appendix A

Organization - 1991

Position Chart

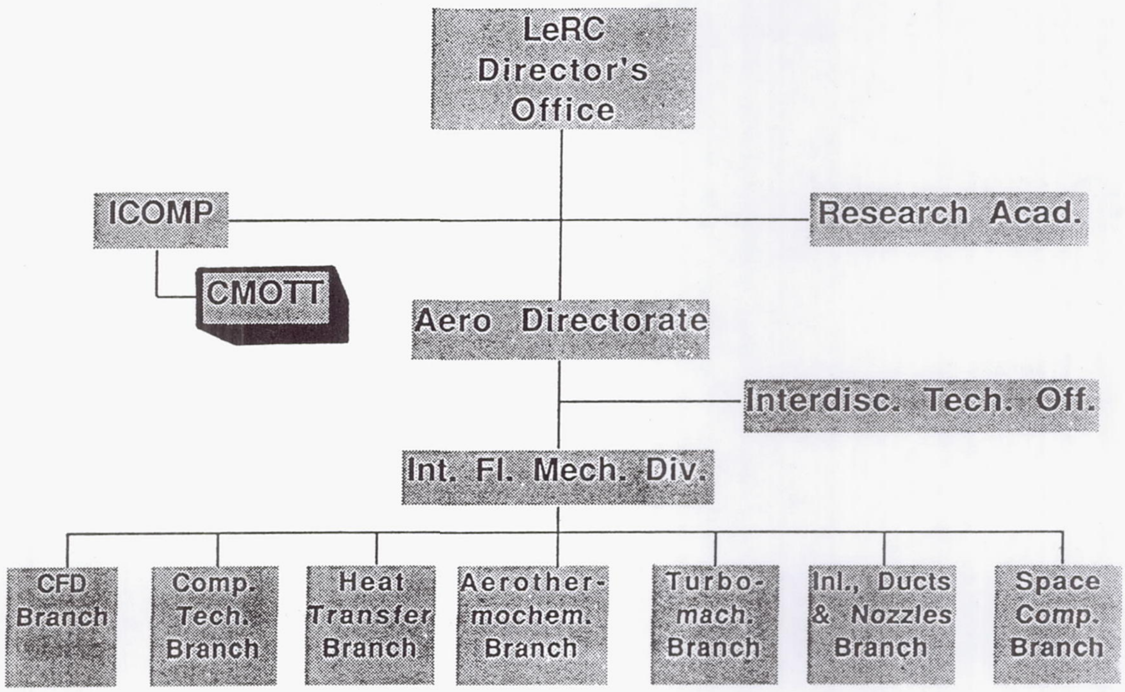

Preceding Page Blank

ICOMP Director	Dr. Louis A. Povinelli Deputy Chief Internal Fluid Mechanics Division NASA Lewis Research Center
Coordinator	Dr. Meng-Sing Liou Senior Scientist Internal Fluid Mechanics Division NASA Lewis Research Center
CMOTT Technical Leader	Dr. Tsan-Hsing Shih Senior Research Associate ICOMP, NASA Lewis Research Center
Advisors	Dr. Marvin E. Goldstein Chief Scientist NASA Lewis Research Center
	Professor John L. Lumley Sibley School of Mechanical and Aerospace Engineering Cornell University
	Professor Eli Reshotko Department of Mechanical and Aerospace Engineering Case Western Reserve University

Current Member Listing

Names/Term	Affiliation	Research Areas
Duncan, Beverly 7/1991 - present	Sverdrup Tech., Inc.	Multiple-Scale Turbulence Models
Hsu, Andrew T. 5/1990 - present	Sverdrup Tech., Inc.	PDF Turbulence Modeling, DNS
Liou, Meng-Sing 5/1990 - present	NASA LeRc	CFD Algorithms, High-Speed Flow
Liou, William W. 11/1990 - present	ICOMP	Compressible Flow Modeling, Weakly Nonlinear Wave Models
Rubinstein, Robert 7/1991 - present	Sverdrup Tech., Inc.	Analytical Theories of Turbulence
Shabbir, Aamir 5/1990 - present	ICOMP	Buoyancy Effects on Turbulence, Turbulence Modeling
Shih, Tsan-Hsing 5/1990 - present	ICOMP	Turbulence Modeling
Steffen, Christopher J. Jr. 10/1990 - present	NASA LeRc	Upwind Algorithms Incompressible Flow Two-Equation Turbulence Models
Van der Vegt, Jacobus J. 10/1991 - present	ICOMP	DNS Compressible Flows High Order Shock Capturing Schemes
Yang, Zhigang 7/1990 - present	ICOMP	Modeling of Bypass Transition
Yu, Sheng-Tao 3/1991 - present	Sverdrup Tech., Inc.	Modeling of Chemical Reacting Flows, DNS
Zhu, Jiang 4/1992 - present	ICOMP	Application of Turbulence Models in Complex Flows

Appendix B

CMOTT Biweekly Seminars / Technical Meetings

The purpose of these seminars is to exchange ideas and opinions on the latest developments and current state of turbulence and transition research. The speakers are invited from within and without of the NASA LeRC, including foreign speakers. The seminars were intended not noly to keep the members informed of the latest development of local turbulence and transition modeling research but also to increase interactions between group members and other researchers at the NASA LeRc.

The following is the meeting schedule and the abstract of the semainars during the reporting period.

CENTER FOR MODELING OF TURBULENCE AND TRANSITION

Date: July 3, 1991

To: CMOTT Members and SVR and IFMD Staff

From: William W. Liou (6682)

Subject: CMOTT Biweekly Meeting

The following is a tentative schedule for the CMOTT biweekly get-together from July 10, 1991 to August 28, 1991.

The presentations will be informal and active participation is expected from the attendants. Soda and snack will be served in the meetings. These meetings complement the CMOTT Seminar Series, which are mainly formal presentations.

We would also appreciate some contributions from you. Subjects related to either the theoretical, experimental or computational aspects of turbulence and transition modeling are welcomed. Those who are willing to share their experience in these areas can contact me or Dr. T.-H. Shih at 6680 for further arrangement.

The meeting will start at 4:00 p.m. in Room 228, Sverdrup Building.

July 10, 1991	J. Lepicovsky (61-6753) **LDV Measurement of Large Structures in a Tone Excited Turbulent Jet**
July 24, 1991	C. R. Wang (5865) **Computations of Turbulence in a Shock/Turbulent Boundary Layer Interaction Flow**
August 7, 1991	A. Hsu (61-6648) **PDF Turbulence Model and Its Applications**
August 28, 1991	C. Steffen (8508) **DTNS: An Accurate and Efficient Testbed for Incompressible Flow Turbulence Modeling**

CENTER FOR MODELING OF
TURBULENCE AND TRANSITION

Date: September 4, 1991

To: CMOTT Members and SVR and IFMD Staff

From: William W. Liou (6682)

Subject: CMOTT Biweekly Meeting

The following is a tentative schedule for the CMOTT biweekly get-together from **September 11, 1991** to **October 23, 1991** .

The presentations will be informal and active participation is expected from the attendants. Soda and snack will be served in the meetings. These meetings complement the CMOTT Seminar Series, which are mainly formal presentations.

We would also appreciate some contributions from you. Subjects related to either the theoretical, experimental or computational aspects of turbulence and transition modeling are welcomed. Those who are willing to share their experience in these areas can contact me or Dr. T.-H. Shih at 6680 for further arrangement.

The meeting will start at 4:00 p.m. in Room 228, Sverdrup Building.

Sept. 11, 1991	T. Bui (5639) **Implementation of the Chien Low-Re k-ϵ Models into the Proteus Code**
Sept. 25, 1991	K. Ahn (5965) **A 2-D Oscillating Flow Analysis Using Quasi-steady Turbulence Model**
October 9, 1991	J. Schwab (8446) **Variable-density Turbulence Modeling for Turbomachinery**
October 23, 1991	M. Mawid (5965) **Multiphase Turbulent Combustion**

CENTER FOR MODELING OF TURBULENCE AND TRANSITION

Date: November 4, 1991

To: CMOTT Members and SVR and IFMD Staff

From: William W. Liou (3-6682)

Subject: CMOTT Biweekly Meeting

The following is a tentative schedule for the CMOTT biweekly get-together from **November 6, 1991** to **December 18, 1991**.

This will be the last session of the CMOTT group-meetings/informal- seminars this year but the series will resume in mid-January 1992. Thank you for your patience and participation through out the year. The group-meetings/informal-seminars of CMOTT are meant not only to serve CMOTT members but also to provide an informal forum for those who are involved in transition/turbulence predictions. I thank all the speakers and participants who have made these objectives "realizable". Now, we are planing for 1992. If you have any suggestions or like to give a talk or two in the coming year, please call me or Dr. T. H. Shih at 3-6680. In the mean time, don't forget to mark your calendar for the following talks !

HAPPY HOLIDAYS !!!

The meeting will start at 4:00 p.m. in Room 228, Sverdrup Building.

Nov. 6, 1991 W. Liou (3-6682)
Weakly Nonlinear Models for Turbulent Free Shear Flows (2) - A Self-Contained Energy Transfer Model

Nov 20, 1991 D. Ashpis (3-8317)
DNS of Disturbances in Boundary Layer Flow

Dec. 4, 1991 B. Rubinstein (61-6612)
Analytical Theory of Turbulence and Turbulence Modeling: TSDIA and RNG

Dec. 18, 1991 B. Duncan (61-2998)
A New Three-Equation Model for Turbulence

CENTER FOR MODELING OF TURBULENCE AND TRANSITION

Date: January 30, 1992

To: CMOTT Members and SVR and IFMD Staff

From: William W. Liou (3-6682)

Subject: CMOTT Biweekly Meeting

The following is a tentative program for the CMOTT biweekly get-together/seminar from **February 5, 1992** to **March 18, 1992**. You are welcomed to join us.

Thanks to the your suggestions, we have made a few changes from last year's format. First, we have scheduled the CMOTT Seminar Series, which are mainly formal presentations, into the biweekly time frame of the CMOTT group-meeting/informal-talks. Also, the abstract of each presentation, formal or informal, will be distributed about one week prior to its scheduled date. Again, if you are interested in giving a presentation, please contact us.

The meeting will run from 1:30-2:15 PM in Room 145, Sverdrup Building, unless otherwise noted.

(1) Feb. 5, 1992 D. Davis
Weakly Nonlinear Vortex/Wave Interactions in Incompressible Cross-flow Boundary Layers in Transition

(2) Feb. 19, 1992 Z. Yang
A Modeling of Bypass Transition

(3) March 4, 1992 K. Zaman
Effect of "Delta-Tabs" on the Evolution of Axisymmetric Jets

(4) March 18, 1992 Professor R. M. C. So, Arizona State University
Near Wall Heat Transfer Modeling

CENTER FOR MODELING OF TURBULENCE AND TRANSITION

Date: March 26, 1992

To: CMOTT Members and SVR and IFMD Staff

From: William W. Liou (3-6682)

Subject: CMOTT Biweekly Meeting

The following is a tentative program for the CMOTT biweekly get-together/seminar from **April 1, 1992** to **May 13, 1992**. You are welcomed to join us. Also, if you are interested in giving a presentation, please let us know.

The meeting will run from 1:30-2:15 PM in Room 228, Sverdrup Building, unless otherwise noted.

(5) April 1, 1992 J. Van der Vegt
The Development of an ENO-Osher Scheme for Direct Simulation of Compressible Flows

(6) April 15, 1992 J. Goodrich
Unsteady Time Asymptotic State: Incompressible Results,

New Directions for Algorithms

(7) April 29, 1992 T.-H. Shih
Kolmogorov Behavior of Near-Wall Turbulence and Its Application in Turbulence Modeling

(8) May 13, 1992 Z. Yang
A Modeling of Bypass Transition

CENTER FOR MODELING OF TURBULENCE AND TRANSITION

Date:	June 1, 1992
To:	CMOTT Members and SVR and IFMD Staff
From:	William W. Liou (3-6682)
Subject:	CMOTT Biweekly Meeting

The following is a tentative program for the CMOTT biweekly get-together/seminar from **June 10, 1992** to **July 22, 1992**. You are welcomed to join us.

The talks will be informal and active participation will be expected from the audience.

Also, if you are interested in giving a presentation about the progress or some results of your own work on turbulence or transition, please let us know.

The meeting will run from 1:30-2:15 PM in Room 228, Sverdrup Building, unless otherwise noted.

(9) June 10, 1992 J. Zhu
Finite Volume Computations in Incompressible Flows with Complex Geometries

(10) June 24, 1992 J. Lee
RPLUS Code and Standard $k-\epsilon$ Models and Applications

(11) July 8, 1992 R. Mankbadi
Unsteady Turbulent Flows

(12) July 22, 1992 D. Rigby
The Effect of Spanwise Variations in Momentum on Leading Edge Heat Transfer

CENTER FOR MODELING OF TURBULENCE AND TRANSITION

Biweekly Meeting Series (1)

Weakly Nonlinear Vortex/Wave Interactions in Incompressible Crossflow Boundary Layers in Transition

by

Dominic Davis
ICOMP

Wed., 5 February, 1992
1:30-2:15 PM
Room 145, SVR Building

ABSTRACT

The instability of an incompressible three-dimensional boundary layer is considered theoretically and computationally in the context of vortex/wave interactions.Specifically the work centres on two low-amplitude, lower-branch Tollmien-Schlichting (TS) waves which mutually interact to induce a weak longitudinal vortex flow;the vortex motion,in turn,gives rise to significant wave-modulation via wall-shear forcing.The characteristic Reynolds number is taken as a large parameter and,as a consequence,the TS waves and the vortex are governed primarily by triple-deck theory.The nonlinear interaction is captured by a viscous partial-differential system for the vortex coupled with a pair of amplitude equations for the wave pressures. Computations were performed for relatively small crossflow values.Three distinct possibilities were found to emerge for the nonlinear behaviour of the flow solution downstream - an algebraic finite-distance singularity,far- downstream decay or repeated oscillations - depending on the various parameter values,the input amplitudes and the wave angles.

CENTER FOR MODELING OF TURBULENCE AND TRANSITION

Biweekly Meeting Series (1992-2)

A k-ϵ Model for Near Wall Turbulence and its Application in Turbulent Boundary Layer with/without Pressure Gradient

by

Z. Yang
ICOMP

Wed., 19 February, 1992
1:30-2:15 PM
Room 145, SVR Building

ABSTRACT

A $k - \epsilon$ model is proposed for turbulent wall bounded flows. In this model, turbulent velocity scale and turbulent time scale are used to define the eddy viscosity. The time scale used is bounded from below by the Kolmogorov time scale. The dissipation equation is reformulated using this time scale, removing the singularity of the high Reynolds number $k - \epsilon$ equation at the wall and rendering the introduction of the pseudo-dissipation unnecessary. The damping function used in the eddy viscosity is chosen to be a function of $R_y = \frac{k^{1/2}y}{\nu}$ instead of y^+. Thus, the model could be used for flows with separation. The model constants used are the same as the model constants in the commonly used high turbulent Reynolds standard $k - \epsilon$ model. Thus, the proposed model would reduce to the standard $k - \epsilon$ model when it is far away from the wall. Boundary layer flows at zero pressure gradient, favorable pressure gradient, adverse pressure gradient and increasingly adverse pressure gradient are calculated respectively. The comparisons of model predictions and the available experimental data are found to be good.

CENTER FOR MODELING OF TURBULENCE AND TRANSITION

Biweekly Meeting Series (1992-3)

Effect of Tabs on the Evolution of Axisymmetric Jets

by

Khairul Zaman
IFMD

Wed., 4 March, 1992
1:30-2:15 PM
Room 145, SVR Building

ABSTRACT

Vortex generators, in the form of small tabs at the nozzle exit, can have a profound influence on the evolution of an axisymmetric jet. Using tabs of certain shapes, the jet cross section can be distorted almost arbitrarily. Such distortion is accompanied by elimination of screech noise from supersonic jets and a significant increase in jet mixing. Key results obtained so far, covering a jet Mach number range of 0.3 and 1.8, will be summarized in this presentation. Observations will be made on the mechanisms of the effect including the likely vorticity dynamics in the flow.

CENTER FOR MODELING OF TURBULENCE AND TRANSITION

Biweekly Meeting Series (1992-4)

Near-Wall Modeling of Turbulent Heat Transfer

by

Professor Ronald M. C. So

Mechanical and Aerospace Engineering
Arizona State University

Wed., 18 March, 1992
1:30-2:30 PM
Room 119, Building 5

ABSTRACT

A near-wall two-equation model for turbulent heat fluxes is derived from the temperature variance and its dissipation-rate equations and the assumption of gradient transport. The near-wall asymptotics of each term in the exact equations are examined and used to derive near-wall correction functions that render the modeled equations consistent with these behavior. Thus modeled, the equations are used to calculate fully-developed pipe and channel flows with hear transfer. It is found that the proposed two-equation model yields asymptotically correct near-wall behavior for the normal heat flux, the temperature variance and its near-wall budget and correct limiting wall values for these properties compared to direct simulation data and measurements obtained under different wall boundary conditions.

CONTACT: T.-H. Shih, PABX 3-5698

CENTER FOR MODELING OF
TURBULENCE AND TRANSITION

Biweekly Meeting Series (1992-5)

The Development of an ENO-Osher Scheme for Direct Simulation of Compressible Flows

by

Jaap Van der Vegt

ICOMP

Wed., April 1, 1992
1:30-2:30 PM
Room 228, SVR Building

ABSTRACT

Direct simulation of turbulence and transition in compressible wall bounded flows presents an alternative to investigate important physical phenomena which are difficult to measure or study otherwise. It also provides data useful for turbulence modeling. A new program is being developed which solves the three-dimensional compressible Navier-Stokes equations using a higher order, fully implicit and time accurate ENO scheme together with Osher flux splitting. In this presentation an overview will be given of the numerical scheme and several test cases, both for supersonic and subsonic flow, will be presented and further improvements will be discussed.

CENTER FOR MODELING OF TURBULENCE AND TRANSITION

Biweekly Meeting Series (1992-6)

Unsteady Time Asymptotic States: Incompressible Results and New Directions for Algorithms

by

John Goodrich

IFMD

Wed., April 15, 1992
1:30-2:15 PM
Room 228, SVR Building

ABSTRACT

Unsteady time asymptotic flow states for high Reynolds number viscous incompressible flow problems are presented. Discrete frequency flows are shown for the square driven cavity, with periodic cases for $Re = 9000$ and $Re = 9600$, and with aperiodic cases for $Re = 9700$ and $Re = 10000$. The algorithm for these calculations is based on the fourth order PDE for incompressible fluid flow which uses the streamfunction as the only dependent variable, it is second order accurate in space and time, and it has a stability constraint of $CFL \leq 1$. The algorithm is extremely robust with respect to Reynolds number.

The direct numerical simulation of transition and turbulence requires numerical methods to be more than second order accurate in order to accurately represent the relevant scales of the physical processes. Recently developed finite difference algorithms are presented for unsteady convection equations, including the advection and inviscid Burgers equation in one space dimension, and the wave equation treated as a system, with remarks on diffusion equations and extension to higher space dimensions. The new algorithms that will be discussed all use local stencils, they range from third to seventh order in accuracy, they all have the same order of accuracy in both space and time, and they are all one step explicit methods (except for diffusion equations). Since all of the algorithms use a small local stencil, the number of degrees of freedom of known data required for higher order accuracy is obtained by higher information density than just the solution data. The use of a two point stencil (for some of the methods) allows for arbitrary grid spacing, though a convective stability constraint must be observed at each grid point. The use of local data for an explicit algorithm with high order accuracy avoids the requirement of using a global solution method such as compact differencing or spline based algorithms. There will be computational results for all of the algorithms that are presented.

CENTER FOR MODELING OF TURBULENCE AND TRANSITION

Biweekly Meeting Series (1992-7)

Kolmogorov Behavior of Near-Wall Turbulence and Its Application in Turbulence Modeling

by

Tsan-Hsing Shih

ICOMP

Wed., April 29, 1992
1:30-2:15 PM
Room 228, SVR Building

ABSTRACT

The near-wall behavior of turbulence is re-examined in a way different from that proposed by Hanjalic and Launder[1] and followers[2],[3],[4],[5]. It is shown that at a certain distance from the wall, all energetic large eddies will reduce to *Kolmogorov* eddies (the smallest eddies in turbulence). All the important wall parameters, such as friction velocity, viscous length scale, and mean strain rate at the wall, are characterized by *Kolmogorov* microscales. According to this *Kolmogorov* behavior of near-wall turbulence, the turbulence quantities, such as turbulent kinetic energy, dissipation rate, etc. at the location where the large eddies become "*Kolmogorov*" eddies, can be estimated by using both direct numerical simulation (DNS) data and asymptotic analysis of near-wall turbulence. This information will provide useful boundary conditions for the turbulent transport equations. As an example, the concept is incorporated in the standard k-ϵ model which is then applied to channel and boundary layer flows. Using appropriate boundary conditions (based on *Kolmogorov* behavior of near-wall turbulence), there is no need for any wall-modification to the k-ϵ equations (including model constants). Results compare very well with the DNS and experimental data.

CENTER FOR MODELING OF TURBULENCE AND TRANSITION

Biweekly Meeting Series (1992-8)

A Modeling of Bypass Transition

by

Z. Yang

ICOMP

Wed., May 13, 1992
1:30-2:15 PM
Room 228, SVR Building

ABSTRACT

A model for the calculation of bypass transitional boundary layers due to the freestream turbulence is proposed. The model combines a near wall $k-\epsilon$ model proposed for the fully developed turbulent flows with the intermittency of the transitional boundary layers. The intermittency factor is assumed to be a function of both the free stream turbulence and the shape factor of the boundary layer. Transitional boundary layers over a flat plate with different freestream turbulence level are calculated using the proposed model. It is found that the model calculations agree well with the experimental data and give a better prediction compared with other low Reynolds number $k-\epsilon$ models, which do not incorporate the intermittency effect.

CENTER FOR MODELING OF TURBULENCE AND TRANSITION

Biweekly Meeting Series (1992-9)

Finite-Volume Computations of Incompressible Flows with Complex Geometries

by

J. Zhu

ICOMP

Wed., June 10, 1992
1:30-2:30 PM
Room 228, SVR Building

ABSTRACT

A brief review is given of finite-volume procedures developed at the Institute for Hydromechanics, University of Karlsruhe, for calculating incompressible elliptic flows with complex boundaries. The procedures include: numerical grid generation, higher-order bounded convection schemes, zonal solution, simulation of two-phase flows, and near-wall turbulence modelling. Various application examples will be given.

CENTER FOR MODELING OF TURBULENCE AND TRANSITION

Biweekly Meeting Series (1992-10)

Development of the RPLUS code with Standard $k-\epsilon$ model and Their Applications

by

Jinho Lee

Sverdrup Technology, Inc.

Wed., June 24, 1992
1:30-2:30 PM
Room 228, SVR Building

ABSTRACT

The primary goal of this research effort is to develop a CFD tool which can be used in a variety of practical supersonic/hypersonic propulsion device development/analysis environments. One focus of this work has been to develop and validate the Reactive Propulsion code based on LU Scheme(RPLUS). This effort also includes the development of turbulence models which can be used in the predictions of highly complex flow environments inside of combustors.

This presentation will cover only a small part of a larger development effort and focus will primarily on the analysis, implementation, and development of the turbulence model capabilities of the RPLUS code.

Some of the issues which will be covered are; formulation of the turbulence models, the numerical technique used to solve the turbulence model equations, and modeling of compressibility effects. The primary numerical technique used in the RPLUS code is the LU-SSOR(LU scheme based on Successive Symmetric Over Relaxation) technique. Therefore, the turbulent kinetic energy transport and dissipation transport equations are also solved using the LU-SSOR numerical technique.

Both two and three dimensional turbulence model development are being developed for the RPLUS code. However, the majority of the presentation will focus on the development of the two dimensional k-ϵ models for the RPLUS code. Issues regarding compressible wall-function boundary conditions and compressibility effects will be addressed. Both low and high Reynolds number forms of the k-ϵ models are being developed. The "standard" low Reynolds number model of Launder-Sharma and Chien has been used in this study. The problems of primary interests are supersonic turbulent boundary-layers, shock-wave/boundary-layer interactions, and shear-layers in two or three dimensional environments.

CENTER FOR MODELING OF TURBULENCE AND TRANSITION

Biweekly Meeting Series (1992-11)

Unsteady Turbulent Flows

by

Reda R. Mankbadi
NASA Lewis Research Center

Wed., July 8, 1992
1:30-2:30 PM
Room 228, SVR Building

ABSTRACT

Current research activities emphasize computation/modelling of turbulent flows when basic flow is time-periodic. Wall-bounded flows and free shear flows exhibit different features when the basic flow is unsteady; and as such, different approaches are used to model them.

(A) In wall-bounded, oscillatory flows, two approaches are used to model turbulence: (I) Turbulence is assumed to behave in a quasi-steady manner, and steady-state models are directly extended to the unsteady case. This approach fails at high frequencies of oscillations. (II) Rapid distortion theory (RDT) is successfully adapted to aid in turbulence modelling of highly unsteady flows (high frequencies). The eddy viscosity hypothesis is replaced by the ratio of turbulent stresses/kinetic energy; which is given by RDT as a function of the accumulated rate of strain.

(B) In free shear flows (naturally unsteady, or excited to be unsteady), two approaches are investigated: (I) The large-scale (organized, coherent) component is modelled as instability waves interacting with each other as well as with the mean flow and the fine-scale (random, background) turbulence. Integrated kinetic-energy equations are then obtained for each scale of motion. The approach is successful in predicting results in good agreements with experiments in which excitation devices are used to control jet mixing and turbulence. (II) The other approach adopted is Large-Eddy Simulations (LES) with application to predicting the far-field noise of a supersonic jet.

CONTACT: William W. Liou, PABX 3-6682

CENTER FOR MODELING OF TURBULENCE AND TRANSITION

Biweekly Meeting Series (1992-12)

The Effect of Spanwise Variations in Momentum on Leading Edge Heat Transfer

by

David Rigby
Sverdrup Tech. INc.

Wed., July 22, 1992
1:30-2:30 PM
Room 228, SVR Building

ABSTRACT

A study of the effect of spanwise variation in momentum on leading edge heat transfer is discussed. Numerical and experimental results are presented for a circular leading edge and for a 3:1 elliptical leading edge. Direct comparison of the two-dimensional results, that is with no spanwise variations, to the analytical results of Frossling is very good. The numerical calculation, using the PARC3D code, solves the three-dimensional Navier-Stokes equations, assuming steady laminar flow on the leading edge region. Experimentally, increases in spanwise averaged heat transfer coefficient as high as 50% above the two-dimensional value were observed. Numerically, the heat transfer coefficient was seen to increase by as much as 25% percent. In general, the circular leading edge, under the same flow conditions, produced a higher heat transfer rate than the elliptical leading edge. As a percentage of the respective two-dimensional values, the circular and elliptical leading edges showed similar sensitivity to spanwise variations in momentum. By equating the root mean square of the amplitude of the spanwise variation in momentum to the turbulence intensity, a qualitative comparison between the present work and turbulent results was possible.

CONTACT: William W. Liou, PABX 3-6682

Appendix C
List of Member's Publications

Barton, J. M., Rubinstein, R. and Kirtley, K. R. "Nonlinear Reynolds Stress Model for Turbulent Shear Flows, " AIAA Paper No. 91-0609, (Jan. 1991).

Barton, J. M. and Rubinstein, R., "Nonlinerar Algebraic Reynolds Stress Model for Anisotropic Turbulent Flows, " 11th U. S. National Congress of Applied Mechanics, Tucson, AZ (May 1990).

Barton, J. M. and Rubinstein, R., "Renormalization Group Theory and Turbulence Modeling, " 2nd International Workshop on Chaos and Turbulence, Tsukuba, Japan (Jan. 1992).

Barton, J. M. and Rubinstein, R., "Renormalization Group Analysis of Turbulence-Driven Secondary Fows, " 11th Australian Fluid Mechanics Conference, Hobart, Australia (Dec. 1992).

Brown, S., Leibovich, S. and Z. Yang, "On the linear instability of the Hall-Stewartson vortex," Theoretical and Computational Fluid Dynamics, **2**, 27-46, (1990).

Duncan, B. S., Liou, W. W. and Shih, T.-H., "A Multiple-scale turbulence model for incompressible flow," NASA TM (to appear) (1992).

Duncan, B.S., Lumley, J.L., Shih, T.H. and To, W.M., "A new model for the turbulent dissipation" International Conference of Fluid Mechanics and Theoretical Physics, Bejing, China (1992).

Hsu, A.T. and Liou, M., "Computational analysis of underexpanded jets in the hypersonic regime," Journal of Propulsion and Power, **7**, No. 2, (1991).

Hsu, A.T., "Progress in the development of PDF turbulence models for combustion," 10th NASP Symposium, April 23-16, 1991, Monterey, California.

Hsu, A.T., "A study of hydrogen diffusion flames using PDF turbulence model," AIAA 91-1780, AIAA 22nd Fluid Dynamics Conference, June 24-26, 1991, Honolulu, Hawaii.

Hsu, A.T. and Chen, J.Y., "A continuous mixing Model for PDF simulations and its applications to combusting shear flows," 8th International Symposium on Turbulence Shear Flows, Sept. 9-11, 1991, Munich, Germany.

Lang, N.J. and Shih, T.-H., "A critical comparison of two-equation turbulence models," NASA TM 105237, (1991).

Liou, M. S. and Steffen, Jr., C. J., "A New Flux Splitting Scheme," NASA TM 104404 (1991).

Liou, W. W. and Shih, T.-H., "A two-scale model for compressible turbulent flows," NASA TM (to appear) (1992).

Liou, W. W. and Shih, T.-H., "On the basic equations for sencond-order modeling of compressible turbulence," NASA TM 105277 (1991).

Liou, W. W. and Morris, P. J., "Weakly nonlinear models for turbulent mixing in a plane mixing layer," Phy. Fluids (to appear).

Liou, W. W. and Morris, P. J., "The eigenvalue spectrum of the Rayleigh equation for a plane shear layer," Int. J. Num. Fluids, (to appear).

Liou, W. W., "A new energy transfer model for turbulent free shear flow," NASA TM (to appear) (1992).

Mansour, N N. and Shih, T.-H. and Reynolds, W. C., "The effects of rotation on initially anisotropic homogeneous flows," Physics of fluid A, **3**, 10, 2421-2425 (1991).

Michelassi, V. and Shih, T.-H., "Low Reynolds number two-equation modeling of turbulent flows," NASA TM 104368, (1991).

Michelassi, V. and Shih, T.-H., "Elliptic flow computation by low Reynolds number two-equation turbulence models ," NASA TM 105376, (1991).

Moin, P., Shih, T.-H., Driver, D. and Mansour, N., "Direct numerical simulation of a three-dimensional turbulent boundary layer," Physics of Fluids A **2**, 10, 1846-1853 (1990).

Rubinstein, R. and Barton, J. M., "Nonlinear Reynolds stress models and the renormalization group," Phys. Fluids A **2**, 1472 (1990).

Rubinstein, R. and Barton, J. M., "Renormalization group analysis of anisotropic diffusion in turbulent shear flow," Phys. Fluids A **3**, 415 (1991).

Rubinstein, R. and Barton, J. M., "Renormalization group analysis of the Reynolds stress transport equation," to appear in Physics of Fluids A, (July 1992).

Shabbir, Munich. A., "Experimental balances for the second moments for a buoyant plume and their implication on turbulence modeling," Eighth Symposium on Turbulent Shear Flows, 27-1-1 to 27-1-6 (1991).

Shabbir, A. and Shih, T.-H., "Critical comparison of second order turbulence models in homogeneous flows," Submitted to AIAA Annual meeting in Reno, Jan. 1992.

Shih, T.-H. and Lumley, J.L., "Kolmogorov behavior of near-wall turbulence and its application in turbulence modeling," NASA TM 105663 (1992)

Shih, T.-H., Chen, J.-Y. and Lumley, J. L., "Second order modeling of free turbulent shear flows," AIAA Journal, **30**, 6, 1553-1560 (1992).

Shih, T.-H. and Lumley, J.L., "A critical comparison of second order closures with direct numerical simulation of homogeneous turbulence," NASA TM 105351 (1991).

Shih, T.-H. and Hsu, A.-T., "An improved $k - \epsilon$ model for near-wall turbulence," AIAA paper, 91-0611 (1991).

Shih, T.-H. Shih, Shabbir, A. and Lumley, J.L., "Advances in Modeling the pressure correlation terms in the second moment equations," *The Lumley Symposium: Resent Developments in Turbulence*, November, 12-13, 1990, ICASE, NASA Langley Research Center, Edited by Gatski, T.B., Sarkar, S., Speziale, C.G.

Shih, T.-H., "An improved $k - \epsilon$ model for near-wall turbulence and comparison with direct numerical simulation," NASA TM 103221 (1990).

Shih, T.-H. and Mansour, N. N., "Modeling of near-wall turbulence," *Engineering Turbulence Modeling and Experiments*, September 24-28, 1990, Dubrovnik, Yugoslavia, Editors: W.Rodi, E.N. Ganic.

Shih, T.-H. and Reynolds, W. C., "A spectrum model for weakly anisotropic turbulence," Physics of Fluids A, **2**, 8, (1990).

Steffen, Jr., C. J., "An Investigation of DTNS2D for Use as an Incompressible Turbulence Modelling Test-Bed," NASA TM 105593 (1992).

Steffen, Jr., C. J. and Beard, L. M., "Incompressible Navier Stokes Solutions Using the Pseudo Compressibility Technique," *Proceeding of the 23rd Annual Pittsburgh Conference on Modeling and Simulation*, in print (1992).

Van der Vegt, Jaap, "ENO-Osher schems for Euler equations," submitted for publication (1992).

Van der Vegt, Jaap, "Overview of the Osher approximate Riemann solver for three-dimensional flows," NASA TM, in print (1992).

Yang, Z. and Leibovich, S "Nonlinear dynamics near the stability margin in rotating pipe flow," J. Fluid Mech. **233**, 329-347, (1991).

Yang, Z. and Leibovich, S., "Unstable viscous wall modes in rotating pipe flow," AIAA Paper 91-1801, (1991). Also submitted to Physics Fluids A for publication.

Yang, Z. and Shih, T.H., "A $k - \epsilon$ modeling of near wall turbulence," Proc. of 4th Intl. Sym. on CFD, Davis, CA, 1305-1310, (1991). Also available as NASA TM 105238.

Yang, Z. and Shih, T.H., "A $k - \epsilon$ calculation of transitional boundary layers," To appear in *Transition and Turbulence*, Springer-Verlag, 1992. Also available as NASA TM 105604.

Yang, Z. and Shih, T.H. "A new time scale based $k - \epsilon$ model for near wall turbulence," Submitted for publication. It is also to appear as a NASA TM (1992).

Yang, Z. and Shih, T. H., "A modeling of transitional boundary layers," In preparation.

Zhu, G., Lai, M.-C and Shih, T.-H., "Second-order closure modeling of turbulent buoyant wall plumes," NASA TM (in print) (1992).

REPORT DOCUMENTATION PAGE

Form Approved
OMB No. 0704-0188

1. AGENCY USE ONLY *(Leave blank)*

2. REPORT DATE
September 1992

3. REPORT TYPE AND DATES COVERED
Technical Memorandum

4. TITLE AND SUBTITLE
Center for Modeling of Turbulence and Transition (CMOTT)
Research Briefs–1992

5. FUNDING NUMBERS
WU–505–62–21

6. AUTHOR(S)

7. PERFORMING ORGANIZATION NAME(S) AND ADDRESS(ES)
National Aeronautics and Space Administration
Lewis Research Center
Cleveland, Ohio 44135–3191

8. PERFORMING ORGANIZATION REPORT NUMBER
E–7274

9. SPONSORING/MONITORING AGENCY NAMES(S) AND ADDRESS(ES)
National Aeronautics and Space Administration
Washington, D.C. 20546–0001

10. SPONSORING/MONITORING AGENCY REPORT NUMBER
NASA TM–105834
ICOMP–92–12; CMOTT–92–08

11. SUPPLEMENTARY NOTES
Report compiled by William W. Liou and T.-H. Shih, NASA Lewis Research Center (work funded under NASA Cooperative Agreement NCC3–233). ICOMP Program Director: Louis A. Povinelli, (216) 433–5818.

12a. DISTRIBUTION/AVAILABILITY STATEMENT
Unclassified - Unlimited
Subject Category 34

12b. DISTRIBUTION CODE

13. ABSTRACT ***(Maximum 200 words)***

This research brief contains the progress reports of the Research Staff of the Center for Modeling of Turbulence and Transition (CMOTT) from May 1991 to May 1992. It is intended as an annual report to the Institute for Computational Mechanics in Propulsion and NASA Lewis Research Center. A separate report entitled, "Workshop on Engineering Turbulence Modeling," covering some of the 1991 CMOTT Summer research activities was released earlier this year. The main objective of the CMOTT is to develop, validate and implement the turbulence and transition models for practical engineering flows. The flows of interest are three-dimensional, incompressible and compressible flows with chemical reaction. During this period, the research covers two-equation (e.g., k-ε) and algebraic Reynolds-stress models, second moment closure models, probability density function (pdf) models, Renormalization Group Theory (RNG), Large Eddy Simulation (LES) and Direct Numerical Simulation (DNS). Last year was CMOTT's second year in operation. CMOTT now has eleven members from ICOMP, NASA LeRC, and Sverdrup Technology Inc., working on various aspects of turbulence and transition modeling in collaboration with NASA-Lewis scientists and Case Western Reserve University faculty members. The CMOTT members have been continuously and actively involved in the international and national turbulence research activities. A biweekly CMOTT seminar series has been conducted with speakers invited from within and without the NASA Lewis Research Center, including foreign speakers. The current CMOTT roster and its organization are listed in Appendix A. Listed in Appendix B are the abstracts and the scientific and technical issues discussed in biweekly CMOTT seminars. Appendix C gives a list of references which are the papers contributed by CMOTT members in the last two years.

14. SUBJECT TERMS
Turbulence models

15. NUMBER OF PAGES
192

16. PRICE CODE
A09

17. SECURITY CLASSIFICATION OF REPORT	18. SECURITY CLASSIFICATION OF THIS PAGE	19. SECURITY CLASSIFICATION OF ABSTRACT	20. LIMITATION OF ABSTRACT
Unclassified	Unclassified	Unclassified	

NSN 7540-01-280-5500

Standard Form 298 (Rev. 2-89)
Prescribed by ANSI Std. Z39-18
298-102